ON THE NATURE OF EXPLOSIVELY DEVELOPING CYCLONES IN THE NORTHERN HEMISPHERE EXTRATROPICAL ATMOSPHERE

by

JOHN RICHARD GYAKUM

B.S., The Pennsylvania State University, 1975

S.M., Massachusetts Institute of Technology, 1977

SUBMITTED IN PARTIAL FULFILLMENT

OF THE REQUIREMENTS FOR THE

DEGREE OF

DOCTOR OF PHILOSOPHY

at the

MASSACHUSETTS INSTITUTE OF TECHNOLOGY

August, 1981

Signature of Author_____

Department of Meteorology and Physical Oceanography
August, 1981

Certified by_____

Thesis Supervisor

Accepted by_____

Chairman, Departmental Committee on Graduate Students

Undergrad
WITHDRAWN
MASSACHUSETTS INSTITUTE OF TECHNOLOGY
FROM
MAR 29 1982
MIT LIBRARIES

ON THE NATURE OF EXPLOSIVELY DEVELOPING CYCLONES IN THE NORTHERN HEMISPHERE EXTRATROPICAL ATMOSPHERE

by

John R. Gyakum

Submitted to the Department of Meteorology
and Physical Oceanography on 7 August 1981
in partial fulfillment of the requirements
for the degree of Doctor of Philosophy

ABSTRACT

Extratropical cyclones which intensify at rates greater than, or equal to 12 mb/12 h, are defined as explosively developing. This class of cyclone is primarily a maritime, cold-season phenomenon, and is often associated with hurricane-force winds, and cloud patterns not unlike that of a tropical cyclone. These cyclones may also be a necessary component in a realistic general circulation simulation, for explosive deepening is a characteristic of the vast majority of the hemisphere's deepest cyclones, which usually track toward their final resting places in the vicinity of the Icelandic and Aleutian lows.

A survey of four years of twice-daily NMC maps indicates an average of about 150 occurrences each year, with 12-h central pressure falls ranging up to 50 mb. A more detailed study for the 1978-1979 season shows that explosive development occurs over a wide range of sea-surface temperatures but, preferentially, near the strongest gradients. A quasi-geostrophic diagnosis of a composite incipient explosively-developing cyclone indicates instantaneous central pressure falls far short of those observed. An inspection of both 6-layer and 7-layer NMC primitive equation (PE) model sea-level pressure forecast maps indicates these models both consistently underforecast this class of cyclogenesis, in spite of the horizontal computational resolution in the latter model being one-half of the former. A similar study using the FNWC operational PE model yields comparable results.

A better documentation of this class of cyclone is achieved with a detailed case study of an intense storm which battered the liner *Queen Elizabeth II*, with the aid of an unusually large and timely data base. This cyclone had deepened nearly 60 mb in the 24-h period subsequent to 12 GMT, 9 September 1978, during which time deep cumulus

convection was observed in and around the storm center. Hurricane-force winds, a deep tropospheric warm core, and a clear eye in the cyclone center were all observed in this cyclone at 12 GMT on 10 September. Despite the existence of NOAA surface buoys, and the relatively high density of mobile ships in the North Atlantic, real-time weather analyses, subjective forecasts, and numerical prognoses of NMC and of FNWC all grossly erred in the intensity and track of this storm. Deficiencies in the real-time surface analysis of this case were compensated for by the addition of Seasat-A surface wind fields, and by reports from the freighter *Euroliner*.

In order to assess the amount of baroclinic forcing operating in this well-documented case, we have solved analytically the non-linear quasi-geostrophic omega and vorticity equations for an idealized thermodynamic structure, which can resolve baroclinic waves as shallow, or as deep as we choose. Calculations from this three-layer adiabatic, inviscid quasi-geostrophic model yield instantaneous vertical motions and deepening rates which are far less than those observed.

In order to assess the importance heating had on this cyclone's development, a method to evaluate the three-dimensional thermodynamic and dynamic structure of the atmosphere is proposed, so that we may evaluate potential vorticity changes in the vicinity of this cyclone. Results indicate a 24-h lower tropospheric generation of from 5 to 13 times the value observed at 12 GMT, 9 September. An evaluation of physical effects on thickness change following the surface center shows a large mean tropospheric temperature rise to be due to bulk cumulus heating effects, which implicate these effects as being a potentially significant factor in the extraordinary potential vorticity generation concurrent with this cyclone's explosive development.

These vertically-integrated values of heating provide a motivation for solving the non-linear quasi-geostrophic omega and vorticity equations forced by an idealized heating function, with specified horizontal scale, level of maximum heating, and total heating. Resulting theoretical omega profiles and height falls during the 24-h period of explosive development for the observed integrated values of heating, vorticity-stability parameter, and over a wide range of levels of maximum heating, easily account for the observed explosive cyclogenesis. It is hypothesized that the relatively weak baroclinic forcing operative in this case helped to organize the convective bulk heating effects on a scale comparable to the cyclone itself in an atmosphere which is gravitationally stable for large-scale motions, and gravitationally unstable for the convective scale. This CISK-like mechanism, evidently operative in the QEII case, is further hypothesized to be important in other explosively-developing extratropical cyclones, just as it is generally regarded to be crucial in tropical cyclone development.

Thesis Supervisor: Frederick Sanders
Title: Professor of Meteorology

ACKNOWLEDGMENTS AND DEDICATION

I am especially grateful to my advisor, Professor Frederick Sanders, who suggested the topic, made important suggestions at critical junctures of this research, and whose comments helped considerably to improve upon earlier versions of this thesis. I would also like to thank Professor Mark Cane and Professor Lance Bosart of the State University of New York at Albany for reading an early version of this thesis, making helpful comments, and engaging in many stimulating discussions about maritime cyclogenesis. Professor Cane, along with Dr. Vince Cardone of Oceanweather, Inc., introduced me to, and provided me with the Seasat data set. Members of the MIT convection club and fellow students, including George Huffman, Frank Colby, Brad Colman, Randy Dole, and Dr. Frank Marks made many helpful comments during the course of this research. Gene Norman contributed sutstantially to the data compilation for the work reported in Chapter 2, through the MIT Undergraduate Research Opportunities Program. Dr. Steve Tracton of the National Meteorological Center helped me to obtain the *Euroliner* log and barogram from the British Meteorological Office. Gratitude is expressed to the Fleet Numerical Oceanographic Center for providing me with sea-surface temperature analyses, and operational model output. My first four years at MIT were funded by a teaching assistantship under Professor James Austin, whose guidance, good nature, and helpful advice will long be cherished. This research was supported by the Office of Naval Research, and by the Naval Environmental Prediction Research Facility (NEPRF) under contract N 00014-79-C-0384. Special thanks go to Dr. Alan Weinstein, Director of Research at NEPRF, for his genuine interest in this work. Ms Isabelle Kole did a superb job in drafting the many figures for this thesis, while Ms Elizabeth Manzi typed the manuscript.

My days at MIT have been made much more pleasant by my association with fellow students Jim Barnard, Norma Gordon, and Tom Sterling. Fellow inhabitant of room 1616, Frank Colby, must also be acknowledged for his friendship and patience in allowing me to indulge in inundating the entire office with old and seemingly useless meteorological paraphernalia. I particularly want to thank Barbara Feer for her friendship, love, and understanding these last 5.5 years. Finally, I wish to thank my parents, to whom this thesis is dedicated, for their persistent loving support, guidance, and friendship.

TABLE OF CONTENTS

		Page
TITLE		1
ABSTRACT		2
ACKNOWLEDGEMENTS AND DEDICATION		4
TABLE OF CONTENTS		5
LIST OF FIGURES		7
LIST OF TABLES		10
CHAPTER 1:	INTRODUCTION	11
	1.1 Purpose and Background	11
	1.2 Approach and Specific Goals	15
CHAPTER 2:	SYNOPTIC-DYNAMIC CLIMATOLOGY OF THE "BOMB"	18
	2.1 Introduction	18
	2.2 Geographic Distribution	21
	2.3 Temporal Distribution and Intensities	24
	2.4 Relationship to Sea-Surface Temperature	29
	2.5 Quasi-geostrophic Diagnosis for 1978-1979 Sample	33
	2.6 Bomb Prediction by Operational Primitive-Equation Models	42
	2.7 Concluding Remarks	51
CHAPTER 3:	ON THE EVOLUTION OF THE QEII STORM	56
	3.1 Introduction	56
	3.2 Data Base	57
	3.3 Mesoscale and Synoptic Overview	60
	3.4 Operational Model Performance	104
	3.5 Vertical Motions and Quasi-geostrophic Diagnosis	112
	3.6 Thermodynamic Structure	129
	3.7 Potential Vorticity Fields	146
	3.8 Concluding Remarks	168
CHAPTER 4:	DYNAMICAL EFFECTS OF HEATING	176
	4.1 Introduction	176
	4.2 Model Description, Equations, and Solutions	177
	4.3 Geopotential Tendency	183
CHAPTER 5:	CONCLUSIONS AND SUGGESTIONS FOR FUTURE WORK	198

Page

APPENDIX 3.A 207

REFERENCES 218

BIOGRAPHICAL NOTE. 224

LIST OF FIGURES

Figure		Page
2.1	Surface maps of 4-5 February 1975.	19
2.2	Visible DMSP satellite view of February 1975 storm	20
2.3	Geographical distribution of bomb events	22
2.4	Petterssen's (1956) map of cyclogenesis frequency.	25
2.5	Frequencies of bomb occurrence as a function of month. . .	26
2.6	Bomb frequencies as a function of 12-h deepening rate. . .	28
2.7	Sea-surface temperature (SST) vs. bomb's 12-h central pressure falls	30
2.8	Maps of SST gradient magnitude	32
2.9	Composite of the incipient bomb.	35
2.10	Quasi-geostrophic intensification as a function of static stability	40
2.11	Bomb intensification vs. corresponding NMC PE intensification.	45
2.12	Bomb intensification vs. corresponding FNWC PE intensification.	48
2.13	Locations of NMC-PE simulated bombs.	50
2.14	Histogram of the intense low deepening rates	52
2.15	Frequency distribution of maximum 24-h deepening of typhoons.	52
3.1	Surface sectional plots at three-h intervals from 18 GMT, 8 September 1978 through 06 GMT, 9 September . .	61
3.2	Conventional radar summaries for 8-9 September 1978. . . .	67
3.3	GOES-east MB-enhanced satellite images covering the period 0030 GMT through 0600 GMT, 9 September. . . .	69
3.4	Upper-air charts for 00 GMT, 9 September 1978.	75
3.5	Hourly buoy time section	79

Figure		Page
3.6	Surface winds at 12 GMT, 9 September 1978.	80
3.7	Surface relative vorticity field for 12 GMT, 9 September 1978	83
3.8	Surface and upper-level charts for 12 GMT, 9 September 1978	85
3.9	Surface cyclone track along composite SST analysis	86
3.10	Surface and upper-air charts for 00 GMT, 10 September 1978.	89
3.11	Surface and upper-air charts for 12 GMT, 10 September 1978.	90
3.12	*Euroliner* barograph trace for 9-10 September 1978.	91
3.13	NMC final surface analysis for 12 GMT, 10 September 1978.	93
3.14	Surface winds for 12 GMT, 10 September 1978.	94
3.15	Surface relative vorticity field for 12 GMT, 10 September 1978.	96
3.16	GOES-east and DMSP satellite images of the cyclone covering the period 12 GMT, 9 September through 1330 GMT, 10 September 1978.	97
3.17	LFM-II initial analysis and forecasts initialized at 12 GMT, 9 September 1978.	105
3.18	FNWC initial analysis and forecasts initialized at 12 GMT, 9 September 1978.	109
3.19	Kinematically-computed omega profiles for WAL-JFK-IAD triangle at 00 GMT, 9 September 1978	113
3.20	Surface and 250-mb divergence fields, and 250-mb wind field for 12 GMT, 9 September 1978.	116
3.21	Observed vertical motions for 12 GMT, 9 September 1978 . .	117
3.22	Surface and 250-mb divergence fields, and 250-mb wind field for 12 GMT, 10 September 1978	119
3.23	Observed vertical motions for 12 GMT, 10 September 1978. .	120

Figure		Page
3.24	1000-850 mb thickness analysis and quasi-geostrophic omega profiles for 12 GMT, 9 September 1978.	124
3.25	Tropopause and 250-mb temperature analyses.	131
3.26	Observed and idealized temperature soundings for Caribou and Portland, Maine at 12 GMT, 9 September 1978.	135
3.27	Idealized temperature soundings for 12 GMT, 9 and 10 September 1978	140
3.28	Chatham soundings of temperature, dewpoint temperature, and equivalent potential temperature (θ_e) for 12 GMT, 9 September 1978	141
3.29	Meridional profiles of θ_e for 12 GMT, 9 September 1978.	144
3.30	Meridional profiles of θ_e for 12 GMT, 10 September 1978	145
3.31	Meridional profiles of potential vorticity for 12 GMT, 9 and 10 September 1978	149
3.32	Lower and upper tropospheric wind fields for September cyclone	158
3.33	Station locator map	174
4.1	Vertical profile of heating function.	179
4.2	Values of geopotential tendency $\hat{\chi}_H$ as a function of wavelength and peak level of heating	185
4.3	Geopotential tendency $\hat{\chi}_1$, as a function of wavelength and meridional temperature gradient, for $\hat{T}$ = 1°C	188
4.4	Heating-induced vertical motion profiles and corresponding pressure traces for various values of P_I, and for B = 21.9 (m/sec) mb.	190
4.5	Heating-induced theoretical pressure traces corresponding to B = 30.7 (m/sec) mb	194
4.6	Baroclinically-forced pressure traces	196

LIST OF TABLES

Table		Page
2.1	Summary of (6-L) PE and (7-L) PE model performance for observed cases of bombs.	44
2.2	Summary of FNWC PE model performance for observed cases of bombs	44
2.3	Summary of atmospheric performance for cases of (7-L) PE predicted bombs	49
3.1	Quasi-geostrophic parameters for 00 GMT, 10 September 1978	121
3.2	Quasi-geostrophic parameters for 12 GMT, 9 September 1978.	126
3.3	Quasi-geostrophic parameters for 03 GMT, 9 September 1978.	128
3.4	Potential vorticity changes due to diabatic effects of saturated storm-scale ascent	153
3.5	Thickness change budget	160

CHAPTER 1

INTRODUCTION

1.1 Purpose and Background

The purpose of this dissertation is to explore the problem of explosively intensifying extratropical cyclones. Great strides have been made in understanding the physics of extratropical cyclogenesis through baroclinic stability theory (Charney, 1947; Eady, 1949), and through the use of a simple two-layer quasi-geostrophic model (Phillips, 1954). Routinely forecasting the phenomenon, even with the more accurate primitive equations, operational forecasts employing this latter set of equations often fail to capture important cyclogenesis found over maritime regions (Leary, 1971), and occasionally fall short in continental cases (Tracton, 1972). These poorly forecasted, and often rapidly developing, cyclones are frequently associated with hurricane-force winds and therefore, are of great practical importance to their victims -- mainly shipping interests and coastal denizens, as we shall see later in this study.

Research into the nature of these explosive storms has been rather limited. The fact that surface intensification predicted by current operational dynamical models often falls far short of that which is observed suggests that computational or data resolution may be inadequate, or that some physical effect other than the commonly understood synoptic-scale baroclinic mechanism may be important. Indeed, investigators have suggested appreciable vorticity advection

over many deepening storm centers is decidedly lacking. Petterssen et al. (1962) have found that, while most of the sea-level development of land cases can be explained by upper-level vorticity advection alone, the intensification of oceanic cyclones commonly occurs under a generally unperturbed large-scale upper-level flow. Böttger et al. (1975) have shown a case of rather rapid cyclogenesis southwest of the British Isles to have taken place under a mainly zonal 500 mb flow. Thus, much of the research into the subject has been geared toward an alternative intensification mechanism.

Winston (1955) has documented a case in the Gulf of Alaska in which the most rapid intensification was confined to a 12-24 h time period, soon after an arctic airmass moved from the Alaskan continent out over the Gulf. Particularly, during this period, he found unspecified diabatic effects to have been responsible for much of the observed height changes aloft. Indeed, Pyke (1965) and Simpson (1969) have used data taken from weather ship P (located at 50°N, 145°W) for Winston's case to suggest the importance of sensible and latent heat exchange, from the ocean to the atmosphere, on cyclone development. Simpson has further suggested that organized deep convection, brought on by the large-scale static instability caused by advection of cold air over the relatively warm ocean waters, could be the mechanism responsible for low-level convergence, and the resulting rapid increase in cyclonic vorticity, "thus accounting for the rapid deepening that vorticity advection alone miserably failed to predict" (p. 66 of Simpson, 1973). The actual evidence she presents for deep convection initiating

explosive development of this cyclone was negligible, for the temperature soundings and exchange computations at ship P were located well to the west of the storm center.

Recently, there has been a considerable amount of controversy in the literature over whether the relatively weak polar lows in the eastern Pacific, and in the eastern Atlantic basins are fundamentally driven by baroclinic, or by convective processes. Mansfield (1974) has examined two polar lows which affected the British Isles, and found them to be generally confined below 700 mb throughout their lifetimes. He also found that, by applying Eady's (1949) perturbation theory for shallow baroclinic waves, the computed wavelength, phase speed, and growth rates are consistent with the observed values. Thus, instead of ascribing the evolution of polar lows to the cumulus convection sometimes observed in these systems, Mansfield, along with Harrold and Browning (1969) have argued in favor of the polar low being a well-understood baroclinic disturbance. Reed (1979) has agreed that polar lows are essentially baroclinic disturbances, although he has also indicated the possibility of Conditional Instability of the Second Kind (CISK, originally proposed by Charney and Eliassen, 1964 for the hurricane problem) playing an important role. Rasmussen (1979), in fact, has suggested that the polar low is fundamentally a CISK phenomenon, just as tropical cyclones have been hypothesized to be.

There have been even more explicit suggestions in the literature that cyclones in extratropical regions have common characteristics with that of the tropical cyclone. Spiegler (1971) has given an example of a

low which contained hurricane-force winds, a clear eye at the center, and yet was associated with horizontal temperature contrasts typical of the extratropical atmosphere. Bosart (1981) has shown the President's Day (19 February 1979) snowstorm, which dumped up to 60 cm of snow on the Washington, D.C. area, to have been associated with a cyclone whose explosive intensification was concurrent with the appearance of deep convection near its center, along with the display of an open eye at the low center.

Much prose exists in issues of the *Mariner's Weather Log*, and in the *Marine Observer* describing shipping interests encountering hurricane-force winds associated with cyclones of extratropical origin. Perhaps, however, there is none to match the strength of the following passage's implication that the cyclone which hit the British weather ship west of the British Isles had a structure similar to that found in a tropical cyclone:

> 20 March 1976. At 0600 GMT the weather chart had shown a small deepening depression centred to SW of station, it was expected to move NE and turn N later.
>
> The *Weather Surveyor* was keeping station in position 56°58'N, 20°58'W. During the afternoon of the 20th the vessel was lying stopped in a strong to gale SE'ly wind with a heavy swell from E and SE. From 1510 onwards, rapid moderation of the wind occurred and small breaks in the cloud cover appeared.
>
> At the time of the 1600 observation, visibility was 8 n miles and there were 7 oktas of strong convective cloud in all sectors, with a small clear area above the vessel. At 1630 the atmosphere appeared somewhat heavy, there was no wind and the

> vessel was rolling heavily in 'mixed' sea with a heavy southerly swell with a heavy easterly interposed. The pressure reached its lowest level -- 949.6 mb -- at this time.
>
> By 1640 the wind had become light NW'ly but then increased rapidly to severe gale force 9 by the time of the 1715 pilot balloon ascent. Within the next hour the visibility was reduced to 45 metres in hail and blowing spray. During the next three violent hours, mean winds in excess of 70 knots were measured with gusts exceeding the limit of the wind-indicator scale (90 knots), one gust was estimated to be 95 knots. From 2100 onwards a moderation set in with a decrease in wind speed to gale force 8 to severe gale 9 with occasional gusts to storm force 10.
>
> (1977, Meteorological Office)

1.2 Approach and Specific Goals

We shall approach the problem by defining a "bomb" in Chapter 2, and exploring its geographical and temporal distribution over a period of 4 years. Since many of the bombs occur over maritime areas, a detailed study of the 1978-1979 season will be conducted to examine the relationship of bomb activity to the temperature of the underlying sea-surface. A composite bomb for this same season is constructed, and a quasi-geostrophic model is used to diagnose its dynamical characteristics. We will also examine the current capabilities of the operational models at the National Meteorological Center (NMC), and at Fleet Numerical Weather Central (FNWC) in forecasting this class of cyclogenesis.

A better documentation of this class of cyclone is achieved in Chapter 3 with a case study of an extreme case of a bomb. Every piece of available information will be used to construct a rather detailed

picture of the dynamic and thermodynamic structure of this extraordinary case. A comparison of the findings of this case with known characteristics of tropical cyclones will be made, along with an evaluation of why operational forecast models performed so poorly in this case. The fundamental question of whether baroclinic and/or convective effects were important in this disturbance will be addressed.

The dynamical effects of heating will be quantified in Chapter 4 through solving the non-linear omega and vorticity equations analytically for a specified three-dimensional heating function. We will use as input to these equations results similar to those found in our case study of Chapter 3. Results of the computations will be compared with those of other investigators who have studied cyclogenesis -- both tropical and extratropical. Aside from assessing quantitatively the importance heating likely had on the explosive cyclogenetic development of our case, we will examine the probable physical relationship of the bomb to that of the tropical cyclone. It is generally accepted that cumulus convection plays a crucial role in the development and maintenance of tropical cyclones. Riehl and Malkus (1961) have shown this to be the case observationally, while Charney and Eliassen (1964), Kuo (1965), Ooyama (1969), and more recently Willoughby (1979) have shown theoretically that tropical cyclones are forced circulations driven by diabatic effects of cumulus convection. A means by which cumulus convection can act as crucial forcing for explosive extratropical cyclogenesis is discussed.

It is hoped this study will help to answer some of the questions raised by many of the investigators mentioned in this chapter. Chapter 5 will summarize the results of this dissertation, and make suggestions for future operational and research efforts germane to the problem.

CHAPTER 2

SYNOPTIC-DYNAMIC CLIMATOLOGY OF THE "BOMB"

2.1 Introduction

We shall arbitrarily define a bomb as an extratropical low whose sea-level central pressure falls at least 1 mb h^{-1} for 12 h. The manner in which this criterion separates this class of cyclone from that of all extratropical cyclones will be discussed later in this chapter. An extreme example of the development of a storm of this type has appeared in Sanders and Gyakum (1980), and is shown here in Fig. 2.1. The central intensity is known only at the initial and final times, for the coverage of ship observations near the center during the period of extraordinary deepening is sparse. Note the strongest winds occur only 110 km from the center, and the radial profile of wind near the center likely resembles that of a tropical cyclone. The storm develops along the leading edge of a bitterly cold air outbreak over the western Atlantic, but the cold air does not penetrate to the low center.

A Defense Meteorological Satellite view (Fig. 2.2), showing this storm about midway through the illustrated period, shows a major "head cloud" mass of great meridional extent, considered by Jalu (1973), and by Böttger *et al.* (1975) to be characteristic of explosive deepening. Deep convection is shown along the rear edge of the main cloud mass, corresponding to the cold front. There is also an eye-like circular clear area about 60 km in diameter near 43°N, 43°W, and at the estimated

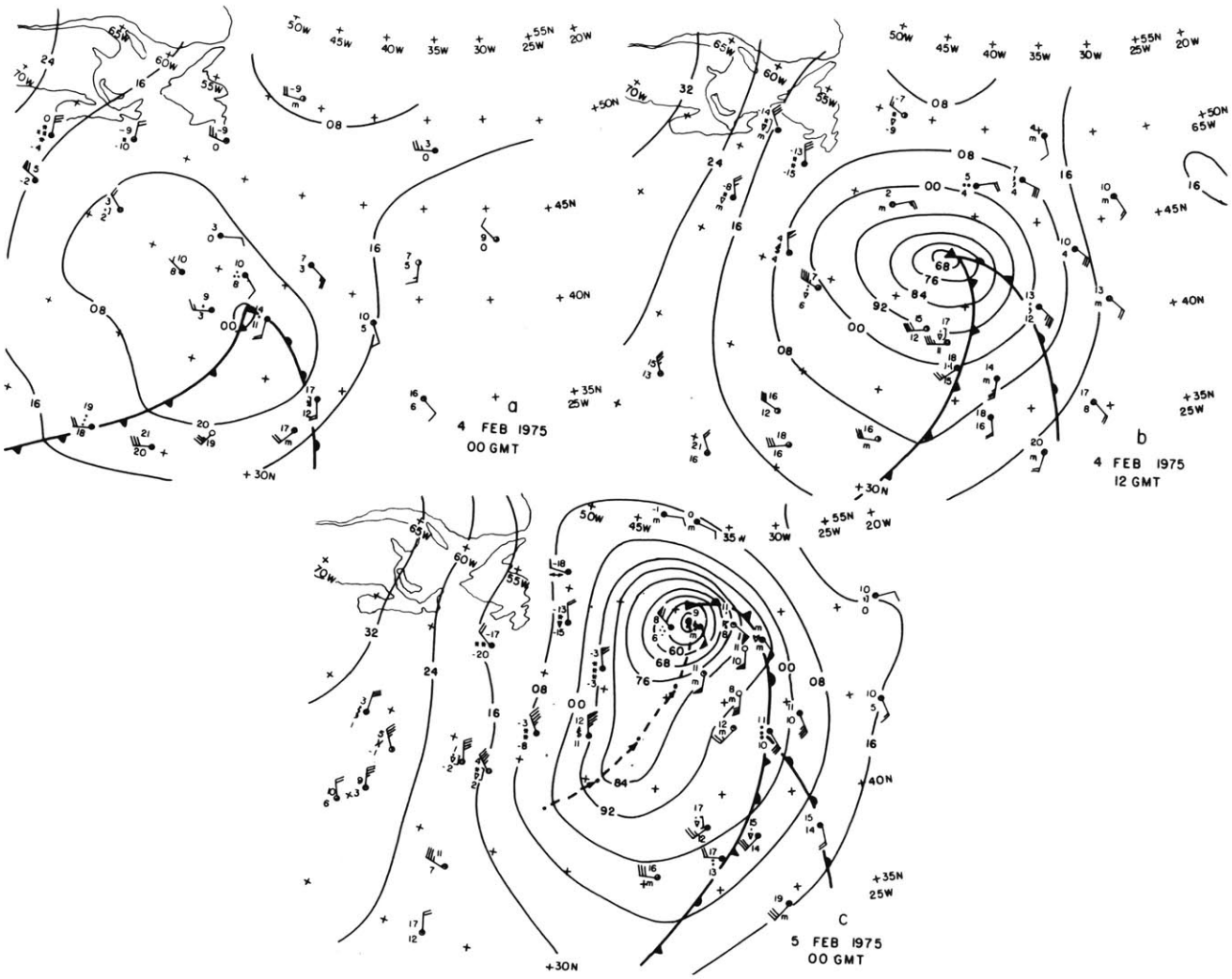


Fig. 2.1. (from Sanders and Gyakum, 1980) Surface maps, with isobars of sea-level pressure at 8-mb intervals. Selected ship observations are represented by a simplified plotting model. Pressures, not shown, agree closely with isobars. Six-h positions along the track of the center are shown as dots along the dashed trajectory.

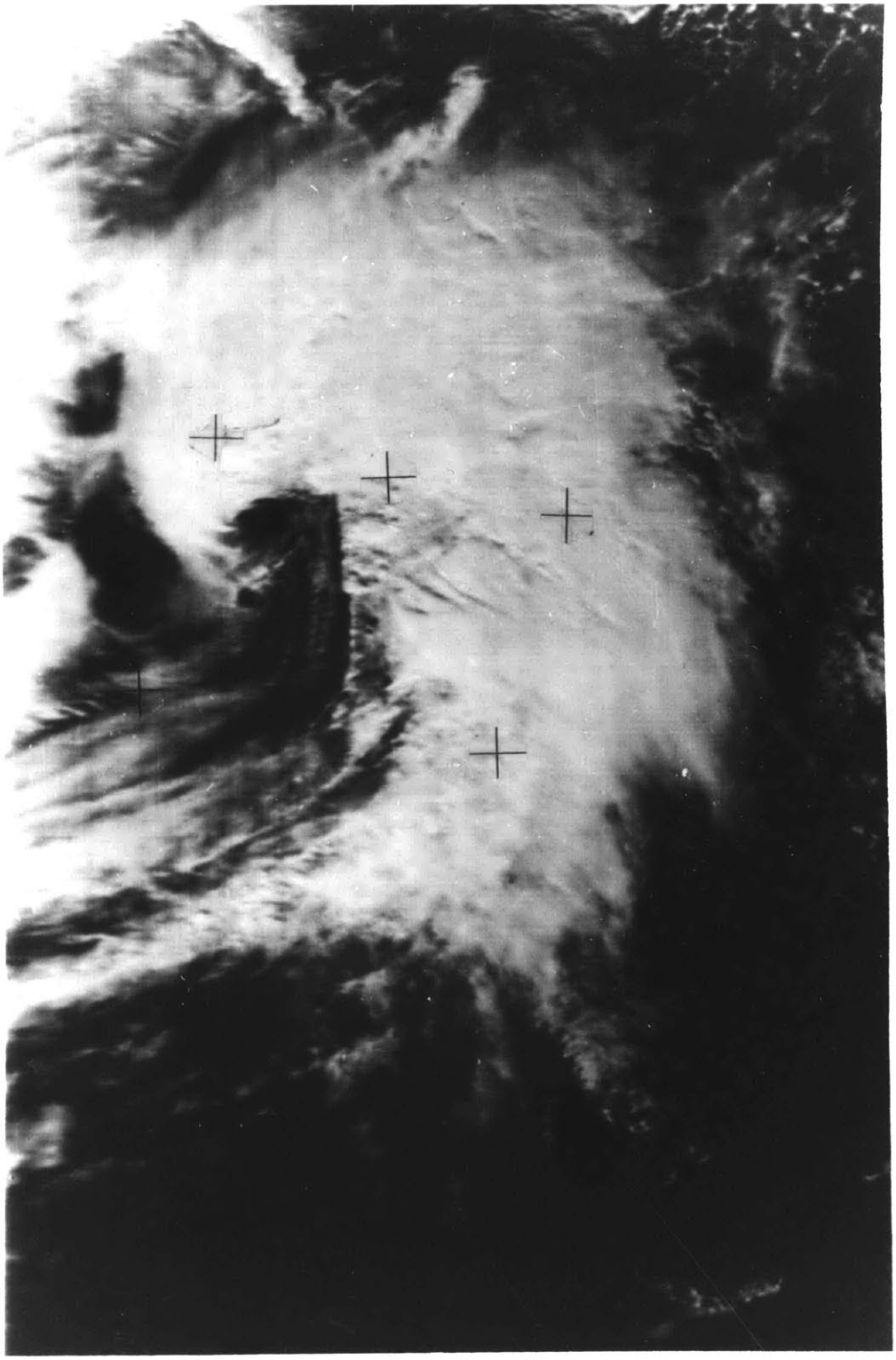


Fig. 2.2. Visible Defense Meteorological Satellite Program (DMSP) view of the storm at 1345 GMT 4 February. Three co-linear cross-hairs represent locations, from left to right, 45°N, 45°W, 45°N, 40°W, and 45°N, 35°W. The remaining two represent similarly, locations 40°N, 45°W and 40°N, 35°W.

surface center position. Although these characteristics appear to be typical, we shall explore in more detail the thermodynamic and dynamic structure of a similarly intense case in the next chapter.

2.2 Geographical Distribution

This class of cyclone has been studied for the 44-month period beginning 1 September 1977 through an examination of the twice-daily NMC-analyzed surface analyses of the Northern Hemisphere from longitudes 130°E eastward to 10°E. A geostrophically equivalent critical deepening rate was obtained for a latitude ϕ by multiplying our 12 mb $(12\ h)^{-1}$ rate by $(\sin\phi/\sin\phi_0)$, where ϕ_0 was chosen arbitrarily as 45°N. This critical rate therefore varies from 17 mb $(12\ h)^{-1}$ at the pole to 7 mb $(12\ h)^{-1}$ at latitude 25°N, the southern limit of the phenomenon in our sample.

Fig. 2.3 shows the geographical distribution of the bomb for this period. The smoothed area-normalized frequencies shown are obtained as one-eighth of the sum of four times the raw central frequency plus the sum of surrounding raw frequencies. The normalization factor is $(\cos 42/\cos\phi)$, where ϕ is the mean latitude for the 5° x 5° quadrilateral. Clearly the bomb is mainly a maritime event, with appreciable continental occurrences being confined to eastern North America. Maximum frequencies generally occur in the western portions of both the Atlantic and Pacific oceans, and within or just to the cold side of the Florida-Gulf Stream and Kuroshio currents, respectively.

In the Pacific, there is an additional area of maximum bomb

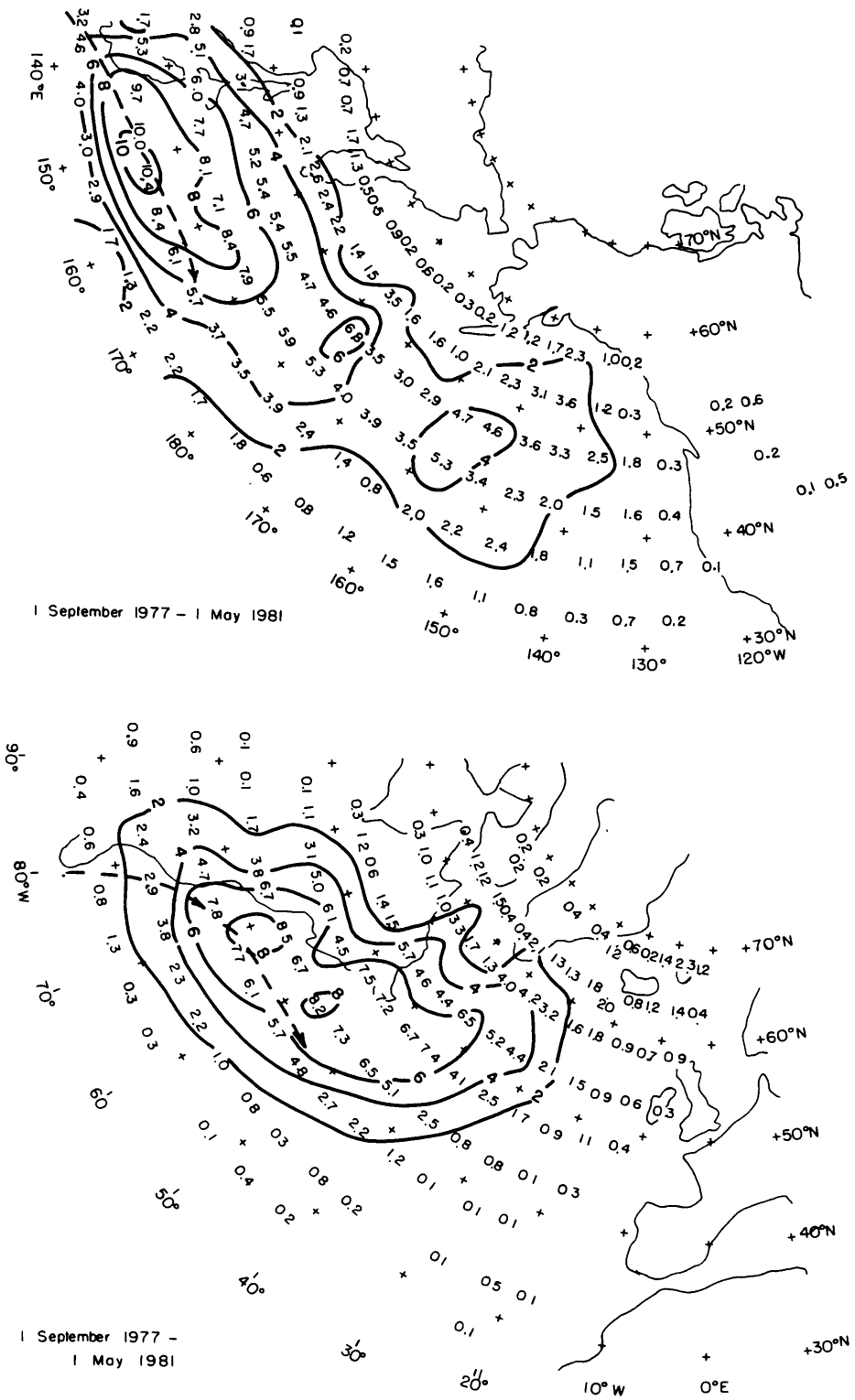


Fig. 2.3. Geographical distribution of bomb events for the Atlantic and Pacific basins for the 44-month period beginning 1 September 1977. The position of the bomb is the origin of the track segment for the qualifying 12-h period. Smoothed area-normalized non-zero frequencies appear in the appropriate 5° x 5° quadrilateral of latitude and longitude. Heavy-dashed lines represent the mean winter position of the Florida and Gulf Stream currents in the Atlantic, and the Kuroshio current in the Pacific (after Sverdrup et al. 1942, Chart VII).

activity, north of 40°N and east of 160°W. This area is close to where Petterssen (1956, p. 267) shows a minor maximum of cyclogenesis frequency, and where others (including Haurwitz and Austin, 1944) show a mean winter position of a polar front separate from the one in the western part of the ocean. This feature persists each of the four years, but is of strength comparable to the westernmost maximum only in 1977-1978. There is a third center of activity, which is north of 40°N, and fluctuates from as far west as 168°E in the 1978-1979 12-month period (beginning September 1) to 177°W in 1980-1981.

Virtually all of the explosive cyclogenesis in the North Atlantic is confined between 30°W and 80°W, and between 30°N and 60°N. There is a decided lack of bomb activity in the vicinity of the Icelandic and Aleutian lows, which are simply statistical ensembles of the many cyclones present in these regions. These two regions are the resting places of the mobile cyclones, rather than where active cyclogenesis occurs.

Our area of study excludes most of Europe, North Africa and Asia, where the explosively deepening cyclone is probably either absent altogether or quite rare, even over the Mediterranean Sea. Indeed, an inspection of daily sea-level pressure charts compiled by the Free University of Berlin (Berlin, 1978) for the one-year period beginning 1 September 1978, and covering the area from longitudes 0° eastward to 35°E and from 35°N to the pole, reveals no explosively developing (using a normalized 24 mb/24 h deepening criterion) cyclones in the Mediterranean Sea, and only one in the entire domain, northeast of Finland.

Figure 2.4 shows Petterssen's (1956, p. 267) chart of initial cyclogenesis frequency. Note the major maximum of cyclogenesis in the Mediterranean Sea has been eliminated by our 24-h bomb selection criterion described above, and that virtually all of the extensive cyclogenesis found by Petterssen on the North American continent has also been eliminated by our bomb selection criterion.

2.3 Temporal Distribution and Intensities

Figure 2.5 shows mean 30-day frequencies for each of the 12 months. Clearly, this phenomenon is found mainly during the cold season, although a few bombs do occur in the summer months, as is evidenced by the bomb associated with the tragic loss of life during the August 1979 Fastnet yacht race (Rice, 1979). September is a relatively quiet month for bombs with the mean 30-day frequency being about six, but a dramatic increase takes place during October to almost 18. A more gradual increase occurs through February, when an average of over one bomb occurs each day in our domain. The bomb frequency then declines rapidly until only one each three days occurs in April, one in five days in May, and less than one in 30 in June.

There is, however, substantial year-to-year variability in these monthly frequencies -- peaks may be expected in any of the months November through February. The Atlantic (east of 80°W) and Pacific (west of 120°W) basin frequencies, also shown in Fig. 2.5, closely follow the total pattern, although the total field is generally not representative of the concurrent strong cyclogenetic behavior in the individual basins.

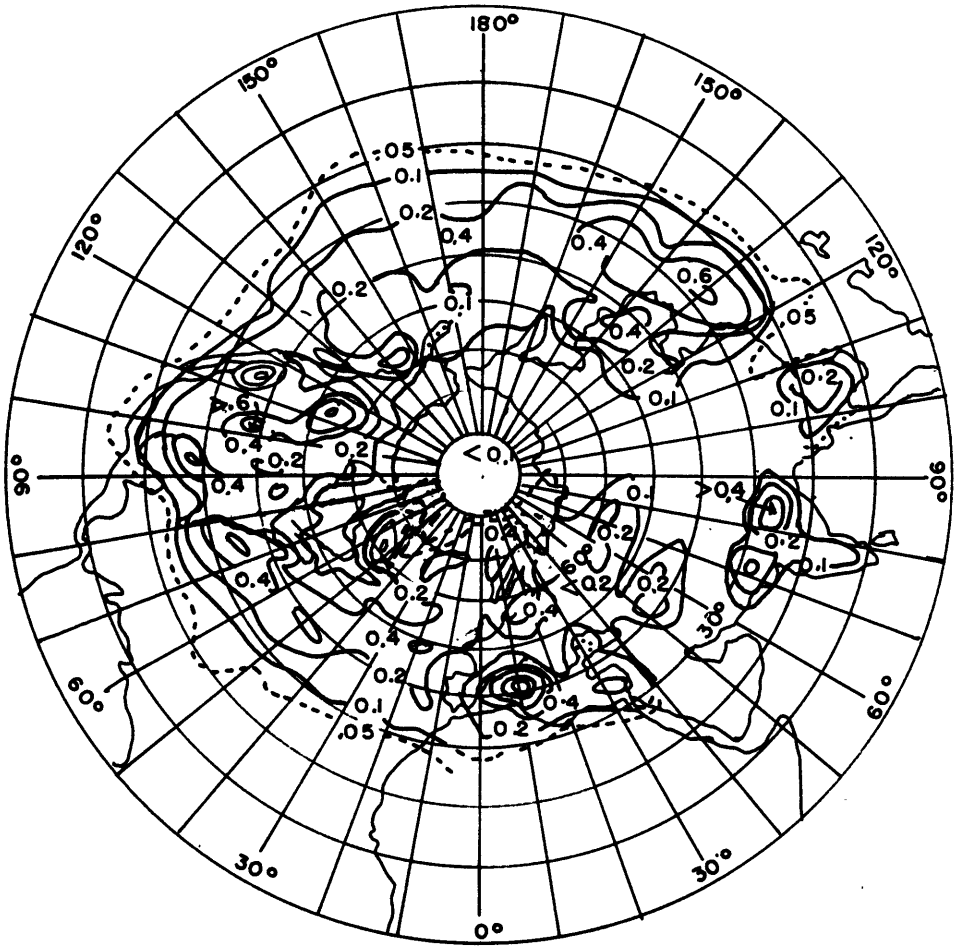


Fig.2.4. (from Petterssen, 1956, p. 267) Percentage frequency of occurrence of cyclogenesis in squares of 100,000 km^2 in winter (1899 to 1939).

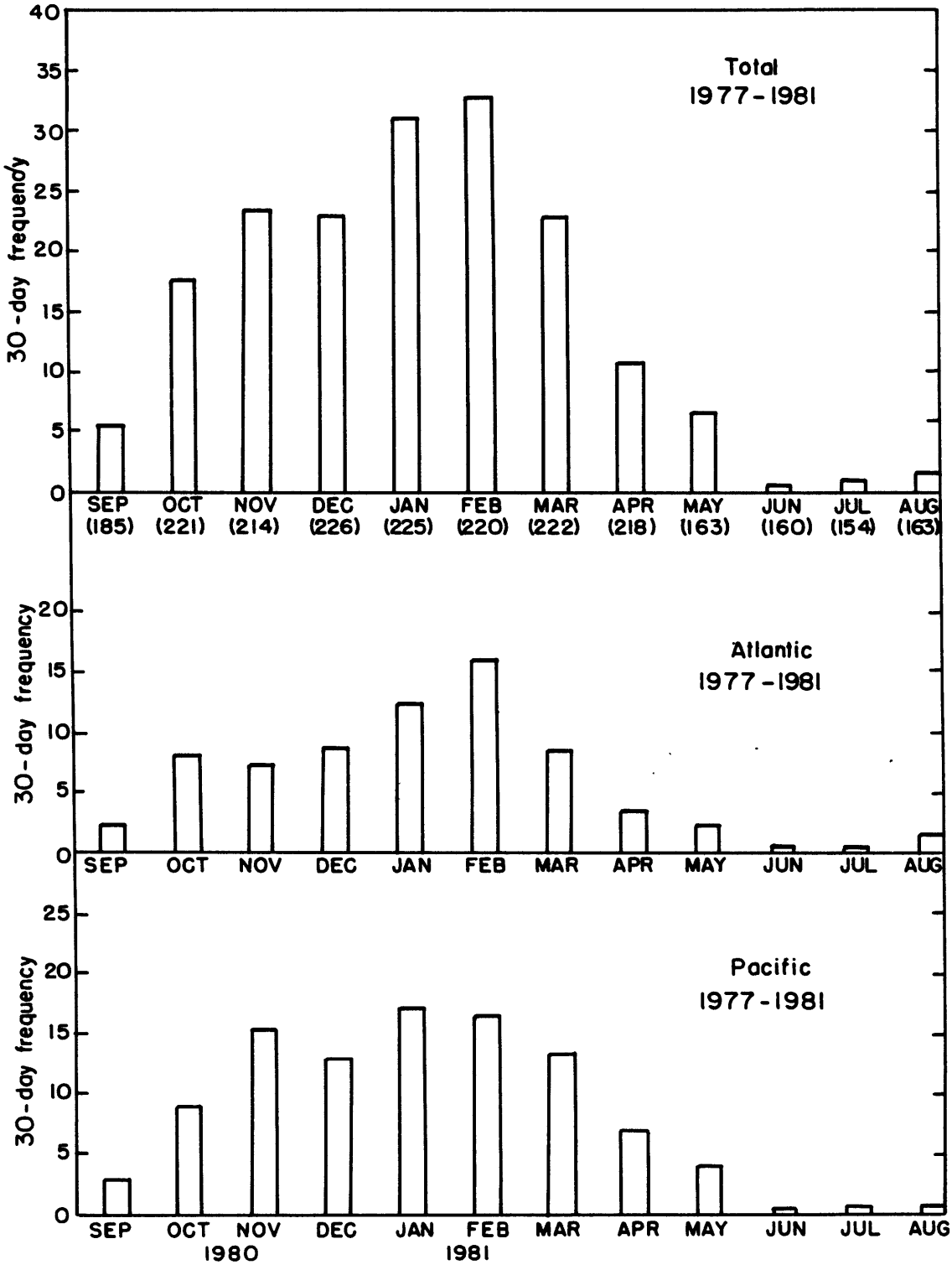


Fig.2.5. 30-day frequencies of bomb occurrence for 1977-1981 as a function of month for the total domain, and for the Atlantic and Pacific basins. As implied in the text, four years of data were obtained for the months September through April, and three years for May through August. Numbers below each month indicate the number of 12-h periods considered for that month.

Of course, our results are based almost entirely on the NMC analyses and, owing to a lack of key ship observations at critical times and places, some bombs either escaped detection altogether, or their intensities were greatly underestimated. An excellent example of the fact that these analyses will inevitably err on the side of conservatism concerning this phenomenon is that of our reanalysis of the incredible Atlantic storm of 9-10 September 1978, in which the dragger *Captain Cosmo* was lost and the liner *Queen Elizabeth II* was damaged (NOAA, 1979). Our reanalysis of this case, shown in the next chapter, shows a central pressure of 945 mb at 12 GMT on the 10th, with the preceding 12-h central pressure fall being 45 mb, while the NMC analysis showed a value of 980 mb, attributable to lack of real-time information from the freighter *Euroliner*, which defined the great intensity of the center.

The bomb frequency as a function of deepening rate Y is shown in Fig. 2.6. Y is the 12-h central pressure fall (mb) times the normalization factor (sin 45/sin ϕ), where ϕ represents the mean latitude of the cyclone center during its 12-h track. These distributions are skewed toward the lower value of 12 mb $(12\ h)^{-1}$ with the most extreme value the result of a reanalysis of the QE II case. The issue of whether these more extreme cases are fundamentally different from those of more typical cyclogenesis will be discussed later in this chapter, and in Chapter 3.

Fig. 2.6 indicates the Pacific basin contains about 40% more bombs than the Atlantic. We can, from this sample, examine a possible

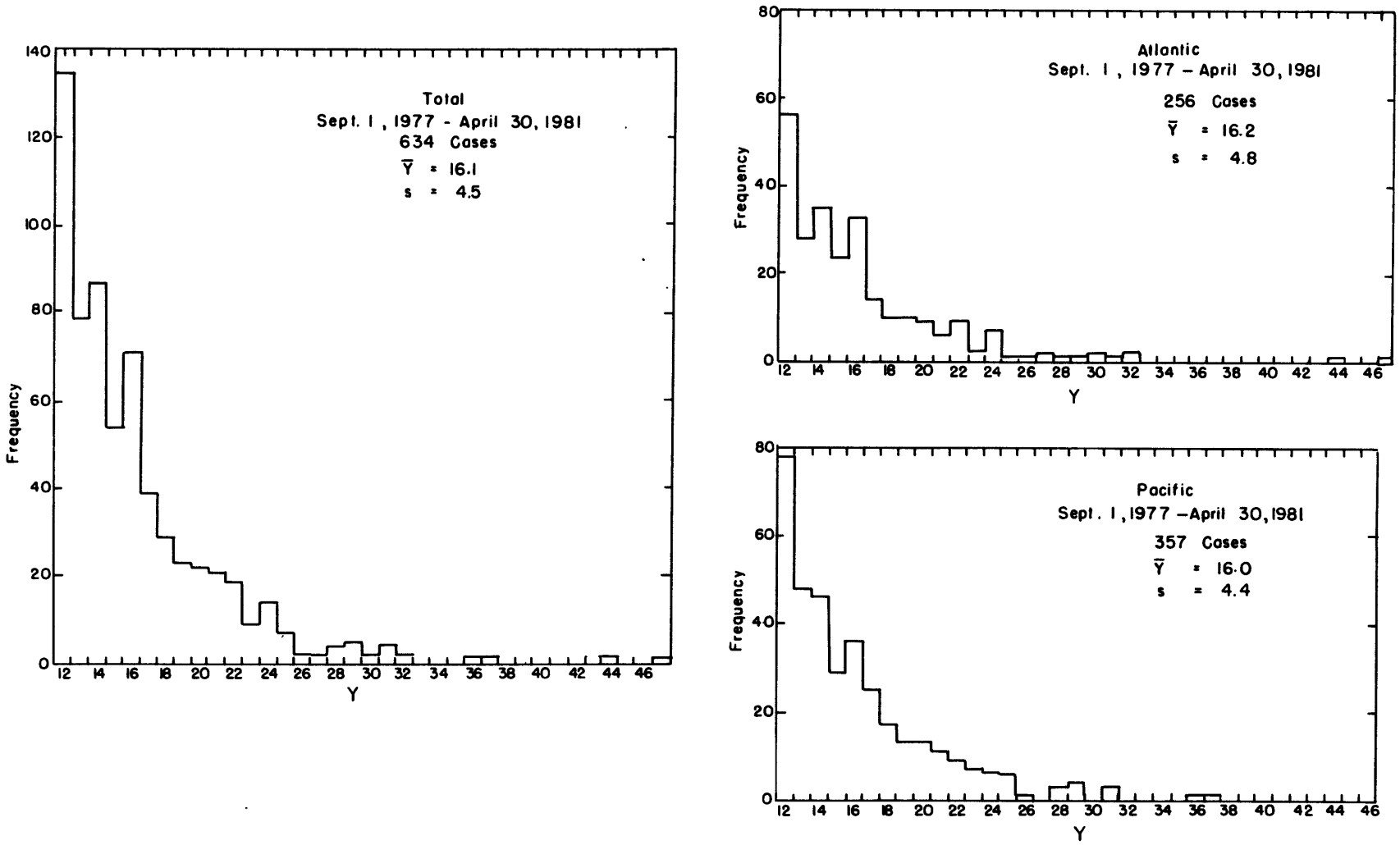


Fig. 2.6. Bomb frequencies as a function of normalized 12-h deepening rate Y for the 44-month period beginning 1 September 1977. $\bar{Y}$ and s indicate the mean and standard deviation, respectively, of each sample.

time bias in the data. The 00-12 GMT deepeners represent 48.4% of the total sample, 46.5% of the Pacific sample, and 50.8% of the Atlantic sample. An unbiased normal distribution of 00-12 GMT frequencies for the Pacific yields a 9.3% probability of so few 00-12 GMT deepeners. Although this statistic does not give us great confidence that a time bias exists in this basin, generally poor Pacific ship coverage at 12 GMT (2100 through 0300 local time) relative to 00 GMT may play a role in this statistic.

2.4 Relationship to Sea Surface Temperature

The deepening rates discussed above are comparable to those shown by Holliday and Thompson (1979) for tropical cyclones. We considered whether a minimum sea surface temperature is required for explosive extratropical cyclogenesis, as for tropical cyclone development. Sea surface temperatures (SST's) at the bomb center for the season 1978-1979 at the beginning of the 12-h growth period were obtained from daily charts provided by the Fleet Numerical Oceanographic Center. A plot of these SST's against the normalized deepening rate appears in Fig. 2.7.

Bombs occur over a large range of SST's, from 0 to 23°C. When deepening was related to the warmest SST within 90 n mi of the center, results were virtually identical. There is a slight positive (0.22) correlation between the underlying SST and the 12-h deepening rate. Evidently, extratropical bombs do not display the sensitivity

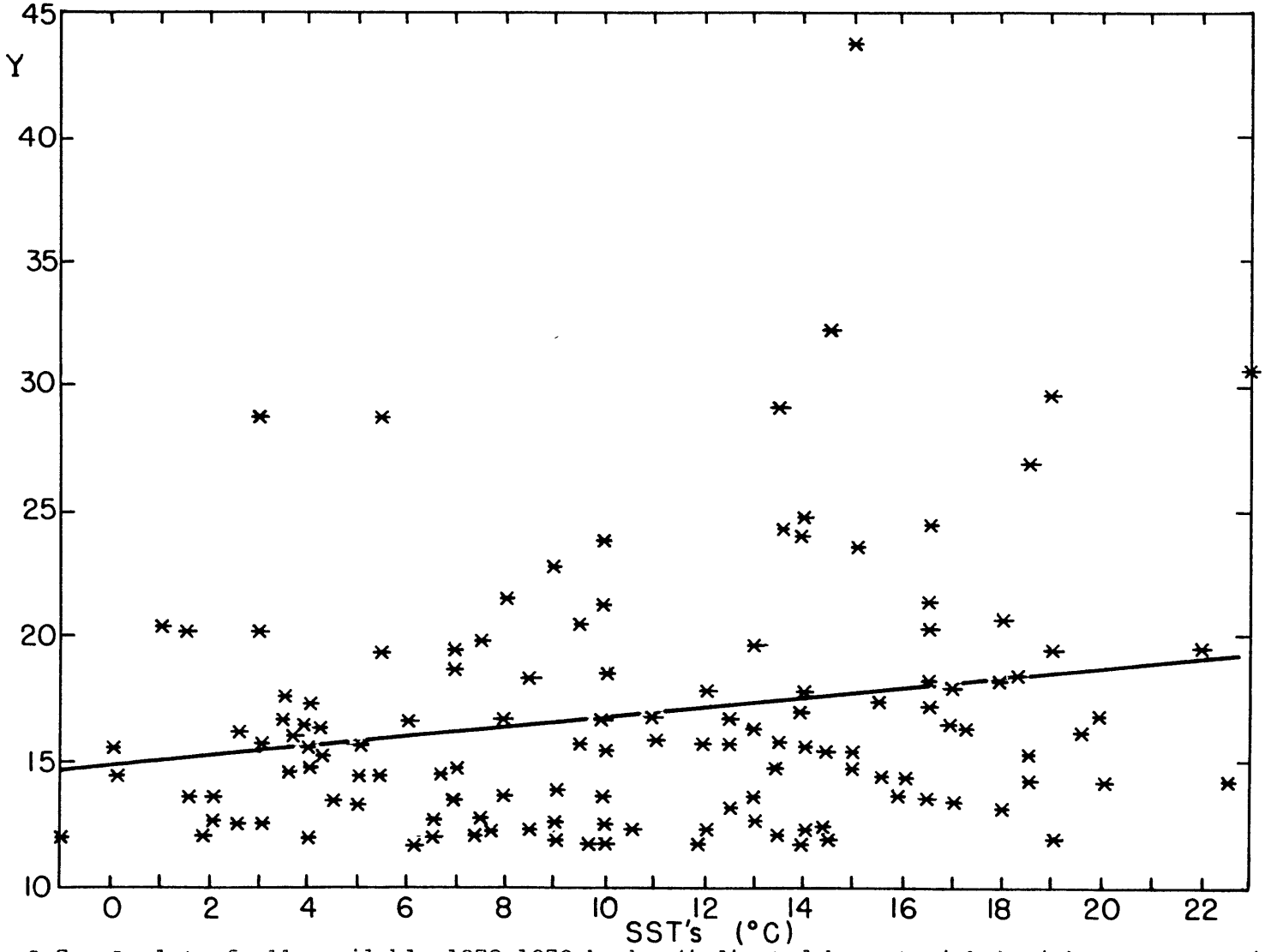


Fig. 2.7. A plot of all available 1978-1979 bombs (indicated by asterisks) with respect to its underlying SST and its subsequent 12-h central pressure fall. The ordinate Y is defined as in Fig. 2.6. Solid line is the least squares fit.

to SST's which tropical cyclones do, as shown observationally by Holliday and Thompson (1979), and theoretically by Miller (1958).

Nevertheless, Winston (1955) and Pyke (1965), among others, have associated rapid cyclogenesis with the strong sensible and latent heat exchange between cold continental air and the relatively warm sea surface. This exchange should be particularly intense for cold air which moves rapidly across a strong SST gradient toward relatively warm water. The resulting low static stability, in addition to low-level baroclinicity, may also play a role in rapid cyclogenesis. Staley and Gall (1977) have used a four-level quasi-geostrophic model to indicate the importance of low static stability and strong vertical wind shear in the lower layers in enhancing growth rates of relatively short baroclinic waves. An analysis of the SST gradients would then indicate maritime areas with strong low-level baroclinicity, and with a susceptibility to a dramatic air-mass modification.

Fig. 2.8 shows the 15 January 1979 analyses of the magnitude of SST gradients for the Atlantic and Pacific oceans. This date was chosen because it is close to the peak period of bomb frequency. Maps for other times throughout the winter season indicate similar fields. A comparison with Fig. 2.3 reveals that explosive cyclogenetic events tend to occur in and around the areas of most intense SST gradients. These gradients in the Atlantic basin are strongest in longitudes west of 40°W and between latitudes 35 and 50°N, the same region where most of the Atlantic bombs occur. The gradient fields in the Pacific are more diffuse with at least 2°C differences noted throughout the

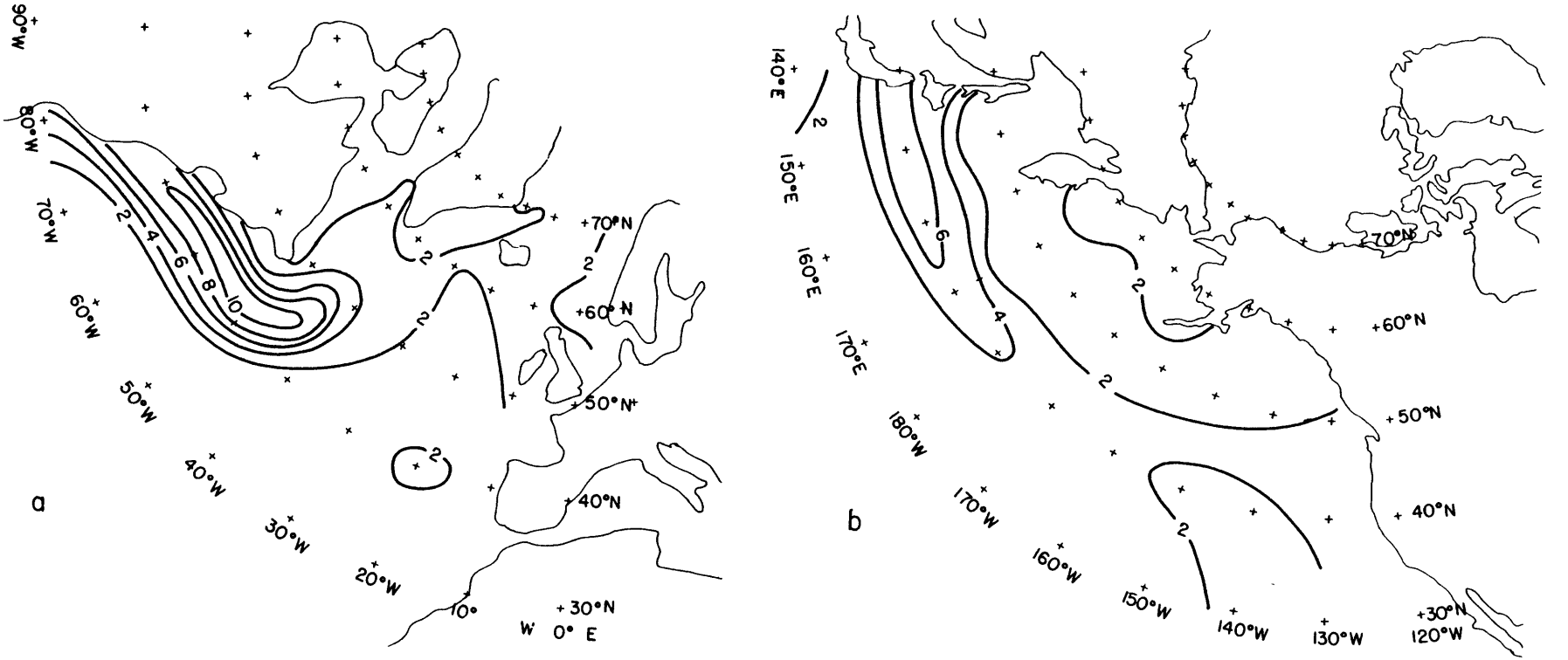


Fig. 2.8. Analysis of the magnitudes of the local SST gradient evaluated over a 180 n mi distance interval for 15 January 1979 in the Atlantic and Pacific basins. Isopleth units are in °C (180 n mi)$^{-1}$.

band between latitudes 40 and 50°N. The maximum gradients are observed east of Japan, close to the location of the frequency maximum of Pacific bombs.

The maximum gradients in the western Atlantic are nearly twice as large as their counterparts in the western Pacific. This difference characterizes the long-term mean patterns as shown, for example, by Sverdrup et al. (1942, Chart II). The difference in maximum gradients suggests that any preference for the more explosive bombs to occur in the Atlantic basin may be physically real, rather than an artifact of uneven data coverage. This preference was, in fact, observed in Sanders and Gyakum (1980) for the 1978-1979 season. However, Fig. 2.6 indicates that for the four-year period, any such preference is not observed in our sample.

2.5 Quasi-geostrophic Diagnosis for 1978-1979 Sample

Sanders and Gyakum (1980) have described the relationship of the bomb to the 500 mb flow patterns, and have found, on the basis of 252 cases, that the mean displacement from the surface center of the developing bomb to the 5520 m contour trough (which, during the cold season, lies along or just poleward of the center of the belt of strongest flow) was 400 n mi toward the west-southwest. This relationship of the developing surface low center with respect to the mobile 500 mb trough is qualitatively typical of deepening baroclinic cyclones, and is similar to the scenario provided by Petterssen (1956, p. 335). The quantitative aspects of this explanation will be explored in this section.

To diagnose dynamical characteristics of the storm, we have constructed composite patterns of sea-level pressure and thickness from 1000 to 500 mb for the beginning of the 12 h period of explosive deepening. We studied disturbances originating between latitudes 40 and 50°N, a region containing 84 of the year's 150 bombs. For each case we obtained, from routine facsimile maps, three thickness lines -- one for the value directly over the low center and one each for values 12 dam lower and higher. These lines were traced from 20° longitude west to 20° longitude east of the center. We also constructed two isobars representing pressures 8 and 16 mb greater than the central pressure of the low. The composite thickness patterns were obtained by averaging the patterns for the individual cases. The isobars for each case were determined by finding the radii in a polar coordinate system every 45° in direction from the low center, and composites were obtained by averaging. Because of illegible or faulty maps, missing thickness patterns, and occasional unusually distorted patterns felt to be nonrepresentative, we could use only 45 of the 84 cases in the composites. However, the frequency distribution of the normalized deepening rates in this smaller sample is quite similar to the one shown in Fig. 2.6. The sample was stratified on the basis of the pressure rise from the low center to the adjacent northward col. If the value was less than 16 mb the case was classified as one of weak circulation: otherwise one of strong circulation. Figs. 2.9a and 2.9b show the composites for weak and strong circulation, respectively. Although the

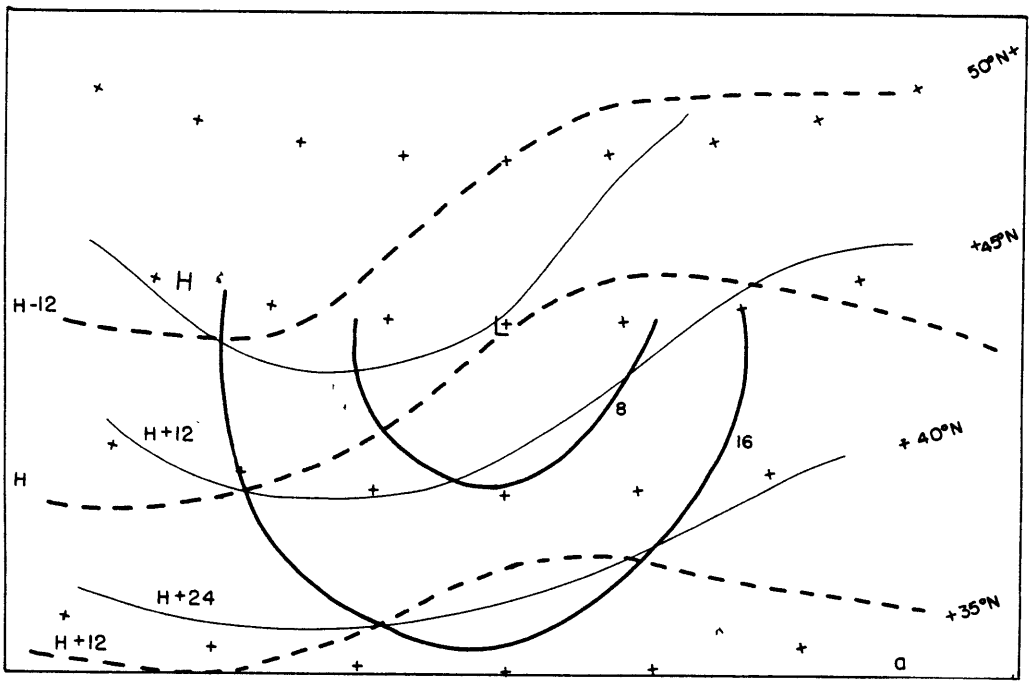
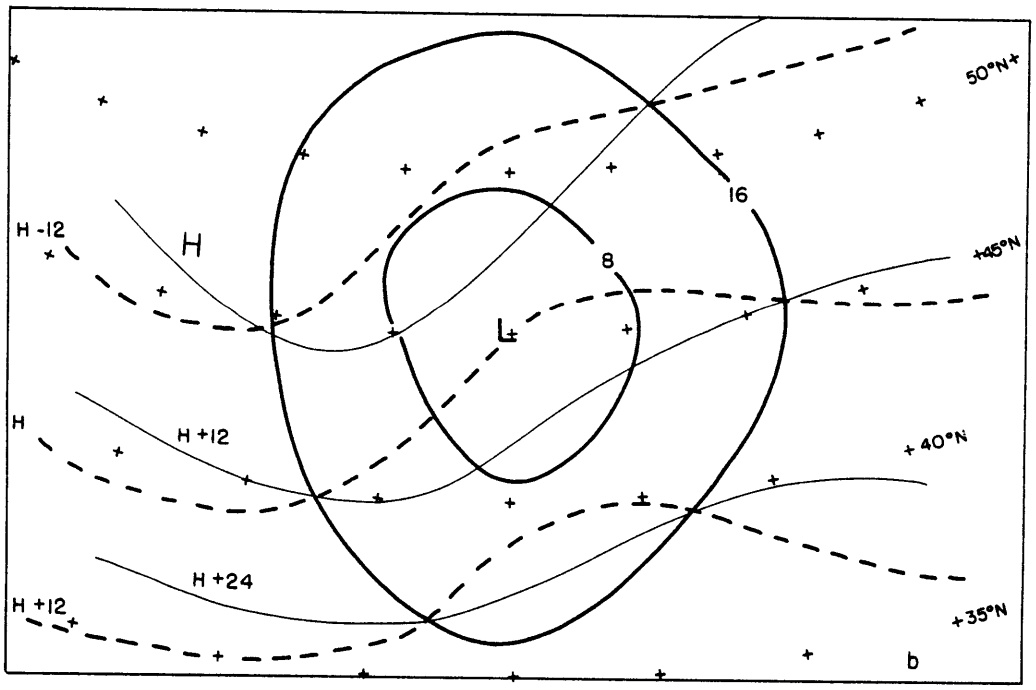


Fig. 2.9. Composite of the incipient bomb. Solid isopleths represent the number of mb greater than the analyzed sea-level pressure of the surface center. Dashed isopleths are 1000-500 mb thickness lines (dam). Light solid isopleths represent the graphical addition of the 1000-mb height field to the 1000-500 mb thickness field.



H is the thickness value over the surface center. (a) Weak circulation composite is based on 28 cases. (b) Strong circulation composite based on 17 cases.

reliability of the thickness analyses in the data-sparse regions occupied by these cyclones is especially questionable when an excessively-smoothed upper-level flow field is superposed upon an intense 1000 mb vortex (see Sanders, 1976), it is hoped this problem has been minimized by our focusing on a time sufficiently early in the surface cyclone development to render such effects small.

The westward displacement of the thermal trough from the surface center is 600-800 n mi, and the 500-mb height field, also shown in Fig. 2.9, indicates an upper-level flow field which is not in the unperturbed state suggested by the investigators mentioned in the introduction.

Each of the composites lend themselves readily to a diagnostic quasi-geostrophic calculation of central pressure tendency. We computed the geopotential tendencies in a quasi-geostrophic model similar to the one proposed by Sanders (1971, hereafter referred to as S). The major difference from the model in S is that we assume a horizontal temperature gradient independent of height, and a vanishing vertical motion at the 250-mb level. The expression for the geopotential tendency used for the surface center is

$$\chi_{sc} = \hat{\chi}_1(1000\,mb)\sin(2\pi\lambda/L) \tag{2.1}$$

The variable L indicates the wavelength of the tropospheric thermal trough-ridge pattern, and λ indicates the upstream displacement of

the surface center from the warm ridge. Thus, $\hat{\chi}_1$ (1000 mb) is the geopotential tendency of the low center when it is located a distance L/4 upstream from the warm ridge. In the present model

$$\hat{\chi}_1(1000\text{ mb}) = \frac{-\eta_0 R a \hat{T}}{(2\pi/L)T_0\gamma}\left\{\frac{\left[(1-2q)+q4^{q}-(1-q)4^{(1-q)}\right]k-(1-2q)\ln 4}{4^{(1-q)}-4^{q}}+k+1\right\}$$

$$+\frac{f_0\eta_0\hat{T}}{4(2\pi/L)^3}\left(\frac{\partial f}{\partial y}\right)_0\left(\frac{1}{T_0\gamma}\right)\left\{\frac{(2q-1)-q4^{q}+(1-q)4^{(1-q)}}{4^{(1-q)}-4^{q}}-1\right\} \qquad (2.2)$$

The analogous expression in S is Eq. (29). The variables defined above are identical to those in S. Thus η_0 is the domain-average absolute vorticity, R is the gas constant, T_0 the mean tropospheric temperature (assumed a constant 250°K), and γ a dimensionless static stability parameter. A saturated atmosphere is assumed in our γ value so the static stability structure refers to the moist adiabat. The resulting γ value of .063 used in the calculations is based upon 68 ship radiosonde observations taken at 00 GMT in the vicinity of rapidly deepening cyclones during the period 1971-74. The variable q is

$$q = .5 + .5\left(1+4/k\right)^{\frac{1}{2}}, \text{ where } k=\frac{f_0\eta_0}{2(2\pi/L)^2 R T_0\gamma}.$$

As in S, the first term in (2.2) represents the active deepening mechanism for the surface center and it is due to the

positive thermal vorticity advection (PTVA) over the low center. The variables a, representing the basic large-scale temperature gradient and $\hat{T}$, indicating the perturbed part of the temperature field, are the ingredients used to estimate this PTVA. An evaluation of a and $\hat{T}$ was accomplished through a decomposition of the thickness fields in Fig. 2.9 into their mean and perturbed parts, using the graphical technique of Fjørtoft (1952). A 12-h central pressure fall of 3.3 mb and one of 4.0 mb were computed for the cases in Figs. 2.9a and 2.9b, respectively. This compares with the respective observed 12-h mean falls of 16.5 and 17.8 mb. These calculations were made without regard to the sin $(2\pi\lambda/L)$ factor. The λ changes from L/6 in the weak circulation case to L/7 in the strong circulation composite. Thus, the computed pressure falls would be attenuated to 75-85% of their maximum values. In addition, the frictional filling effect was ignored. Thus, we have extracted about the maximum amount of deepening allowed by this quasi-geostrophic model.

One might question whether the averaging process destroyed much of the PTVA, since it is a nonlinear quantity, and the PTVA of the mean state is not equal to the mean of the individual values. However, an inspection of the individual cases indicates structurally similar situations, so that there does not appear to be a correlation between the basic meridional temperature gradient and the longitudinal one of sufficient magnitude to obscure the basic results of the composite. Furthermore, we have examined bomb cases individually, and

have found computed central pressure falls quite similar to the above computations.

The sensitivity of the computed quasi-geostrophic deepening rate for the strong circulation composite to variations in static stability is shown in Fig. 2.10. Also shown is a histogram of static stabilities found in the aforementioned sounding sample. These static stabilities were computed by referring to the dry adiabat, where the mean relative humidity in the 850-500 mb layer is less than 75%; otherwise the γ value was computed in this layer by referring to the moist adiabat. The soundings in this latter category are indicated with an encircled "X". Note that had we used the mean of these values (.094), the computed pressure fall would have been only 3 mb/12 h. Even a zero static stability value will yield a deepening of only 8 mb/12 h, which is still less than 1/2 of the observed rate. Although the quasi-geostrophic approximation breaks down as the static stability (and therefore the Richardson number) approaches zero, the dynamics of this system are not discontinuous at positive γ's approaching zero. Furthermore, it is clear from this sounding sample that this zero static stability computation would be unjustified, for the explosively developing surface cyclone occurs over a wide range of positive static stabilities within its domain. A preference for lower static stability to occur close (within about 200 km) to the center is also not observed. Even though the cyclone-scale averaged static stability is likely a relatively small positive value, it is quite possible for sub-cyclone

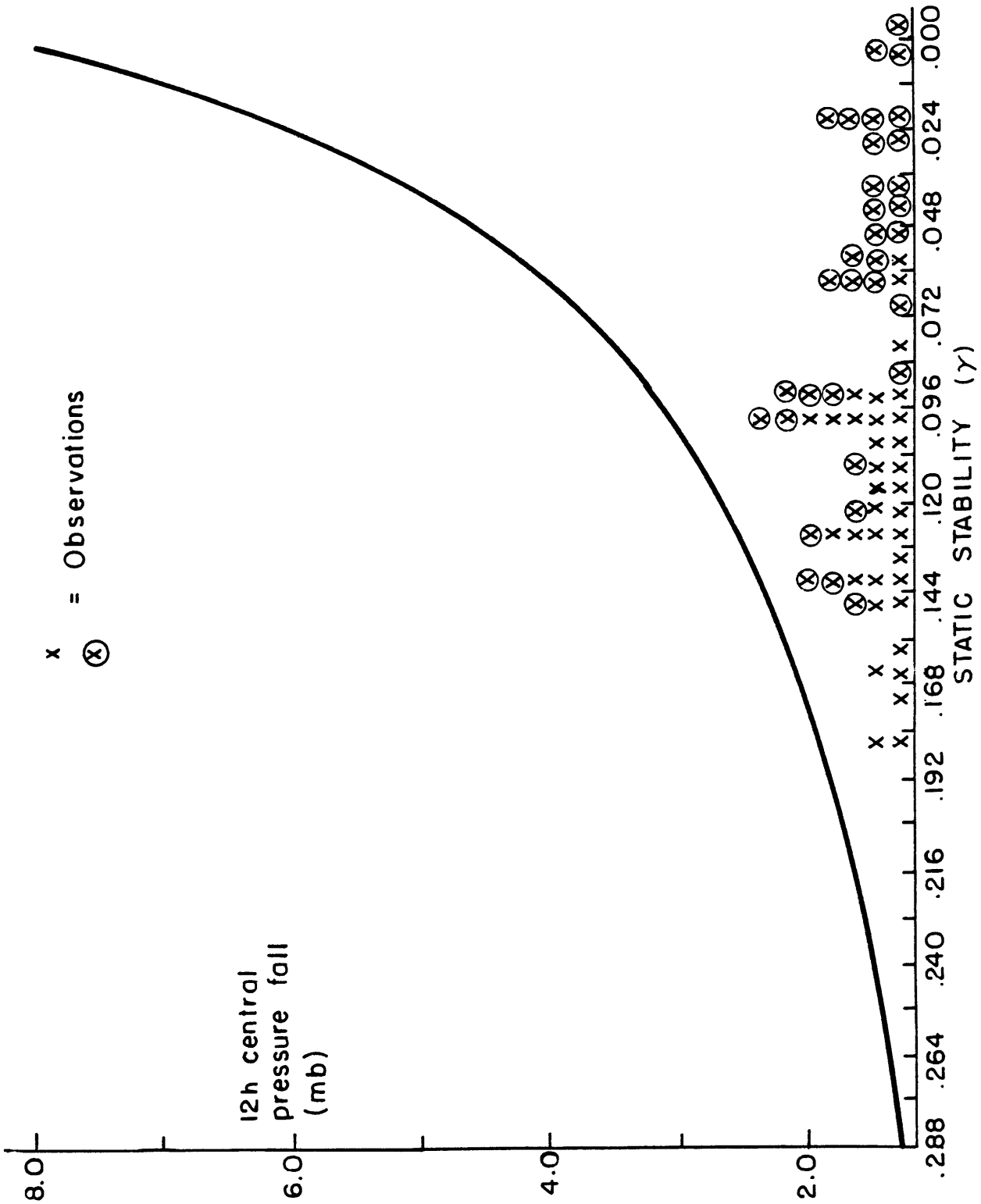


Fig. 2.10. Quasi-geostrophic central pressure falls as a function of static stability, γ, for the forcing implied by the strong circulation composite found in Fig. 2.9b. Histogram of observed static stabilities within the domain of the explosively deepening cyclones described in the text.

scale areas of positively buoyant air to exist within the domain. In fact, the presence of deep convective cells in the storm shown in Fig. 2.2 confirms such a possibility, and suggests that bulk heating effects of cumulus convection may provide additional forcing not accounted for by this inviscid, quasi-geostrophic model.

There remains the possibility that poor data coverage aloft is responsible for this finding of extremely limited quasi-geostrophic forcing. However, in order to compute the observed intensification of the composite bomb in the strong circulation case, we would have to increase $\hat{T}$ from 1.5°K to 6.7°K for the same wavelength, and for the same large-scale temperature gradient, a. The consistency of the upper-air features in these cases makes this scenario extremely unlikely, for the 500-mb height analyses are almost entirely based upon frequent and reliable wind observations taken by commercial aircraft flying at about 250 mb. The correlation of geopotential perturbations at 250 mb with those found at 500 mb is generally quite high. The 250-mb wind coverage of oceanic areas is, in many cases, superior to that found over the North American continent. The weak upper-level baroclinic forcing associated with our composite explosive cyclone is documented for a specific case in the next chapter.

For another specific extreme example, a careful reanalysis of the tropospheric thickness and sea-level pressure fields associated with the development of the February 1975 case discussed earlier reveals corresponding diagnostic central pressure falls of

only 3 mb $(12\ h)^{-1}$ at 00 GMT 4 February 1975 and 9 mb $(12\ h)^{-1}$ at 12 GMT 4 February 1975. These computations compare with the observed 12-h central pressure falls of 34 and 30 mb, respectively.

Finally, Fig. 2.9 indicates a pattern of diffluence in the 1000-500 mb thickness fields. The thermal wind 10° longitude downstream of the surface low is no more than two-thirds the value of the corresponding thermal wind 10° longitude upstream of the surface system. Bjerknes (1954) has associated the diffluent upper-level trough with developing surface cyclones, and has argued for the development of such a trough in a cyclonic-shear vorticity zone aloft. Although this forecasting rule is consistent with our composite indicating a pattern of diffluence in the upper-level flow, a quantitative determination of surface development is still lacking.

2.6 Bomb Prediction by Operational Primitive-Equation Models

Although Leary (1971) has documented systematic errors in the NMC primitive-equation (PE) model (Shuman and Hovermale, 1968) predictions of surface cyclone development, a brief summary of recent NMC model performance with respect to bombs seems appropriate. The NMC PE performance was tested during the period from September 1977 - May 1978, and from November 1978 - March 1979. We had a unique opportunity to study the effect of horizontal resolution in the model during this period of study, for 20 January 1978 was the date NMC began operationally using the 7-layer (7-L) PE with a horizontal mesh length one-half that of the older 6-layer (6-L) PE's 381 km at 60°N. The horizontal grid resolution represents the essential difference between

the two models, since the additional layer was added in the stratosphere.

A summary of performance of the two models for cases when bombs occurred appears in Table 2.1. The sample size is limited because the PE forecast domain on the facsimile maps extends westward only to the dateline, and thus excludes the major region of explosive cyclogenesis in the western Pacific. The mean non-normalized 12-h pressure fall of the observed bomb is 16.5 mb in all cases. This sample indicates the (6-L) PE captures close to one-quarter of the observed 12-h central pressure tendency while the (7-L) PE captures about one-third of the observed deepening. Both models dramatically underforecast this oceanic cyclogenesis. Leary (1971) also found systematic underprediction of the depth of maritime cyclones by the (6-L) PE. Druyan (1974) has found the Goddard Institute for Space Studies model (Somerville et al., 1974) to be similarly deficient in forecasting deepening cyclones. Figure 2.11 indicates plots of the observed versus predicted central pressure tendencies for the 12-24 h forecast category. Very few forecasts approach the observed tendencies in either model. However, the slope of the regression lines is steeper in the (7-L) PE forecasts than in the (6-L) PE predictions. The correlation coefficient for the linear regression in the (7-L) PE case is about 0.32, while the (6-L) PE coefficient is only 0.08. The corresponding charts (not shown) for other forecast periods indicate almost identical linear regressions for each of the respective models. Thus, while the (7-L) PE model drastically underforecasts this class

TABLE 2.1

Summary of (6-L) PE and (7-L) PE model performance for observed cases of bombs. N is the number of observed bombs.

	(6-L) PE					(7-L) PE				
	Observed 12-h ΔP (mb)			Model 12-h ΔP (mb)		Observed 12-h ΔP (mb)			Model 12-h ΔP (mb)	
Forecast Period (h)	N	Mean	Standard Deviation	Mean	Standard Deviation	N	Mean	Standard Deviation	Mean	Standard Deviation
12-24	46	16.3	4.7	4.7	3.8	67	16.5	5.4	6.2	5.4
24-36	45	16.4	4.7	3.8	3.8	67	16.3	5.2	4.3	5.0
36-48	43	16.7	4.8	4.0	4.1	74	16.2	5.1	5.0	5.5

TABLE 2.2

Summary of FNWC PE model performance for observed cases of bombs. N is the number of observed bombs.

	Observed 12-h ΔP (mb)			Model 12-h ΔP (mb)		
Forecast Period (h)	N	Mean	Standard Deviation	Mean	Standard Deviation	
0-12	68	15.5	3.8	2.8	4.5	
12-24	76	15.8	5.5	5.8	4.0	
24-36	67	15.6	3.9	5.0	3.6	
36-48	64	16.0	5.9	4.9	3.1	

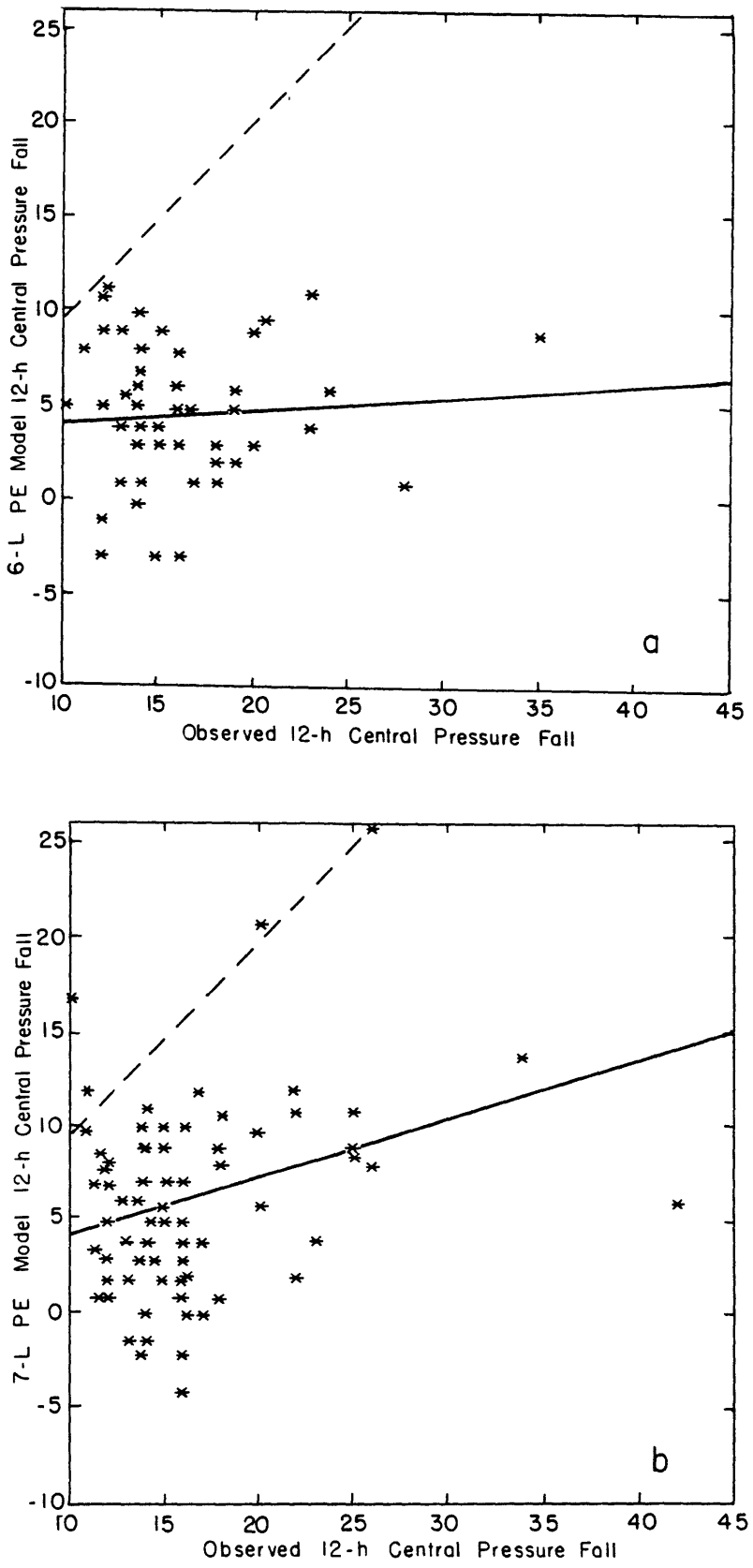


Fig. 2.11. Plots of observed atmospheric bombs indicating their 12-h central pressure fall, and the corresponding PE-predicted fall at a forecast range of 12-24 h. Straight line is the least-square regression of the points. Dashed line is the perfect forecast line.

of cyclogenesis, Table 2.1 and Fig. 2.11 show that it does not perform as badly as the coarser mesh (6-L) PE model. Table 2.1 shows that only ~10% of the model error is eliminated when the mesh length is halved. Since the diagnostic calculations discussed earlier, based on a continuous model, also underpredict the deepening rate by about the same amount, it seems unlikely that further improvement in the forecasts can be achieved simply by increasing the horizontal resolution. In addition to possible problems with data resolution, important physical ingredients for explosive deepening appear to be missing in the models. The appearance of Fig. 2.2 suggests that one of the missing ingredients is an adequate representation of the bulk effects of cumulus convection. Additionally, our finding of strong SST gradients being associated with bomb events implies inadequate vertical resolution and representation of the planetary boundary layer physics.

We also obtained surface prognoses (only those forecasts initialized at 12 GMT) of the FNWC PE model for the period 1 September 1979 through 31 March 1980. This operational PE model has a rather coarse horizontal grid spacing of about 381 km, and is documented by Kesel and Winninghoff (1972). An exercise similar to the one just described was performed for this model. A summary of performance for cases when 12-h bombs occurred appears in Table 2.2. In spite of a claim by Kesel and Winninghoff that this model successfully forecasts explosive extratropical cyclogenesis, our results indicate this model also dramatically underforecasts this oceanic cyclogenesis, and captures about a third of the observed central pressure fall for all periods,

except the initial 12 h, when only 18% is captured. The plot of the observed versus predicted central pressure tendencies for the 12-24 h forecast category, shown in Fig. 2.12, indicates a similar regression to that of the (6-L) PE, with a correlation coefficient of .10. The other three scatter plots (not shown) all indicate a similarly poor performance, with the best correlation coefficient (.16) occurring in the 24-36 h forecast period, and the worst (-.09) in the 36-48 h forecast period.

We have performed an experiment in which a search was conducted for 12-h bombs occurring in the PE model atmosphere. The results are presented in Table 2.3 for the (7-L) PE model during the time period indicated. The sample size is quite small, indicating that, though the (7-L) PE is not incapable of simulating explosive storms, it does not do this nearly as often as does the real atmosphere. The (7-L) PE also generally overdevelops these cyclones in comparison with reality. The geographical locations of these 24 PE bombs are indicated in Fig. 2.13. The individual PE bombs are not mutually exclusive, for three forecast atmospheres are used for the same time period. This one and a half season composite indicates the (7-L) PE develops virtually none of the existing bombs in the Pacific east of the dateline. Most of the (7-L) PE bombs occur in the eastern United States and in the western Atlantic. A comparison with Fig. 2.3 indicates the simulation of bombs in the PE atmosphere is displaced well to the south and west of the real atmosphere bombs. The relatively high percentage of continental cases in the PE bomb

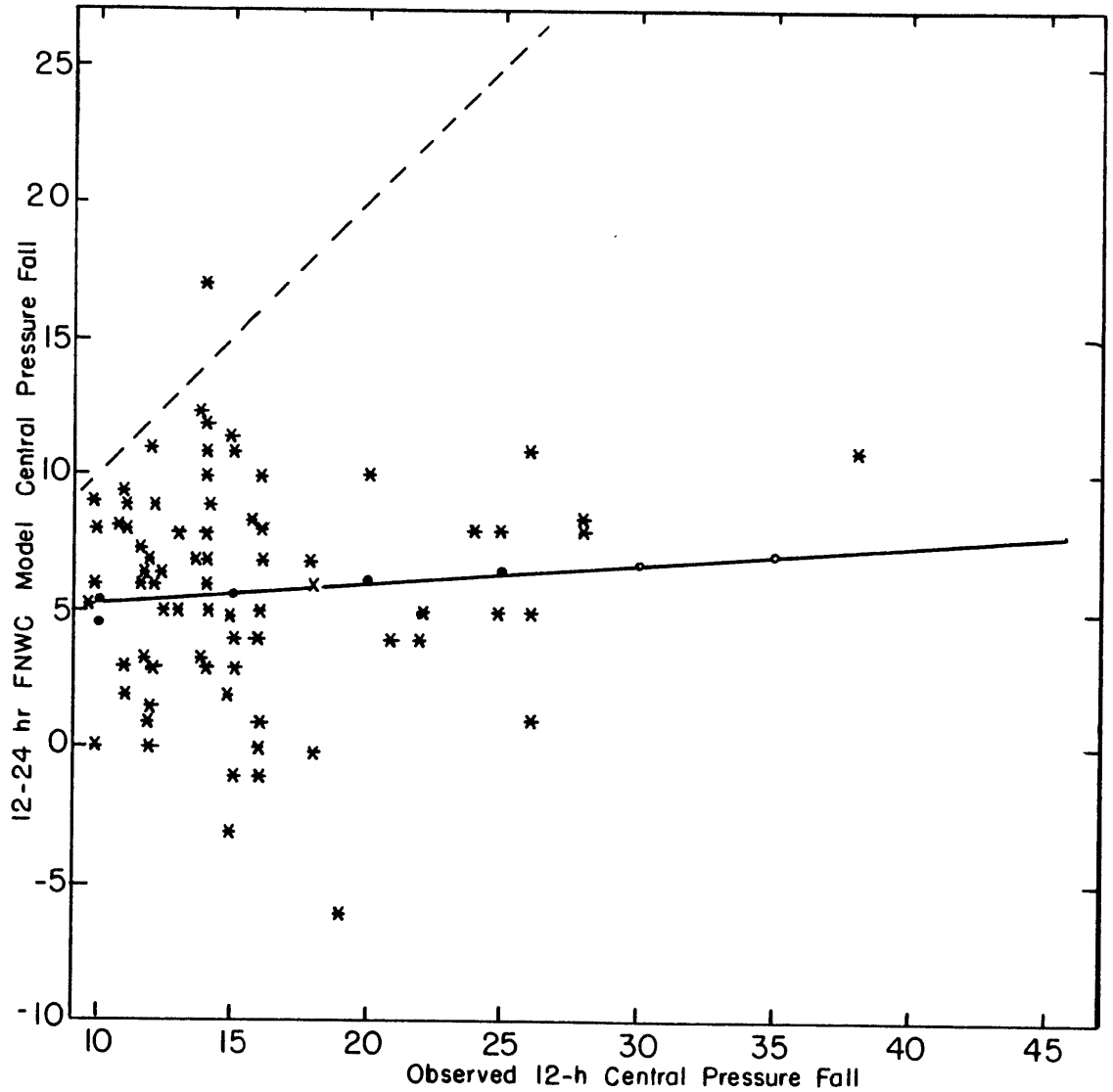


Fig. 2.12. As for Fig. 2.11, except for 1979-1980 season of the FNWC model performance.

TABLE 2.3

Summary of atmospheric performance for cases of (7-L) PE predicted bombs. Format is the same as in the previous tables.

Forecast Period (h)	N	Model 12-h ΔP (mb)		Observed 12-h ΔP (mb)	
		Mean	Standard Deviation	Mean	Standard Deviation
12-24	9	11.9	2.1	7.1	8.5
24-36	9	11.6	1.1	9.8	7.2
36-48	6	13.3	1.2	9.2	14.1



Fig. 2.13. Locations (indicated by asterisks) of the 22 (7-L) PE bombs at the beginning of their 12-h tracks in the eastern United States, and in the Atlantic basin. The two (7-L) PE bombs in the western United States-Pacific domain were located at 42°N, 137°W, and at 36°N, 101°W.

list and the general overdevelopment of these systems thus appears consistent with Leary's (1971) finding that the (6-L) PE systematically overdevelops some continental cyclones. Leary's sample, including all cyclones for the winter of 1969-1970, showed most of the (6-L) PE overdevelopment to be in the lee of the Rockies.

2.7 Concluding Remarks

A rapidly deepening extratropical cyclone has been characterized as one in which the central pressure drops 1 mb h^{-1} for 12 h. Adopting this rate (suitably adjusted for latitude) as the definition of a meteorological bomb, we have studied this phenomenon during the 44-month period beginning September 1977 in the Northern Hemisphere longitude zone from 130°E eastward to 10°E. We find this explosive cyclogenesis to be a predominately maritime, cold-season phenomenon, often with hurricane-like features in the wind and cloud fields.

Although this phenomenon poses a grave threat to shipping interests, the rapid deepening process may be a necessary component in a realistic model simulation of the general circulation. We have tested the notion that most of the hemisphere's deepest cyclones (which usually track toward their final resting places in the vicinity of the Icelandic and Aleutian lows) have deepened explosively. The maximum deepening rate for each of the 36 cyclones intensifying to 960 mb or lower in the nine-month period beginning 1 September 1978 has been found, and the frequency distribution of these rates is shown in Fig. 2.14. Note that all but one case deepened at least 11

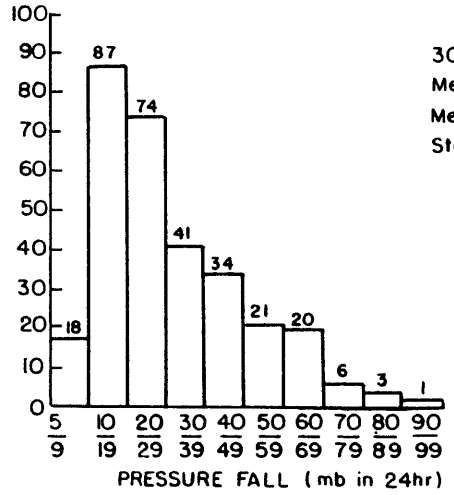


Fig. 2.15

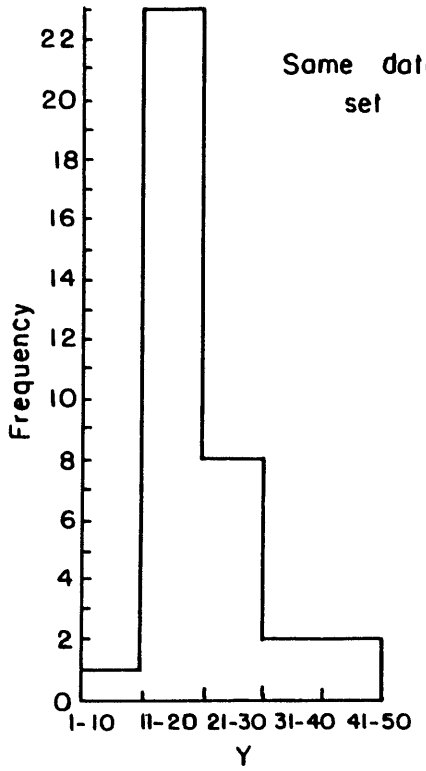


Fig. 2.14

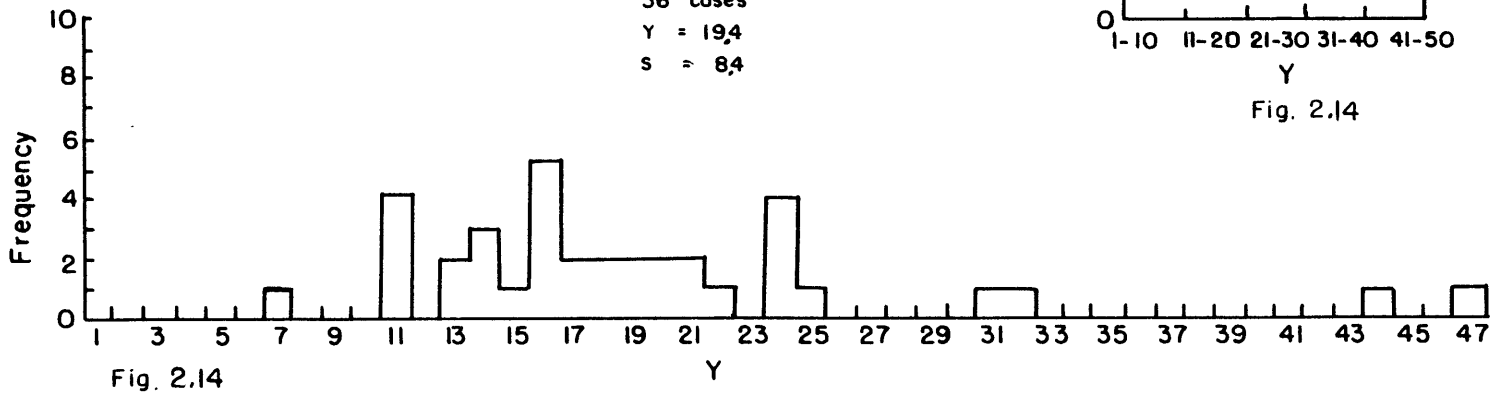


Fig. 2.14

Fig. 2.14. Histogram of the 1978-1979 intense low deepening rates. Y is defined as in Fig. 2.6.

Fig. 2.15. (from Holliday and Thompson, 1979) Frequency distribution of maximum 24-h deepening of typhoons (1956-1976).

mb (12 h)$^{-1}$, and that 31 deepened 12 mb (12 h)$^{-1}$ or greater. Thus, explosive deepening is a characteristic of the vast majority of the hemisphere's deepest cyclones. This fact provides us with a posteriori evidence that the phenomenon we are studying may be quite important for large-scale general circulation features. In fact, when this histogram is compared with that of Holliday and Thompson (1979) for hurricanes (see Fig. 2.15), we see a similar cut-off deepening rate for both phenomena. Virtually all typhoons have a deepening of at least 10 mb/24 h. Since these typhoons intensified at about 18°N, this translates into a central pressure fall for 45°N of 11.4 mb (12 h)$^{-1}$, remarkably close to our 11 mb (12 h)$^{-1}$ lower cut-off seen in Fig. 2.14. This result suggests that a more detailed examination be undertaken to discover whether cumulus convection, which is apparently fundamentally important in the relatively short time-scale found in hurricane intensification, is similarly operative in these extratropical systems. This will be undertaken in the next chapter.

Our results generally confirm those of recent studies (e.g., Blackmon et al., 1977) emphasizing the importance of transient eddy transports of heat and momentum in the cyclogenetic regions found in this chapter for the operation of the Northern Hemisphere winter circulation. In fact, our results suggest that their actual dominance may be substantially greater than illustrated in data based on NMC coarse-mesh analyses. Consistent with our results is the study of Holopainen and Oort (1981), which found the transient eddies to be important in maintaining the circulation of the Icelandic and the

Aleutian lows against frictional dissipation.

The bomb is generally found about 400 n mi downstream from a mobile 500 mb trough, and within or ahead of the planetary-scale troughs (Sanders and Gyakum, 1980). The converse effect of cyclone-scale instability on larger scale wave development, an issue which was addressed earlier in this section, has received more attention. Gall et al., (1979) have studied this type of behavior, which is well exemplified by the extraordinary increase in amplitude of the planetary waves in the eastern Atlantic and western Europe following the 10-16 February 1979 western Atlantic bomb cluster described by Sanders and Gyakum (1980).

We have studied 1978-1979 bombs in more detail. This study has shown that explosive cyclogenesis occurs over a wide range of SST's, but, preferentially near the strongest gradients. A composite of surface isobars and tropospheric thicknesses, centered on the incipient bomb, indicates development typically occurs in a region of upper-level diffluence. Quasi-geostrophically computed central pressure falls in the composite bomb are far less than the observed falls. Current NMC and FNWC PE models also perform poorly in their attempted simulation of observed bombs. However, bombs produced by the NMC models indicate a much higher percentage of continental cases than was observed in the real atmosphere. These latter results are consistent with Leary's (1971) study of systematic NMC errors.

Clearly, some of the explosive surface cyclone intensification in a typical bomb is due to a baroclinic mechanism. Furthermore,

the preferential development of explosively-developing cyclones in areas of strong SST gradients implies this baroclinic forcing may be particularly intense in the lower troposphere, and this raises the possibility that current operational models have inadequate vertical computational and data resolution to handle such an event. The quasi-geostrophic model discussed in this chapter also has no capability of resolving this possibly intense lower tropospheric baroclinic forcing. The suggestion has also been made in this chapter that bulk heating effects due to cumulus convection have a profound positive effect in the rapid intensification of these storms, just as they do in hurricane intensification. The studies of Reed (1979) and Rasmussen (1979) suggest such a possibility. The case study in the next chapter will further explore these issues.

CHAPTER 3

ON THE EVOLUTION OF THE QEII STORM

3.1 Introduction

The hurricane-force winds and heavy seas which battered the liner *Queen Elizabeth II* (QEII) on 10 and 11 September 1978 (NOAA, 1979) were associated with an extraordinary example of a meteorological "bomb". This cyclone deepened nearly 60 mb in the 24-h period subsequent to 9 September, 12 GMT. Despite the existence of NOAA surface buoys and the relatively high density of mobile ships in the North Atlantic ocean, real-time weather analyses, subjective forecasts, and numerical prognoses of the National Meteorological Center (NMC) and Fleet Numerical Weather Central (FNWC) all grossly erred in the intensity and track of this storm. The impact of such a disastrous simulation on marine interests in terms of wind and wave height analyses and forecasts is obvious.

The cyclone originated as a shallow baroclinic disturbance west of Atlantic City, New Jersey. Explosive deepening occurred once the storm propagated offshore, and in association with cumulus convection adjacent to the storm center. The purpose of this chapter is to examine in detail the meteorological conditions associated with this dramatic intensification.

Section 3.2 will describe the data set used to document this case. The mesoscale and synoptic-scale conditions surrounding the cyclone will be discussed in Section 3.3. The performance of the

operational numerical models in this case will be discussed in Section 3.4. Section 3.5 examines the vertical motions associated with this storm. We will also discuss the quasi-geostrophic forcing associated with the cyclone in this section. A procedure by which we can document the three-dimensional thermodynamic structure of the atmosphere is discussed, and applied to this case in Section 3.6. An examination of the potential vorticity fields associated with this cyclone is performed in Section 3.7, with the goal of assessing quantitatively the importance of heating and frictional effects in this case. Concluding remarks are presented in Section 3.8.

3.2 Data Base

Surface information for this case consists of Service A hourly reports and Service C 6-hourly synoptic land and ship reports. Several NOAA data buoys were operational during this period, and these hourly reports were obtained from the archives at NOAA's National Climatic Center (NCC) in Asheville, North Carolina. NCC also furnished its complete listing of synoptic reports from weather and transient ships in the North Atlantic, along with barograms and copies of weather logs. These reports were supplemented by the Department of the Navy synoptic data file, the NMC surface data file, and ship weather logs and barograms from the British Meteorological Office.

This study was aided by the availability of an additional source for a wealth of surface wind reports from the Seasat-A instrumentation package. This satellite was launched on July 26, 1978 into

near-polar orbit from Vandenberg Air Force Base, California. Fortunately, the massive electrical short circuit which caused the Seasat instruments to fail did not occur until October 10, 1978. The impact that such an operational system could have on the present maritime observing network is likely to be revolutionary. The appropriate surface wind data from Seasat-A were kindly furnished by Professor Mark Cane of MIT and by Dr. Vince Cardone of Oceanweather, Inc. These surface winds are derived from the Seasat-A scatterometer system (SASS), which is a microwave radar, the characteristics of which are described in AAAS (1979). The wind data are presented in the form of: the latitude and longitude of the observation, and up to four wind speeds and four directions per observation. The wind speeds are all within 1 m/sec of each other for each set of the four readings. Thus, the ambiguity lies in the wind direction, which varies widely for a given observation. The selection of the "correct" wind direction has been performed subjectively for this case, and was based upon consistency with the nearby ship wind reports, and *a priori* knowledge of the sea-level pressure field. Several hundred reports of these wind vector sets exist for each time and region of interest for this study. As many wind vectors as could legibly be plotted on a polar stereographic projection of scale approximately 1/ 5.3×10^6 were used. The wind data sets used were from orbits 1066 and 1080 of Seasat, the measurements of which corresponded to within 55 minutes of the desired synoptic time. An appropriate time-space correction was applied to each observation.

Upper-level data were obtained from Service C radiosonde reports, and the NMC upper-air data file. This file includes land and weather ship-based radiosonde data, commercial and military aircraft wind, temperature, and height information, along with NOAA's geostationary (GOES-east) satellite temperature profiles. A set of GOES-east satellite cloud-top winds was furnished by the Space Science and Engineering Center at the University of Wisconsin.

GOES-east satellite visible and infrared images were obtained from the Satellite Data Services Division of NCC in Washington, D.C. Visible and infrared imagery of much higher horizontal resolution were obtained from the polar-orbiting Defense Meteorological Satellite. Images had to be overlayed onto a 9.5 inch normal mode universal grid using a listing of the predicted satellite track and known geographic features on the images. The grid, images, and listings were furnished by the Space Science and Engineering Center at the University of Wisconsin.

Radar data were obtained from NCC in the form of nationwide summary charts of precipitation echoes, data sheets containing observations at individual radar stations, and film records of the actual plan-position indicator (PPI). The individual stations used in this study are Atlantic City, New Jersey, Fort Totten, New York, Patuxent River, Maryland, and Chatham, Massachusetts, the locations of which are indicated in Fig. 3.33.

3.3 Mesoscale and Synoptic Overview

Fig. 3.1 shows mesoscale surface charts for the 12-h period beginning 18 GMT, 8 September 1978. At this time, a surface front extended from upstate Michigan through southwestern New York, central Pennsylvania, and southeastern Virginia. This frontal system separated an area of anomalously warm temperatures prevalent in the southwestern Great Lakes from a relatively cool surface ridge centered over Long Island. This general pattern persisted for much of the month (Taubensee, 1978). Horizontal temperature contrasts in the frontal zone at this time were in excess of 8°C/100 km. Precipitation was mainly confined to the cool side in west-central New York and in northeastern Pennsylvania in the form of light rain showers and moderate thunderstorms. The 1735 GMT radar summary (not shown) indicates maximum cloud tops of 10 and 13 km in association with this convection. By 21 GMT, the precipitation area penetrated as far southeast as central New Jersey. At 00 GMT on the 9th, a definite cyclonic circulation center appeared about 20 km west of Atlantic City, New Jersey. Note the relatively strong pressure falls (> 2 mb/3 h) along the New Jersey coast. The cool weakening surface ridge in southeastern New York was barely detectable at 850 mb (see Fig. 3.4). The low-level warm advection is particularly impressive in the vicinity of the developing surface trough. Precipitation was now confined just to the north of the surface trough in the form of very strong thunderstorms with a 13 km maximum cloud top and echo intensities of 50-100 mm h^{-1}, shown in the 2335 GMT radar summary (Fig. 3.2), just west of Trenton, New Jersey.

Fig. 3.1. Surface sectional plots in conventional format at 3-h intervals for the 12-h period beginning 18 GMT, 8 September 1978. Temperatures are in °C, are analyzed in dashed lines, and winds are plotted in knots. Sea-level isobars (mb) are given by solid lines. Surface front is shown by heavy solid line. Winds only are shown where space for the additional information is unavailable. SST's, where appropriate, are underlined.

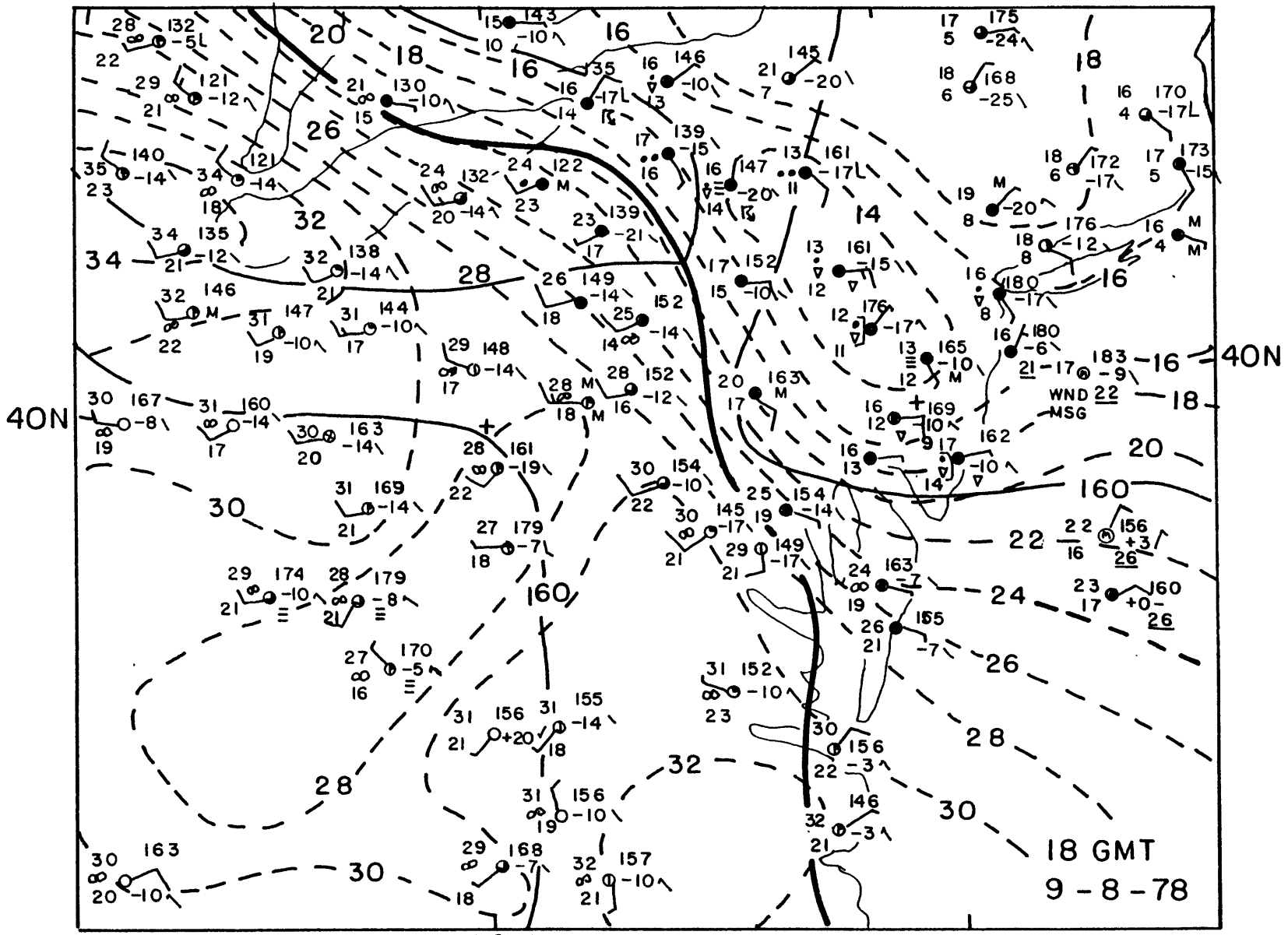


Fig. 3.1a

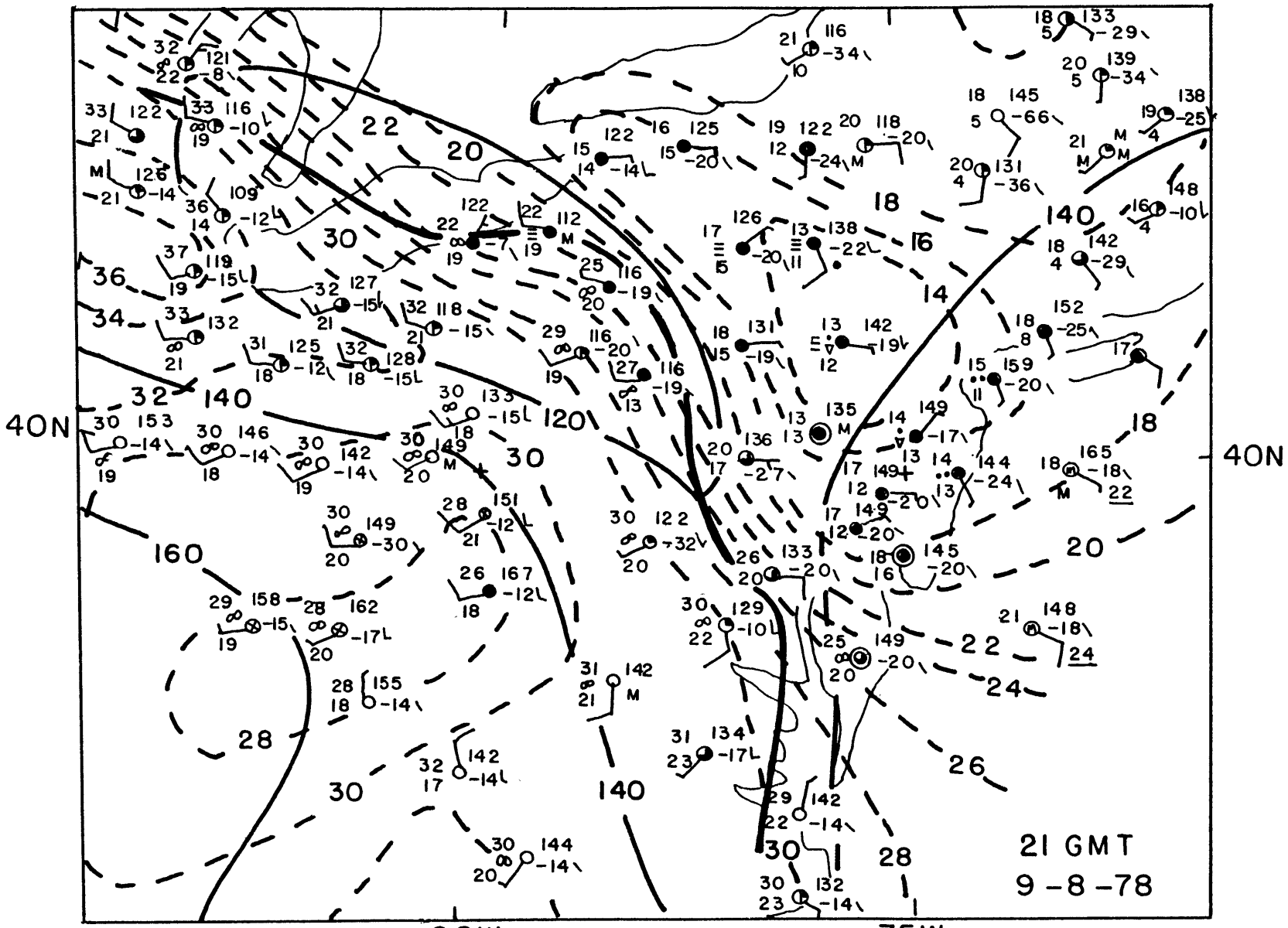


Fig. 3.1b

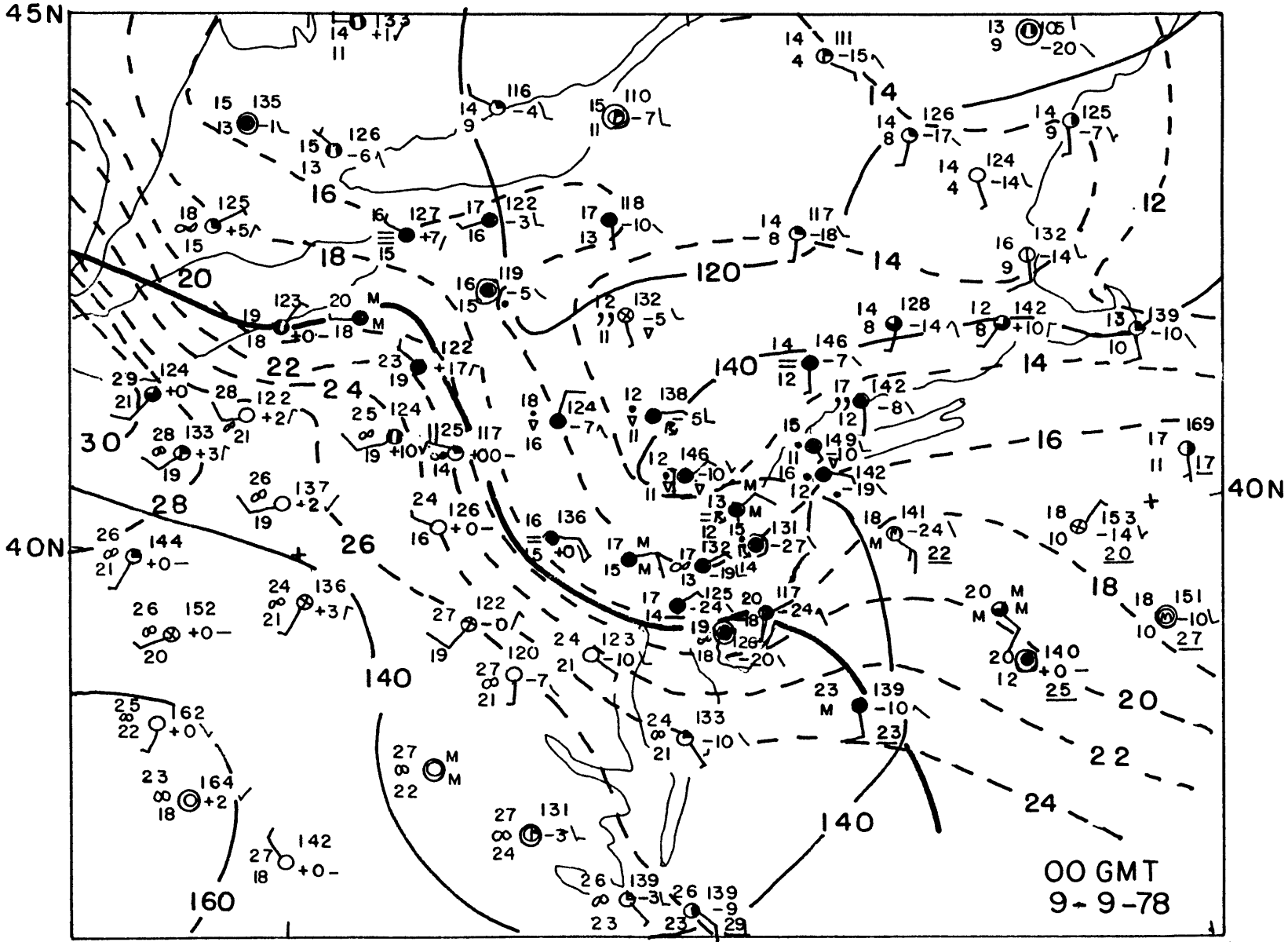


Fig. 3.1c

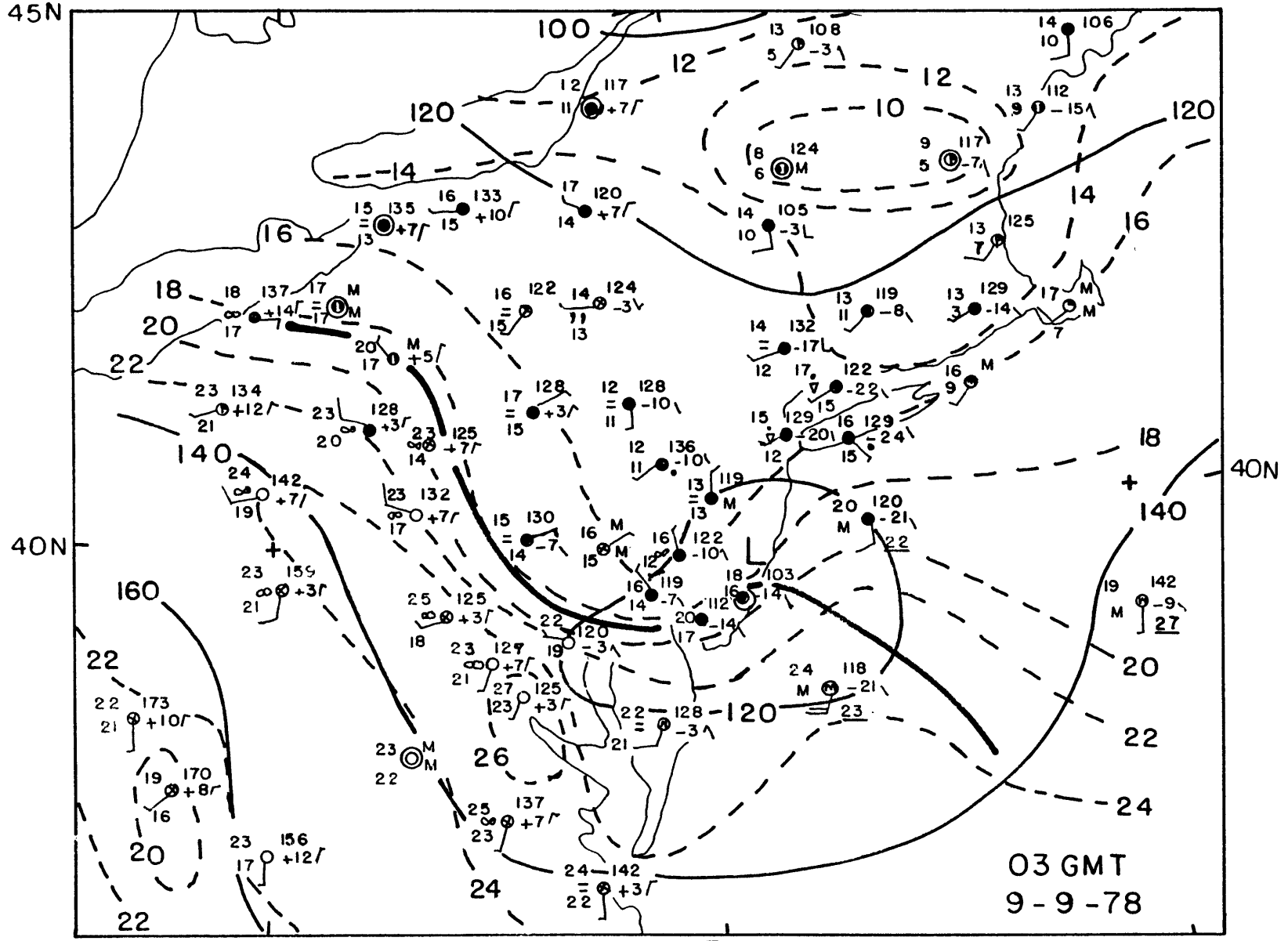


Fig. 3.1d

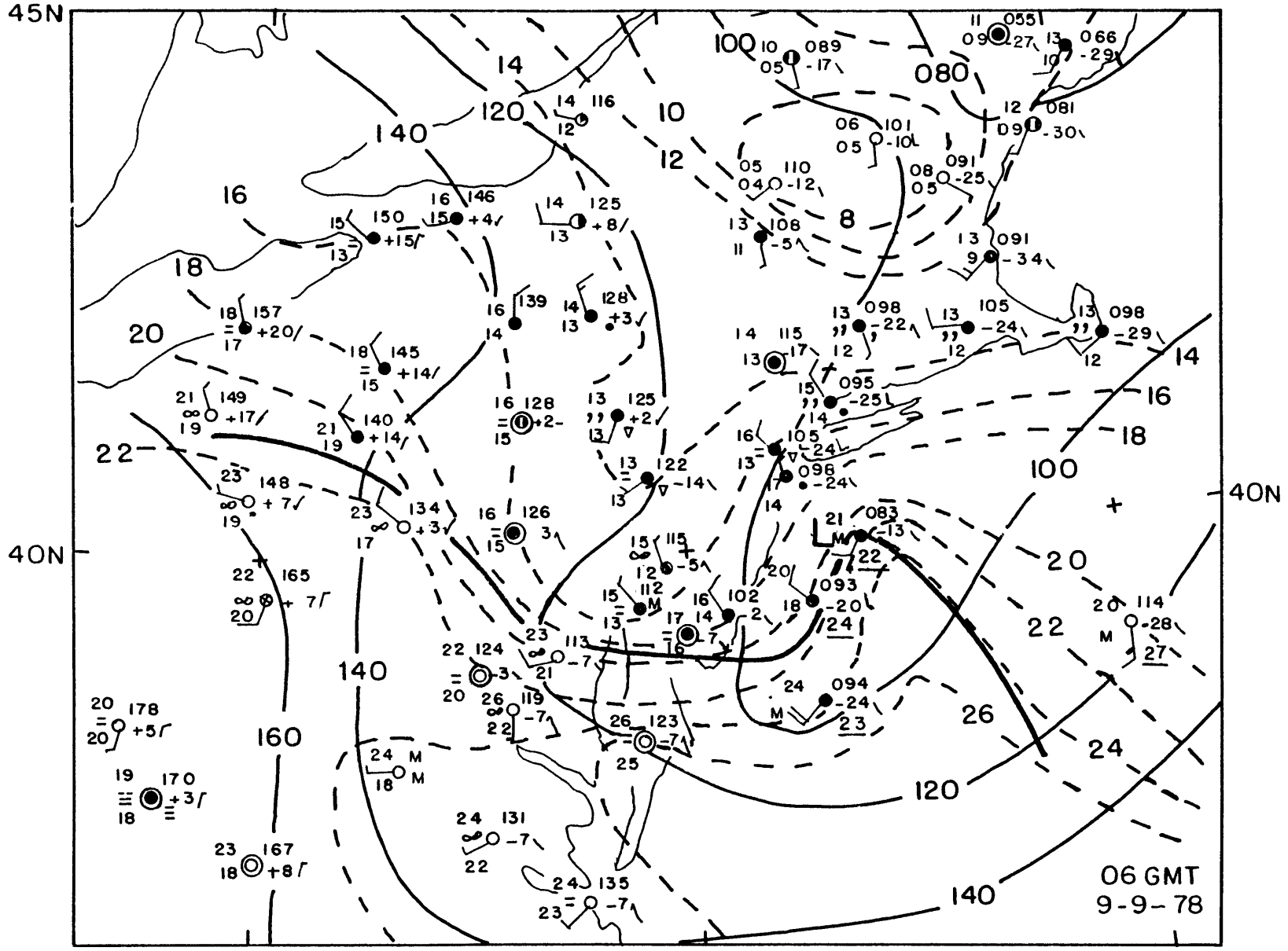


Fig. 3.1e

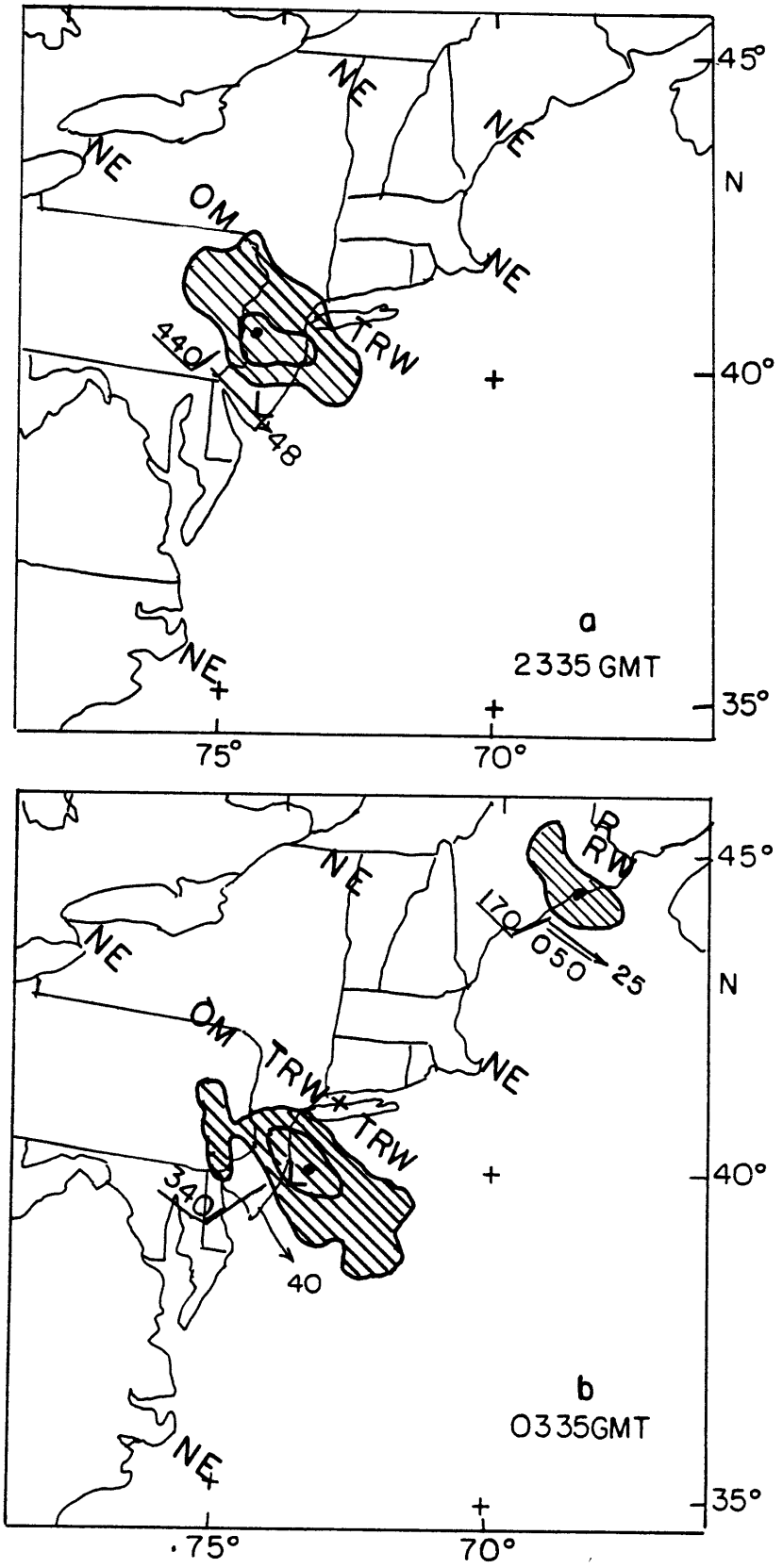


Fig. 3.2. Conventional radar summaries valid (a) 2335 GMT, 8 September 1978, and (b) 0335 GMT, 9 September 1978. Position of the surface cyclone is indicated with an "L". Maximum cloud top heights are indicated by underlined numbers (hundreds of feet), while cell movement is indicated by arrows with speeds (knots).

By 03 GMT, the 1010 low was located 40 km to the north-northwest of Atlantic City, and was then embedded in an area of very strong thunderstorms and rainshowers with maximum echo intensities of 50-100 mm h^{-1}. By 06 GMT, the intensifying low (now 1008 mb) had moved northeastward offshore to just northwest of the NOAA buoy indicated in Fig. 3.1, while the above-described convective cells moved rapidly southeastward.

At this time, the developing cyclone was in the relatively clear air 60 km to the northwest of a rapidly developing convective cloud cluster, which fit Maddox's (1980) criteria for a mesoscale convective complex (MCC). The evolution of this MCC is indicated in the series of satellite images shown in Fig. 3.3. This feature can be traced back in time to a few developing cells in east-central Pennsylvania at 00 GMT on the 9th, and is seen as the small area of thundershowers (10 km maximum tops) in the 0335 GMT radar summary. This is seen in the satellite image (Fig. 3.3d) as the enhanced area near the surface low center. The more impressive-looking area to the southeast (and not seen in the radar summary, Fig. 3.2b) was not a part of the developing MCC. The horizontal area of cold ($\leq$ 32°C) cloud tops of the incipient MCC increased from 2500 km^2 at 0330 GMT to 105,000 km^2 at 06 GMT. The MB enhancement (NOAA, 1976) shows cloud tops within this MCC as cold as -63°C. Given the approximate stratification for this time and location, the cloud tops must therefore range up to 170 mb, or 13 km above sea-level. As can be seen from the images, the MCC propagated an average of 45 knots to the east-southeast. This is similar to the initial movement of the cells detected by radar (see

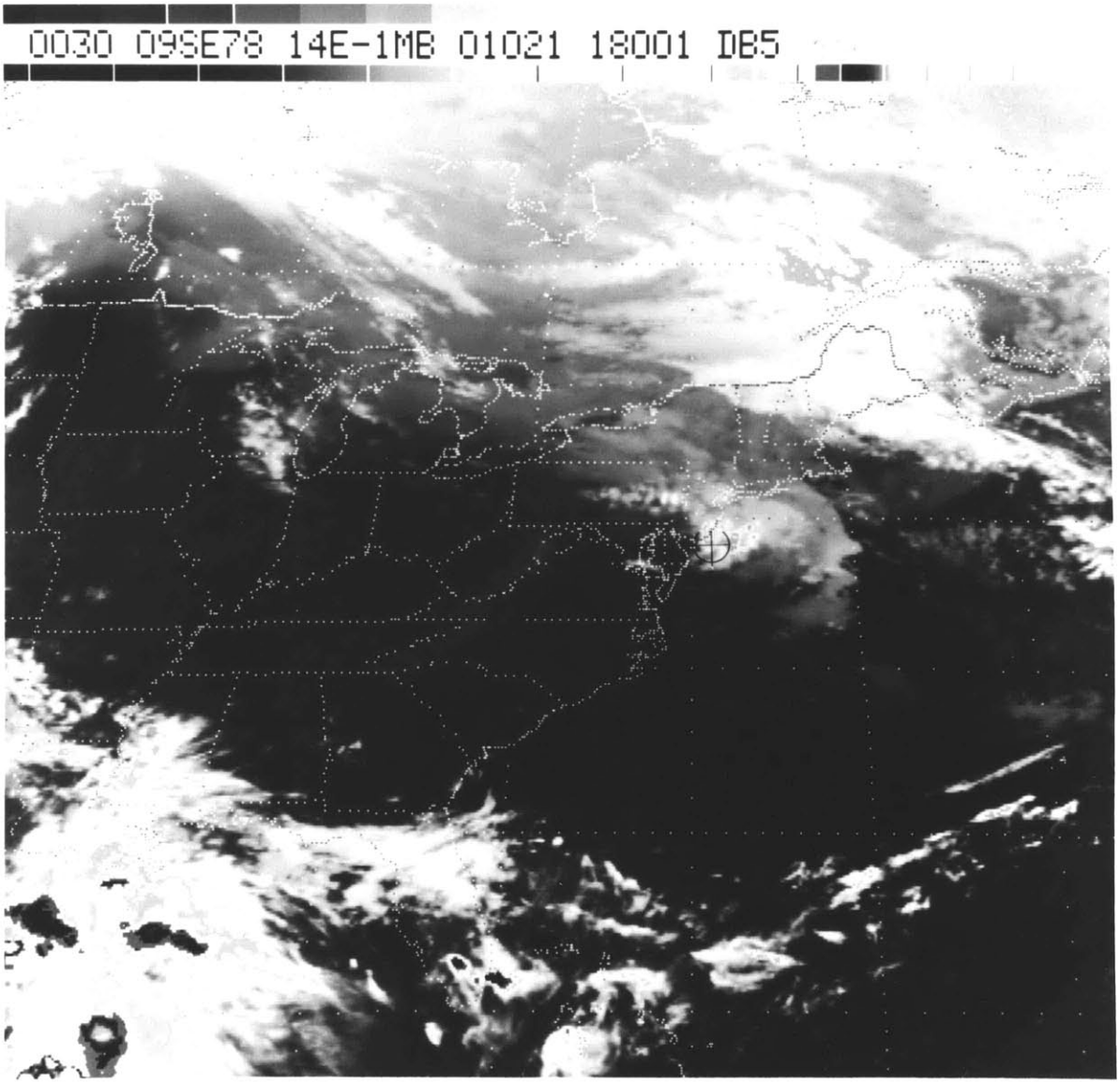


Fig. 3.3a. GOES-east MB-enhanced satellite image for 0030 GMT, 9 September 1978. The circle indicates the surface cyclone center, which is correctly positioned with respect to the image. The gridding is in error up to 50 km in some instances in this series of images.

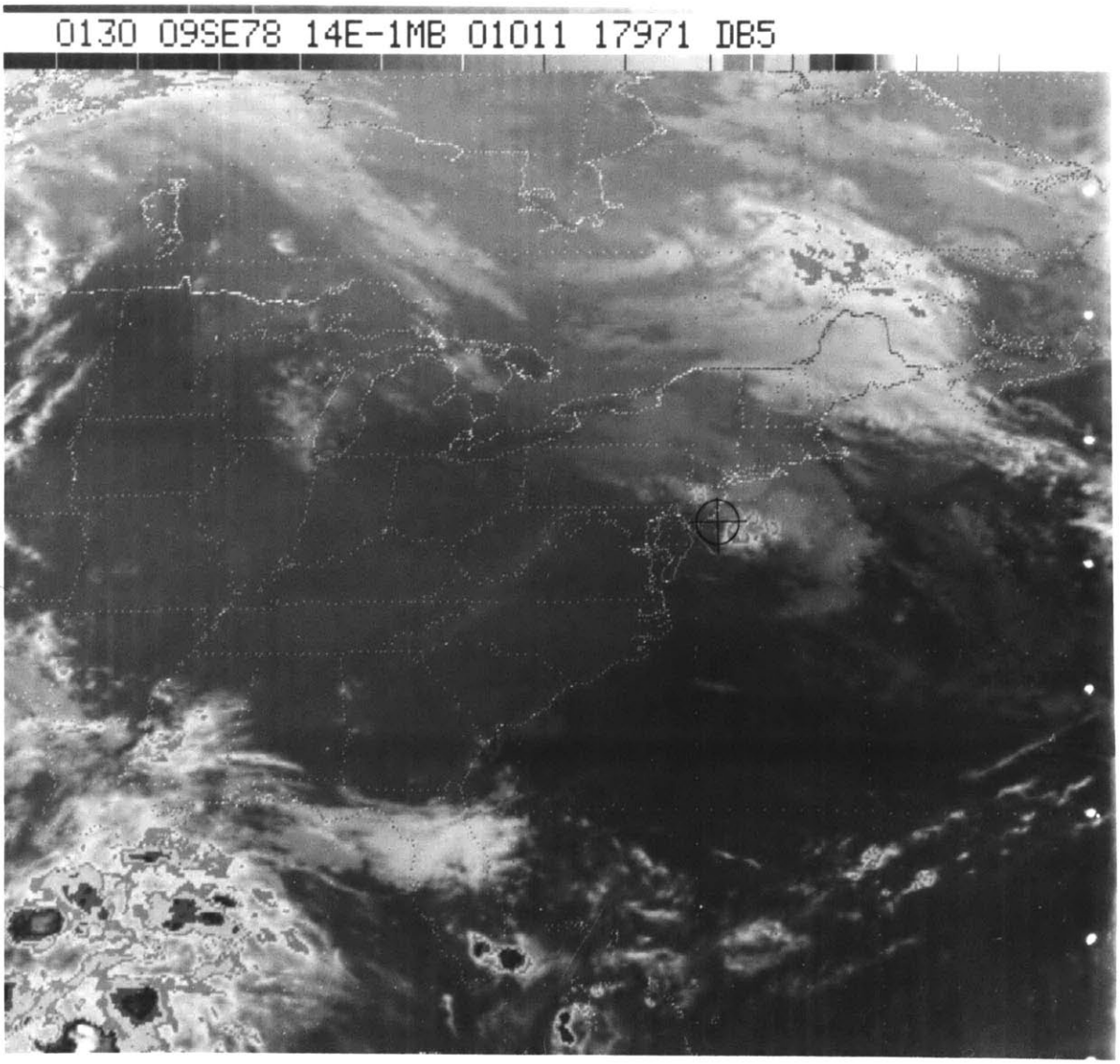


Fig. 3.3b. As for Fig. 3.3a, except for 0130 GMT, 9 September.

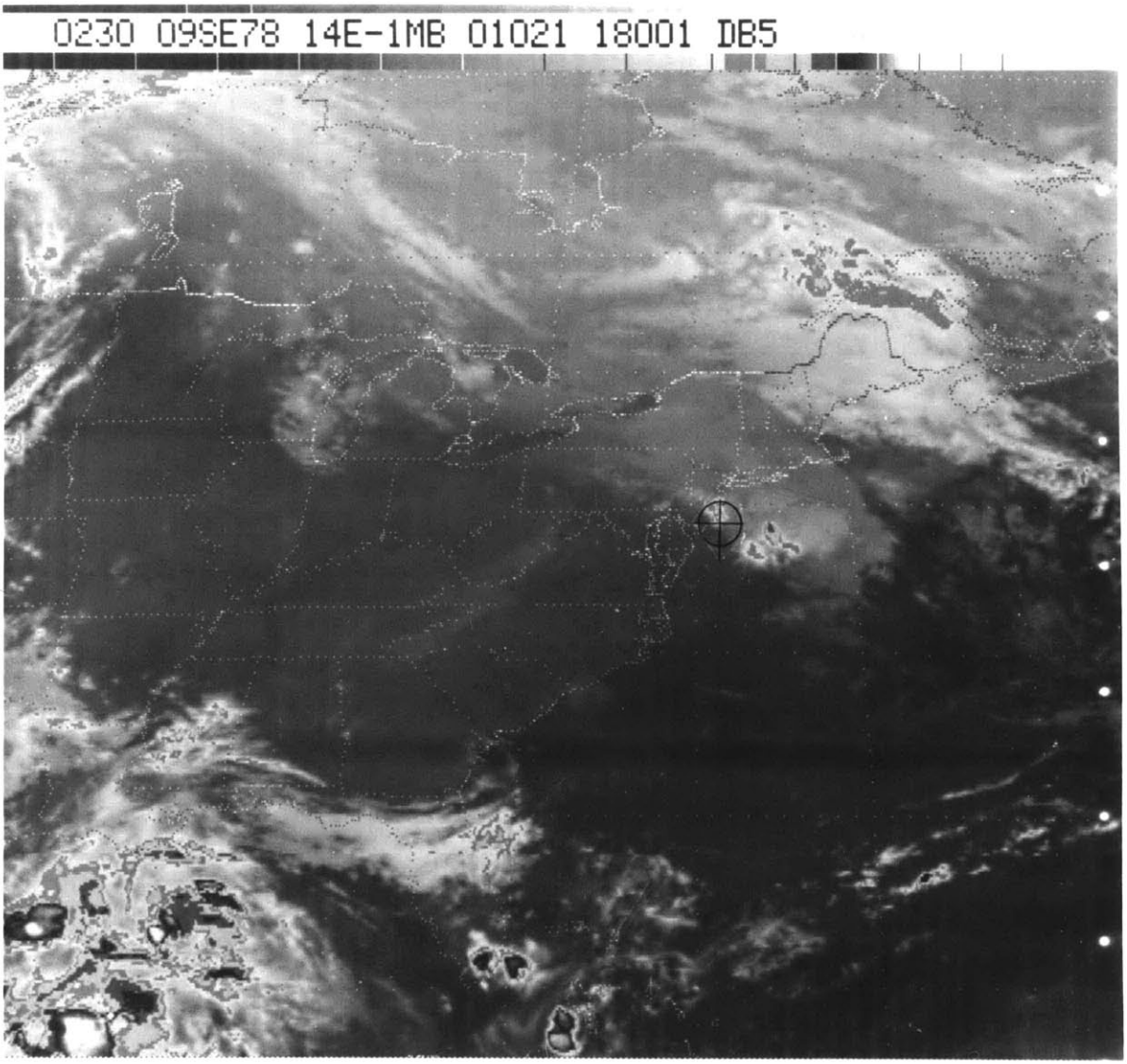


Fig. 3.3c. As for Fig. 3.3a, except for 0230 GMT, 9 September.

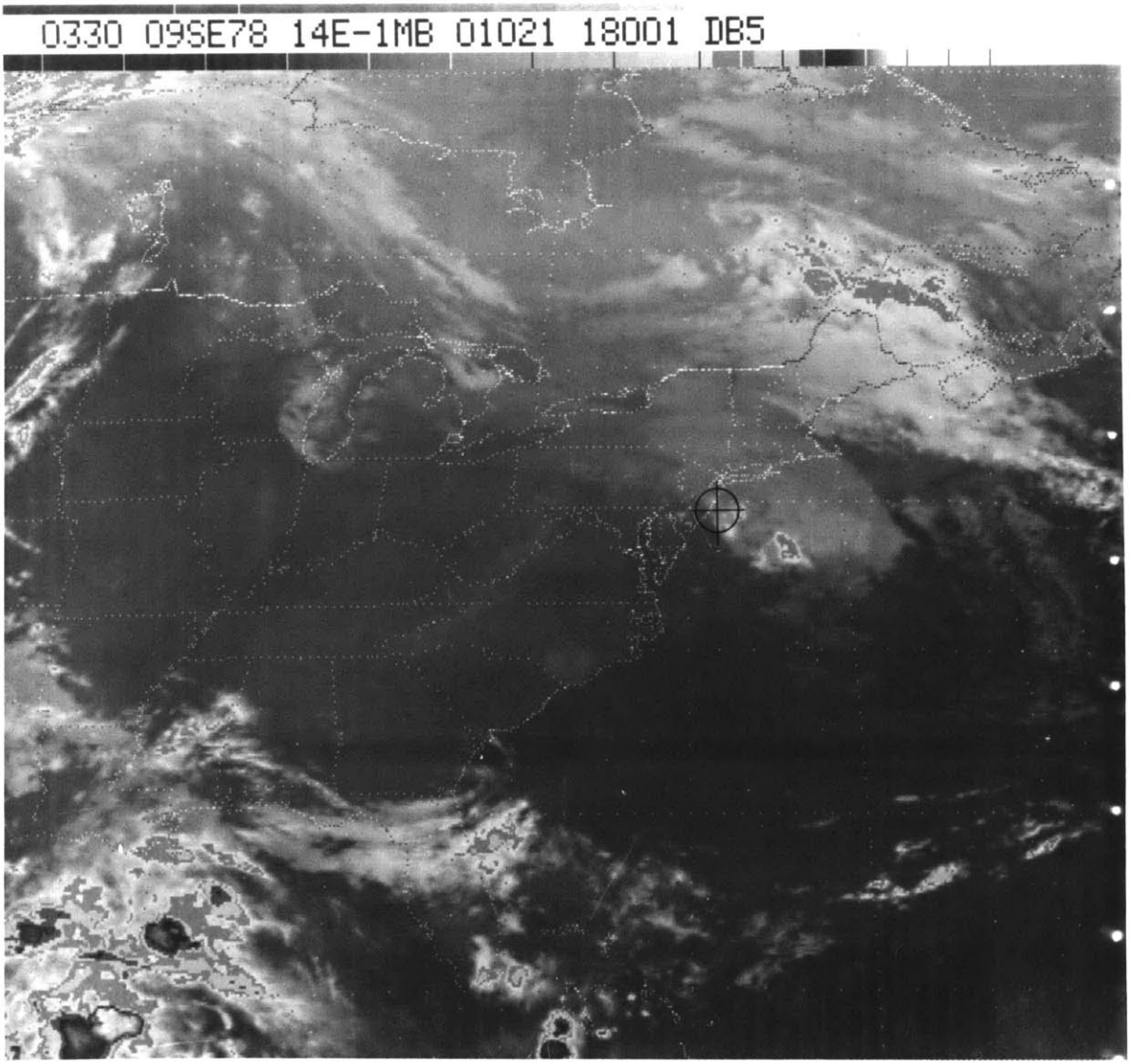


Fig. 3.3d. As for Fig. 3.3a, except for 0330 GMT, 9 September.

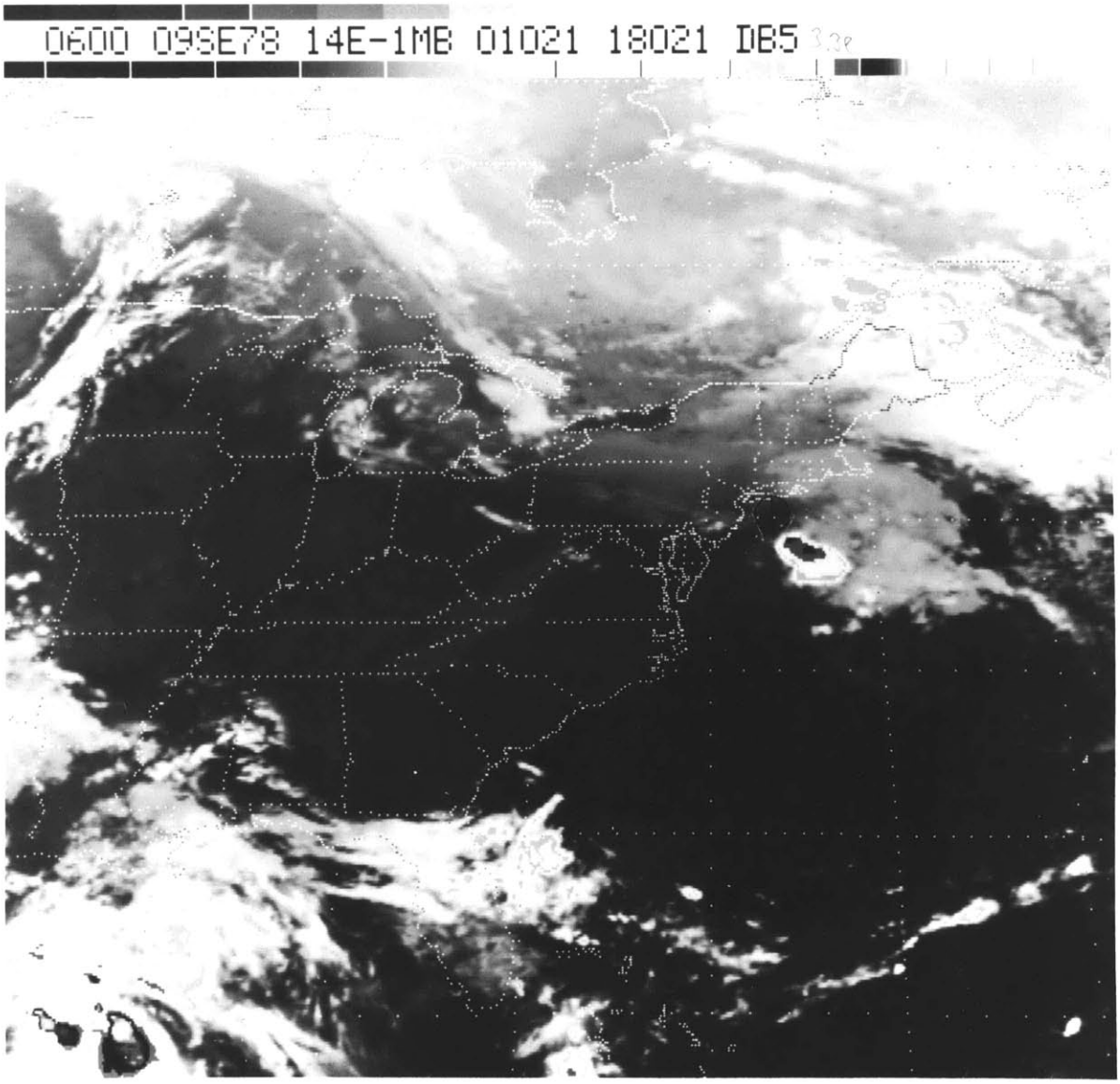


Fig. 3.3e. As for Fig. 3.3a, except for 0600 GMT, 9 September.

Fig. 3.2). The approximate steering level for this MCC was 700 mb. This major complex apparently propagated independently of the east-northeastward moving surface cyclone, and peaked in size to 420,000 km^2 at 10 GMT.

The upper-level charts for 00 GMT on the 9th are shown in Fig. 3.4. The most noteworthy feature is the rapidity with which the surface trough disappears with height. No associated trough exists at either the 500 mb or 250 mb levels. In fact, cyclonic relative vorticity in the Wallops-Fort Totten-Dulles triangle (indicated by WAL, JFK, and IAD in Fig. 3.4) is confined to levels below 890 mb. Fig. 3.25a shows cold, high tropopause air, which is characteristic of a subtropical atmosphere, directly over the surface cyclone.

Once offshore, the cyclone assumed a more eastward track at an increased speed averaging 35 knots between 06 and 12 GMT. Fig. 3.5 shows the time section of buoy observations at 40.1°N, 73.0°W, and at 40.8°N, 68.5°W. The deepening low clearly passed just to the north of the former buoy prior to 07 GMT, and to the south of the latter buoy between 12 and 13 GMT.

By 12 GMT on the 9th, the storm was continuing on its eastward path, and had deepened to 1004 mb, as is shown in Fig. 3.6. This sea-level pressure analysis has been reinforced by the welcome addition of Seasat surface winds.

The Seasat set adds considerable detail to the information given by the existing array of ship reports and buoy observations. This surface wind set was used to construct an isotach-isogon analysis

Fig. 3.4. Heights (solid lines) and isotherms (dashed) on the 850 , 500, and 250 mb surfaces for 00 GMT, 9 September 1978. Winds are plotted in knots, and temperatures are in °C. Solid circles show a temperature-dewpoint spread ≤ 5°C. Surface cyclone is indicated by an "L". Commercial aircraft winds are plotted on the 250-mb chart.

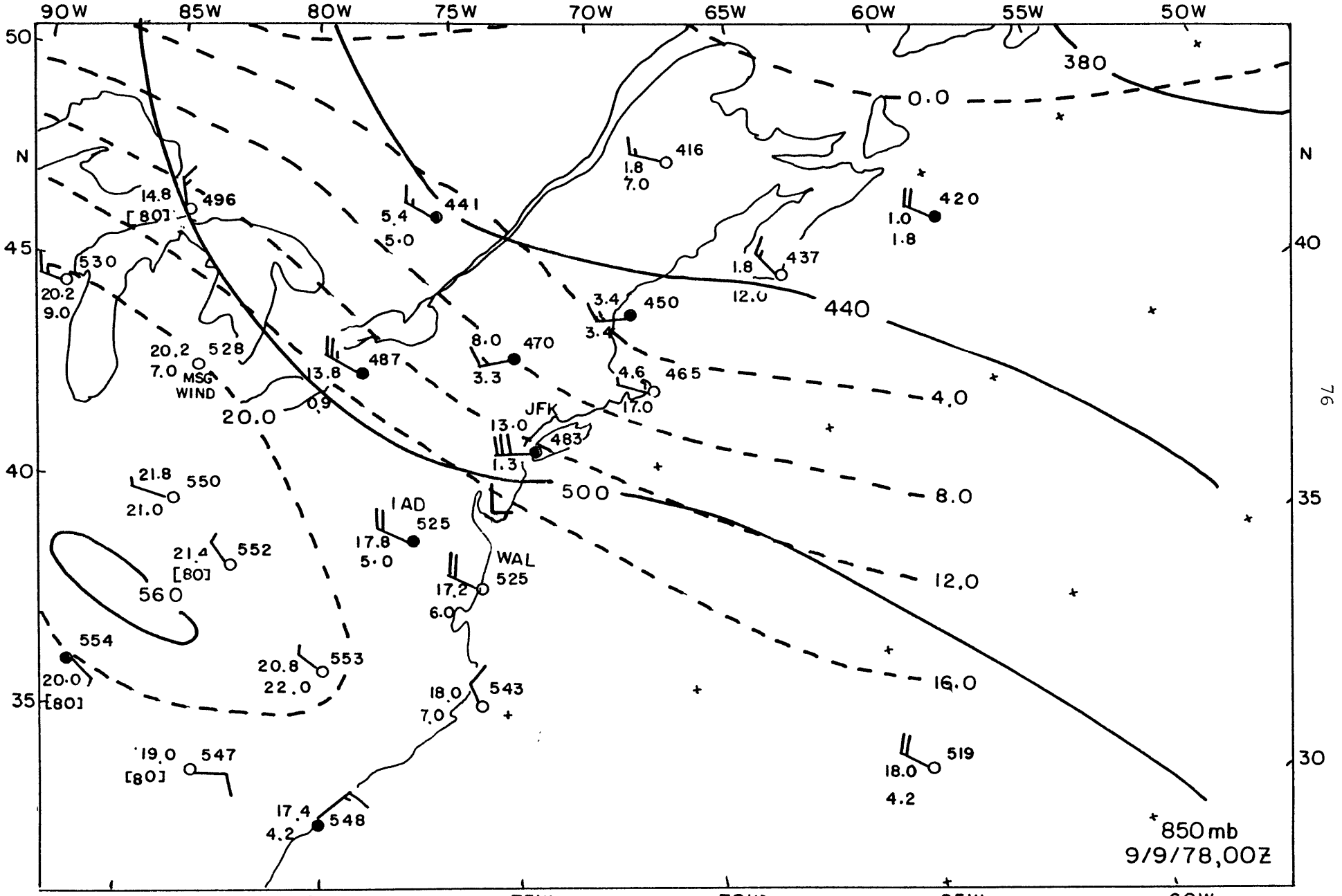

90W
85W
80W
75W
70W
65W
60W
55W
50W
50
N
45
40
35
30
380
0.0
4.0
8.0
12.0
16.0
440
500
560
416
1.8
7.0
420
1.0
1.8
441
5.4
5.0
496
14.8
[80]
530
20.2
9.0
437
1.8
12.0
450
3.4
3.4
470
8.0
3.3
465
4.6
17.0
528
20.2
7.0
MSG
WIND
487
13.8
0.9
20.0
JFK
13.0
483
1.3
550
21.8
21.0
IAD
525
17.8
5.0
552
21.4
[80]
WAL
525
17.2
6.0
554
20.0
[80]
553
20.8
22.0
543
18.0
7.0
547
19.0
[80]
548
17.4
4.2
519
18.0
4.2
850 mb
9/9/78,00Z

Fig. 3.4a

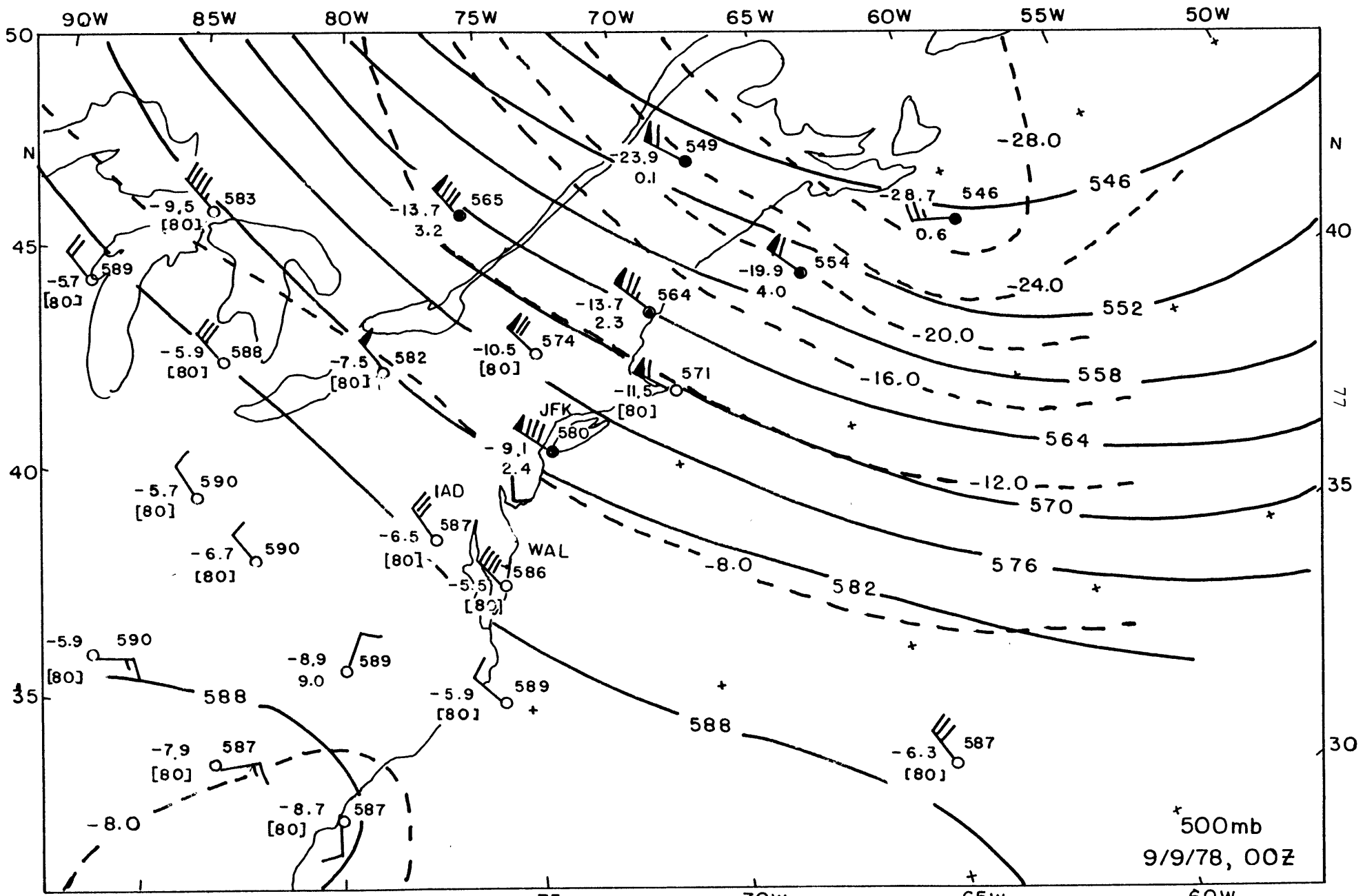

90W
85W
80W
75W
70W
65W
60W
55W
50W
50
N
45
40
35
30
-28.0
546
-24.0
552
-20.0
558
-16.0
564
-12.0
570
576
-8.0
582
588
-23.9
0.1
549
-28.7
546
0.6
-19.9
4.0
554
-13.7
3.2
565
-13.7
2.3
564
-10.5
[80]
574
-11.5
[80]
571
-7.5
[80]
582
-9.5
[80]
583
-5.7
[80]
589
-5.9
[80]
588
JFK
580
-9.1
2.4
IAD
-6.5
[80]
587
WAL
586
-5.5
[80]
-5.7
[80]
590
-6.7
[80]
590
-5.9
[80]
590
-8.9
9.0
589
-5.9
[80]
589
-7.9
[80]
587
-8.7
[80]
587
-6.3
[80]
587
500mb
9/9/78, 00Z

Fig. 3.4b

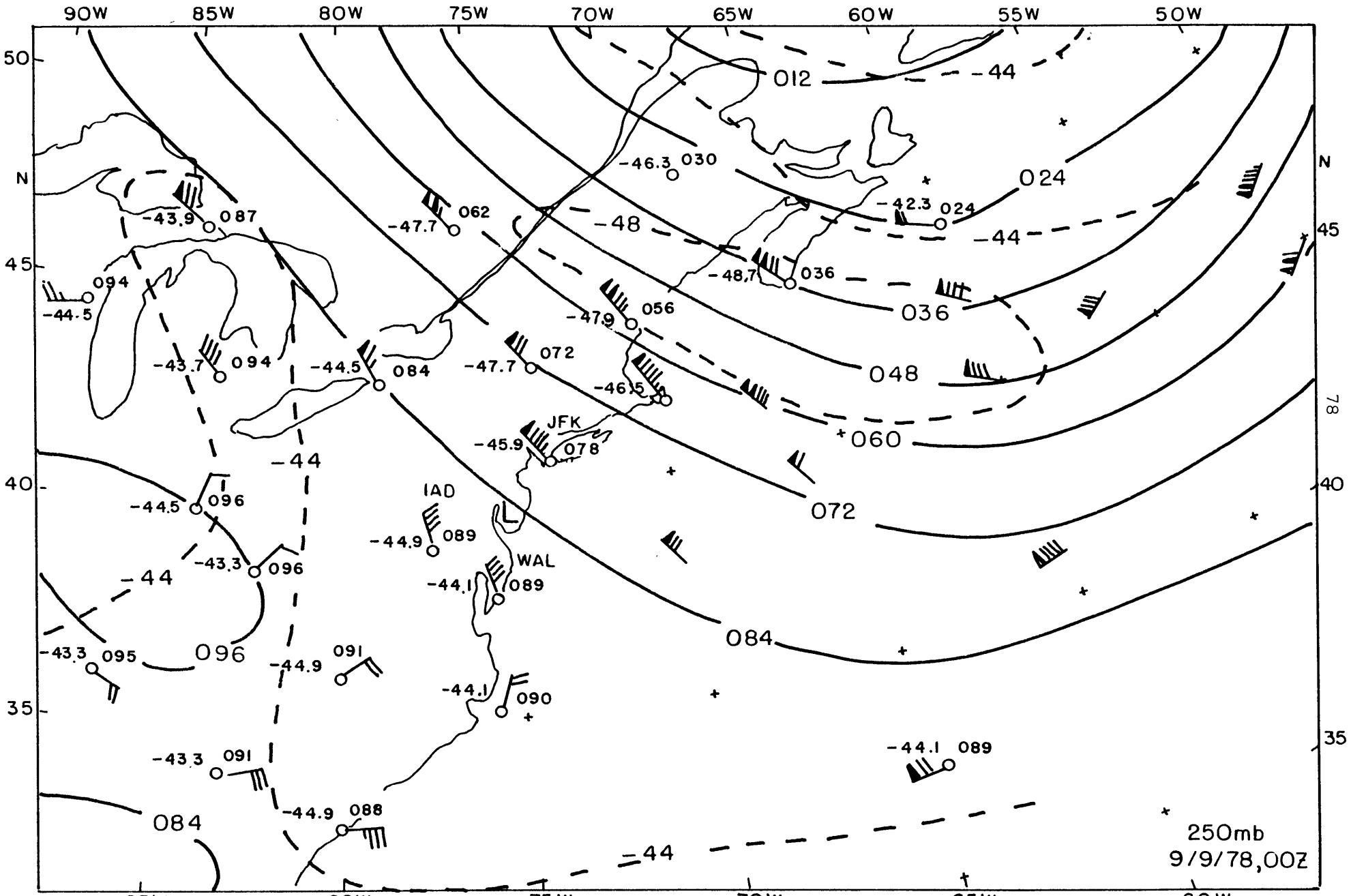

90W
85W
80W
75W
70W
65W
60W
55W
50W
50
N
45
40
35
012
-44
024
-48
036
048
060
072
084
096
-46.3 030
-42.3 024
-48.7 036
-47.9 056
-47.7 062
-47.7 072
-46.5
-45.9 078
JFK
IAD
WAL
-43.9 087
-44.5 094
-43.7 094
-44.5 084
-44.5 096
-43.3 096
-44.9 089
-44.1 089
-43.3 095
-44.9 091
-44.1 090
-43.3 091
-44.9 088
-44.1 089
250mb
9/9/78,00Z

Fig. 3.4c

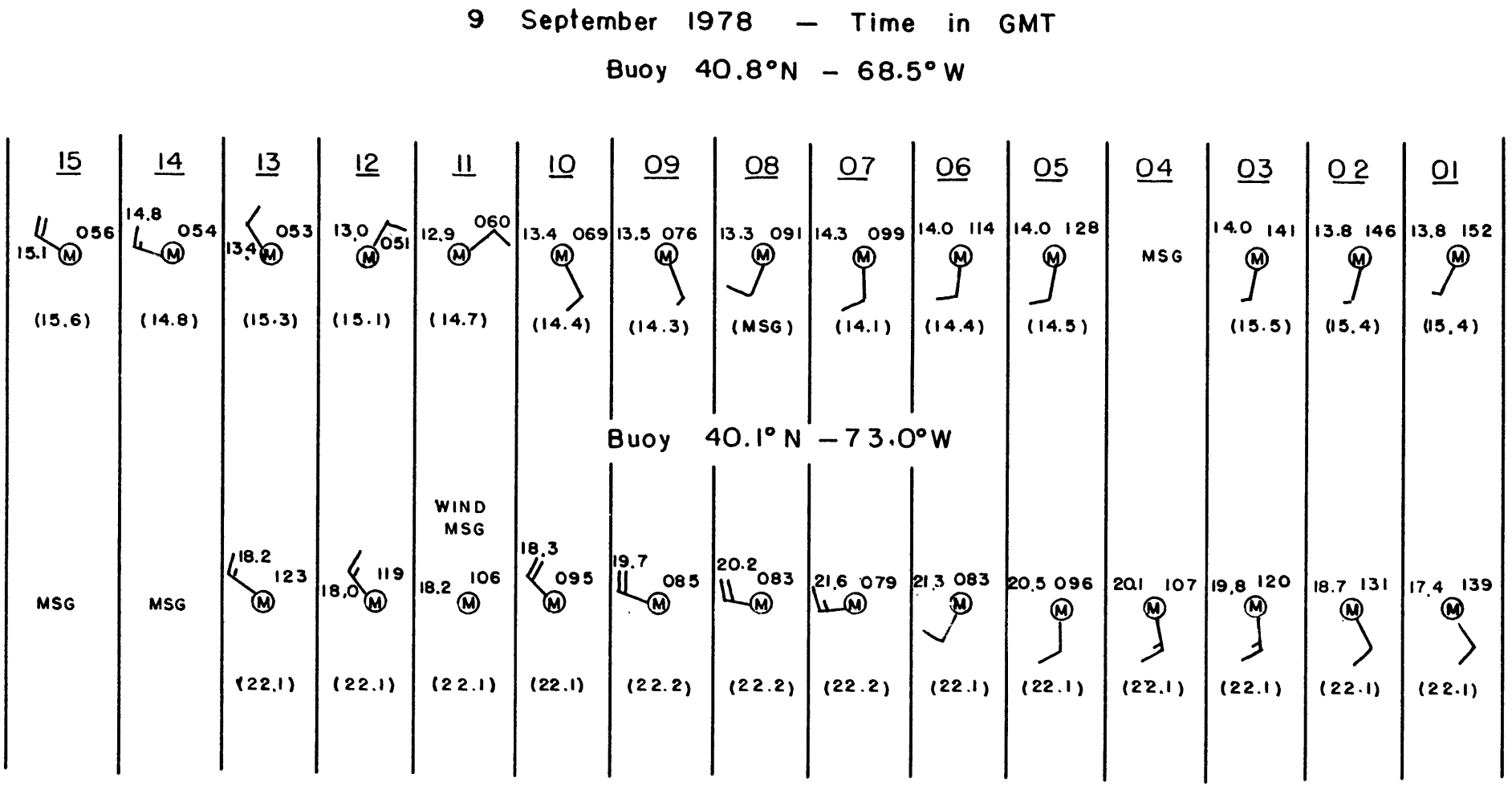


Fig. 3.5. Hourly time section of buoys located as shown, indicating temperature (°C), pressure (mb), wind (knots), and sea-surface temperature (°C).

Fig. 3.6. Surface winds at 12 GMT on 9 September with Seasat, ship, and land station winds included. Seasat observations are plotted without circles, while cloud amounts and sea-level pressures are plotted at the traditional reporting stations.

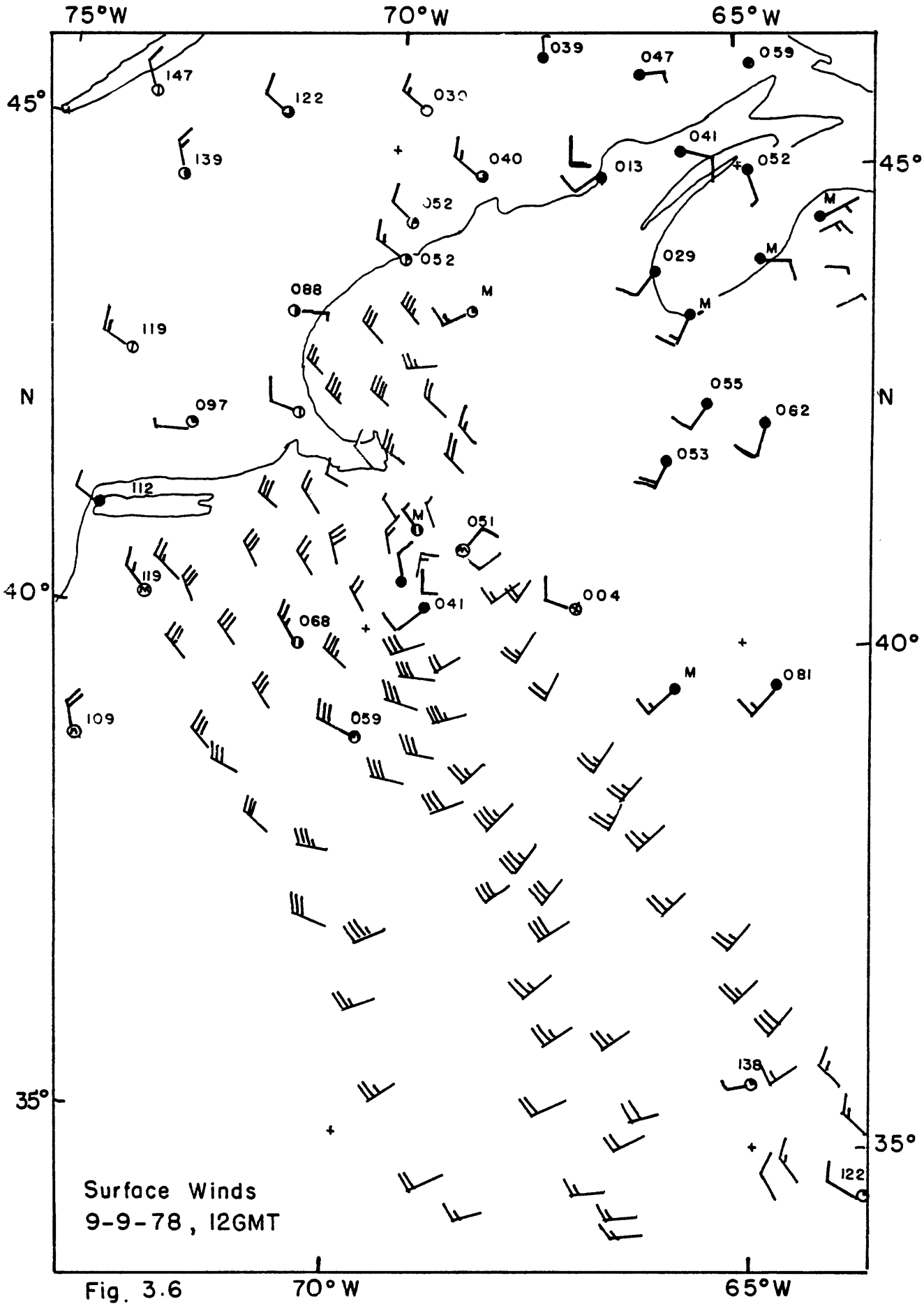

75°W
70°W
65°W
45°
40°
35°
N
147
122
030
039
047
059
139
040
013
041
052
052
052
088
M
029
M
M
119
097
055
062
053
112
M
051
119
004
041
068
081
M
109
059
138
122
Surface Winds
9-9-78, 12GMT

Fig. 3.6

from which divergences and relative vorticities have been computed on a one-degree latitude by a one-degree longitude grid using centered differences for each grid point. The computational domain and the surface relative vorticity field are shown in Fig. 3.7. The 17×10^{-5} sec^{-1} value in the vicinity of the young, developing cyclone is higher than the storm-scale values associated with the decaying cyclone at 45°N, 67°W, in spite of the lower central pressure of the latter system.

The surface system at 12 GMT on the 9th was still quite shallow, as no associated trough is detected at 250 mb. Fig. 3.8 also shows the surface low to be southwest of the maximum mean tropospheric virtual temperature gradient. Commercial aircraft cruise at about 250 mb. These wind reports are used to supplement the radiosonde information at the domain boundaries. Winds are assumed to be geostrophic at this level and, with the subtraction of the corresponding 1000 mb geostrophic wind vector based upon the sea-level pressure analyses, a thermal wind is computed for each data point. This procedure is the basis for the mean tropospheric temperature analysis in Fig. 3.8.

Fig. 3.9 indicates the track of the low subsequent to 12 GMT on the 9th, along with a composite sea-surface temperature analysis constructed using data for the three-day period prior to this time. Note the low center exists over a relatively uniform sea-temperature of about 22°C until after 00 GMT on the 10th. This fact, combined with the movement to the left of the upper tropospheric flow toward cooler mean tropospheric temperatures (see Fig. 3.8) implies a decrease of mean tropospheric static stability following the low center. The possibility

Fig. 3.7. Surface relative vorticity $\frac{\Delta v}{\Delta x} - \frac{\Delta u}{\Delta y} + \frac{u \tan\phi}{a}$ for 12 GMT, 9 September 1978. Units are 10^{-5} sec^{-1}. Surface low centers are indicated with "L".

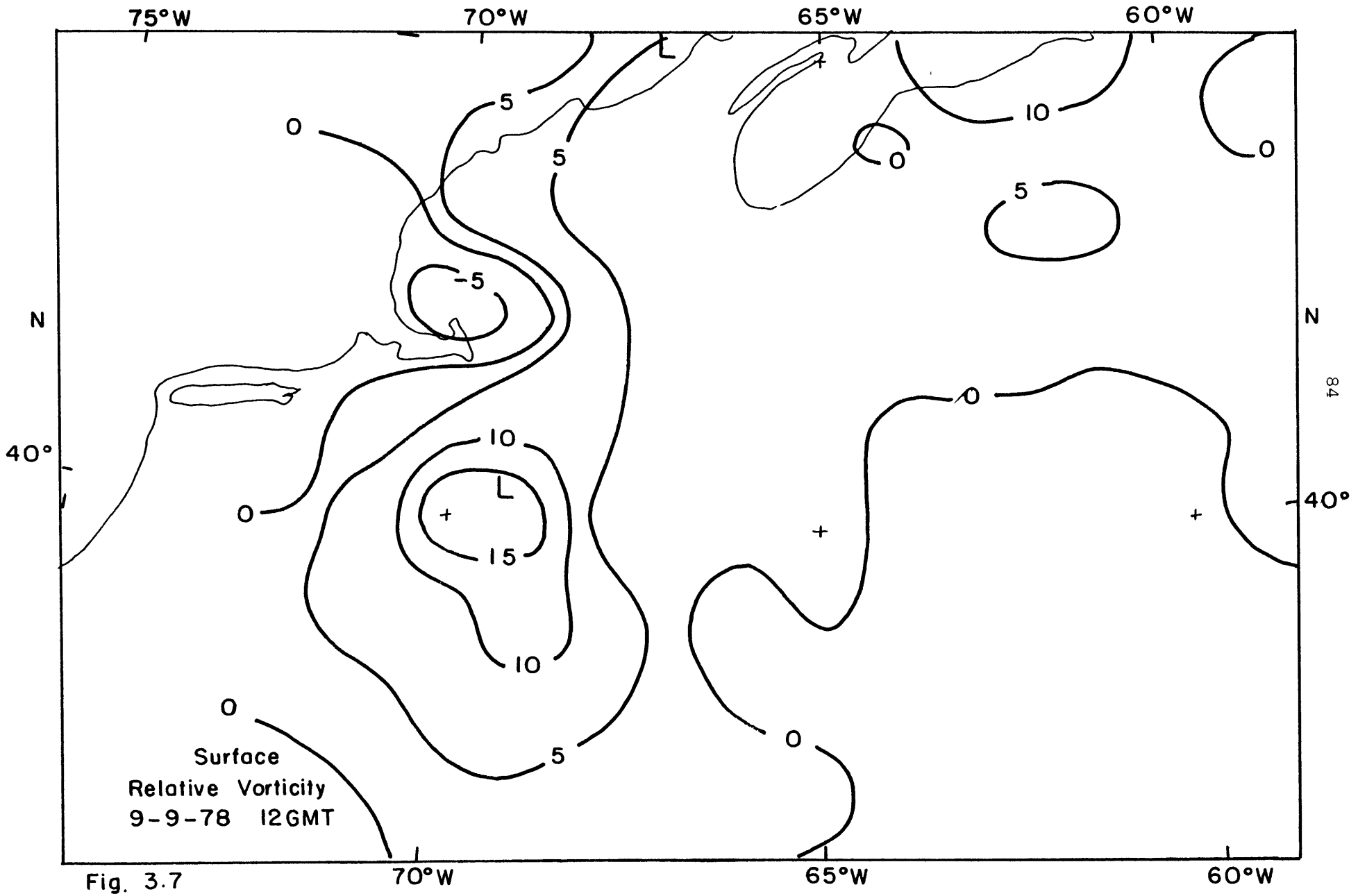

75°W
70°W
65°W
60°W
N
40°
0
5
-5
10
15
L
+
Surface
Relative Vorticity
9-9-78 12GMT

Fig. 3.7

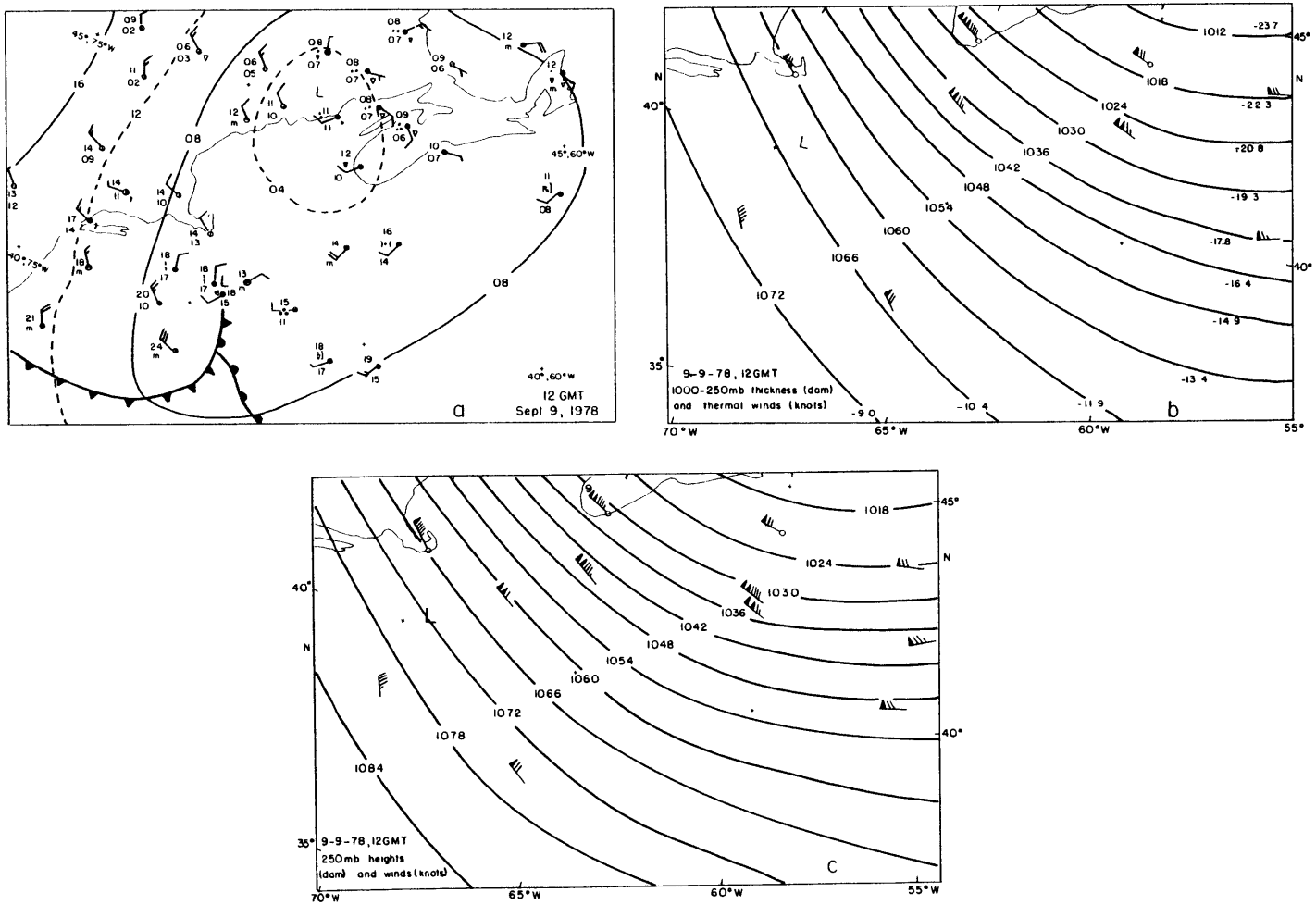


Fig. 3.8. (a) Surface chart for 12 GMT, 9 September 1978 in conventional format, including winds, temperature, and dewpoint temperature.

(b) As for (a), except for the 1000-250 mb thickness analysis. Thickness isopleths are also labeled with the corresponding mean virtual temperatures. Radiosondes are indicated with open circles, and commercial aircraft observations have no circles.

(c) As for (b), except for the 250-mb geopotential height analysis.

Fig. 3.9. Track of the surface cyclone along composite sea-surface temperature analysis based upon ship observations, the locations of which are indicated with dots, for the three-day period prior to 12 GMT, 9 September 1978. Temperatures are labeled in °C x 10.

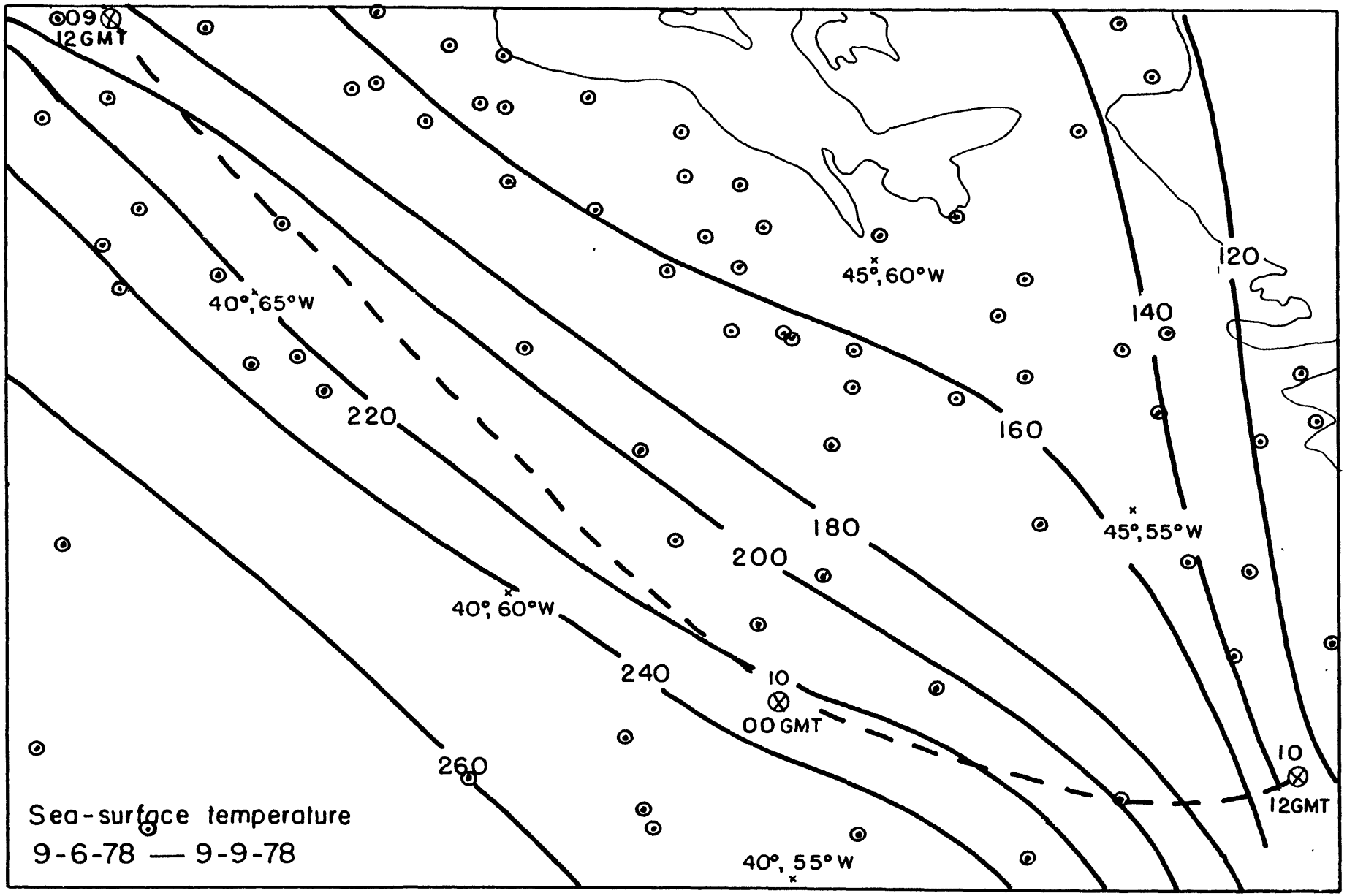

09
12GMT
120
140
160
180
200
220
240
260
45°, 60°W
40°, 65°W
45°, 55°W
40°, 60°W
40°, 55°W
10
00GMT
10
12GMT
Sea-surface temperature
9-6-78 — 9-9-78

Fig. 3.9

of deep convection near the center thus increases with time. An elaboration of this point is presented in later sections. The strong low-level warm advection eastward of the low clearly points to this shallow system propagating to the left of the mean tropospheric flow. This left movement of the surface low is opposite to what is usually observed in a typical, developing baroclinic wave (see Sanders, 1971 and Austin, 1947), primarily because of the above-discussed three-dimensional temperature distribution. This same behavior was noted by Bosart (1981) for the incipient stages of the explosively developing President's Day 1979 cyclone.

By 00 GMT on the 10th, the low was in a more favorable position for interaction with the heretofore downstream upper-level thermal trough (Fig. 3.8b), as is shown in Fig. 3.10. At this time, a slight anticyclonic curvature in the thermal wind pattern directly over the surface low is shown. Unfortunately, there are no reporting ships near the center to confirm the conservative central pressure estimate of 990 mb.

There is little doubt, however, of the extraordinary intensity of the surface system at 12 GMT on the 10th. By this time, the central pressure had plunged to an estimated 945 mb. As is shown in Fig. 3.11, the *Euroliner* had passed very close to the cyclone center. Indeed, the *Euroliner* barogram (fig. 3.12) confirms the incredibly tight pressure gradient surrounding the surface system. The 55-mb pressure fall it experienced during its 12-h odyssey into the vicinity of the eye is followed by an even more dramatic 3-h pressure rise of 31 mb. The

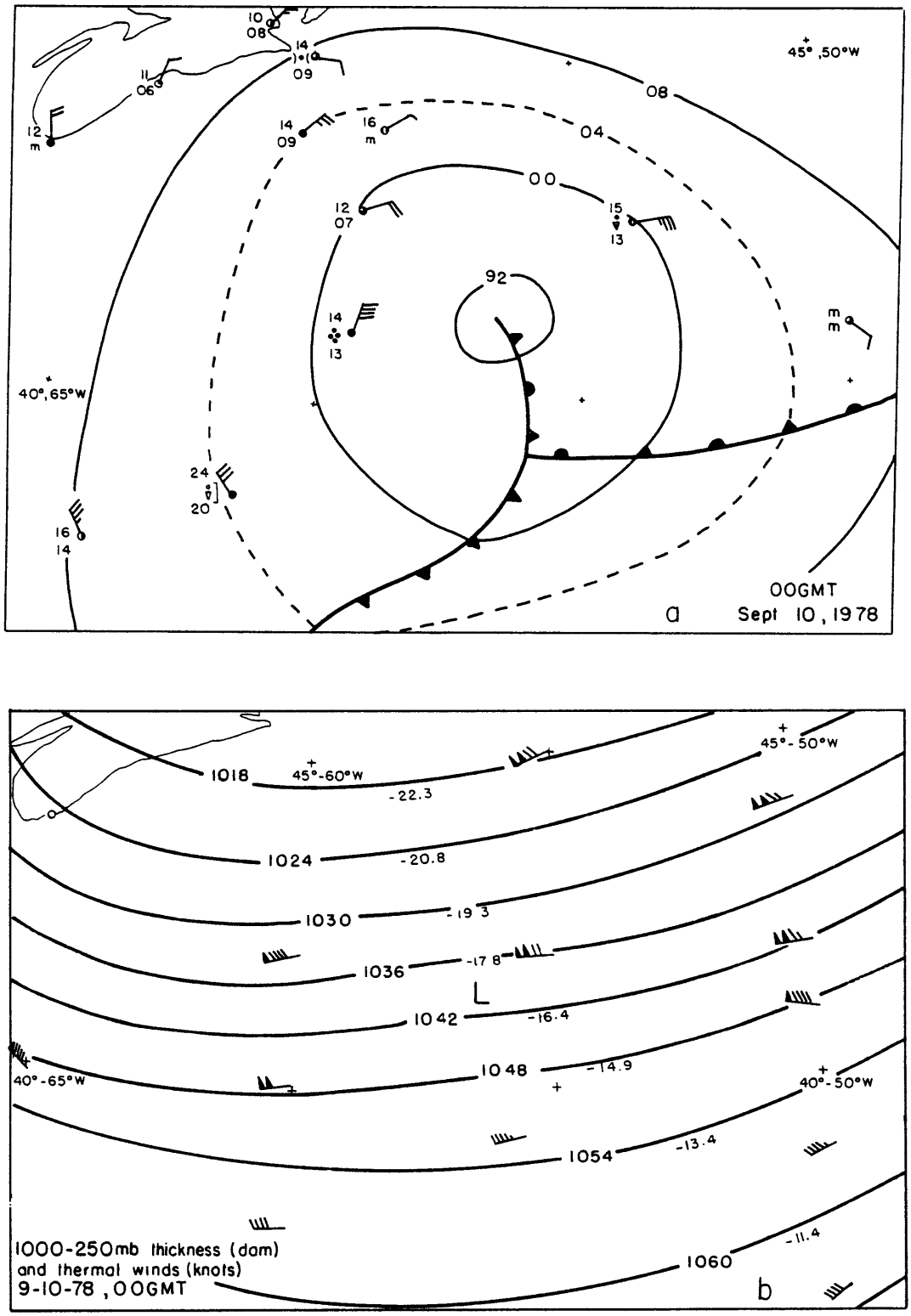


Fig. 3.10. Surface (a) and 1000-250 mb thickness (b) charts for 00 GMT on 10 September. Format as in Fig. 3.8.

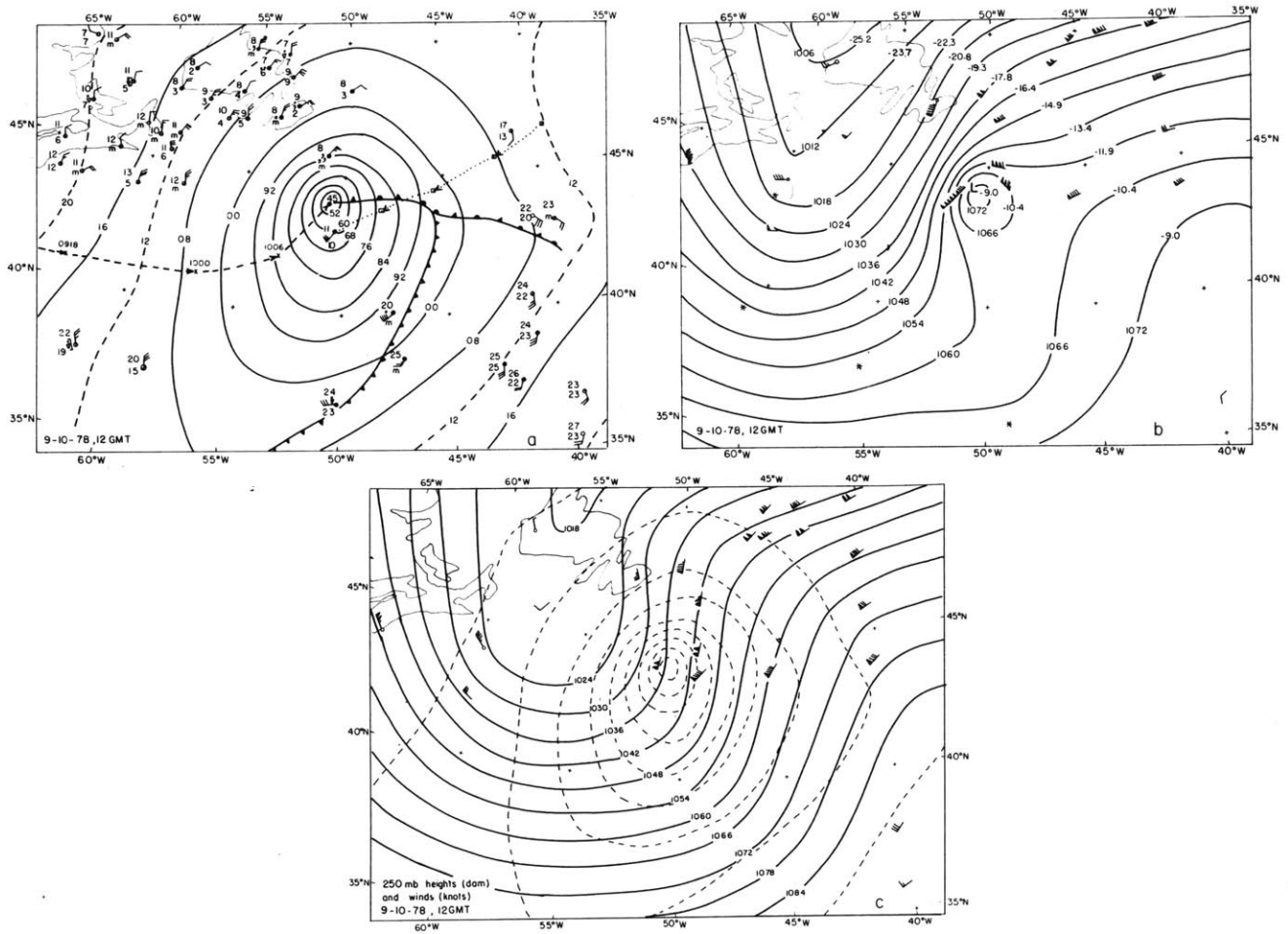


Fig. 3.11. (a) Surface map at 12 GMT, 10 September. Format as in Fig. 3.8.
(b) As for (a), except for the 1000-250 mb thickness analysis. *'s indicate locations of satellite-derived thickness observations.
(c) As for (a), except for the 250-mb geopotential height analysis. Dashed lines are sea-level isobars illustrating how the thermal winds are computed. Full complement of winds is shown for this time in Fig. 3.22c.

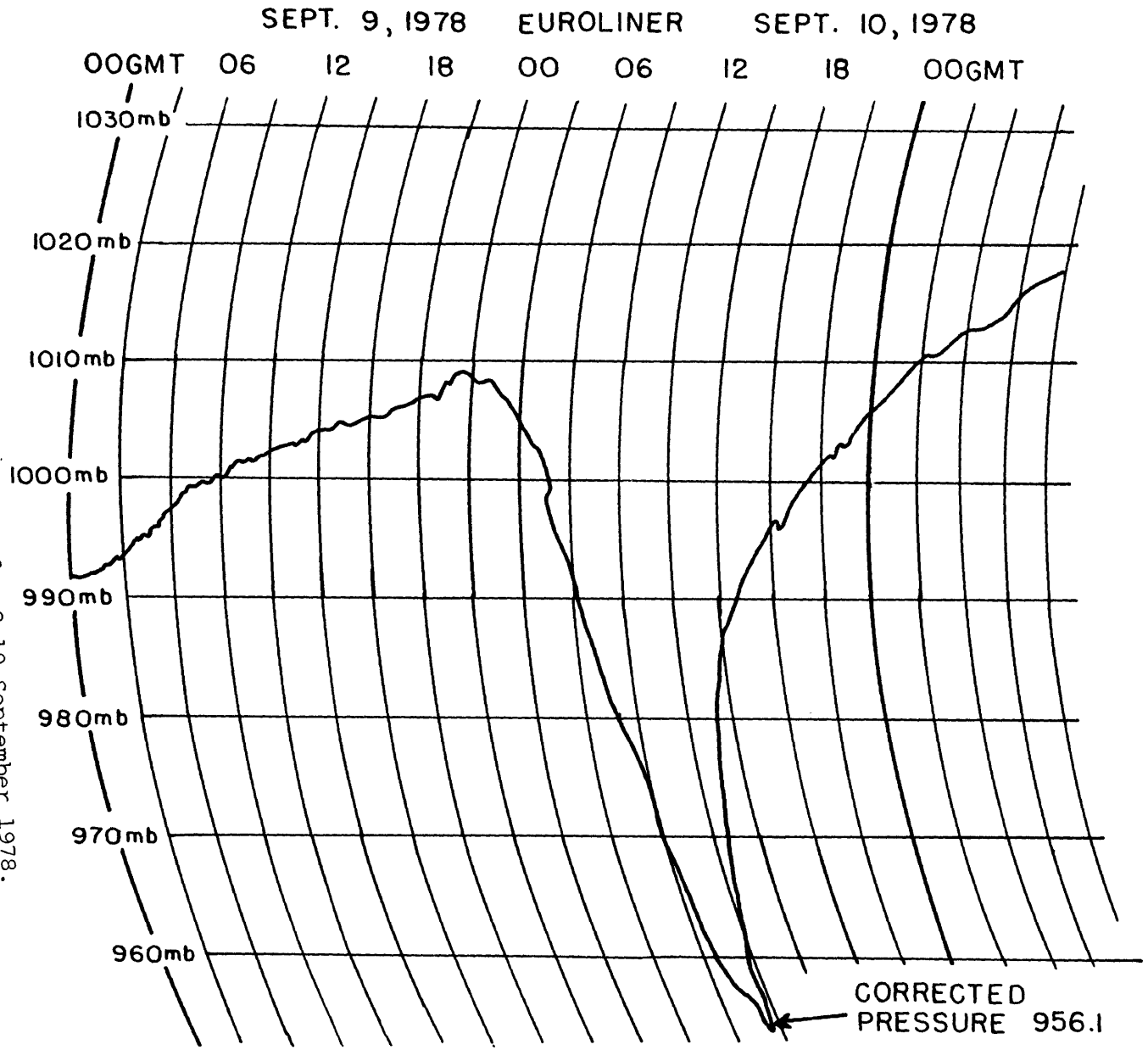


Fig. 3.12. Euroliner barograph trace for 9-10 September 1978.

anomalously warm thickness value of 10780 m (see Fig. 3.11b) above the surface cyclone is supported by three critical commercial aircraft observations (adjusted for time) of wind and temperature. The central thickness value was estimated from the 250 mb height analysis (10370 m over the surface low) and the 945 mb sea-level pressure estimate. This strong warm-core over the surface center resembles that of a tropical cyclone. Unfortunately, the NMC final analysis shown in Fig. 3.13 did not capture the extreme intensity of the cyclone owing to the missing *Euroliner* observation, in spite of its real-time availability on the Service C teletype. Note the ship wind direction of 350° just to the north of the NMC-analyzed surface center was changed to 35° in Fig. 3.11a. The 350° wind direction was indicated in real-time on the Service C teletype, and was probably a faulty transmission that appears credible in the absence of the *Euroliner* information and satellite imagery. The correct position of the surface cyclone at this time is also confirmed by the GOES-east satellite image (not shown), and by the wind reports from orbit 1080 of Seasat. This plot of surface winds is shown in Fig. 3.14. Note the Seasat wind directions confirm the credibility of the aforementioned 35° wind direction indicated with the 987 mb pressure. Although up to four possible directions are given for each SEASAT point, the directions shown represent, in the author's view, the most consistent wind pattern. Since the four speeds generally given for each SEASAT data point are virtually the same, there is little ambiguity in this piece of information. The observed winds reinforce the *Euroliner* 12 GMT pressure and wind report, and show the

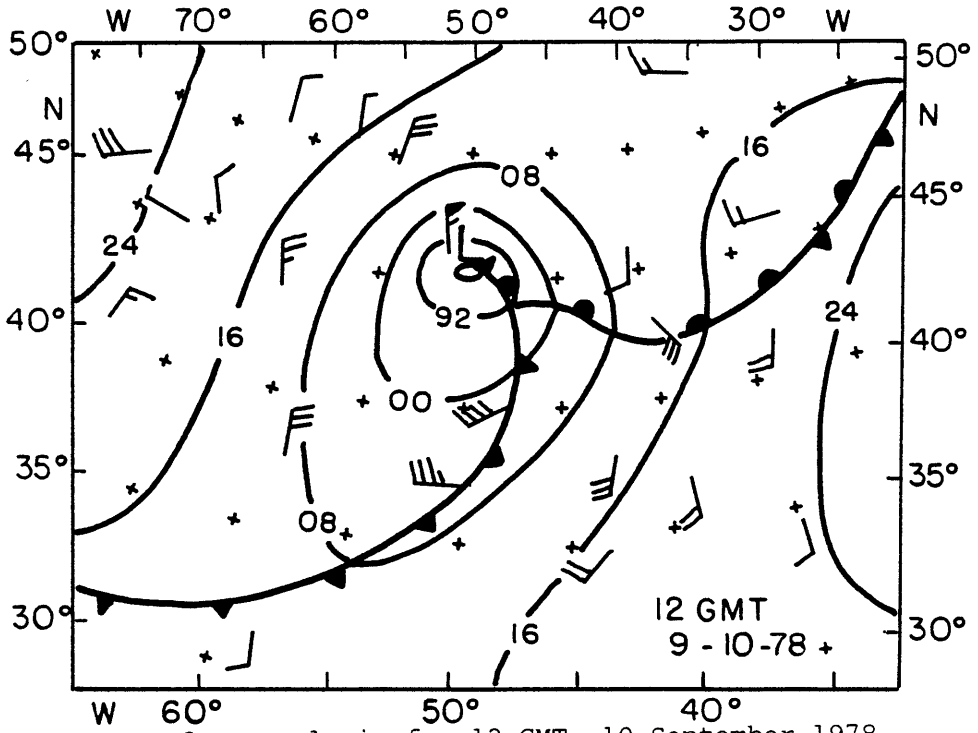


Fig. 3.13. NMC final surface analysis for 12 GMT, 10 September 1978. Winds only are plotted.

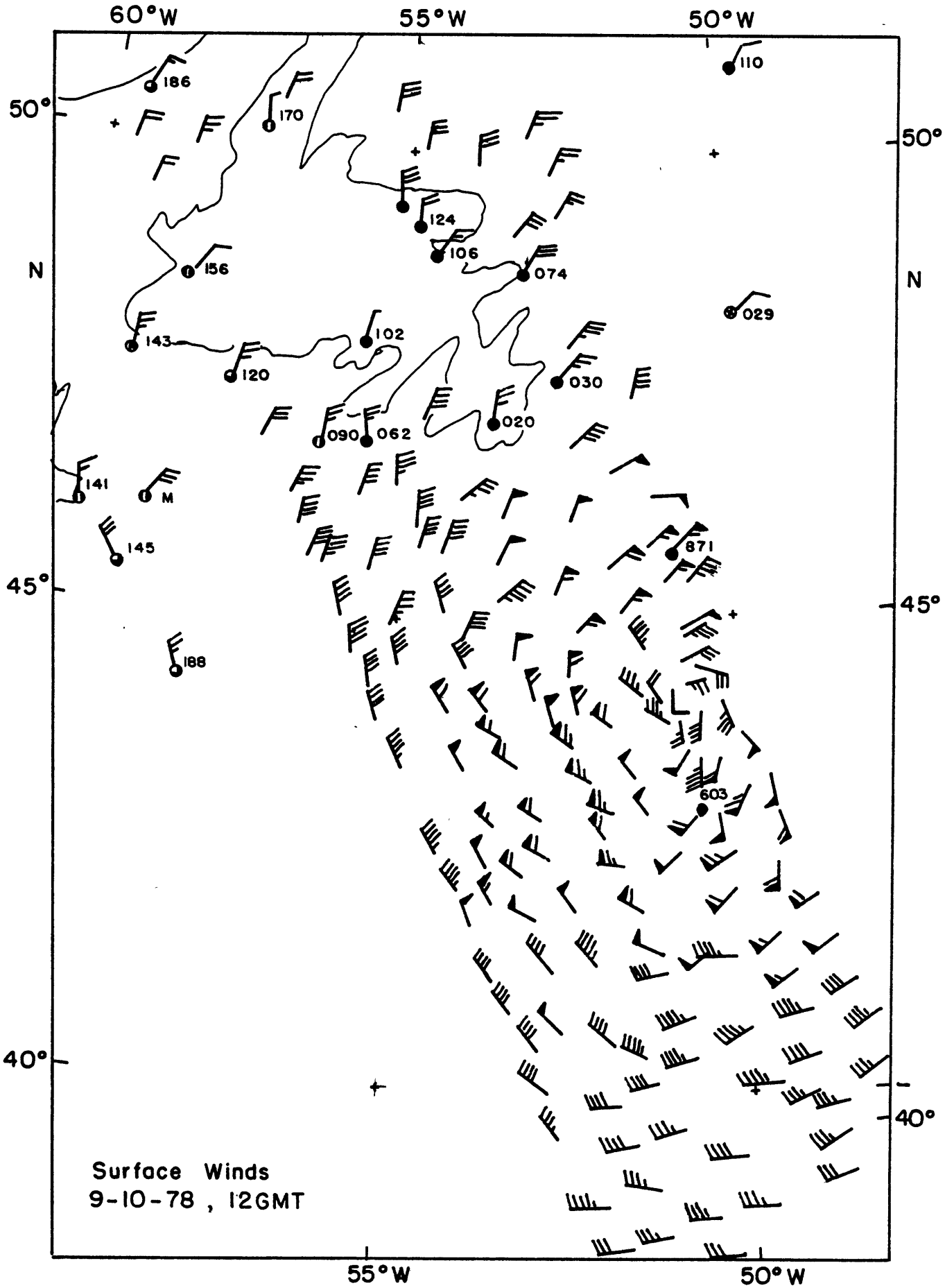


Fig. 3.14. Surface winds for 12 GMT, 10 September 1978, including land, ship, and Seasat reports. Format as in Fig. 3.6.

existence of hurricane-force winds 60-90 n mi south and west of the surface center. Seasat coverage is lacking north and east of the center. However, the resolution of these winds is sufficient to capture the minimum speeds of 20 knots within 15 n mi of the surface center. Our extrapolation of the horizontal pressure gradient yields a central pressure of 945 mb, while an overly conservative estimate of the central pressure, based on inviscid, cyclostrophic flow, the *Euroliner* report, and on the SEASAT winds, yields a central pressure of 947 mb. Although the 60-90 n mi radius of maximum wind (RMW) is generally higher than the 35 n mi RMW usually found for a tropical cyclone (Gray and Shea, 1973), this distinction is a fine one; for RMW's in hurricanes are highly variable, and occasionally do range much higher than the mean. The surface relative vorticity (Fig. 3.15) field for this time, constructed in the manner described earlier, shows a maximum storm-scale value of 47×10^{-5} sec^{-1}. Values of above 20×10^{-5} are shown at 9 grid points. Gray and Shea also show that maximum relative vorticities in the vicinity of the eyewall region are in this range. Clearly, the profiles of wind and pressure bear a close resemblance to that of a tropical cyclone.

A series of satellite images covering the 24-h period prior to 12 GMT on the 10th is shown in Fig. 3.16. The 12 GMT, 9 September MB-enhanced image shows the northern edge of the large MCC to be 280 km south of the developing surface center, whose cloud tops are no higher than 800 mb. By 1700 GMT, however, with the MCC and the surface low apparently independently diverging, a small area of deep convection over the surface low has appeared. This first level

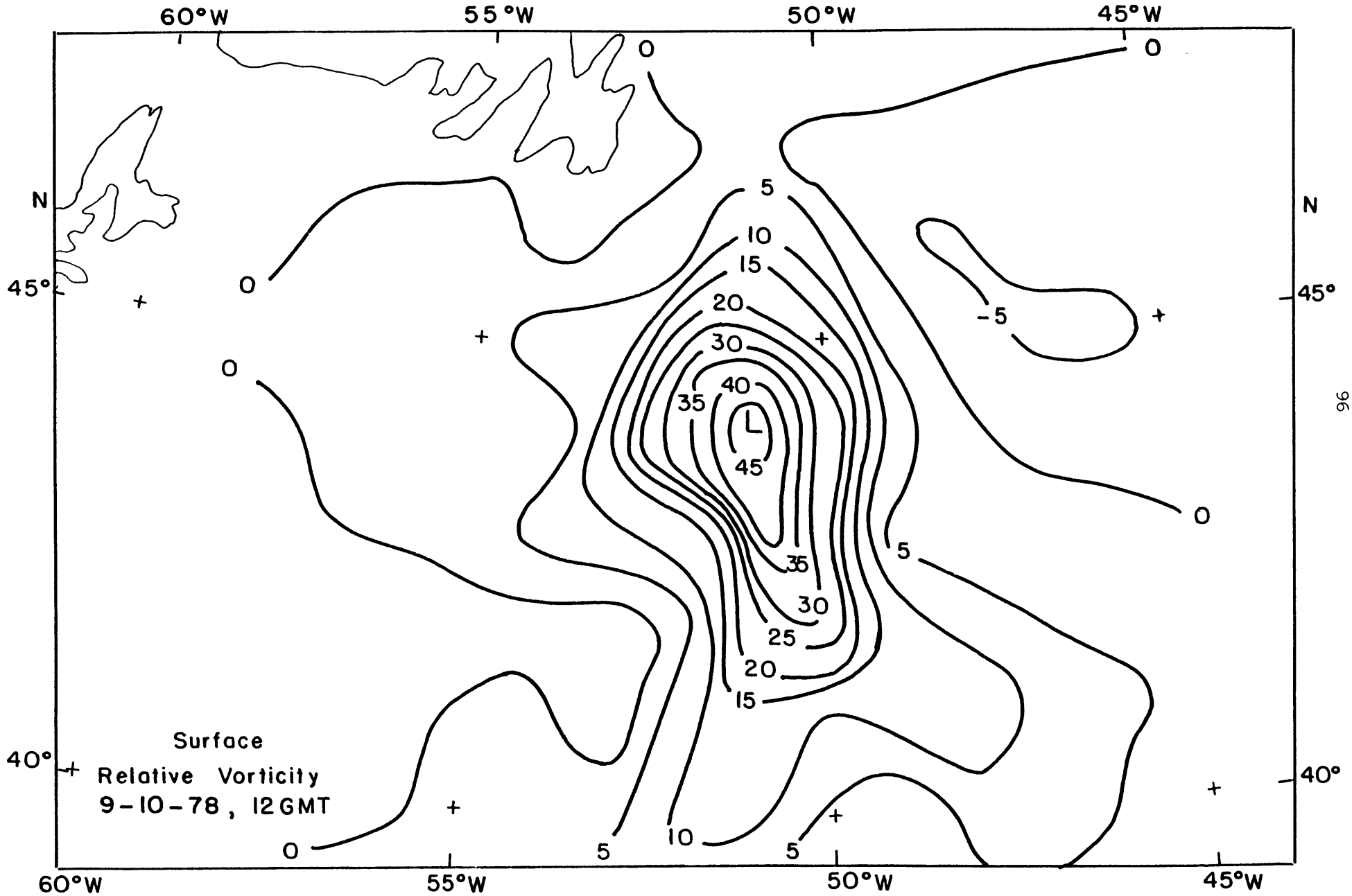


Fig. 3.15. As in Fig. 3.7, but for 12 GMT, 10 September 1978.

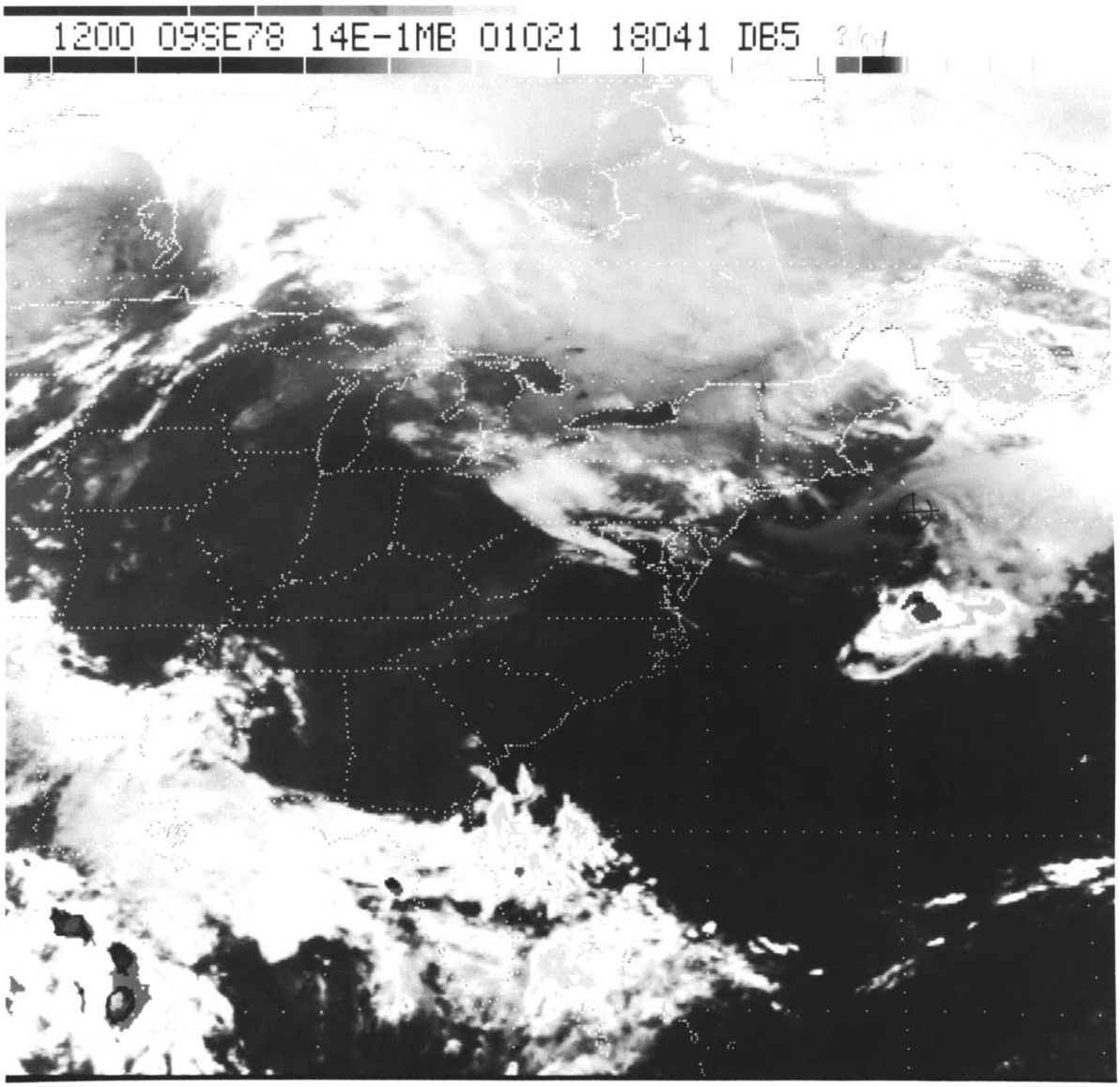


Fig. 3.16a. GOES-east MB-enhanced image for 12 GMT, 9 September 1978. Circle pinpoints the surface cyclone position, and the gridding is in error as is described for Fig. 3.3.

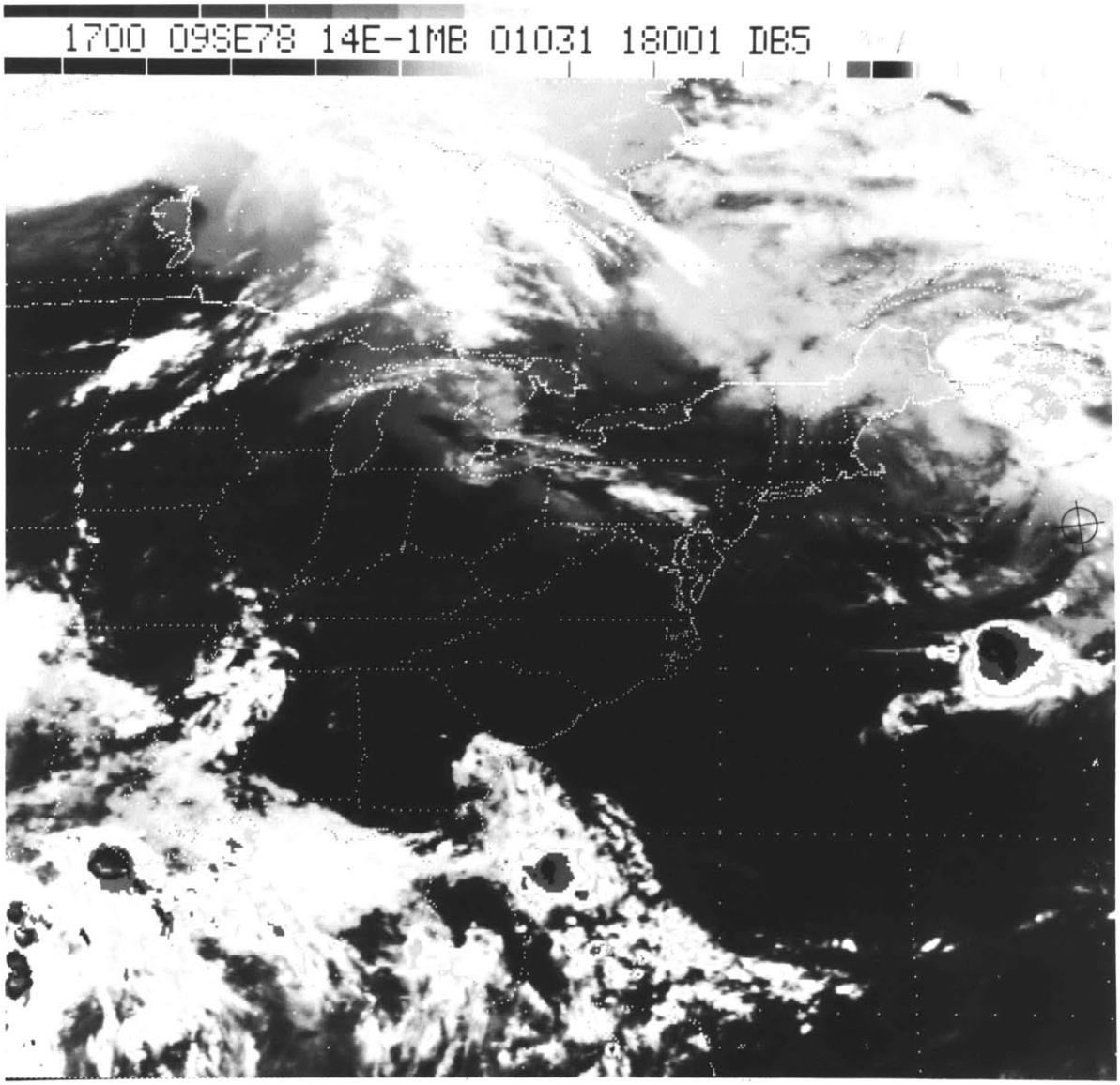


Fig. 3.16b. As for Fig. 3.16a, except for 17 GMT, 9 September 1978.

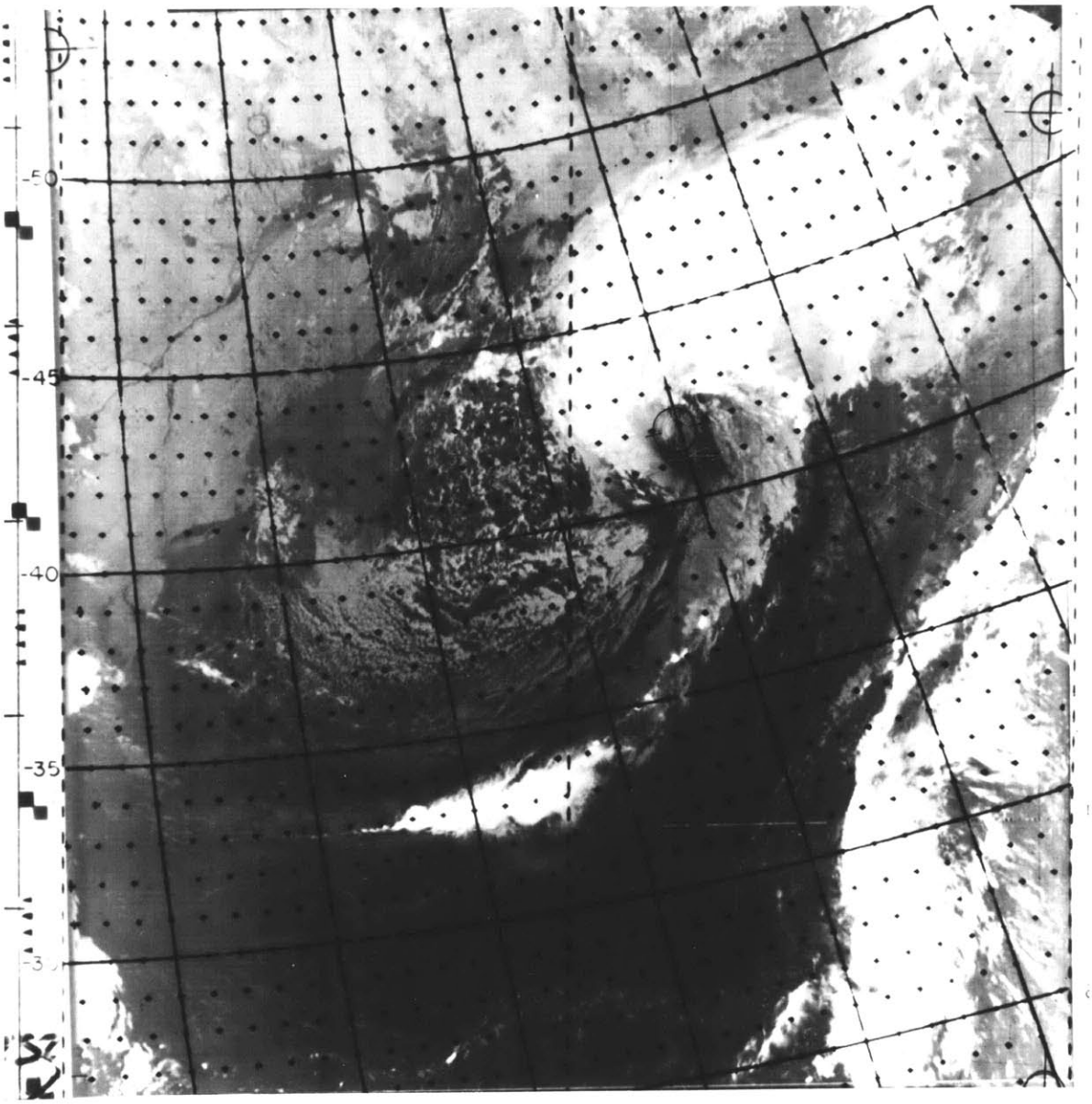


Fig. 3.16c. As for Fig. 3.16a, except for the DMSP infrared image for 0350 GMT, 10 September 1978. Gridding is accurate.

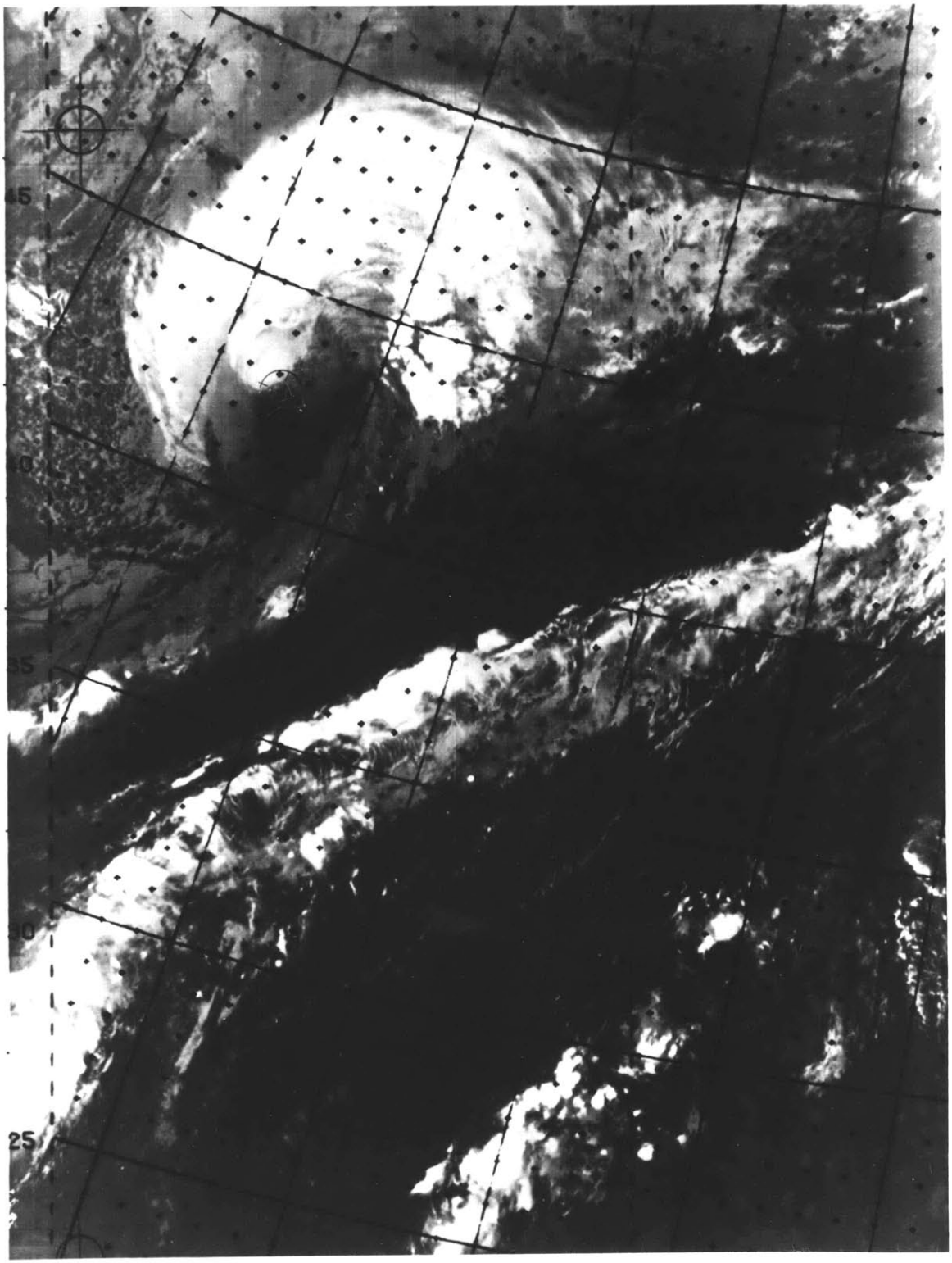


Fig. 3.16d. As for Fig. 3.16c, except for 0859 GMT, 10 September 1978.

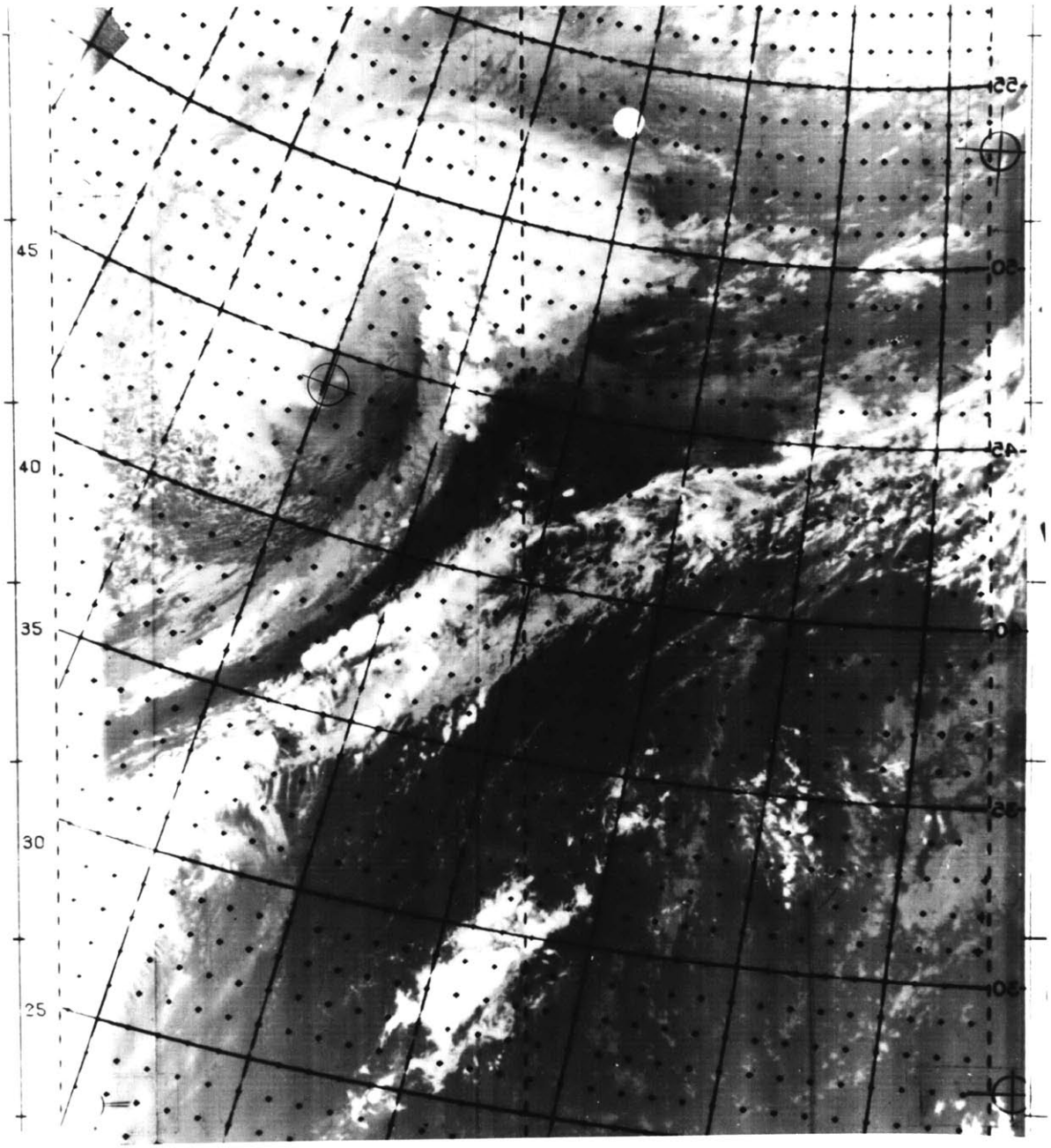


Fig. 3.16e. As for Fig. 3.16c, except for 1330 GMT, 10 September 1978.

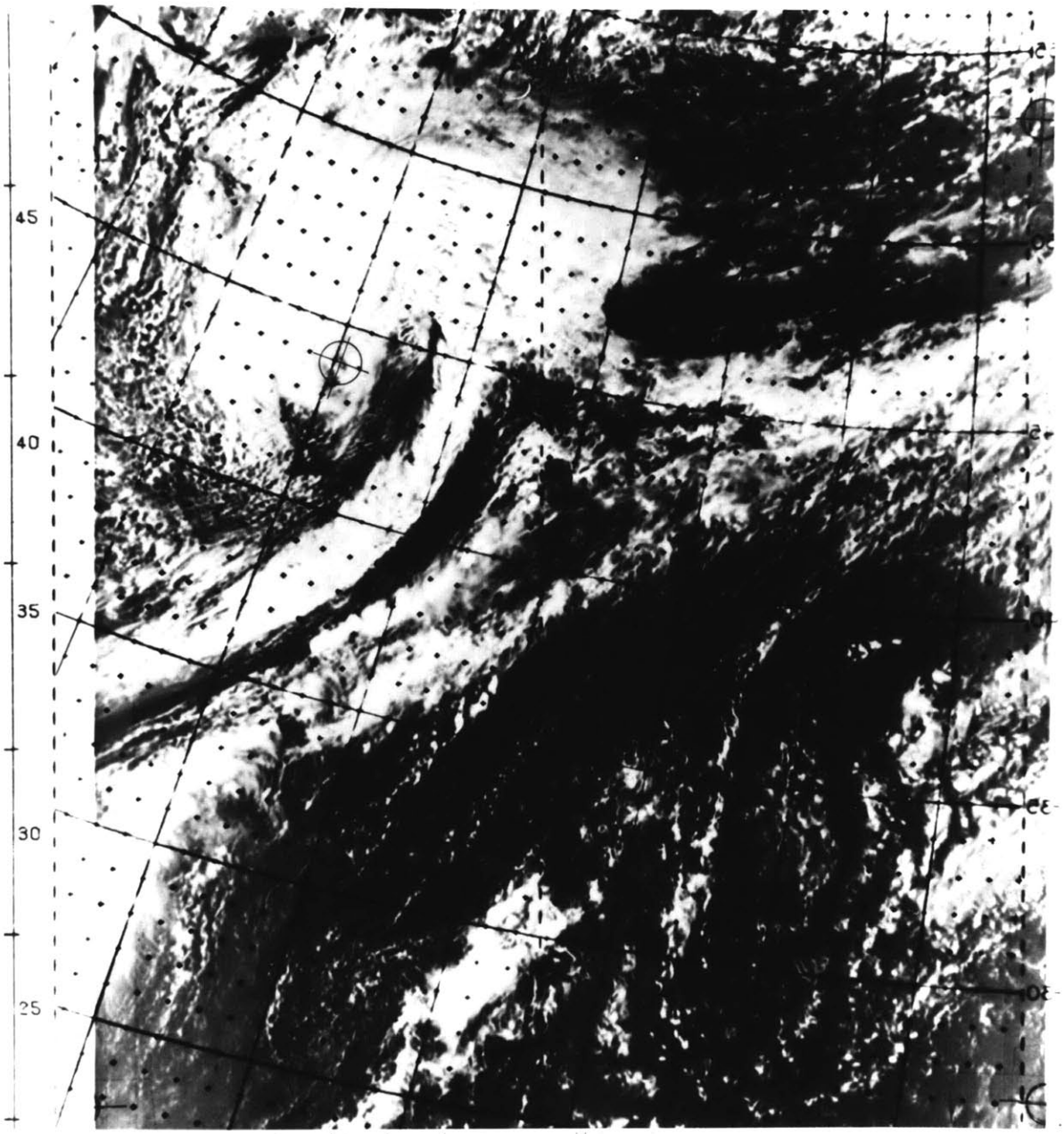


Fig. 3.16f. As for Fig. 3.16c, except for the DMSP visible image for 1330 GMT, 10 September 1978.

contour (medium gray) indicates cloud tops have a temperature of -32°C ranging down to -41°C, or, considering the stratification, from 350 to 290 mb. The area covered by deep convective cells continues to expand and the cloud tops rise during the next 12 h. The DMSP infrared image at 0350 GMT on the 10th shows the extreme intensity of the storm. Evidence for the strong surface circulation is seen in the form of open convection cells to the southwest of the center, and the associated cold air penetrating southward to 33°N. By 09 GMT on the 10th, the area of deepest convection has moved off to ∿ 340 km northeast of the storm center. A cloud-free eye of diameter 90 km, including an additional area of cloud surrounding an inner eye of diameter 15 km, is also seen. It is hypothesized that the surface low has reached peak intensity by this time due to the deepest clouds moving away from the storm center, and (see Fig. 3.9) its movement over cooler waters at this time. This implies the storm intensified even more rapidly than the rate indicated in the previous map discussion, and the low could have reached a central pressure considerably lower than our 12 GMT 945 mb estimate. This information indicates the 09 GMT RMW may have been even less than that described earlier. The visible image for 1330 GMT clearly shows a cloud-free eye at the storm center, while the infrared image for the same time shows the clouds near the center to be relatively shallow, and the deep convection well off to the northeast to be lined up along the frontal band seen in Fig. 3.11.

When compared with Holliday and Thompson's (1979) sample of 305 typhoons at mean latitude 18°N, the extremely rapid development

of this surface cyclone of 59 mb in 24 h would represent a geostrophically equivalent rate of greater than 27 mb. This would place the QEII case at the 57th percentile of their sample of 24-h typhoon deepening rates. The deep convection around the center of the storm along with the hurricane-force winds, the closed eye over the center, and the intense tropospheric warm core are all similarities to that of a tropical cyclone in this otherwise extratropical case. Apparently other cyclones have undergone a similar identity crisis. The morning of 22 November 1980 found a surface cyclone east of Cape Cod explosively intensifying 20 mb in 12 h to an estimated central pressure of 966 mb with mobile ships reporting winds of up to 75 knots. Three days later, as the cyclone was apparently filling, the National Hurricane Center named this same storm Hurricane Karl on the basis of hurricane-like cloud patterns shown in the satellite imagery (see NOAA, 1981).

3.4 Operational Model Performance

The NMC LFM-II initial analysis for 12 GMT on the 9th, along with the resulting 12-h and 24-h forecasts are shown in Fig. 3.17. The model does proceed with cyclogenesis in approximately the correct locations as the forecast maps show. The major problem is with the intensity forecast. The central pressure forecast of 1000 mb for 12 GMT on the 10th is 55 mb higher than what is actually observed. The corresponding wind and wave forecasts for the affected area were thus egregiously erroneous. As an example, the forecasted maximum

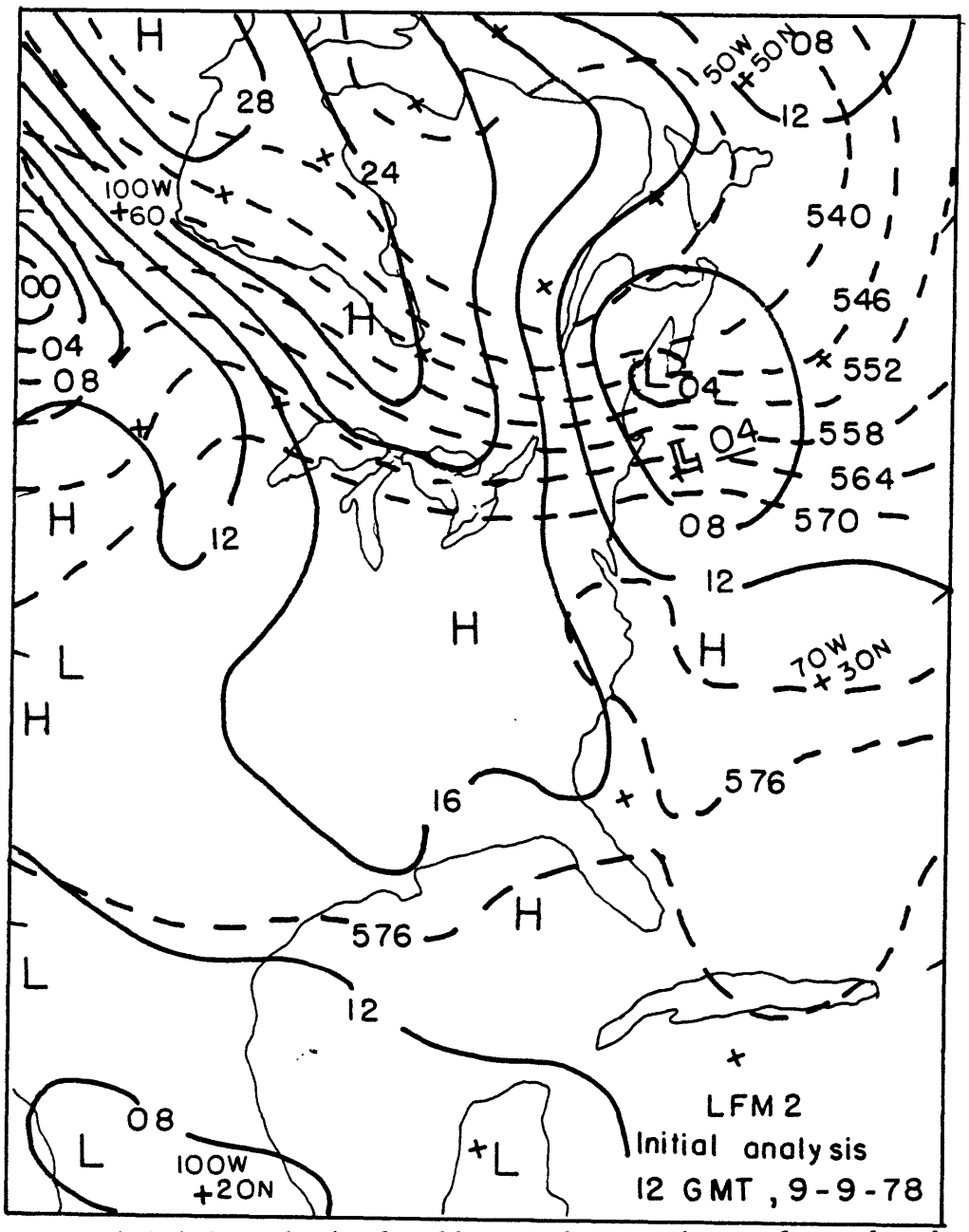


Fig. 3.17a. LFM-II initial analysis for 12 GMT, 9 September, of sea-level pressure, and 1000-250 mb thickness. Sea-level pressures (mb, hundreds and thousands digits omitted) are analyzed in solid lines, and thicknesses are in dashed lines. Observed position (indicated by an L) and central pressure of surface low are also shown.

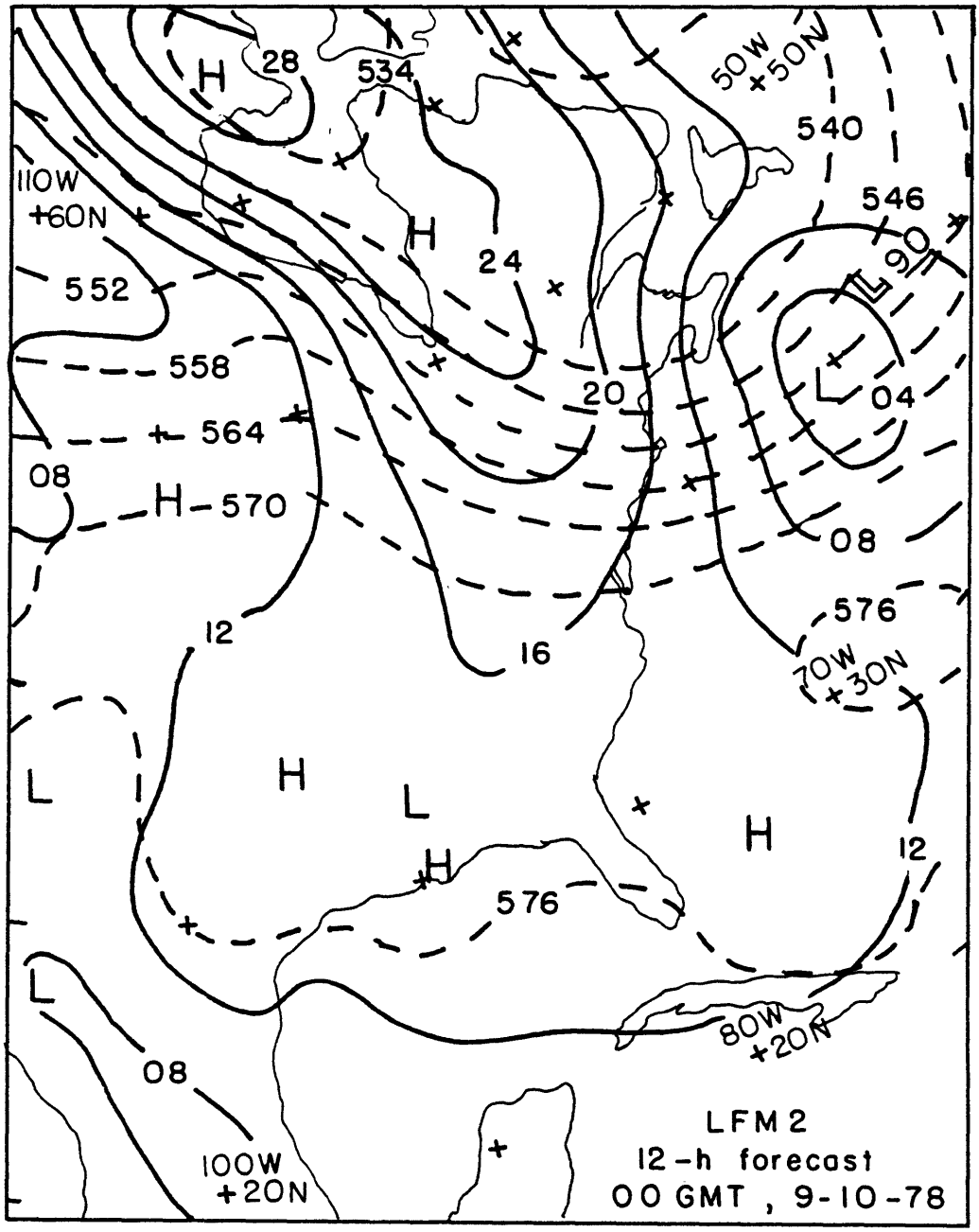


Fig. 3.17b. As for Fig. 3.17a, except for the ensuing 12-h forecast panel.

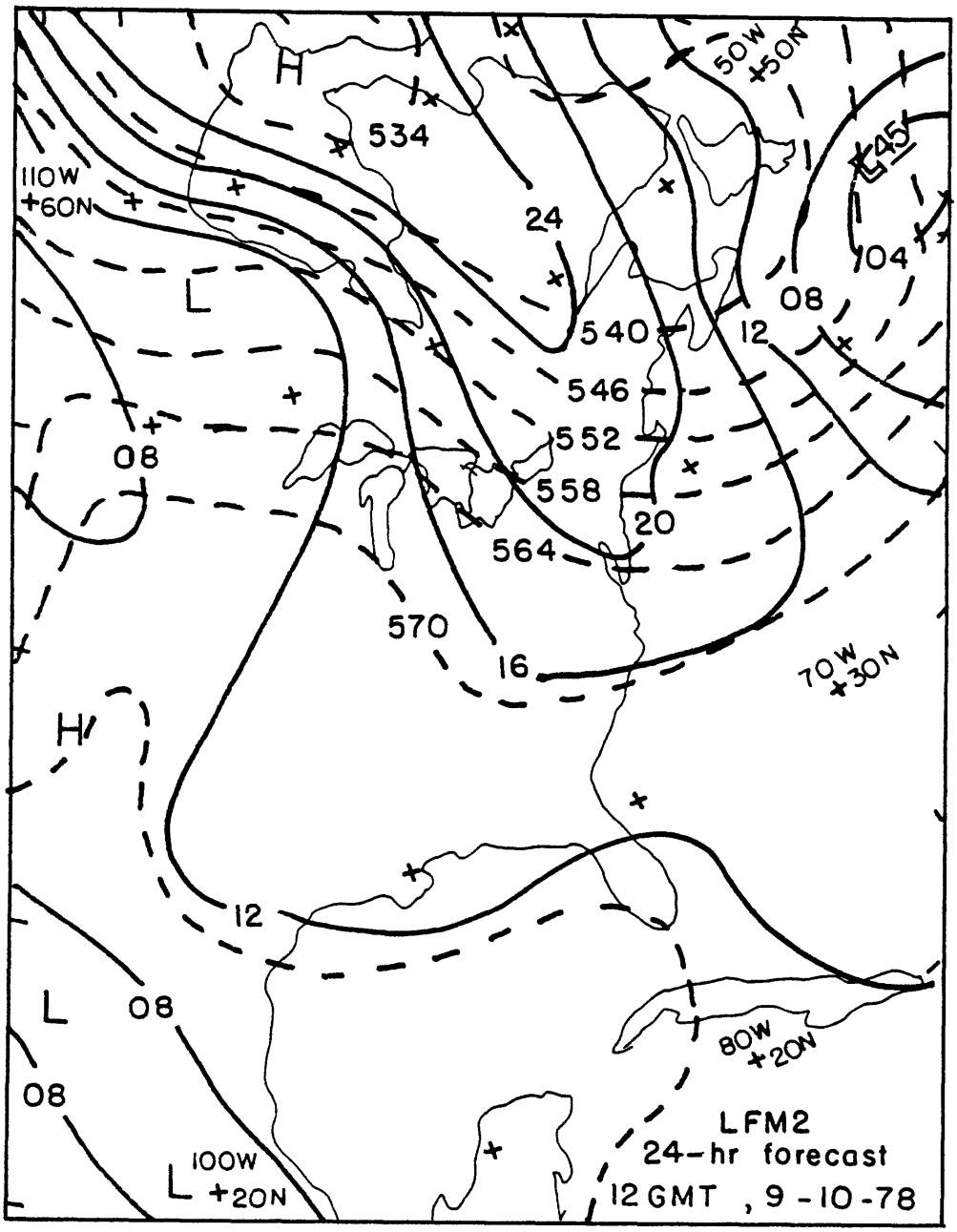


Fig. 3.17c. As for Fig. 3.17a, except for the ensuing 24-h forecast panel.

geostrophic wind just to the north of the center was ∿ 29 knots, while our Fig. 3.6 shows geostrophic wind speeds to the north and west of the center to be 110 knots! The problem was exacerbated by the fact that even the real-time analysis of the situation at 12 GMT on the 10th (see Fig. 3.13) grossly underestimated the severity of this storm. The LFM-II product is the result of a numerical integration of the primitive equations (see Shuman and Hovermale, 1968), and its horizontal grid mesh length is approximately 120 km. For such a large system with observed winds of at least 30 knots extending at least 1100 km from the storm center in all directions (see Fig. 3.14), the 120-km grid spacing does not appear to be the primary source of the problem.

The operational model product of the Fleet Numerical Weather Central (FNWC) is shown for the same three times in Fig. 3.18. The intensity forecast is similarly deficient to that of the LFM-II, with the 999-mb center being forecast for 12 GMT on the 10th. The slow displacement of the surface system is one additional problem the LFM-II did not have, and may be attributed to the FNWC model's coarse horizontal resolution of about 381 km. This primitive equation model is discussed in Kesel and Winninghoff (1972).

The problem of underforecasting maritime cyclogenesis is well-known, and has been discussed in Chapter 2. We found this deficiency to be relatively insensitive to an increase in the horizontal grid resolution and, consistent with the results of this section, we suggest the trend to faster computing machines and therefore to finer mesh models does not represent the sole solution to this problem.

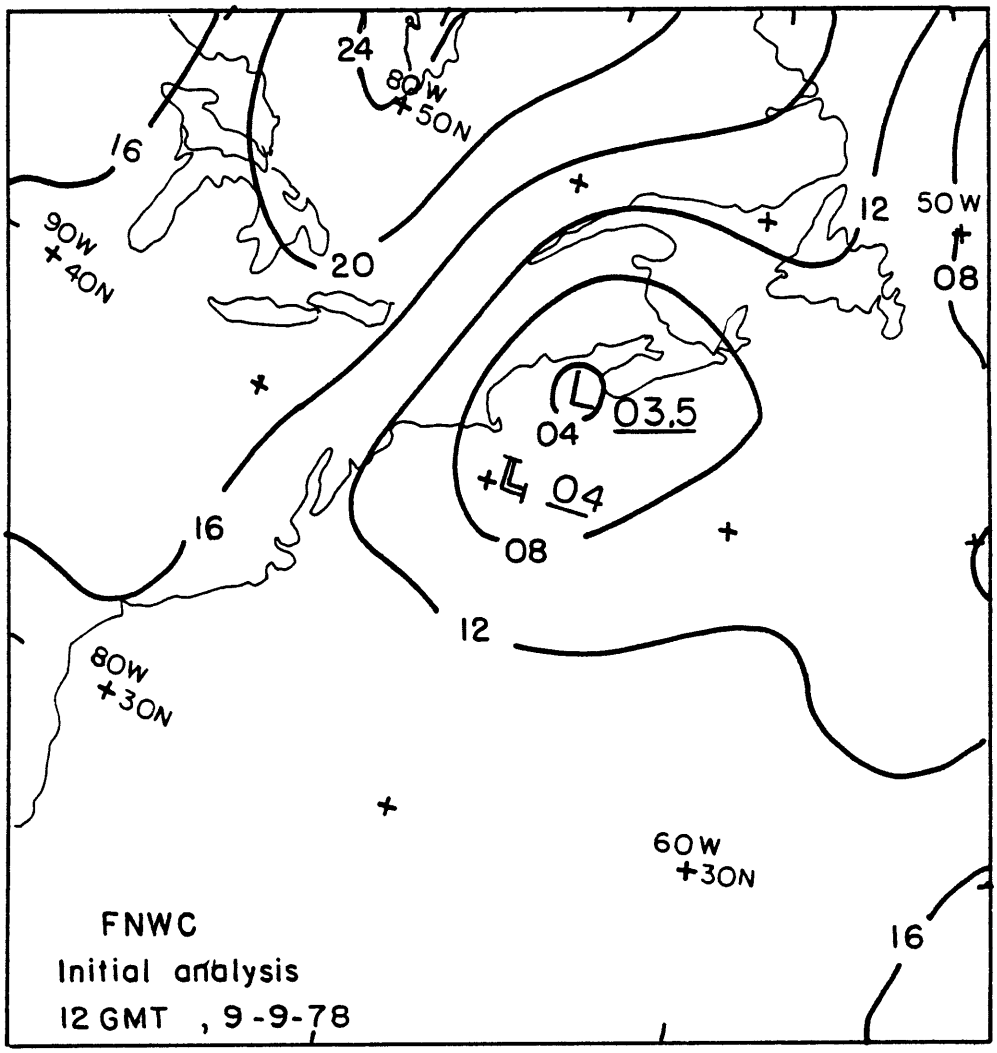


Fig. 3.18a. As for Fig. 3.17a, except for the FNWC-PE model output with thicknesses not included.

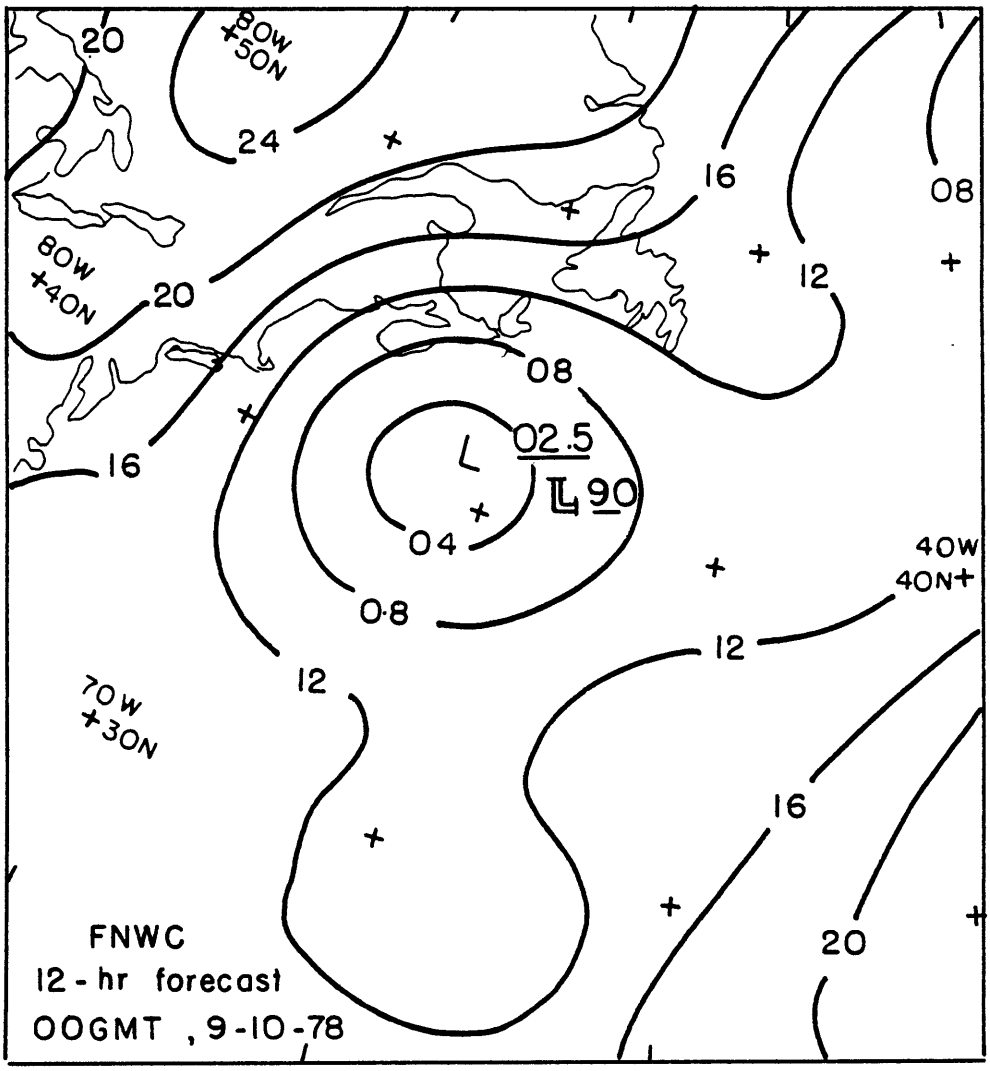


Fig. 3.18b. As for Fig. 3.17b, except for the FNWC-PE model output.

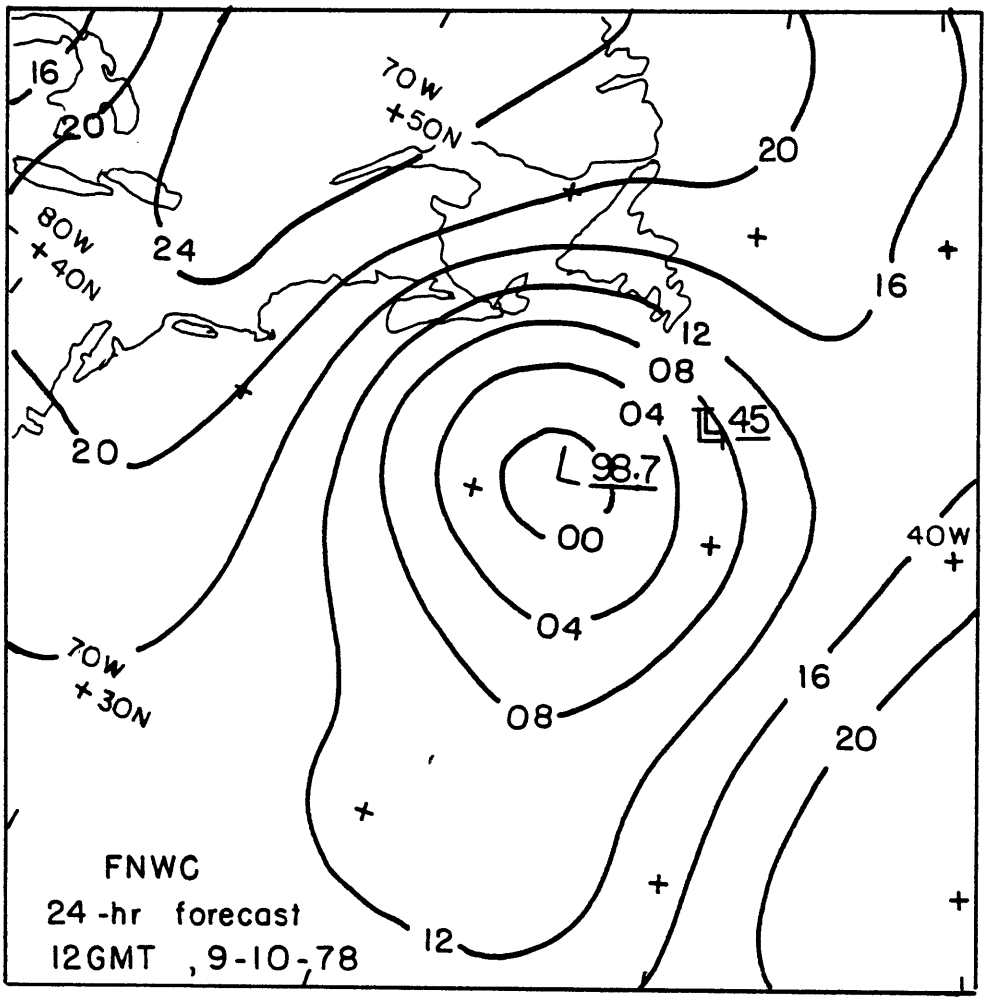


Fig. 3.18c. As for Fig. 3.17c, except for the FNWC-PE model output.

In order to explore possible reasons for the numerical model's poor performance, the next section will examine the role that adiabatic, inviscid quasi-geostrophic dynamics may have played in this storm's evolution. A careful compilation of all existing data for this case will be utilized in order to examine this role as accurately as possible. The relative role that diabatic processes may have played in this case will be explored in later sections. Indeed, the presence of deep convection in and around the developing storm center indicates that bulk heating effects of this convection may have played a role in the storm's intensification. These effects may be improperly simulated in the operational models, as has been suggested by Tracton (1973). The potentially high sensitivity of this cyclone to the cumulus parameterization is discussed in Section 3.8.

3.5 Vertical Motions and Quasi-geostrophic Diagnosis

Kinematically-computed vertical motion profiles for the Wallops-Fort Totten-Dulles triangle for 00 GMT on 9 September are shown in Fig. 3.19. These profiles were computed from wind data at approximately 30 mb intervals from 1000 to 100 mb. Omega is assumed zero at the lower boundary, with a constant correction applied to the divergence profile so that omega is zero at 100 mb. The low at this time is located approximately at the centroid of this triangle. The slight upward motion, peaking below 940 mb in the uncorrected profile, indicates the triangle-scale upward motion is quite shallow, as is the surface low. The area of deep cloudiness is only about

Fig. 3.19. Profiles of kinematically computed omega (units of 10^{-3} mb sec^{-1}) for the triangle defined by Wallops Island, Virginia (WAL), Fort Totten, New York (JFK), and Dulles International Airport (IAD).

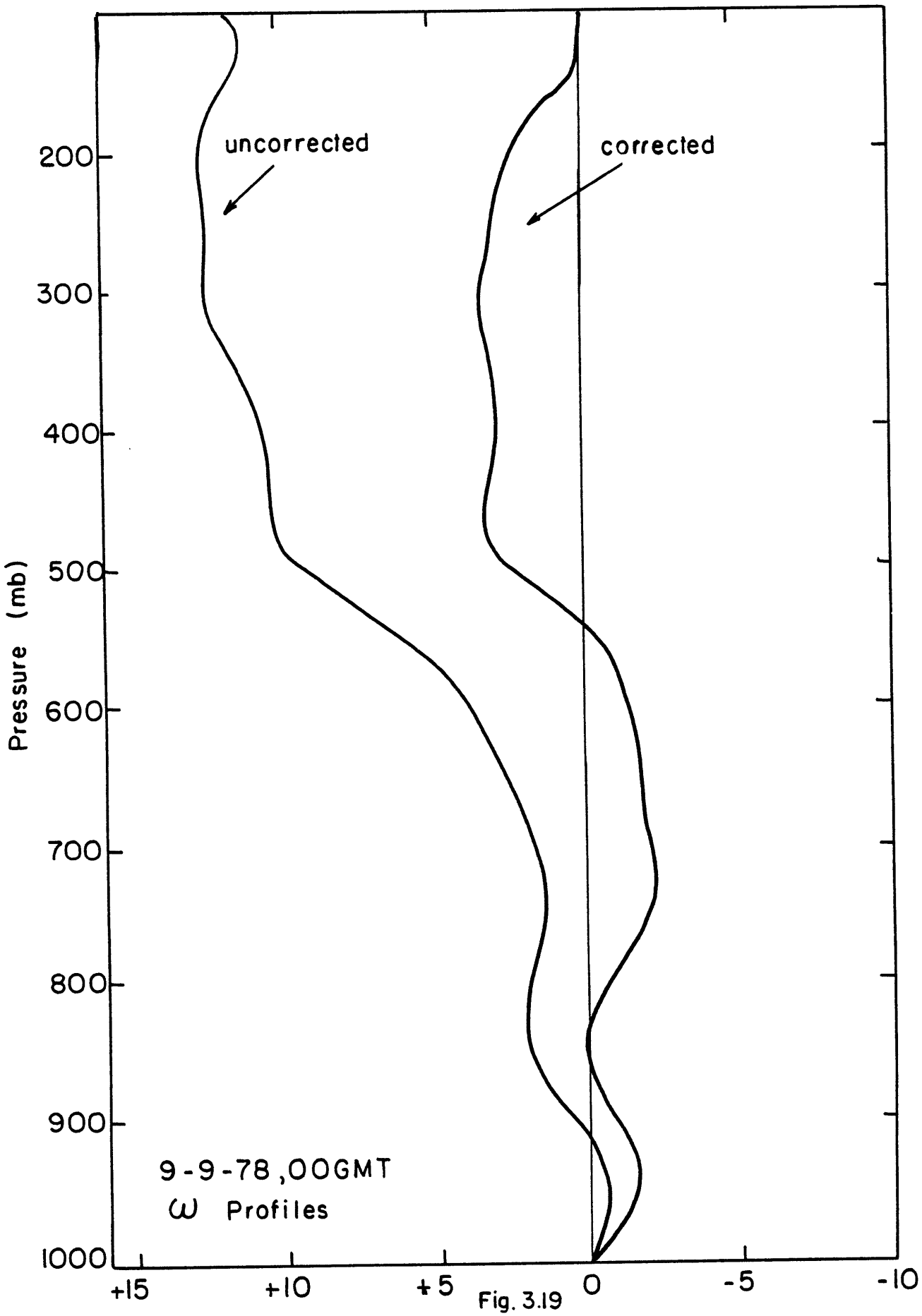

uncorrected
corrected
200
300
400
500
600
700
800
900
1000
Pressure (mb)
9-9-78, 00GMT
ω Profiles
+15
+10
+5
0
-5
-10

Fig. 3.19

12000 km^2 (see Fig. 3.3), which is less than a third of the triangle area. Strong triangle-scale subsidence is shown in the middle and upper troposphere.

Fig. 3.20 shows the horizontal distribution of surface and 250 mb divergence for 12 GMT on the 9th. These divergence computations were accomplished with the same grid used for the relative vorticity calculations discussed earlier. The 250 mb wind field is also shown in Fig. 3.20. The surface and 250 mb analyses were independently derived, and are consistent in that strong surface convergence is shown just to the east of the developing cyclone and to its south in the region of the MCC, while strong divergence at 250 mb is indicated for these same areas. Idealized ω-profiles were constructed for each grid-point by assuming a linear divergence profile from 1000 to 100 mb, with observed values at the surface and 250 mb specifying this line. The resulting kinematically-computed profile for grid-point 40°N, 68°W is shown in Fig. 3.21. The corrected profile was found in the manner discussed above. The agreement in sign of the corrected and uncorrected ω's is encouraging. However, our correction procedure here also specifies the level of maximum vertical motion to be 550 mb -- likely to be unrealistic for this time when the disturbance is still confined to the lower troposphere. In spite of this caveat, the horizontal distribution of ω at 550 mb shown in Fig. 3.21 agrees qualitatively with the known locations of the low and of the MCC.

By 12 GMT on the 10th, with the low at or near peak intensity, the strong outflow at 250 mb over the surface cyclone, and northeastward

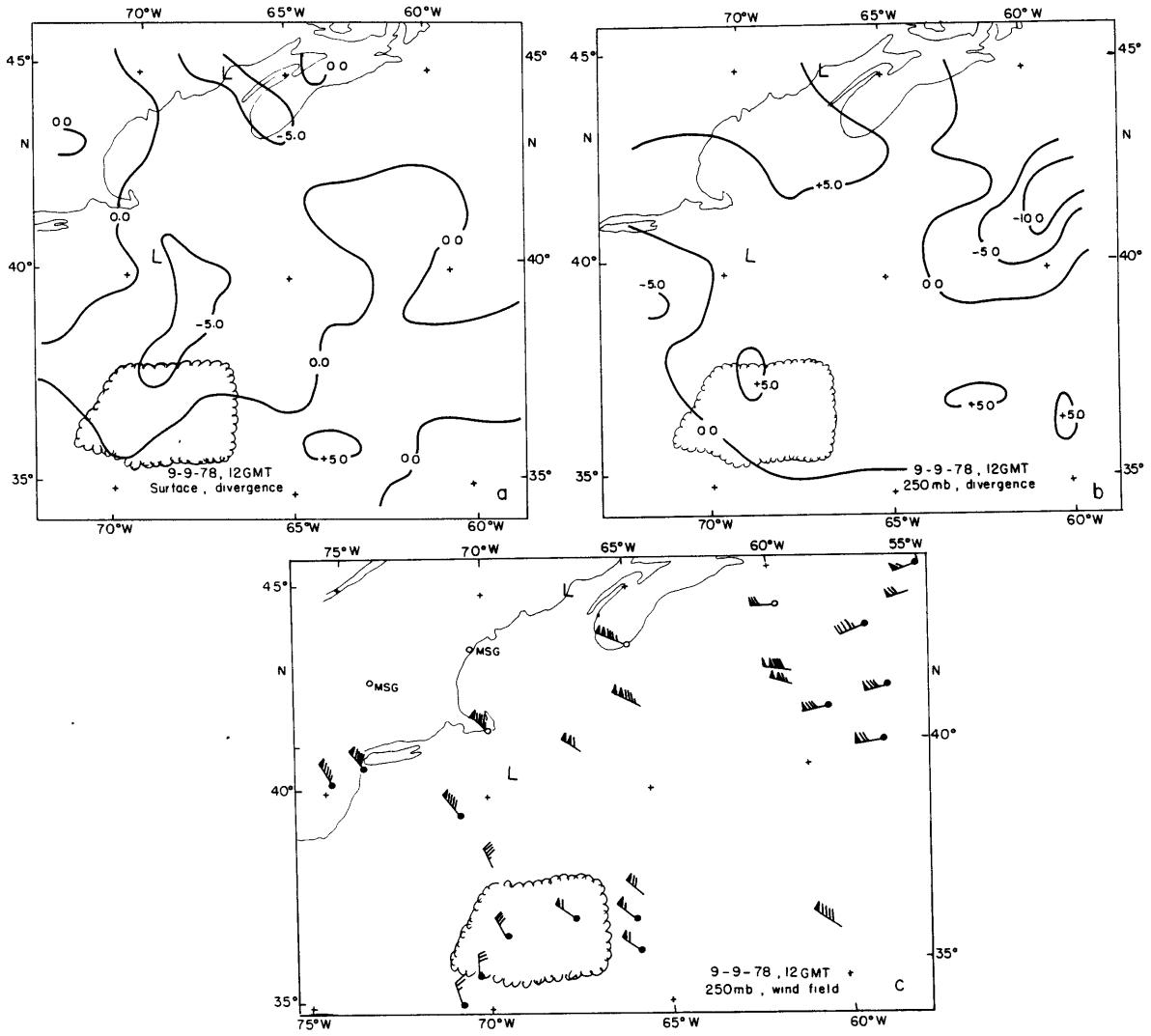


Fig. 3.20. (a) Divergence (units are in 10^{-5} sec^{-1}) $\frac{\Delta u}{\Delta x} + \frac{\Delta v}{\Delta y} - \frac{v \tan \phi}{a}$ for 9 September, 12 GMT for the surface. L's indicate surface cyclone positions, and the curled line outlines the area enclosed by the MCC.

(b) As for (a), except for the 250-mb level.

(c) As for (a), except for the 250-mb wind field on which the divergence calculations are based. Closed circles indicate satellite-derived winds.

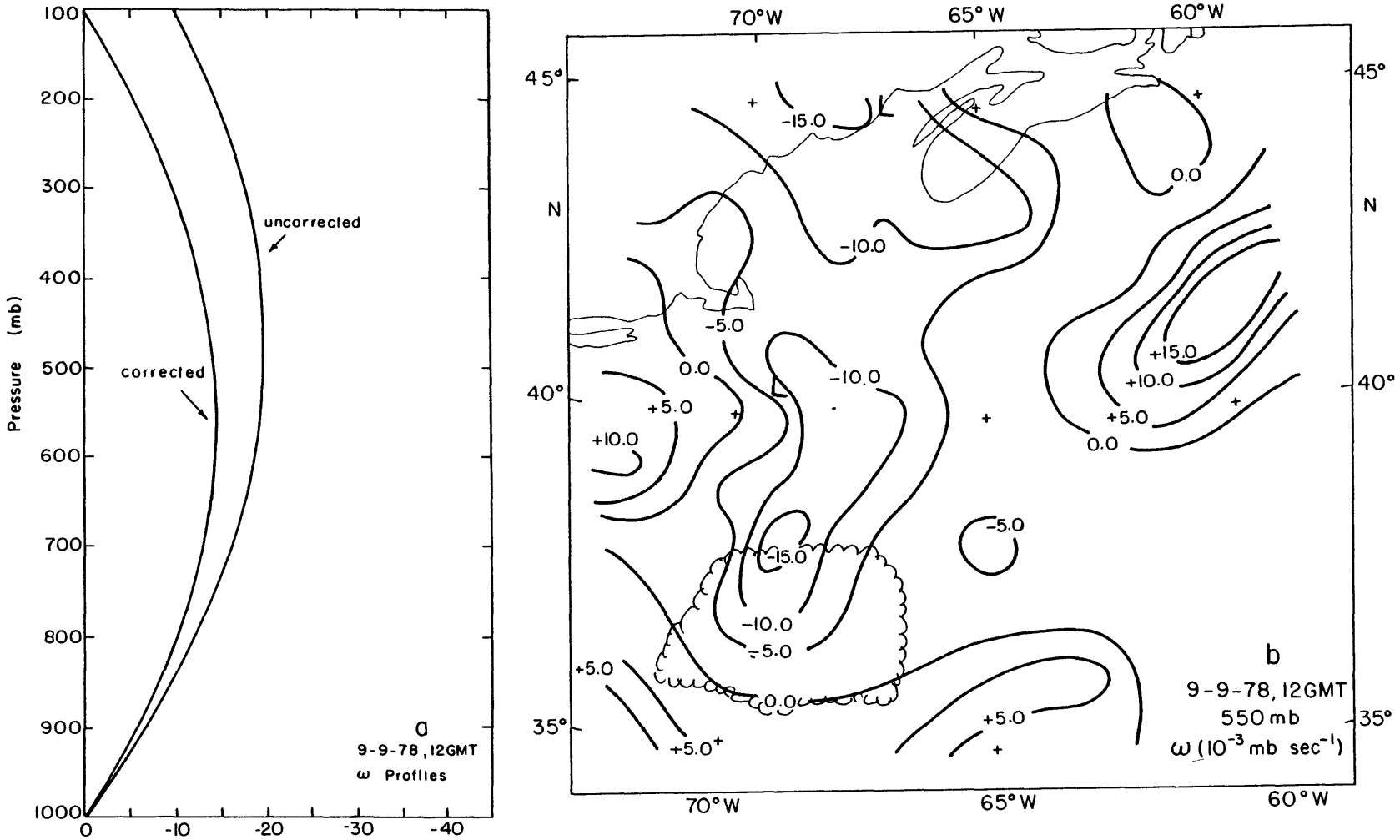


Fig. 3.21. (a) Vertical motion profile close to the storm center (40 °N, 68°W) for 12 GMT, 9 September. Units are in 10^{-3} mb sec^{-1}.
(b) As for (a), except for 550-mb level corrected ω's. L's indicate the surface cyclone positions.

to the deep cumulonimbus cells is shown in the 250 mb wind observations and in the resulting divergence field (see Fig. 3.22). The surface divergence pattern, also shown in Fig. 3.22, is generally consistent with the 250 mb divergences, although the slight positive divergence to the northeast of the storm center, under the deep convection and strong 250 mb outlfow, is suspect due to virtually no surface wind information in this area (see Fig. 3.14). Fig. 3.23 shows the vertical motion profile for grid-point 44°N, 51°W, and for 550 mb throughout the horizontal computational domain. The vertical motions in and around the surface low have more than tripled in 24 h, with corrected ω's on the order of -50×10^{-3} mb/sec at four grid points near the center. These vertical motions are quite close to the -58×10^{-3} mb/sec mean value found in the eyewall region of tropical cyclones (see Gray and Shea, 1973). However, these extreme tropical cyclone values apparently do not extend as far from the center, as Frank's (1977a) composite typhoon shows a rapid decrease in the ascent to -5.8×10^{-3} mb/sec one degree from the eye.

To gain a quantitative understanding of the quasi-geostrophic forcing taking place during cyclone development, the thickness field at 00 GMT on the 10th has been used to diagnose the instantaneous central pressure tendency. This tendency is computed from the geopotential fall found in the quasi-geostrophic model discussed in Chapter 2. Table 3.1 shows the values of the various parameters used in the computation. The static stability of .063 represents the mean thermal stratification (referred to the moist adiabat) found in the 68 weather ship radiosonde observations described in Chapter 2.

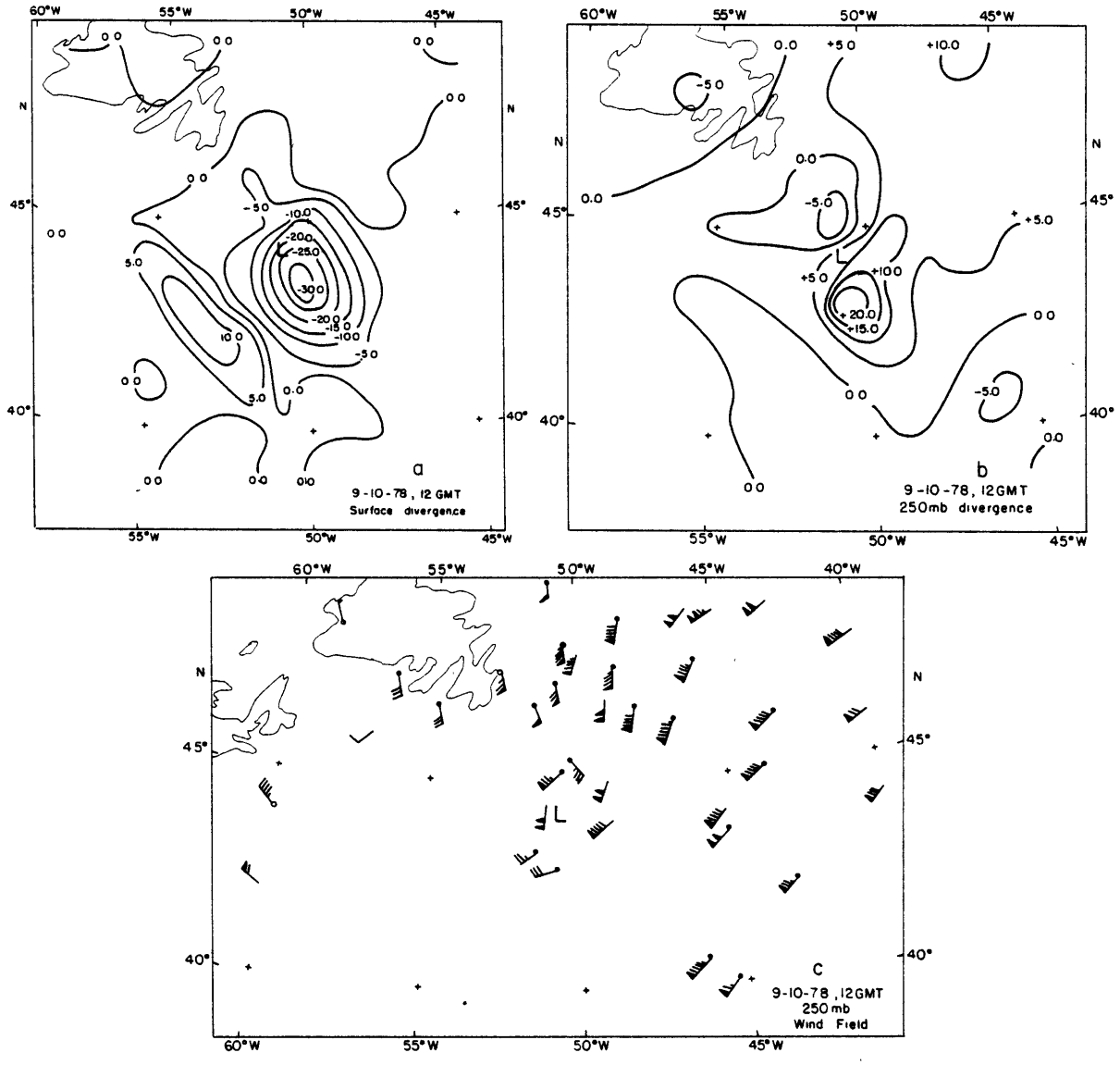


Fig. 3.22. (a) As for Fig. 3.20a, except for 10 September, 12 GMT.
(b) As for Fig. 3.20b, except for 10 September, 12 GMT.
(c) As for Fig. 3.20c, except for 10 September, 12 GMT.

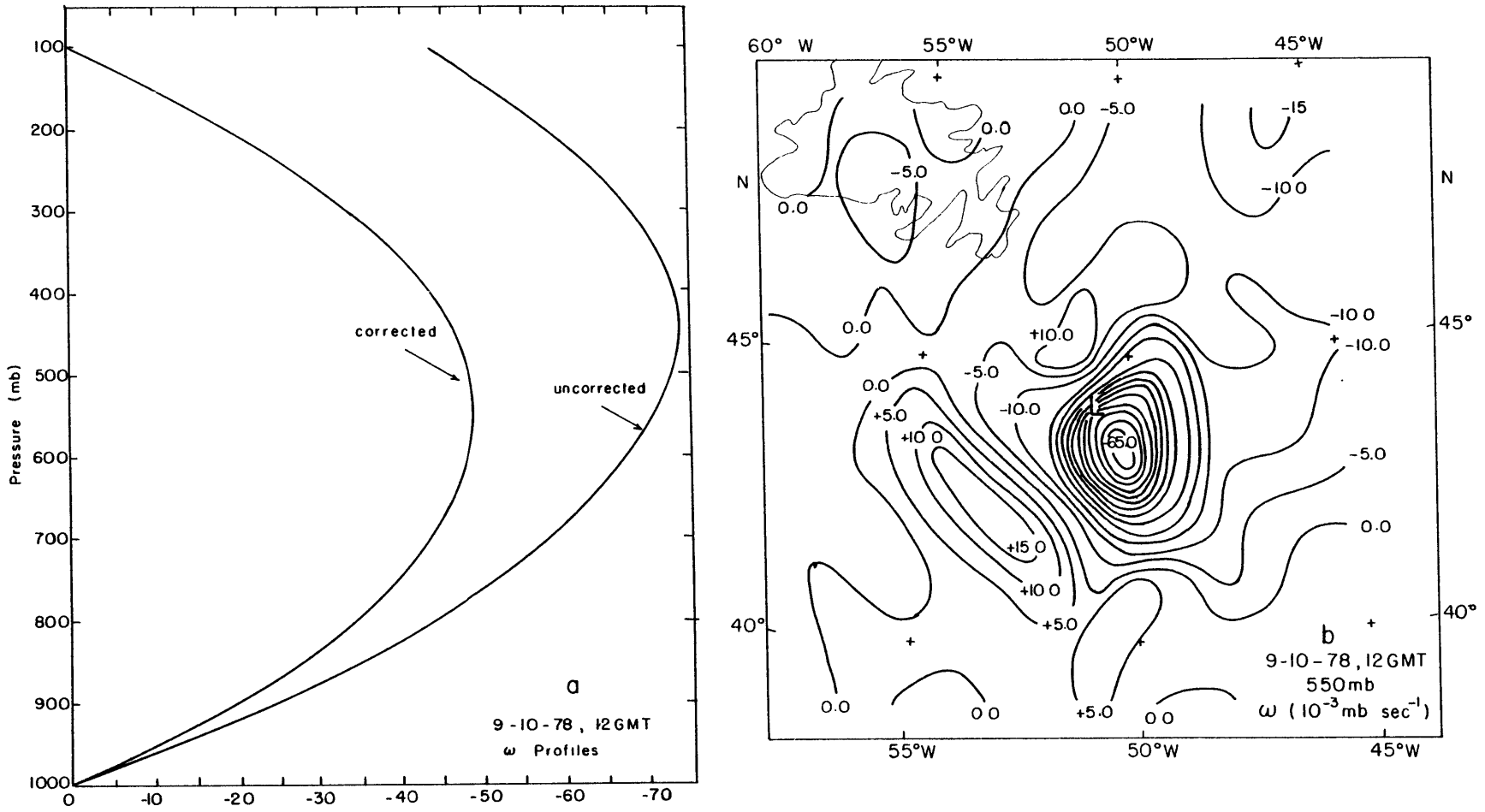


Fig. 3.23. (a) As for Fig. 3.21a, except for 12 GMT, 10 September. The vertical motion profile is for grid point 44°N, 51°W.
(b) As for Fig. 3.21b, except for 12 GMT, 10 September.

TABLE 3.1

9/10/78; 00 GMT

Quasi-geostrophic parameters
(see Sanders and Gyakum (1980) for further details)

$L = 1800$ km
$a = 1.16 \times 10^{-5}$ °K/m
$\hat{T} = 1.0$°K
$f_o = 0.99 \times 10^{-4}$ sec^{-1}
$\eta_o = 1.8 \times 10^{-4}$ sec^{-1}
$T_o = 250$°K
$\gamma = .063$
$\lambda/L = .19$
χ_{10} = -3.3 mb/12 h
(without λ correction) = -3.6 mb/12 h
observed instantaneous central pressure tendency at 00 GMT, 10 September = -29 mb/12 h

The computed instantaneous 12-h central pressure fall of 3.6 mb falls far short of that which is observed. From our knowledge of the storm's evolution, a conservative estimate of the instantaneous deepening rate at this time is 29 mb. The computations were made assuming λ to be L/4, the atmosphere to be saturated (thus minimizing the effective static stability), and the frictional filling effect has been ignored. Thus, the maximum amount of intensification has been extracted from this quasi-geostrophic model, for the above-mentioned physical effects would each tend to reduce our computed central pressure fall.

As an additional check on quasi-geostrophic forcing taking place within this system, we have utilized a more complicated version of the previous model. The goal is to allow for large vertical differences in the horizontal temperature contrast. Thus, we may focus upon the strong low-level vertical wind shear observed in this case. Indeed, we have seen this disturbance to be quite shallow through 12 GMT on the 9th, and a much stronger baroclinic zone exists in the lower troposphere than in upper levels (see Figs. 3.4 and 3.9). Note the development of the favorable configuration of surface isotherms in Fig. 3.1, which is a result of the cooling westward of the relatively warm Atlantic SST's. More generally, we have shown in the last chapter the low-level baroclinicity as being particularly strong in the vicinity of oceanic bomb frequency maxima. Staley and Gall (1977) have used a four-level quasi-geostrophic model to show the importance of both low static stability and strong wind shear in the lower layers in the enhancement of short baroclinic wave growth.

Our three-layer quasi-geostrophic model is more completely described in Appendix 3.A. We used the 1000-850 mb thickness field (derived in precisely the same manner as for the 1000-250 mb thickness fields and shown in Fig. 3.24a) to compute the low-level temperature structure. The winds used were 850 mb radiosonde winds and low-level cloud winds derived from the GOES-east imagery. Table 3.2 presents the results of our computations. The instantaneous deepening rate of 3.2 mb/12 h still falls far short of the observed estimate of 11 mb/12 h, but is a vast improvement over the zero deepening we would have computed had we used the total tropospheric thermal field for this time (see Fig. 3.8).

For these computations, γ is based on the observed stratification (discussed in the next section) with respect to the moist adiabat, λ is assumed to be L/4, and frictional filling has been ignored. Even a halving of the low-level static-stability (the one parameter about which we are most uncertain) will raise the central pressure fall to only 4.7 mb/12 h. As a more graphic illustration of the problem, the quasi-geostrophic vertical motion profiles over the center, on which these calculations are based, are shown in Fig. 3.24b. A comparison with Fig. 3.21 shows this quasi-geostrophic estimate to be only a third of what the probable maximum ascent actually was over the center.

As a further check on these computations, in a relatively data-rich area, we have also used the most optimal pattern of surface isotherms, found at 03 GMT on the 9th (Fig. 3.1d), to diagnose the instantaneous quasi-geostrophic surface cyclone intensification with our three-layer model.

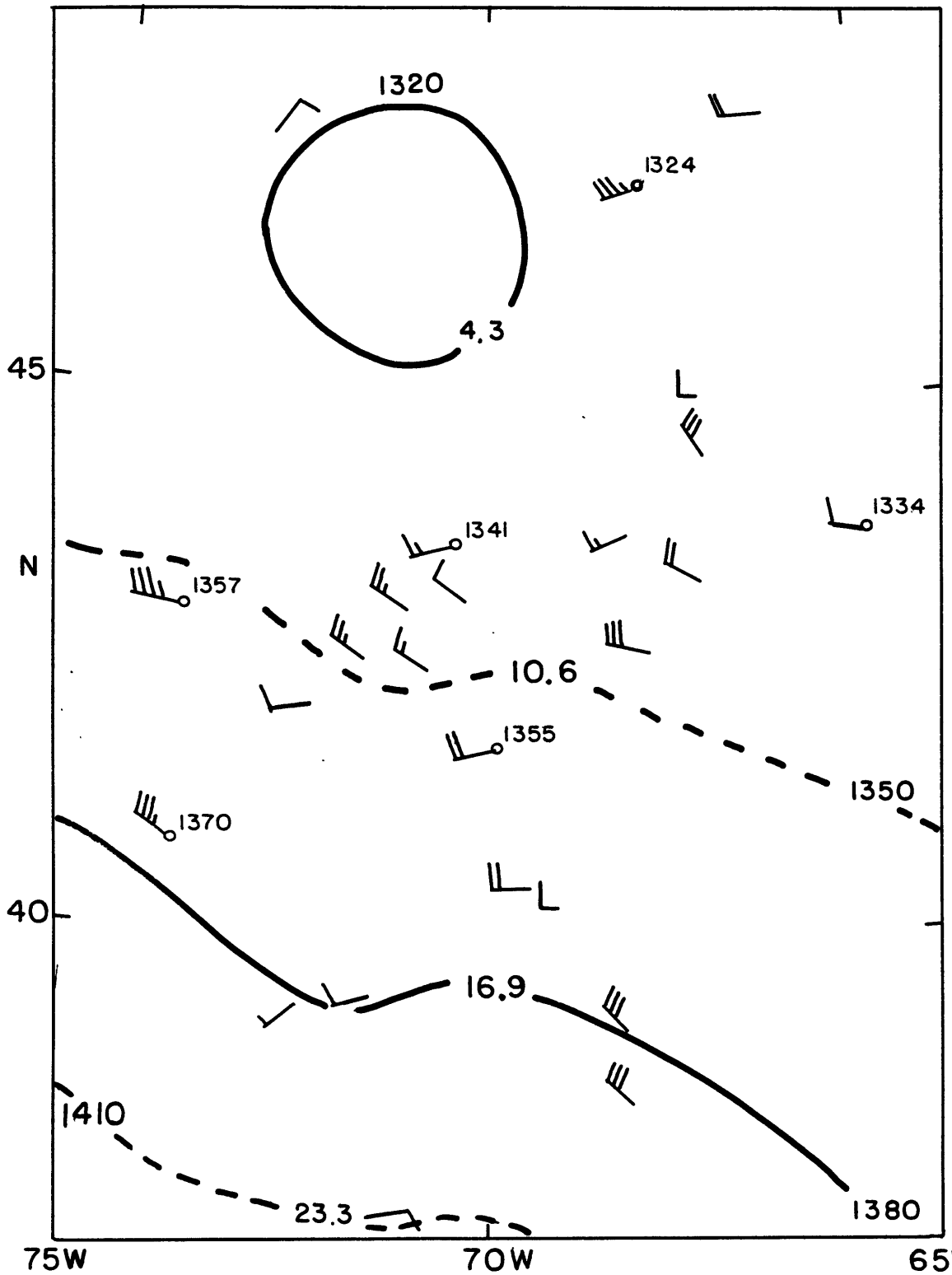


Fig. 3.24a. 1000-850 mb thickness analysis with isopleths also labeled with the corresponding mean virtual temperatures (°C). Radiosondes are indicated with open circles, and satellite wind observation points have no circles. Units are in m.

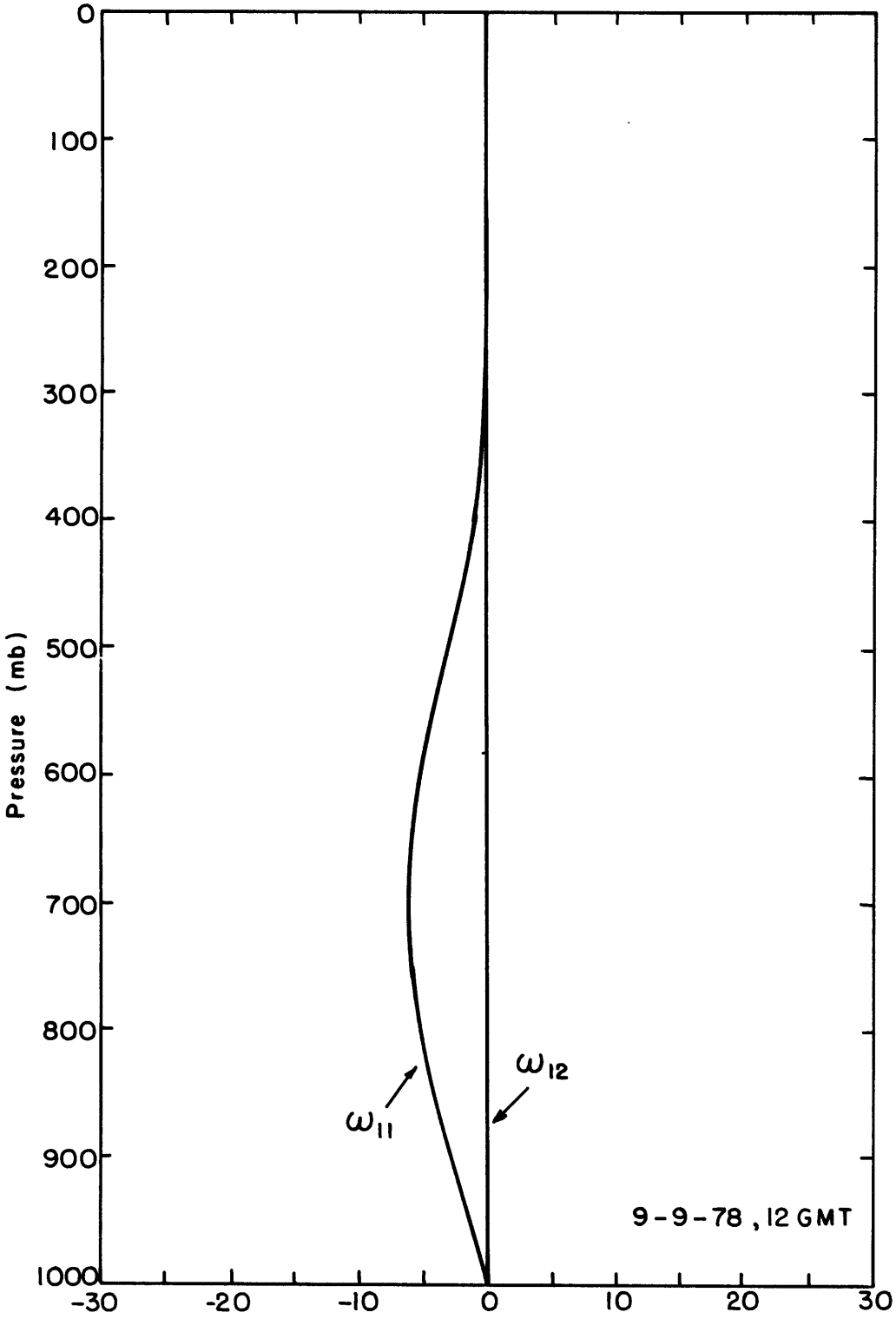


Fig. 3.24b. Quasi-geostrophic profiles of ω_{11} and ω_{12} at λ=L/4. ω_{11} is forced by positive thermal vorticity advection, while ω_{12} is forced by the advection of earth vorticity by the thermal wind. This latter component is negligibly positive, and therefore represents a slight brake on the cyclone's quasi-geostrophic intensification. Units are 10^{-3} mb/sec.

TABLE 3.2

9/09/78; 12 GMT

Quasi-geostrophic parameters
(see Appendix 3.A for further details)

P_2 = 800 mb

P_3 = 400 mb

L = 1100 km

a = 2.50×10^{-5} °K/m

$\hat{T}$ = 0.9°K

f_o = 0.94×10^{-4} sec^{-1}

η_o = 1.3×10^{-4} sec^{-1}

T_o = 250°K

γ = .058

λ/L = .30

χ_{10} = -3.2 mb/12 h (without λ correction)

observed instantaneous central pressure tendency at 12 GMT, 9 September = -11 mb/12 h

The results are summarized in Table 3.3. As a justification for our choices of P_2 and P_3, we find the favorable configuration of surface isotherms disappears rapidly with height, for the 850 mb temperature analysis at 00 GMT (Fig. 3.4a), though not supported by as many observations as at the surface, shows the maximum horizontal temperature contrast to have shifted to northeast of the surface center. The static stability value is an average of values found at JFK, WAL, and IAD radiosonde stations (Fig. 3.4c) in the 1000-700 mb layers. We find that our computed fall of 2.7 mb/12 h still falls far short of the observed rate, although the shortfall is not so great as we have found at the later times. We conclude from all of this that shallow baroclinic forcing initiated the cyclonic surface development at 00 GMT on the 9th, but its accelerated development by 03 GMT on the 9th, and indeed throughout its life cycle, cannot be accounted for by adiabatic (excluding the effect of latent heat release in saturated cyclone-scale ascent), inviscid quasi-geostrophic dynamics. Evidently, some other physical process(es) is(are) responsible for the observed rapid development. The presence of deep convection discussed earlier in this paper in the developing stages of the cyclone is a plausible culprit, through its dynamic and thermodynamic effects on the cyclone scale. These effects have not been incorporated into our models, and the rest of this chapter will be devoted to examining possible effects of the observed cumulus on the dynamic and thermodynamic structure of the cyclone itself.

TABLE 3.3

9/9/78; 03 GMT

Quasi-geostrophic parameters
(see Appendix 3.A for further details)

P_2 = 900 mb
P_3 = 700 mb
L = 700 km
a = 0.86 x 10^{-5} °K/m
$\hat{T}$ = 4.2°K
f_o = 0.94 x 10^{-4} sec^{-1}
η_o = 1.7 x 10^{-4} sec^{-1}
T_o = 285°K
γ = .067
λ/L = .25
χ_{10} = -2.7 mb/12 h
observed instantaneous central pressure tendency at 03 GMT, 9 September = -7 mb/12 h

3.6 Thermodynamic Structure

We have little information on the details of the temperature and moisture structure around this cyclone in its rapidly deepening phase over the open ocean. However, good ship and SEASAT coverage exists at the surface, along with a substantial number of commercial aircraft reports at the nominal 250 mb level. Thus, it was decided to construct vertical profiles of virtual temperature from this information on a one degree latitude by one degree longitude grid for 00 GMT and 12 GMT on 9 September, and for 12 GMT on the 10th. The information given for ecah grid point includes sea-level pressure, surface temperature, dew-point temperature, 1000-250 mb thickness, instrument elevation, 250 mb temperature, and the tropopause level.

The procedure for computing the virtual temperature structure is as follows. A given thickness in the layer from pressure P_1 up to P_2 specifies the mean virtual temperature in this layer

$$\overline{T}_v = \frac{\int_{P_2}^{P_1} T_v(P)\, d\ln P}{\int_{P_2}^{P_1} d\ln P} \tag{3.1}$$

Therefore, since it remains to solve for the numerator on the right side of equation (3.1), we use the observed virtual temperature at the bottom boundary, along with an assumed vertical variation of the virtual temperature. We will assume a virtual temperature structure of the form

$$T_v(P) = T_B\left(\frac{P}{P_B}\right)^{slope} \tag{3.2}$$

where T_B is the virtual temperature at pressure P_B, the reference level. Slope is defined as $\ln\left(\frac{T_v(P)}{T_B}\right)\Big/\ln\left(\frac{P}{P_B}\right)$. By substituting (3.2) into (3.1), we may solve iteratively for slope to any desired accuracy, for this study 1.5×10^{-4}. This procedure will provide a 1000-250 mb temperature structure that will hydrostatically yield a thickness to within .5 m of the order 10^4 m input 1000-250 mb thickness. Note that slope = .288 and 0. represent dry adiabatic and isothermal lapse rates, respectively.

At this stage, we are left with a temperature structure which contains the correct surface virtual temperature, and the correct tropospheric thickness. However, we have not yet used the 250 mb temperature information, and, in general, the above-derived temperature structure will not agree with this given 250-mb temperature information. In fact, the model temperature structure generally yielded 250-mb temperatures too cold in the northern sections of the domain, where the tropopause was lower than 250 mb. Thus, throughout the domain, an analysis was performed of both the tropopause level and 250-mb temperature field. These analyses are shown in Fig. 3.25. Commercial aircraft reports, upon which much of these analyses are based, are generally those at flight levels not precisely at 250 mb. These temperatures were

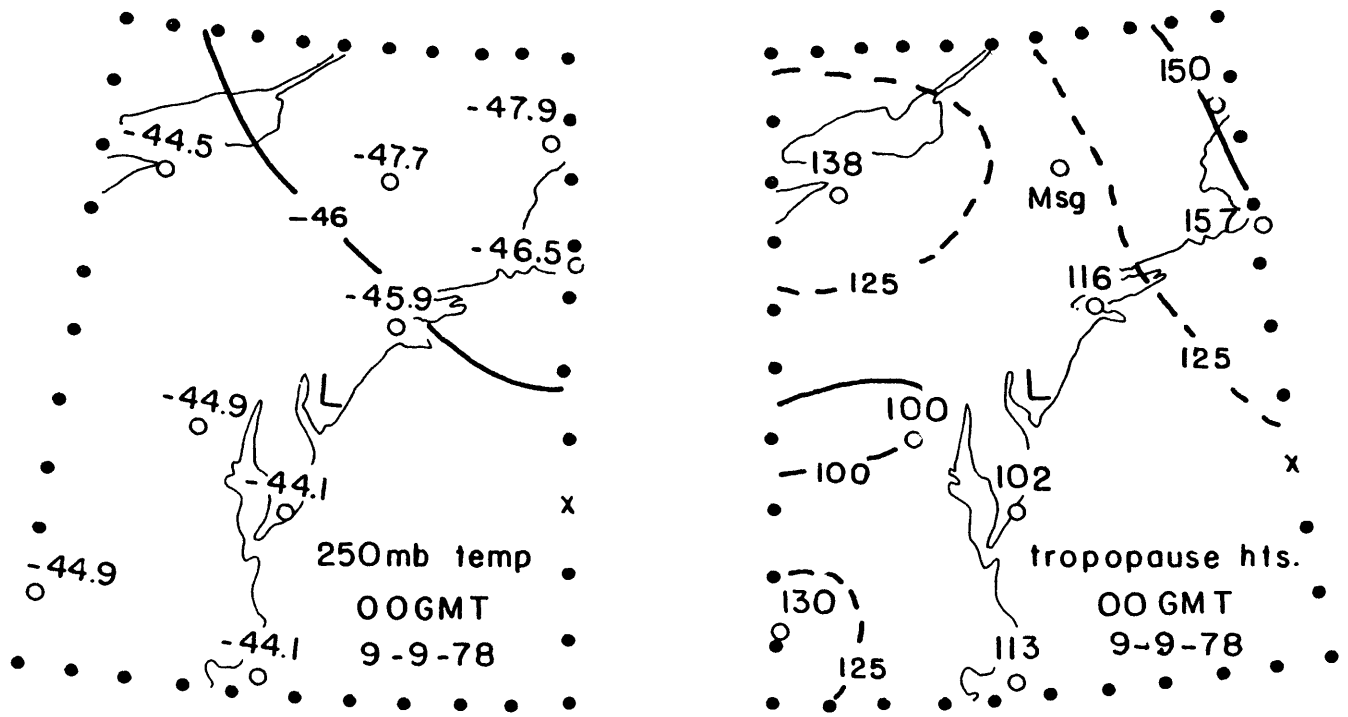


Fig. 3.25a. Tropopause and 250-mb temperature analyses for 00 GMT, 9 September. Circles indicate radiosonde data points, and x's indicate locations of commercial aircraft observations. "L" indicates the position of the surface cyclone center. Dots show the boundary of the computational domain. Tropopause heights are expressed in mb.

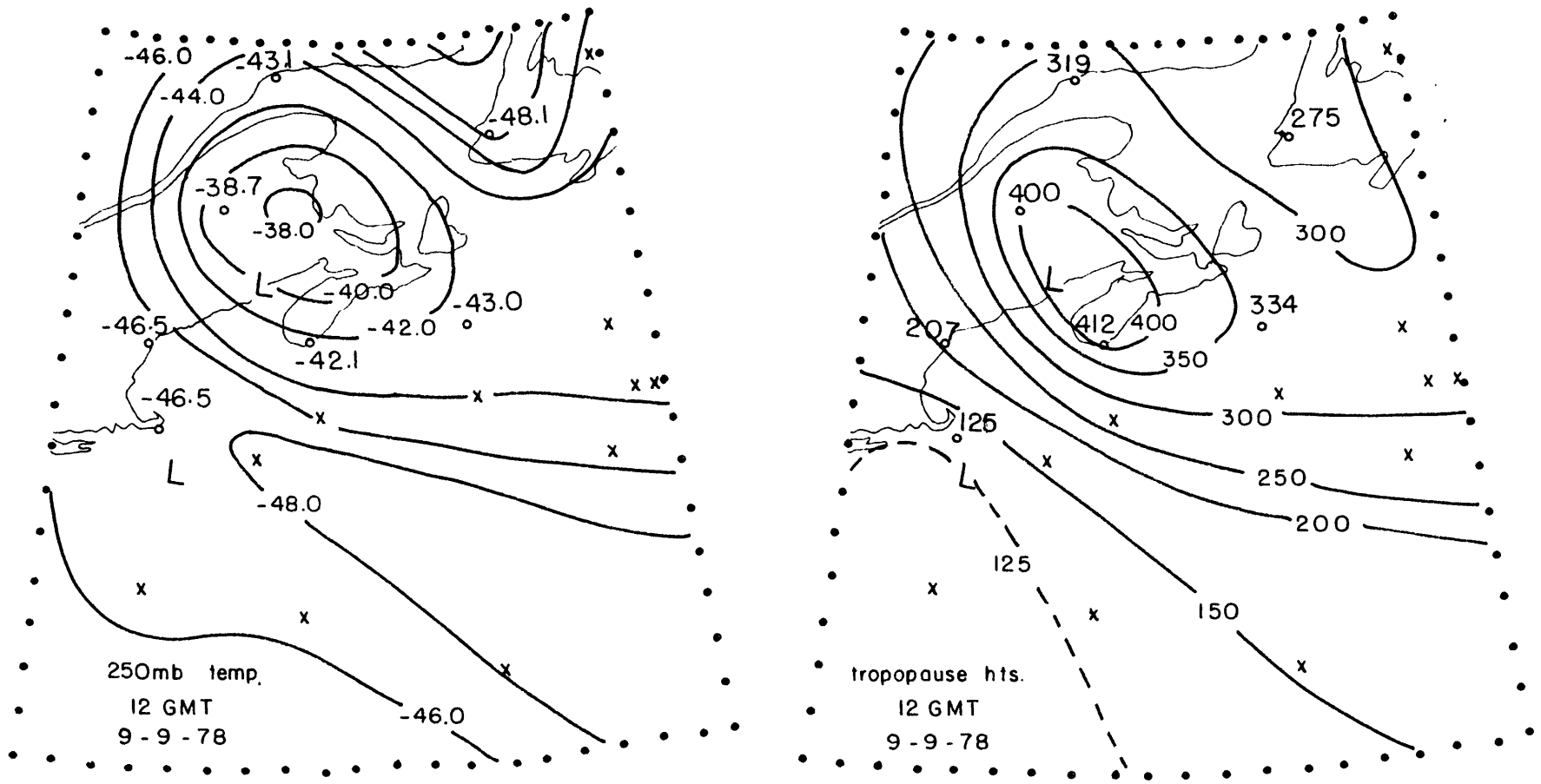


Fig. 3.25b. As for Fig. 3.25a, except for 12 GMT, 9 September.

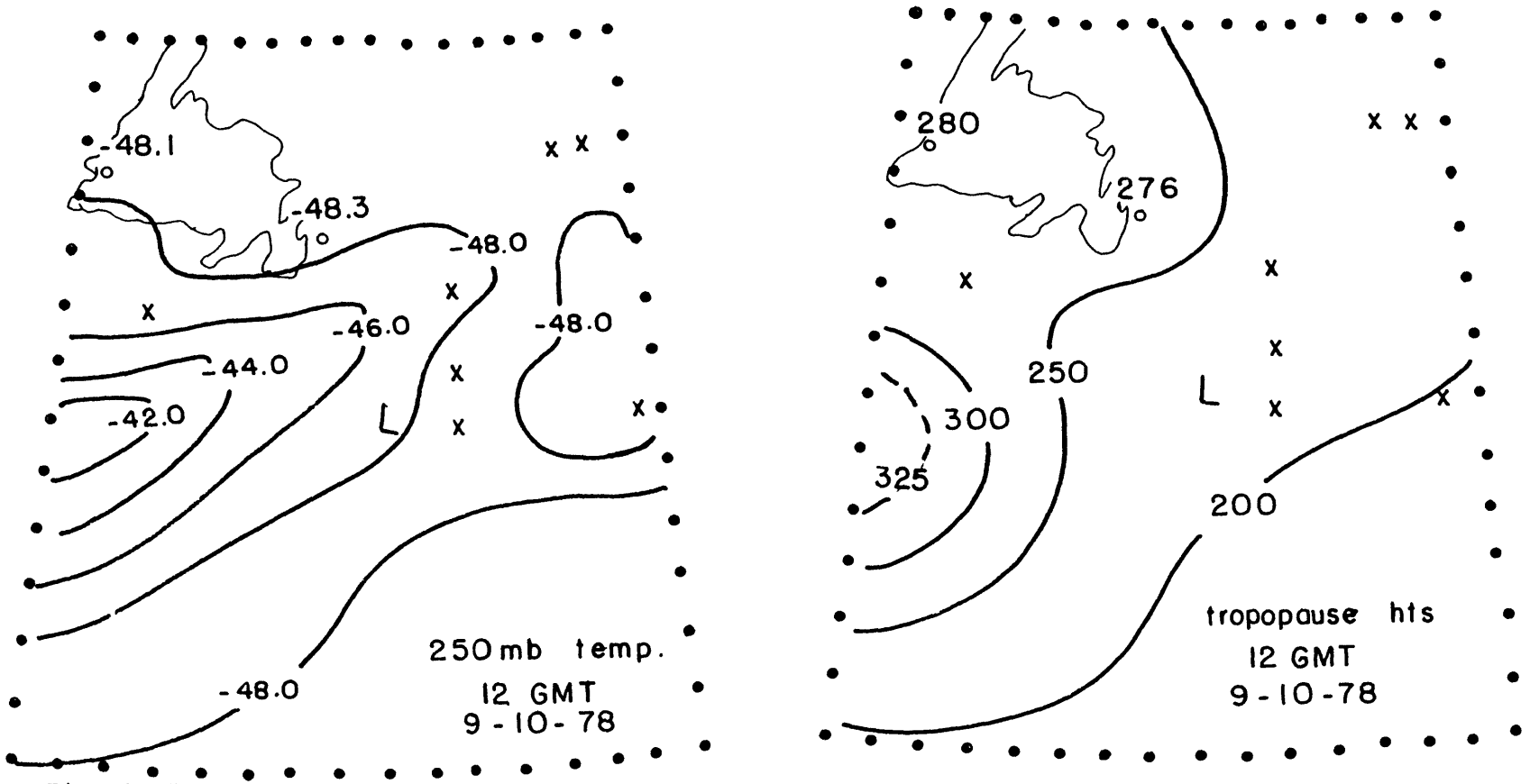


Fig. 3.25c. As for Fig. 3.25a, except for 12 GMT, 10 September.

converted to 250-mb values by assuming the lapse rates found above exist in regions where the tropopause is judged above 250 mb, and by assuming an isothermal lapse rate from the tropopause level up to 250 mb in other areas. Note the relatively high tropopause height directly over the surface center at all three times, and, in particular, the strong northward penetration of high tropopause air characteristic of the tropics at 12 GMT on the 10th.

Lapse rates were then adjusted at each grid point so that surface temperatures, 1000-250 mb thicknesses, and 250-mb temperatures were included as input to the algorithm. This specifies that two slopes are computed for each grid point, with the transition point between the two lines chosen as the tropopause level P_T, where $P_T > 250$ mb, and an arbitrary choice made for this transition level where $P_T \leq 250$ mb. Thus,

$$T_v(p) = T_B\left(\frac{p}{p_B}\right)^{\text{slope 1}} \quad \text{, where} \quad p_{tr} \leq p \leq p_B$$

$$T_v(p) = T_{tr}\left(\frac{p}{p_{tr}}\right)^{\text{slope 2}} \quad \text{, where} \quad 250\,\text{mb} \leq p \leq p_{tr}$$

and where the subscript tr represents the transition level. Slope is constrained to be $\leq .288$ (lapse rate is not to exceed dry adiabatic). Computations were performed for many transition points for the latter condition, and the sensitivity of the results to the various choices will be discussed. Fig. 3.26 shows a comparison of model temperature profiles with observed virtual temperature profiles at nearby radiosonde stations.

Fig. 3.26. (a) Virtual temperature structure for station 72712 (Caribou, Maine) for 12 GMT, 9 September, is indicated by the solid line. Dashed line is the model virtual temperature profile for the same time at the nearest grid point (47°N, 68°W).

(b) As for (a), except for station 72606 (Portland, Maine), and the grid point 44°N, 70°W. Short dashed line indicates model temperatures with transition level of 550 mb, and long dashed line shows the model profile with 400 mb transition point.

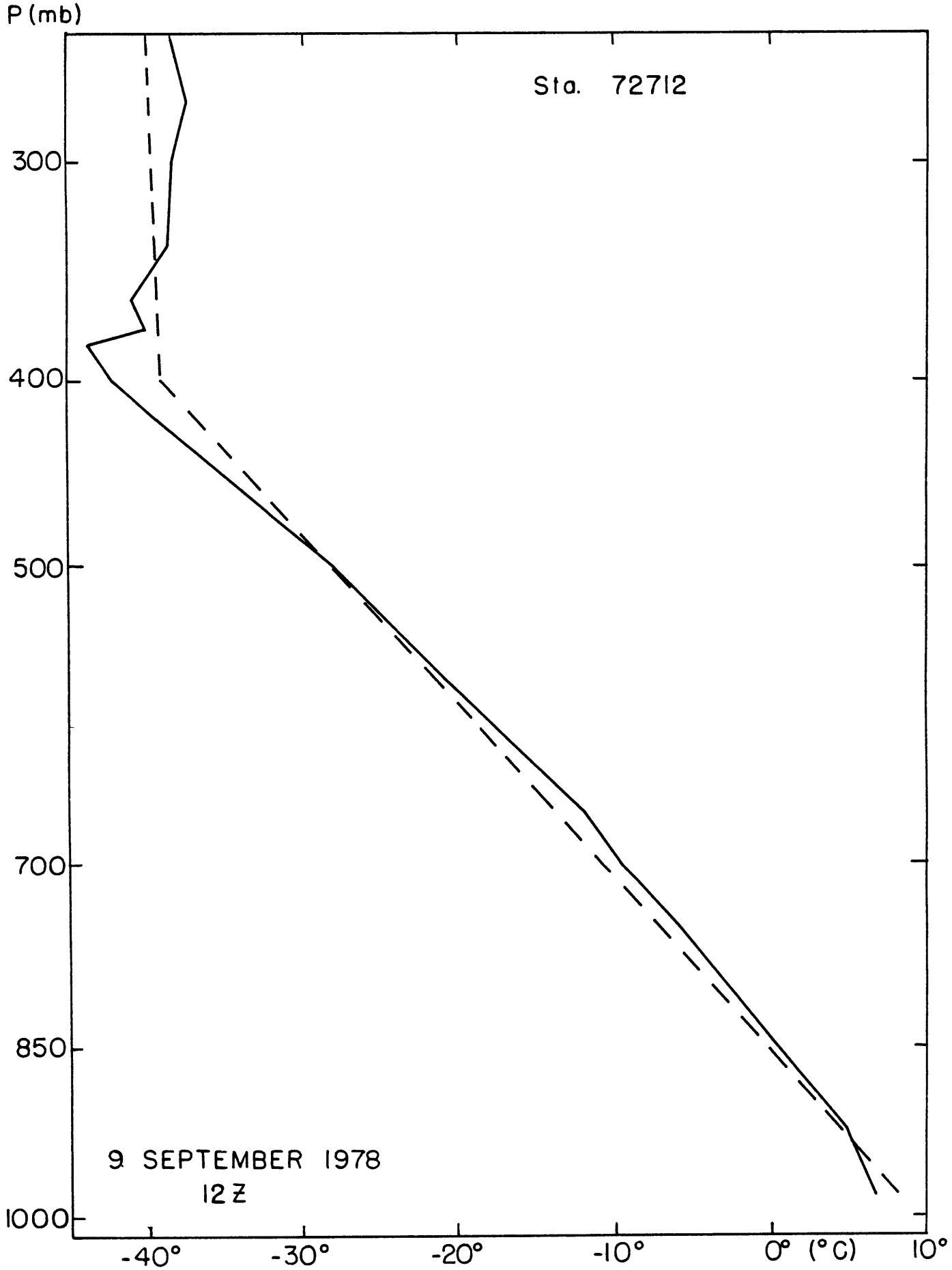

P (mb)
Sta. 72712
300
400
500
700
850
1000
9 SEPTEMBER 1978
12 Z
-40°
-30°
-20°
-10°
0° (°C)
10°

Fig. 3.26a

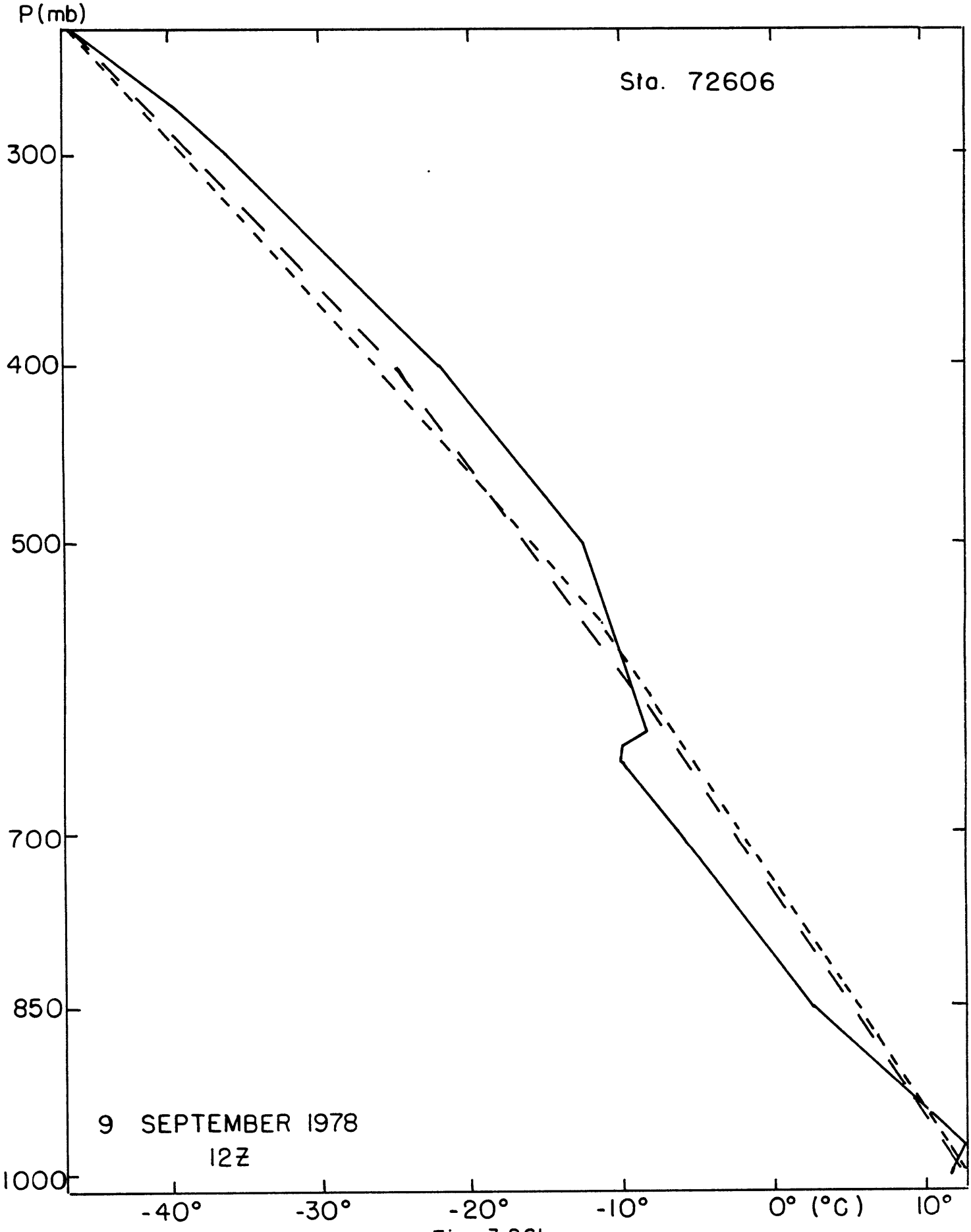

P(mb)
Sta. 72606
300
400
500
700
850
1000
9 SEPTEMBER 1978
12Z
-40°
-30°
-20°
-10°
0° (°C)
10°

Fig. 3.26b

Of course, the mean virtual temperature of each surface to 250 mb profile for a particular chart is specified the same, except for the small difference in thickness brought about by the displacement of the grid point from the radiosonde station. In the case of Caribou, Maine, where the tropopause is just above 400 mb, we have temperature errors of only a fraction of a degree C up to tropopause level, and 2-3°C above the tropopause where the temperature profile contains many changes in slope at 10-15 mb intervals. The Portland, Maine sounding, with its tropopuase at 207 mb, allows us to experiment with different transition points in the model soundings. Note that in spite of a 150 mb difference in the transition point between the two model soundings, temperature differences among the two are order of a fraction of a degree, and never exceed 1°C. What makes both model soundings erroneous is the observed inversion above 640 mb associated with a mid-tropospheric front. In spite of temperature error magnitudes approaching 2°C through much of the sounding, the model lapse rates are within 20% of the observed values, except for the 30-mb layers near the surface and 650 mb. This latter example was the worst case of the many soundings falling within the computational domain. It merely shows the inherent limitations this temperature computing procedure has, simply because of the general lack of any temperature information at intermediate levels. However, this procedure will do a reasonable job of defining static stabilities for layers of depth 100 mb or more.

Examples of constructed soundings over the storm center for 12 GMT

on 9 and 10 September are shown in Fig. 3.27. The most uncertainty in the virtual temperature profile is in the lower troposphere, where differences among the concurrent constructed soundings approach 10°C. However, all six soundings indicate the atmosphere to be absolutely stable, with the more stable atmosphere indicated at 12 GMT on the 10th. At this time, the sounding with the 400 mb transition is in error, for the computed 250 mb temperature is 5.5°C higher than that specified as a result of the algorithm not computing lapse rates greater than dry adiabatic. The 1000-250 mb thickness error in this sounding is thus 40 m or 1°K. The dashed line represents the "correct" (but super-adiabatic) upper part of this sounding. However, the few intermediate-level aircraft temperature observations taken in the vicinity of the low center show the choice of the lower transition points to be the more correct ones, and corroborate these two model soundings. Though the lower troposphere is clearly quite stable, there is still uncertainty about the precise degree of stability and depth of this layer.

In spite of the absolute static stability over the surface center at 12 GMT on the 9th, potential instability at this time is widespread over the storm domain. The Chatham (90 km north-northwest of the center) sounding for this time is shown in Fig. 3.28. In spite of the stable temperature stratification of the 1000-800 mb layer, the concurrent θ_e profile shows a decrease of 12°C from 1000 to 800 mb, above which is seen a dramatic increase until θ_e approaches its 1000 mb value again at 700 mb. This 2 km layer of potentially unstable air is supported by the satellite images (Fig. 3.16) which indicate convective cloud tops

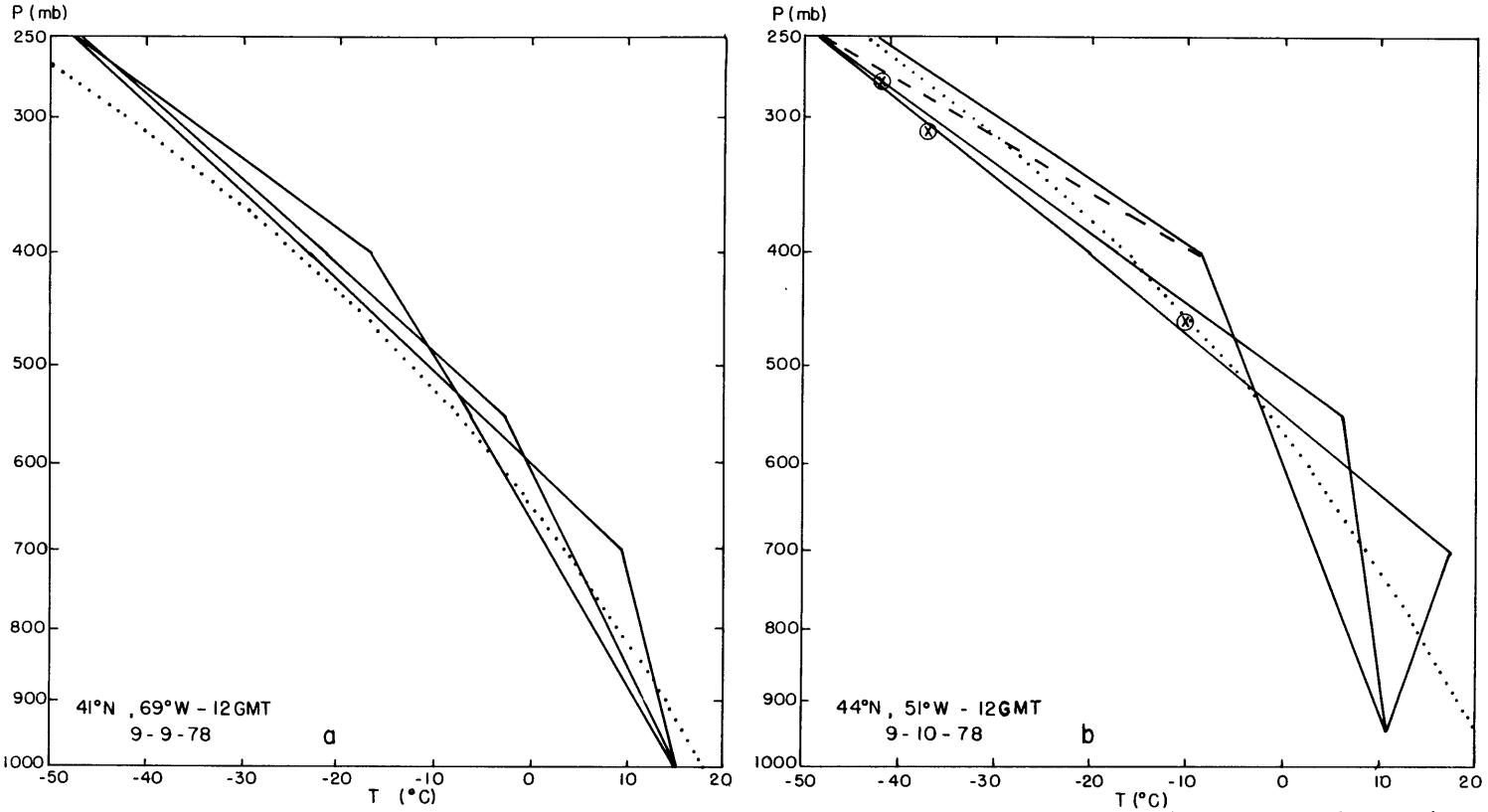


Fig. 3.27 (a) Soundings at grid point 41°N, 69°W for 12 GMT, 9 September for transition points at 700, 550, and 400 mb. Dotted line is representative moist adiabat.

(b) As for (a), except for grid point 44°N, 51°W at 12 GMT on 10 September. Aircraft temperature observations within 200 km of the cyclone center are shown by ⊗'s.

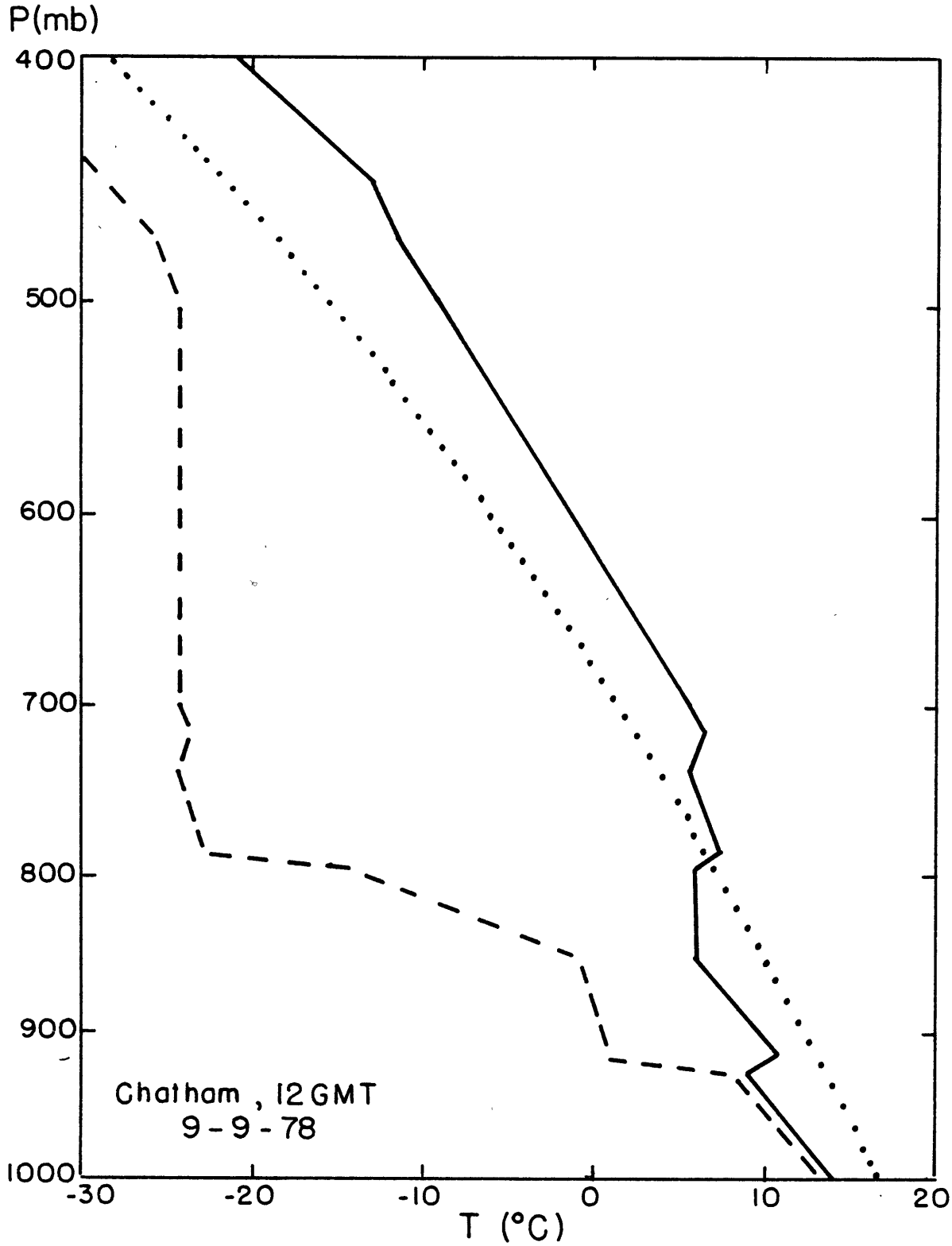


Fig. 3.28a. Chatham sounding for 12 GMT, 9 September 1978 of temperature (solid line), and dewpoint temperature (dashed line). The 321°K saturation equivalent potential temperature isotherm is the dotted line.

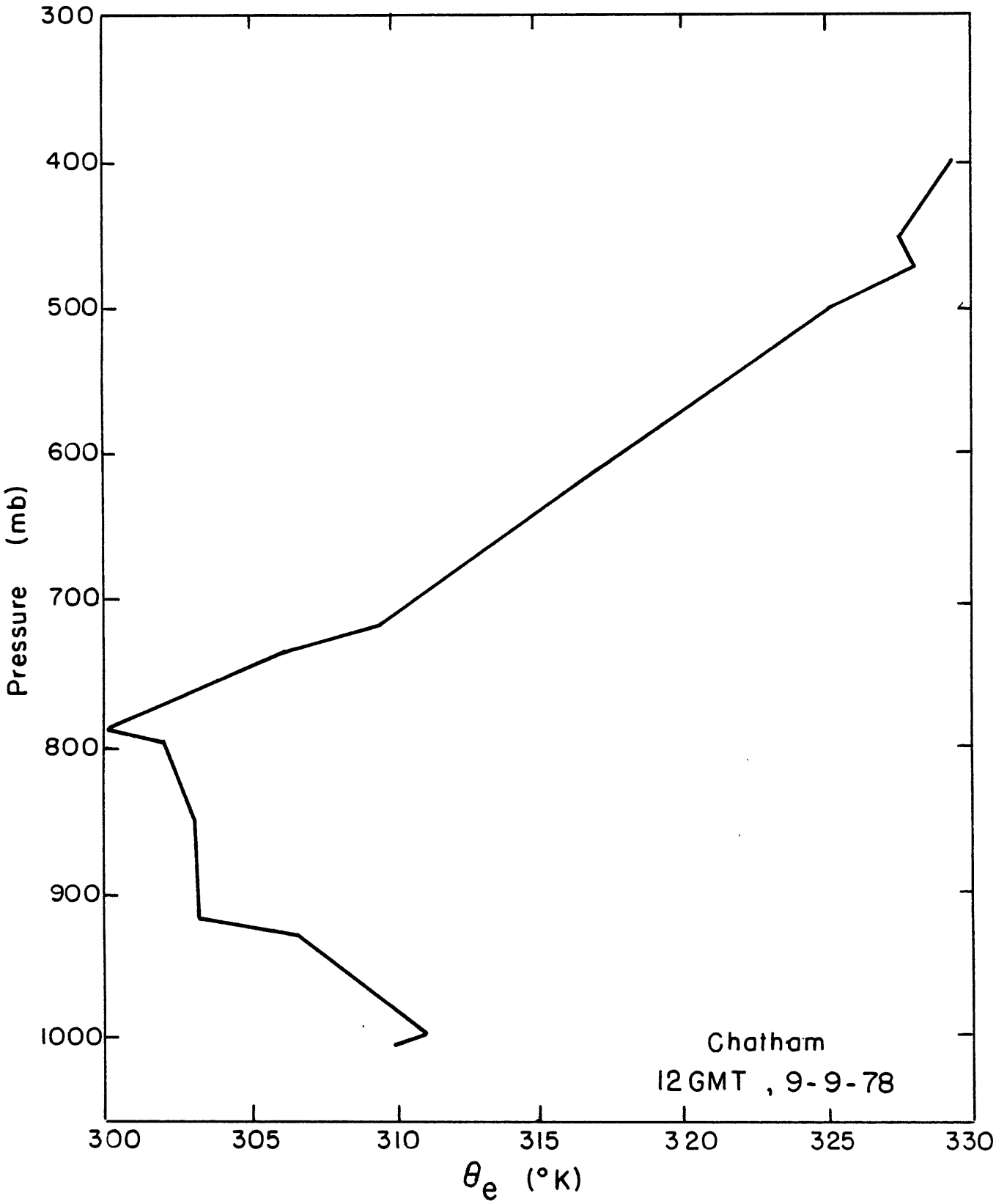


Fig. 3.28b. As for Fig. 3.28a, except for the equivalent potential temperature.

at the 750-800 mb levels near the storm center. Clearly, the lower tropospheric upward motion found quasi-geostrophically (see Fig. 3.24) and observationally (see Fig. 3.21) is sufficient to destabilize the potentially unstable atmosphere. The resulting lower tropospheric static instability thus provides a favorable environment for the observed shallow convective elements over and to the east of the center at this time.

A more expansive (but less accurate) view of the stratification at this time is shown in the model-derived θ_e profiles for the 69°W and 59°W cross-sections in Fig. 3.29. These profiles were derived using saturation mixing ratios consistent with the derived virtual temperatures. The profile through the storm center shows the shallow layer of potential instability discussed above just north of the center, and also a much deeper potentially unstable layer extending southward from the center, and increasing in depth to 550 mb at 34°N. Note the MCC extends from 36 through 38°N in this section. Perhaps more important for the evolution of this shallow storm is the fact that potentially unstable air exists through increasingly deeper layers eastward from the storm center. The 59°W cross-section shows potential instability throughout its meridional extent, and up to 700 mb over the grid point at which the storm will arrive $\sim$10 h hence. This fact may be explained by the decreasing tropospheric thicknesses eastward from the center over the relatively uniform sea-surface temperatures (see Fig. 3.8 and 3.9), and helps to account for the much deeper convective towers observed later in the cyclone evolution (see Fig. 3.16).

The meridional cross-sections of θ_e for 12 GMT on the 10th are found in Fig. 3.30; they show

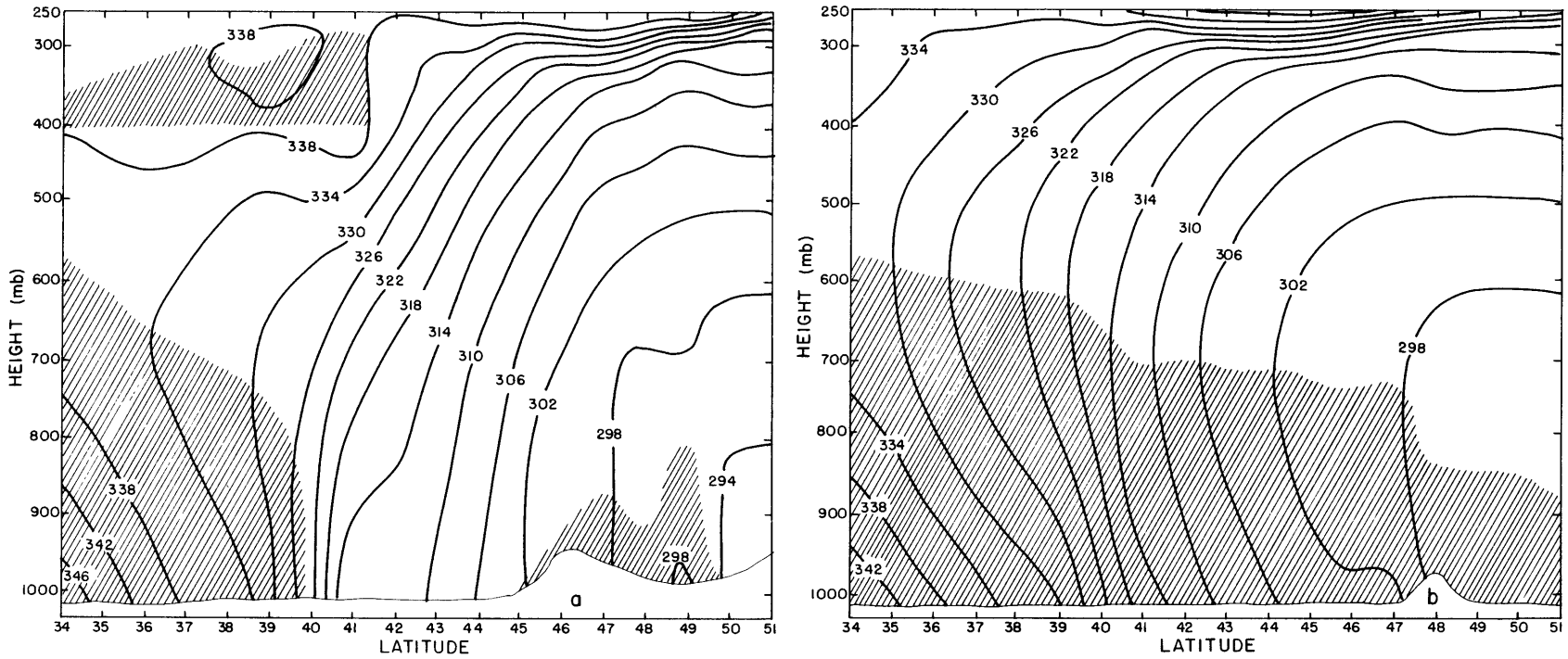


Fig. 3.29. (a) Meridional profiles of equivalent potential temperature (constructed for transition level 400 mb) for 12 GMT, 9 September 1978 for 69°W. Shaded regions indicate a decrease of θ_e with height. Light solid line shows the ground level.
(b) As for (a), except for the 59°W cross-section.

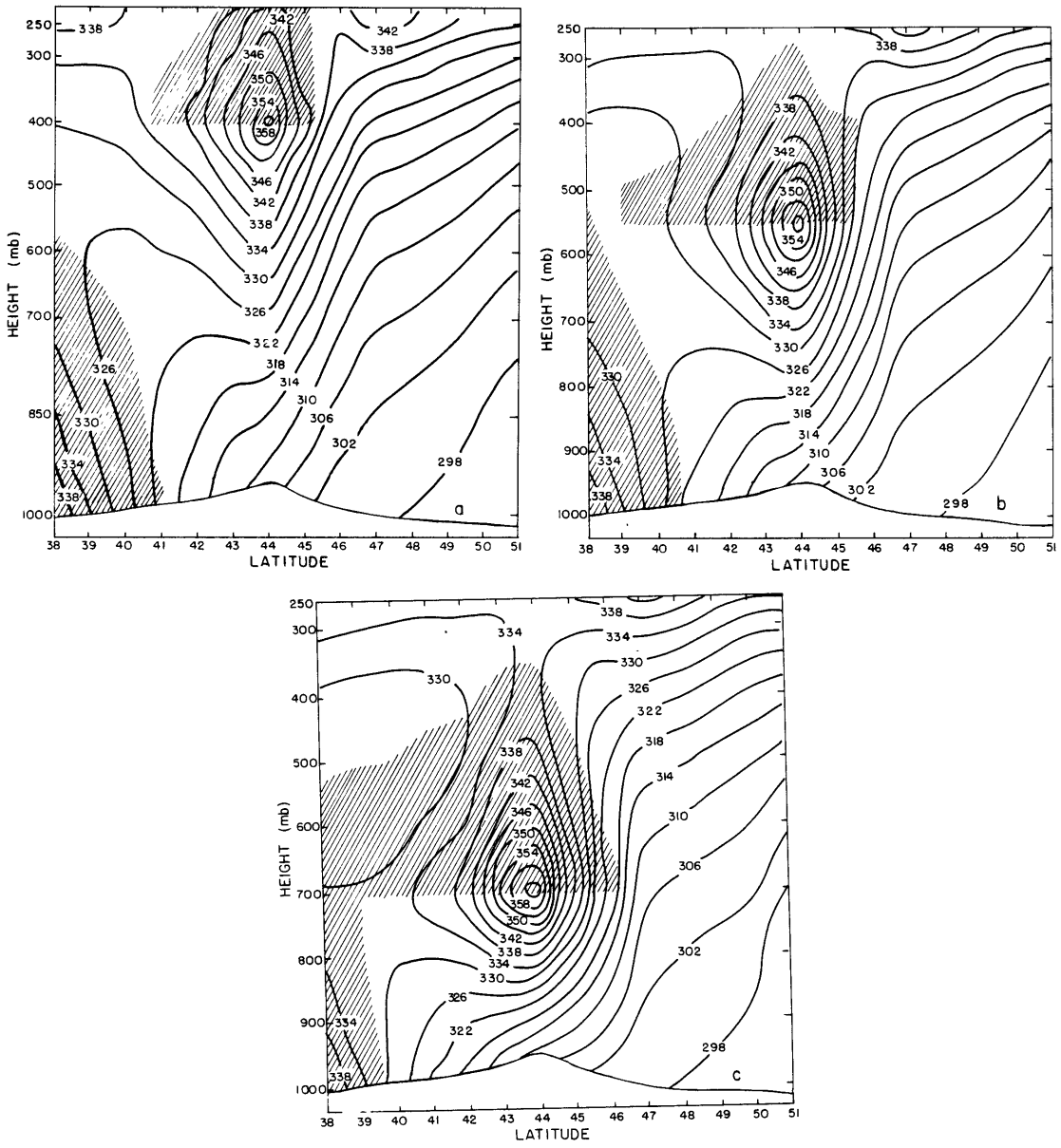


Fig. 3.30. (a) As for Fig. 3.29, except for the 51°W cross-section at 12 GMT, 10 September 1978 for transition point 400 mb.
(b) As for (a), except for the transition level 550 mb.
(c) As for (a), except for the transition level 700 mb.

the lower tropospheric potential instability now confined south of the center, and increasing in depth, southward from the center. Note also the maximum θ_e value in excess of 359°K directly over the center at 550 mb for the 550 mb transition point sounding. This warm temperature anomaly is a reflection of the strong warm core found over this intense surface disturbance at this time (see Fig. 3.11), but the model location of this maximum θ_e is a function of the arbitrarily-chosen transition point between the two slopes of the sounding. However, as discussed earlier, it appears the peak warm temperature anomaly is located well below 400 mb.

3.7 Potential Vorticity Fields

It is the purpose of this section to quantitatively assess the importance of diabatic and frictional effects associated with this extraordinary cyclone through an evaluation of potential vorticity. Ertel (1942) has shown that potential vorticity Q, is conserved for frictionless, adiabatic motion, that is

$$\frac{d(Q)}{dt} = 0 \tag{3.3}$$

where $Q = \frac{\omega \cdot \nabla \eta}{\rho}$, ω is the absolute vorticity vector, η is the function of state, and ρ is the density. If we assume potential temperature θ to be the function of state, note that θ changes most rapidly in the vertical, and use the hydrostatic relation, (3.3) reduces to

$$\frac{d}{dt}\left\{-g\left(\frac{\partial\theta}{\partial p}\right)\left(\zeta_\theta+f\right)\right\}=0 \qquad (3.4)$$

where g is the gravitational acceleration, f is the Coriolis parameter, and ζ_θ is the relative vorticity evaluated on a θ surface.

Gravity-weighted profiles of potential vorticity have been computed for this case in the following manner. The θ profiles for each grid point are constructed according to the procedure outlined in the previous section. Vertical differences of θ are computed over a finite-difference interval of 30 mb. The relative vorticity on a θ surface is evaluated over a horizontal finite difference interval of one degree latitude in the north-south direction, and one degree longitude in the east-west direction. The winds on which the relative vorticity computations are based are computed for each grid point each 15 mb from the surface to 250 mb, and then interpolated onto the appropriate θ surface. The thermodynamic structure found within the cyclone domain hydrostatically specifies geopotential heights for any desired pressure level up to 250 mb. These fields allow the computation of geostrophic winds, which are modified to take into account viscous forces in the planetary boundary layer (assumed 1000 m in depth) with the classical Ekman spiral solutions. Because of the strong cyclonic curvature present in this case, the geostrophic wind speed is an overestimate of the actual wind speed. Therefore, an improvement to this approximation is accomplished through an estimate of the gradient wind, which is specified by

the geostrophic wind speed, and by the radius of the parcel trajectory, R_t. This trajectory radius was calculated using the streamline radius, R_s (approximated by the curvature radius of the geopotential height field), and the instantaneous velocity $\underset{\sim}{c}$ of the surface low. Thus, $R_t = R_s/(1- \frac{|\underset{\sim}{c}|}{v} \cos\gamma)$ (see Holton, 1972, p. 47), where v is approximated by the geostrophic wind speed, and γ is the angle between the streamline (isobar) and the direction of motion of the surface system.

Several experiments with the potential vorticity computation were performed for both 12 GMT on 9 September, and for 12 GMT on 10 September -- both times for which we have a good knowledge of the sea-level pressure and tropospheric thickness fields. Figure 3.31 shows meridional cross-sections through the storm center of potential vorticity, and the θ surfaces on which they are computed. Each time contains runs with transition points in the temperature slope of 700, 550, and 400 mb. The figure clearly shows substantial potential vorticity gain following the center during the 24-h period beginning 12 GMT on the 9th. This result is insensitive to how the stratification varies in the vertical. What does change is the vertical extent of the strong low troposphere potential vorticity values. We may use this set of three charts for each time as specifying the range of uncertainty of our calculations. Thus, 100 mb above the surface center on the 9th, we have calculated potential vorticities ranging from 1.1 to 1.7 x 10^{-5} sec^{-1} $°K\,mb^{-1}$, and for the 10th, values range from 8.0 to 14.0 x 10^{-5} sec^{-1} $°K\,mb^{-1}$. An inspection of the computed gradient wind fields in the lower troposphere above the surface center at 12 GMT

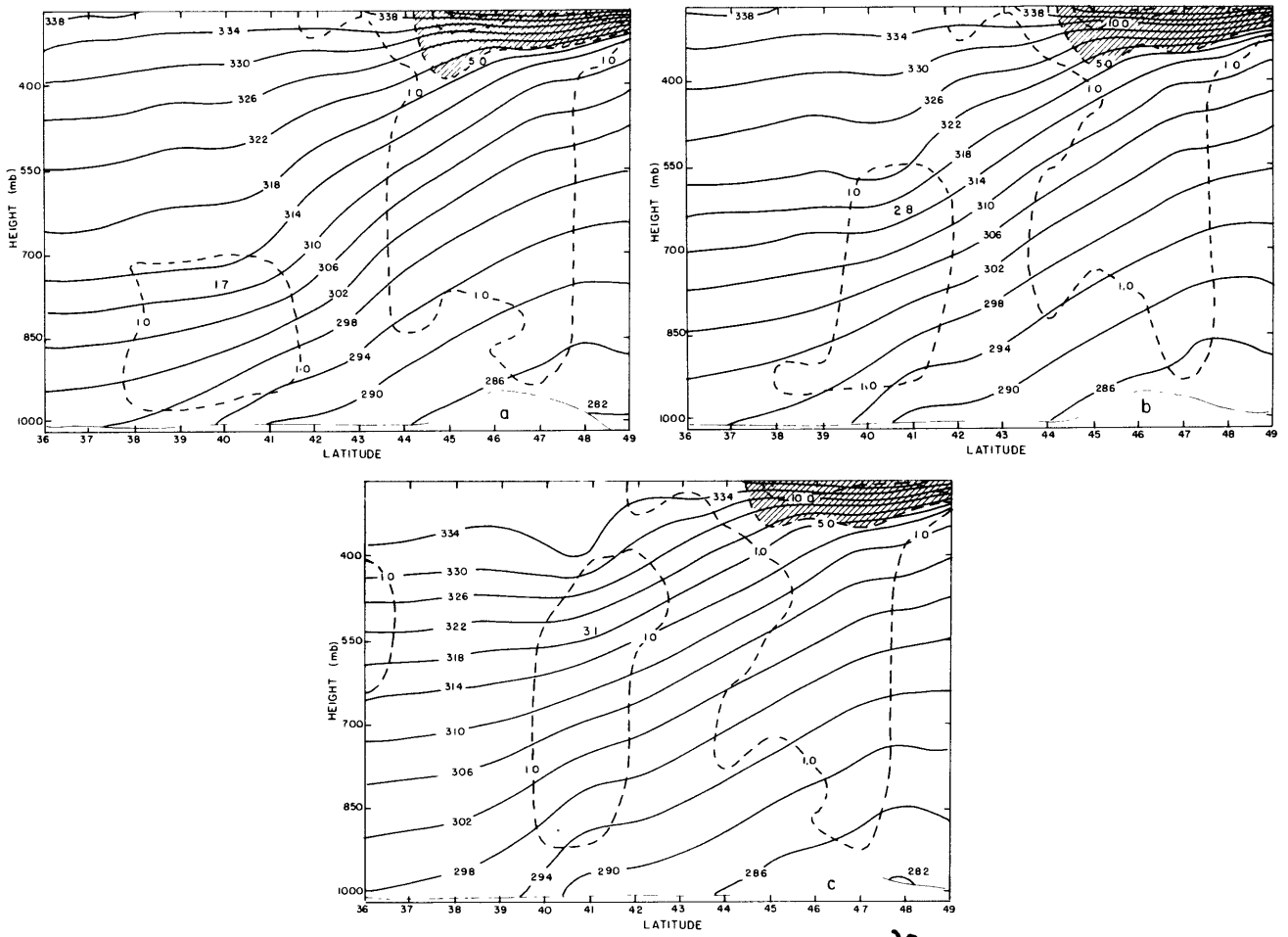


Fig. 3.31 (a) Meridional cross-section of potential vorticity $(-\frac{\partial\theta}{\partial p})\times(\zeta_\theta + f)$, with units of 10^{-5} °K mb^{-1} sec^{-1}, and θ (°K) for longitude 69°W at 12 GMT, 9 September 1978. Light solid line indicates the ground level. Transition level is 700 mb.

(b) As for (a), except for the transition level 550 mb.

(c) As for (a), except for the transition level 400 mb.

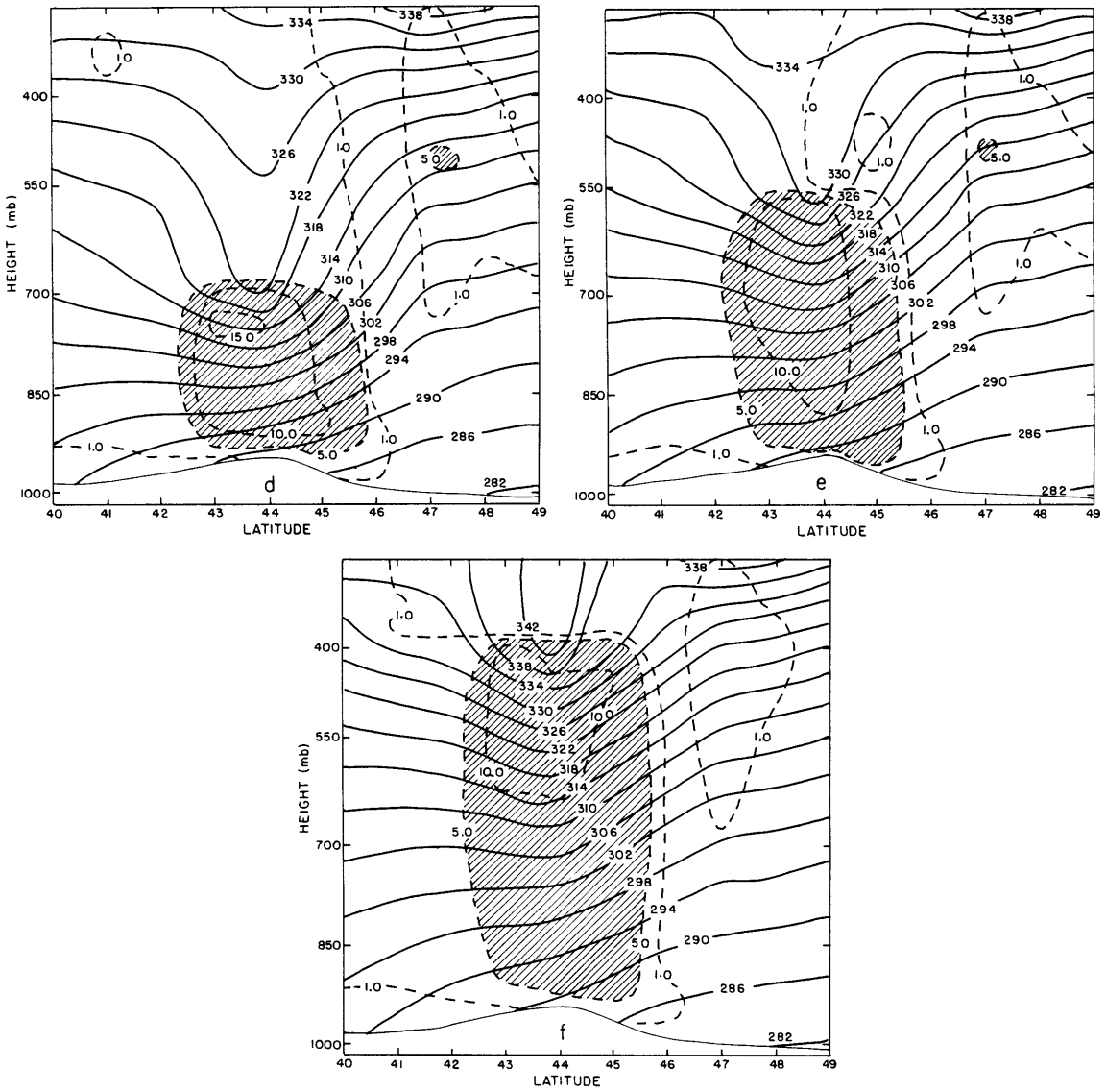


Fig. 3.31. (d) As for (a), except for longitude 51°W at 12 GMT, 10 September.
(e) As for (d), except for transition level 550 mb.
(f) As for (d), except for transition level 400 mb.

on the 10th reveals maximum wind speeds of about 100 knots (which are substantially sub-geostrophic, as we would expect). These speeds are also consistent with the observed speeds near the surface of 60-70 knots. Thus, it appears the maximum error in this computation is about 20% of 50 m/sec. Fluctuations of this magnitude in the computed gradient winds imply a corresponding 20% error in the computation of the isentropic relative vorticity. This is well within the range of typical potential vorticity values just described for 12 GMT on the 10th of September. The range of possible lower tropospheric static stabilities and isentropic slopes has already been accounted for in the former computations. A similar error bound has been found for the wind fields at 12 GMT on the 9th of September.

Our objective is to estimate possible sources of potential vorticity to account for the strong generation found above. As has been shown by Staley (1960), among others, the diabatic source term in the expression for the time rate of change of potential vorticity may be expressed as

$$\frac{dQ}{dt} = g\,\underset{\sim}{\omega}\cdot\nabla\dot{\theta} = -g\left\{\left(\zeta_\theta + f\right)\frac{\partial\dot{\theta}}{\partial p} + \frac{\partial\theta}{\partial p}\left[\zeta_x\frac{\partial\dot{\theta}}{\partial x} + \zeta_y\frac{\partial\dot{\theta}}{\partial y}\right]\right\} \qquad (3.4a)$$

where $\nabla\dot{\theta}$ is the gradient of diabatic temperature change, $\zeta_x = \frac{\partial v}{\partial\theta}$,

and $\mathcal{L}_y = \frac{\partial u}{\partial \theta}$. Gidel and Shapiro (1979) have described the first term on the right as the stability change term, and the second term as the vorticity tilting term. This latter term may be roughly estimated for its potential importance by estimating each component as follows: $\frac{\partial \theta}{\partial P} \sim 1°K/(10\,mb)$, $\mathcal{L}_x \sim 1\,m/sec°K)$, and the condensational heating taken from Table 3.3 at 12 GMT 10 September, and varying over a 10^3 km horizontal interval $\frac{\partial \dot{\theta}}{\partial x} \sim 10^4$ ergs gm^{-1} sec^{-1}/ $(10^6\,m)$. This leads to an order [0] 10^{-6} °K sec^{-1} mb^{-1} $(12\,h)^{-1}$ term which is a small contribution. However, if this heating varied over a 10^2 km distance, or if it were concentrated in smaller, more intense updrafts, this tilting term could become a significant negative or positive factor in the storm-scale potential vorticity budget.

Instantaneous evaluations of the first term on the right of 3.4a for 12 GMT on the 9th and 10th have each been extrapolated 12 h forward to yield an estimate of the 24-h potential vorticity change (see Table 3.4). The storm-scale vertical motions (see Figs. 3.21 and 3.23), and the computed thermal stratifications at these times, are used to compute vertical distributions of storm-scale condensational heating. This information, along with estimates of the vertical component of the absolute vorticity, yields an estimate of the resulting potential vorticity generation. These idealized storm-scale condensational heating profiles, and the well-established absolute vorticities, show a 24-h potential vorticity generation strong enough to account for that which is observed, only if we actually observed this computed static stability increase. In fact, we did not observe such

TABLE 3.4

Potential vorticity changes due to diabatic effects of saturated storm-scale ascent based on 12 GMT 9 September 1978 at grid point 41°N, 69°W

P(mb)	$\omega(10^{-3}$ mb/sec)	Resulting condensation rate in a saturated atmosphere: $L\,dr_s/dt$ ($\dot{\theta}$ ergs gm^{-1} sec^{-1})	$\eta(10^{-4}$ sec^{-1})	$\eta(\partial\dot{\theta}/\partial\rho)$ sec^{-1} °K mb^{-1} (12 h)$^{-1}$
950	- 2.3	1093.	1.7	1.4×10^{-5}
850	- 6.2	2950.		
based on 12 GMT 10 September at grid point 44°N, 51°W				
950	-10.0	4250.	6.6	2.1×10^{-4}
850	-27.0	11500.		

a dramatic static stability increase, and the shortfall is compensated for by the three to four-fold increase in relative vorticity observed in this system. Since this term only accounts for the static stability change, we may conclude that if heating is primarily responsible for the observed dramatic potential vorticity increases, the above "tilting" term is responsible, and the heating is either concentrated into small intense updrafts, or is greater than the magnitude discussed above for this term.

Both of the above analyses indicate that we cannot yet conclude whether a direct appeal to cumulus convection in cyclone-scale potential vorticity generation is necessary. A more detailed examination of the diabatic and frictional effects is thus required to solve the problem.

A clue to the nature of the diabatic influence may be gained from the mean temperature changes observed over the storm center. As we have shown in Figs. 3.8, 3.10, and 3.11, there is a dramatic jump in the column-mean temperature over the center from 00 GMT to 12 GMT on the 10th. Whereas the potential vorticity change is a function of how heating is vertically and horizontally distributed, the thickness change following the center is a good means by which we may see all of the accumulated diabatic effects.

By using a technique based upon the analysis of Sanders (1976), we may evaluate the known physical effects on the thickness change following the low center by first expressing the thermodynamic energy equation as

$$\frac{\partial h}{\partial t} = -\underset{\sim}{v} \cdot \nabla h + \left(\frac{\partial h}{\partial t}\right)_{adi} + \left(\frac{\partial h}{\partial t}\right)_{dia} \tag{3.5}$$

where $\frac{\partial h}{\partial t}$ is the local thickness change rate (for the 1000-250 mb layer in this case), $-\underset{\sim}{v} \cdot \nabla h$ is the vertically-integrated horizontal temperature advection effect. The last two terms consist of the thickness change due to adiabatic warming and cooling associated with storm-scale vertical motions $(\frac{\partial h}{\partial t})_{adi}$, and of all diabatic effects $(\frac{\partial h}{\partial t})_{dia}$, except for large-scale pseudo-adiabatic processes, which will be incorporated into $(\frac{\partial h}{\partial t})_{adi}$.

This adiabatic term may be expressed in terms of the vertical motion and the stratification by noting $\frac{\partial h}{\partial t} = \frac{\partial}{\partial t}\int_{1000}^{250}\left(\frac{\partial z}{\partial p}\right)dp$, and $\frac{\partial \theta}{\partial t} = -\omega\frac{\partial \theta}{\partial p}$, where ω is the vertical motion, and θ is the potential temperature. Thus, the equation of state, hydrostatic assumption, and Poisson's equation combine to yield

$$\left(\frac{\partial h}{\partial t}\right)_{adi} = -\int_{250}^{1000}\frac{RT\,\omega}{g\,\theta}\left(\frac{\partial \theta}{\partial p}\right)d\ln p \tag{3.6}$$

With our knowledge of the stratification over the storm center (described in Section 3.6), and the parobolic profile of ω (described in Section 3.5), we may integrate (6). We will take account of latent heat release in saturated rising-air by expressing as the first law of

thermodynamics

$$\frac{\partial \theta}{\partial t} = -\omega \left[\frac{\partial \theta}{\partial p} - \left(\frac{\partial \theta}{\partial p} \right)_{ma} \right] \tag{3.7}$$

where $(\frac{\partial \theta}{\partial p})_{ma}$ is the change of potential temperature along the appropriate moist adiabat. Thus, this latent heat release only affects (3.6) by the replacement of $\frac{\partial \theta}{\partial p}$ by $[\frac{\partial \theta}{\partial p} - (\frac{\partial \theta}{\partial p})_{ma}]$.

The thickness change following the center may be expressed as the sum of the three physical effects in (3.5) plus the effect of cyclone movement (at velocity $\underset{\sim}{c}$) to air of different mean temperature, $\underset{\sim}{c} \cdot \nabla h$. Thus, (3.5) becomes

$$\left(\frac{\partial h}{\partial t} \right)' = \underset{\sim}{c} \cdot \nabla h - \left(\underset{\sim}{v} \cdot \nabla h \right)' + \left(\frac{\partial h}{\partial t} \right)'_{adi} + \left(\frac{\partial h}{\partial t} \right)_{diq} \tag{3.8}$$

where all the primed terms represent effects observed in a coordinate system moving with the low center. The first term on the right side of (3.8) may be evaluated by using the known track of the cyclone, and the 1000-250 mb thickness analysis shown earlier. By integrating over a time interval $\Delta t = t_f - t_i$, we have

$$\int_{t_i}^{t_f} \left(\underset{\sim}{c} \cdot \nabla h\right) dt \approx \frac{\overline{\Delta h}}{\Delta s} c(\Delta t) = \overline{\Delta h} \tag{3.9}$$

where $\underset{\sim}{c} \cdot \nabla h = c\Delta h/\Delta s$, and Δs is the length of the Δt displacement vector for speed c. The term $\overline{\Delta h}$ may be written approximately as

$$\overline{\Delta h} \approx .5\left[\left(h_{id} - h_{iu}\right) + \left(h_{fd} - h_{fu}\right)\right] \tag{3.10}$$

which is the mean of the thickness differences at each time (t_i and t_f) between the observations at the beginning (upstream = u) and end (downstream = d) of the cyclone displacement over time Δt. As an example, h_{id} represents the thickness value at the initial time t_i, and at the position of the surface system at the final time.

The effect of temperature advection following the surface center may be approximated by using the observed 900-mb (from satellite-derived winds) and 250-mb winds directly over the center, and assuming the winds to be linearly changing with height, and in geostrophic balance. Thus, assuming we are above the planetary boundary layer, any directional change in the wind with height will imply a finite change in temperature due to advection. These low-level winds in the vicinity of the low center are shown in Fig. 3.32, the upper winds for 12 GMT on the 9th are shown in Fig. 3.20c, the 00 GMT, 10 September 250-mb

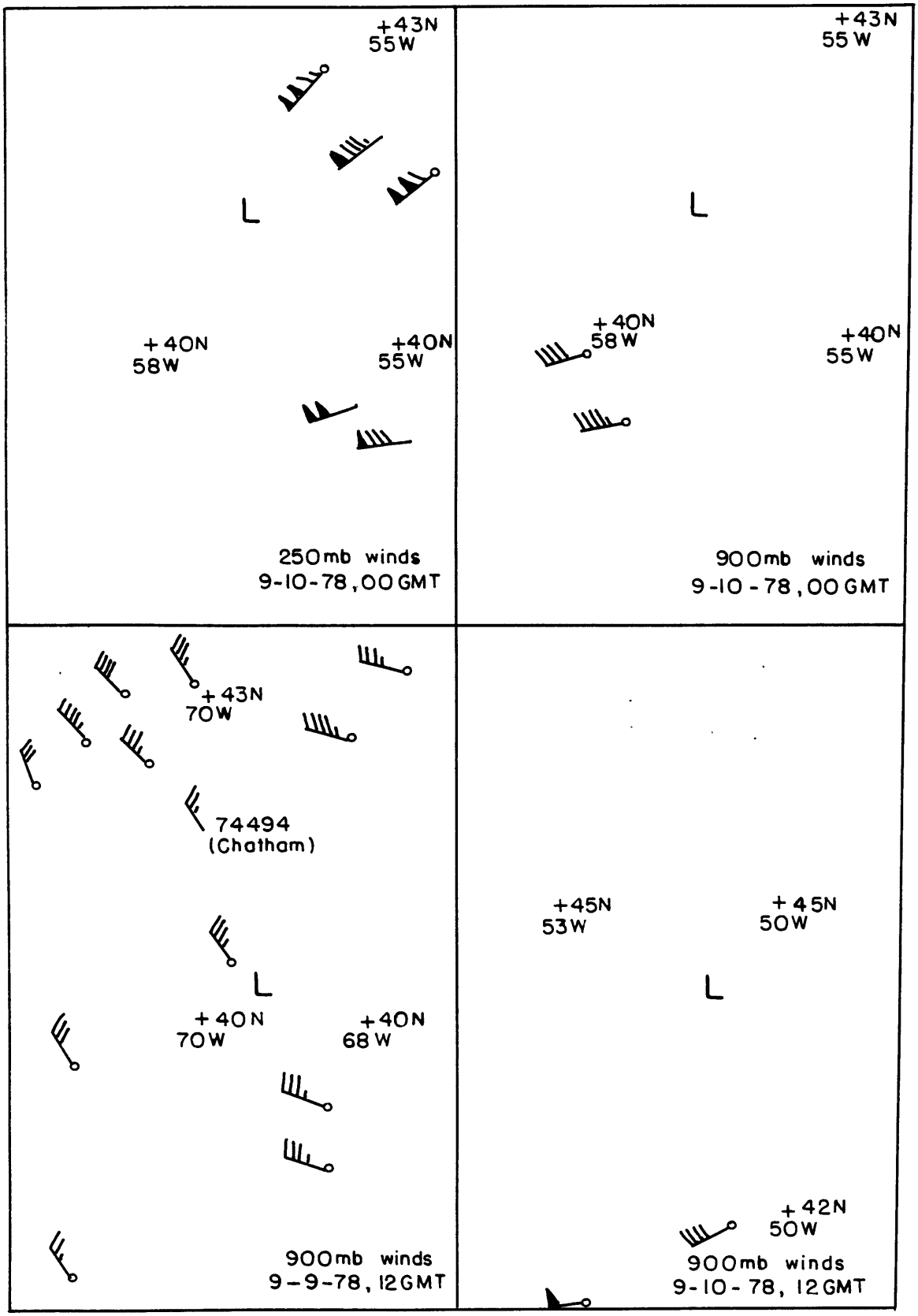


Fig. 3.32. Wind fields described in text. Winds with open circles are satellite-derived, and those without circles are from commercial aircraft. Position of the surface low is indicated with an "L".

winds are shown in Fig. 3.32, and the 12 GMT, 10 September winds are shown in Fig. 3.22c. The coverage is unfortunately sparse near the center at low levels, particularly at 00 and 12 GMT on the 10th. Thus, this temperature advection component is likely to be one of the most unreliable in our thickness change budget. The neglect of any temperature advection effects in the 1000-900 mb layer is due to an ignorance of the wind hodograph here. Of course, the knowledge of only one wind above the low center (where the geostrophic speed is zero) will yield a geostrophic advection of zero above the center, in the layer from the surface to the level of this first known wind. Any deviation from the above straight hodograph assumption in this relatively thin 1000-900 mb layer is likely to have a small effect on the tropospheric mean temperature.

Table 3.5 presents the results of the 24-h budget of thickness change according to expression (3.8). The numbers in column (1) indicate the observed 12-h thickness changes following the center. The numbers in column (2) represent the thickness change following the center as a result of movement toward higher or lower thickness values, $\int_{t_i}^{t_f} (\underset{\sim}{c} \cdot \nabla h)\,dt = \overline{\Delta h}$. The numbers used for this computation are as follows: for the 12-h period beginning 12 GMT on 9 September, h_{id} = 10320 m, h_{iu} = 10640 m, h_{fd} = 10420 m, h_{fu} = 10580 m; for the 12-h period beginning 00 GMT, 10 September, h_{id} = 10265 m, h_{iu} = 10420 m, h_{fd} = 10725 m, h_{fu} = 10335 m. These thickness values may be readily identified from the appropriate thickness charts found in Figs. 3.8b, 3.10b, and 3.11b. The column (3) numbers represent the temperature advection effect following the center. The winds used in this computation are as follows:

TABLE 3.5

Time	observed 1000-250 mb thickness over center	(1) observed 12-h thickness change (m)	(2) $\int_{t_i}^{t_f}(\bar{c}\cdot\nabla h)dt = \overline{\Delta h}$ (m/12 h)	(3) $-\int_{t_i}^{t_f}\bar{v}\cdot\nabla h\,dt$	(4) (m/12 h)	(5) =(2)+(3)+(4) (m/12 h)	(6) residual $(\frac{\partial h}{\partial t})_{dia}$ (1) - (5) (m/12 h)
12 GMT 9/9/78	10640 = -10.9°C						
		-220	-240	-48 m/ 6 h -27 m/ 6 h	-117	-432	+212
00 GMT 9/10/78	10420 = -16.3°C					predicted 10258 = -20.3°C	
		+305	+118	-27 m/ 6 h -34 m/ 6 h	-942	-885	+1190
12 GMT 9/10/78	10725 = -8.8°C					predicted 9535 = -38.2°C	
12 GMT 9/9/78	term (4) parameters for expression 3.17 T_{sL} = 288°K P_{sL} = 1000 mb $f_o = 9.4 \times 10^{-5}$ sec^{-1} $\eta_o = 2.0 \times 10^{-4}$ sec^{-1}	$L = 1.5 \times 10^6$ m $\frac{\Delta P}{\Delta t}$ = -14 mb/12 h			from equation 3.17: -152	-467	+247
00 GMT 9/10/78						predicted 10173 = -22.4°C	
12 GMT 9/10/78	term (4) parameters for expression 3.17 T_{sL} = 288°K P_{sL} = 970 mb $f_o = 9.8 \times 10^{-5}$ sec^{-1} $\eta_o = 3.0 \times 10^{-4}$ sec^{-1}	$L = 1.8 \times 10^6$ m $\frac{\Delta P}{\Delta t}$ = -45/12 h			-417	-360	+665
						predicted 10060 = -25.2°C	

for the first 6-h period, $v_{\sim 250\,mb}$ = 314° at 48 m/sec, $v_{\sim 900}$ = 329° at 18 m/sec, for the second and third 6-h periods, $v_{\sim 250}$ = 249° at 55 m/sec, $v_{\sim 900}$ = 255° at 21 m/sec, and for the fourth 6-h period, evaluated at a point 200 km south of the center where we have some knowledge of the observed winds, $v_{\sim 250}$ = 226° at 28 m/sec, and $v_{\sim 900}$ = 240° at 23 m/sec. The numbers in column (4) are the result of evaluating

$$\left(\frac{\partial h}{\partial t}\right)_{adi} = -\frac{R}{g}\left[\frac{\partial \theta}{\partial p} - \left(\frac{\partial \theta}{\partial p}\right)_{ma}\right]\int_{250}^{1000} \frac{T(p)\,\omega(p)}{\theta(p)}\, d\ln p .$$

Column (5) numbers indicate the sum of numbers in columns (2) through (4). This sum indicates the predicted thickness change due to large-scale pseudo-adiabatic processes. The resulting predicted thickness, due to these processes, is also indicted in column (5) for 00 GMT and 12 GMT on 10 September. Column (6) shows the residual term, which is accounted for by diabatic processes. We may infer from this table that diabatic processes (excluding latent heating in saturated storm-scale ascent) are required to warm the column 5°C for the first 12-h period, and some 30°C in the second 12-h period. In spite of our relative ignorance of the temperature advection effects discussed earlier, and in light of the existing data, it is hard to imagine enough warm advection to warm the column so dramatically. Of course, the largest contribution to the cooling in the second time period is saturated storm-scale ascent, which is based solely on divergence measurements at the surface (based mainly upon Seasat information), and at 250 mb. Another limitation is our knowledge of the vertical motions only at the beginning and end points of the 24-h cyclone track. Also, the

static stability has likely been overestimated for the second 12-h period, for we used the 12 GMT 10 September stratification in this computation. However, even if we arbitrarily cut the vertical motion effect in half for the second time period, we would still be left with an 18°C temperature deficit in the column, to be accounted for by diabatic warming.

We re-estimated term (4) in Table 3.5 by using a somewhat different technique described by Sanders (1976). The frictionless quasi-geostrophic vorticity equation for sea-level flow may be expressed as

$$\frac{\partial \zeta_{SL}}{\partial t} = -\underset{\sim}{V}_{SL} \cdot \nabla\left(\zeta_{SL} + f_0\right) + \eta_0 \left(\frac{\partial w}{\partial p}\right)_{SL} \tag{3.11}$$

where sL indicates sea-level, f_0 is the Coriolis parameter, and η_0 is the absolute vorticity appropriate to the domain under consideration. The vorticity change at the sea-level cyclone center is due solely to divergence, for the advection vanishes here. The relative vorticity may be expressed as

$$\zeta_{SL} = \frac{1}{\rho_{SL} f_0} \nabla^2 p_{SL} \tag{3.12}$$

Assuming a simple two-dimensional harmonic variation of P_{sL} (x,y) with wavelength L and amplitude $\hat{P}_{sL}$, then at the cyclone center

$$\zeta_{SL} = -2\left(2\pi/L\right)^2 \frac{\hat{p}_{SL}}{\rho_{SL} f_0} \tag{3.13}$$

Equation (3.11) can thus be expressed as

$$\frac{\partial \hat{p}_{SL}}{\partial t} = \frac{-\rho_{SL} f_0}{2}\left(\frac{L}{2\pi}\right)^2 \eta_0 \left(\frac{\partial \omega}{\partial p}\right)_{SL} \tag{3.14}$$

We will now use a crude approximation to the vertical motion profile in order to relate the thickness change over the surface low center directly to its central pressure fall. Equation (3.14) becomes, with the assumption of a linear variation of ω from zero at 1000 mb to a maximum magnitude at 550 mb,

$$\frac{\partial \hat{p}_{SL}}{\partial t} = \frac{\rho_{SL} f_0}{2}\left(\frac{L}{2\pi}\right)^2 \eta_0 \left(\frac{\omega_{550}}{450\ mb}\right) \tag{3.15}$$

We approximate the integral in term (4) of Table 3.4 by

$$\left(\frac{\partial h}{\partial t}\right)_{adi} = \frac{-R}{g\, p_0^{(R/c_p)}}\left(\frac{\omega_{550}}{2}\right)\left[\frac{\partial \theta}{\partial p} - \left(\frac{\partial \theta}{\partial p}\right)_{mq}\right]\int_{250}^{1000} p^{R/c_p}\, d\ln p \tag{3.16}$$

The mean value of ω in this layer is approximated by $\omega_{550}/2$. We will use the temperature stratifications found in Section 3.6 for each of the times 12 GMT on 9 and 10 September. By eliminating ω_{550} between (3.15) and 3.16), and using the equation of state, we have

$$\left(\frac{\partial h}{\partial t}\right)_{adi} = \frac{-T_{SL}}{P_{SL} f_o h_o L^2}\left(\frac{\partial \hat{P}_{SL}}{\partial t}\right)\left[1.7\times10^{8}\ m^3 sec^{-2} {}^{\circ}K^{-2} mb\left[\frac{\partial \theta}{\partial p} - \left(\frac{\partial \theta}{\partial p}\right)_{mq}\right]\right] \quad (3.17)$$

Computations using (3.17) are summarized in the lower section of Table 3.4. We can see substantially less pseudo-adiabatic cooling during the second 12-h period, primarily because we are not using the vertical motion found in the cyclone at the end of its development stage, but rather a more correct integrated value. There is still however, a dramatic 17°C mean temperature increase in the column evidently effected by non-pseudo-adiabatic processes. These processes will now be discussed.

An estimate of the sensible heating of air parcels converging to the low center may be made by evaluating their dry-adiabatic cooling as a result of flow across the intense pressure gradient observed at 12 GMT on the 10th. This would cause a sensible heat transfer from the sea-surface to the atmosphere above that which otherwise would not be present, assuming the SST is higher than the adjacent atmospheric temperature. An upper bound on this heating over the surface center is found by assuming parcels travel across the pressure contrast of 12 mb/ 110 km at a speed of 25 m/sec. The exchange coefficient used is

1.87×10^{-3} (see Bunker, 1976). The parcel cools just over 1°C by the time it arrives at the center, and the resulting sensible heat transfer over the area surrounding the center would be about 32 W/m^2, which would warm the 1000-250 mb column a negligible 6 m/12 h. This sensible heat flux is well below the values which we find away from the storm center, and is consistent with findings of Petterssen et al. (1962), where strong sensible heating is confined to the southwest of the storm center in the heart of the cold-air outbreak. A peak in sensible heating near the surface would tend to destroy potential vorticity negligibly, through static destabilization.

The radiative effects, such as long-wave cooling at cloud tops are of order 2-3°K/12 h, and in the 1000-250 mb column, may account for as much as a 1°K temperature decrease (see Manabe, 1956), or a 40 m tropospheric thickness decrease. Resulting storm-scale potential vorticity changes will be small, for the layers in which substantial heating gradients exist are quite thin.

The frictional effect on potential vorticity may be expressed (see Gidel and Shapiro, 1979) as

$$\frac{d}{dt}\left[-g\left(\zeta_\theta + f\right)\frac{\partial\theta}{\partial p}\right] = -g\frac{\partial\theta}{\partial p}\hat{k}\cdot\nabla_\theta \times \underset{\sim}{F} = \left(-g\frac{\partial\theta}{\partial p}\right)\left[\frac{\partial}{\partial x}\left(\frac{-\partial\overline{w'v'}}{\partial p}\right) - \frac{\partial}{\partial y}\left(\frac{-\partial\overline{w'u'}}{\partial p}\right)\right]$$

(3.4b)

where $\underset{\sim}{F}$ is the force per unit mass produced by turbulent stresses, the bar is a time average at a fixed point throughout some characteristic turbulent time scale, and the prime represents a turbulent deviation from the time average. Expression (3.4b) shows that changes in ζ_θ can result from horizontal gradients of the vertical divergence of the turbulent momentum flux. We also see this effect is proportional to the static stability. Thus, the lower troposphere at the later stages of this cyclone is most vulnerable to this effect. The maximum updraft speeds in the cumulus towers are of order 10 m/sec, while the perturbation horizontal speeds are also 10 m/sec. Assuming this turbulent momentum flux occurs over a depth of some 4 km, this vertical momentum flux divergence is of order 10^{-2} m sec^2 assuming the horizontal change of this quantity occurs over an order 100 km distance, and the tropospheric increase of θ with height is order (1°K/10 mb), then the 12-h potential vorticity change is of order 10^{-4} °K mb^{-1} sec^{-1}. This is clearly a potent effect, and the sign of this term depends upon the location and character of the convection with respect to the computational point.

The diabatic effect we have yet to consider is the cumulus-induced subsidence warming. We are particularly interested in the clear eyelike area in the storm center. Smith (1980) has estimated the magnitude of this descent in the eye of a tropical cyclone to be about 10 cm/sec. A parabolic profile of this subsidence with the observed temperature structure will yield a column warming of about 650 m in 12 h, or a 16°C temperature increase. This number is

sufficient to balance the thickness change budget of Table 3.4, for, as explained earlier, the pseudo-adiabatic cooling term (top section of column 4) was likely overestimated by [0] 500 m/12 h. The potential vorticity increase below the peak in the subsidence warming profile is [0] 10^{-5} sec^{-1} °K mb^{-1} $(12\,h)^{-1}$, which is one order less than the observed potential vorticity increase found over the center. However, horizontal variations of this subsidence effect could make the tilting term in (3.4a) important, and it is profoundly important in accounting for the strong warming over the storm center.

Although strong cyclone-scale ascent has been computed for this case, the satellite images, shown in Fig. 3.16, indicate deep convective elements with adjacent cloudless areas, within this region of strong storm-scale ascent. This indicates much of the converging air ascended within these convective elements, rather than uniformly in stratiform ascent. This fact is critical for the thermodynamic and dynamic structure of this cyclone. It is probable that bulk heating effects of the observed convective towers in this case (through the horizontal Laplacian of diabatic temperature changes) drove much of the storm-scale ascent not accounted for by our pseudo-adiabatic, inviscid quasi-geostrophic calculations. Although we cannot rule out the so-called cumulus "frictional" term as being important in our potential vorticity budget, we have found that bulk heating effects were important in accounting for the warm core of this cyclone. This effect likely caused a profound potential vorticity increase in the cyclone, along with the concurrent intensification not accounted for

by the operational PE model forecasts.

Consistent with our observational results, the dramatic effects of cumulus convection on cyclone development have been demonstrated by Anthes and Keyser (1979). They found the manner in which cumulus bulk heating effects were vertically distributed had a first-order effect on a cyclone's evolution along the Florida coast. It is clear from (3.4a), that in an atmosphere in which the absolute vorticity vector is generally pointing up, potential vorticity will be generated as heating increases upward, and destroyed as heating decreases upward. The next chapter will be devoted to an examination of the possible dynamical consequences of the cumulus-induced heating effects found in this chapter.

3.8 Concluding Remarks

The storm which battered the liner *Queen Elizabeth II*, and in which the dragger *Captain Cosmo* was lost originated as a shallow baroclinic disturbance over the middle Atlantic states. This shallow low was "steered" by the low-level warm advection associated with intense sea-surface temperature contrasts to the left of the upper-level flow. The early development also took place in the clear air just to the northwest of a rapidly expanding MCC. Many tropical cyclones also initially develop under similar circumstances, as has been shown observationally by Weickmann et al. (1977), and by Fingerhut and Gray in Grube's (1979) work. Although we have described conditions which point to some of the early rapid cyclogenetic development to have

been associated with the developing MCC (prior to 06 GMT, 9 September), the MCC appears to have been irrelevant to the explosive cyclogenesis documented subsequent to 12 GMT, 9 September. The deep convection which seems important for this purpose appears as the aforementioned hot towers near the center shown in Fig. 3.16b, when the MCC was 450 km southwest of the cyclone center.

The storm deepened nearly 60 mb in the 24-h period subsequent to 12 GMT on 9 September in association with deep cumulus convection in and around the storm center. The rapidity with which this storm intensified and grew in size to super-synoptic scale by 11 September (see James, 1979) makes such a class of cyclone even more dangerous to marine interests than are tropical cyclones. Operational numerical models missed virtually all of the cyclone intensification, and the NMC final surface analysis at 12 GMT on 10 September overestimated the storm central pressure by 35 mb due to the absence of the *Euroliner* observation. This datum existed on the Service C network and, along with the *Euroliner* weather log and barograph trace, proved to be crucial in more correctly estimating the storm's central intensity. This fact should serve as a caveat to those whose sole contact with the current weather is based upon the use of final NMC-analyzed meteorological fields.

The Seasat-A surface wind fields proved to be instrumental in capturing the cyclone's central intensity, and reinforced the *Euroliner* observations. The hurricane-force winds shown by the Seasat instrumentation package represent important information to the meteorologist,

and to the mariner had they been available in real time. This type of instrumentation package will be a major boon to the present surface maritime observing system.

We have shown the surface winds to be of hurricane force, storm-scale surface relative vorticities and ascent to be comparable to those found in tropical cyclones, and the rapid 24-h central pressure fall to be greater than those found in the majority of typhoons. The deep convection in and around the storm center, the clear eyelike center at the storm's mature stage, and the intense tropospheric warm core are all features found in tropical cyclones. The development of the upper-level trough occurred after the surface low appeared, in a manner similar to that discussed by Bosart (1981) for the President's Day snowstorm.

A method for evaluating the three-dimensional thermodynamic and dynamic structure of this cyclone has been used to find potential vorticity over the cyclone domain. Results indicate a 24-h lower tropospheric generation of from 5 to 13 times the value observed at 12 GMT, 9 September. These lower tropospheric storm-scale potential vorticity values found at 12 GMT on 10 September are of the same order as those generally found in the stratosphere, which implies that other similarly intense bombs may have this anomalous characteristic. An evaluation of physical effects on thickness change following the center shows a large-mean tropospheric temperature rise to be due to the bulk cumulus heating effects of subsidence in the eye.

A three-layer quasi-geostrophic model has been used to evaluate

the vertical motions and central pressure tendency. Both computations fall far short of the "observed" vertical motions and intensification. However, the three-layer quasi-geostrophic model reveals upward motion at 12 GMT on the 9th sufficient to lift the potentially unstable air, and set off the deep convection in and around the storm center a few hours later. Thus, while the quasi-geostrophic ascent was insufficient alone to account for the observed instantaneous intensification, this effect may have been critical for the cyclone evolution, through its lapse rate destabilization, and subsequent convection. All of the above evidence points to the probability that the observed cumulus convection was of first-order importance in this storm's intensification, as it appears to be in tropical cyclones. Our results indicate both baroclinic and convective mechanisms cooperate to produce such a monster cyclone. We also find from the potential vorticity analysis that how convective heating and frictional effects are distributed with respect to the incipient cyclone is crucial to its development, and that simply the presence of, or the intensity of the cumulus activity has little to do with whether a cyclone intensifies explosively. These results appear not to conflict with Rasmussen's (1979) hypothesis that a CISK-like mechanism can be of profound importance in extratropical cyclone development, although the growth rates associated with the polar lows that he studied are generally much less than those found in the QEII case. Further, Reed (1979) has suggested that polar lows are essentially baroclinic disturbances. The QEII case originated as a shallow baroclinic wave which was aided crucially by the accompanying

cumulus convection. Rasmussen's CISK mechanism (originally proposed by Charney and Eliassen, 1964 for the hurricane problem) is a plausible means by which this storm's development may have been enhanced. Recently, Yip and Cho (1980) have suggested that mechanical effects of cumulus convection may have a significant positive effect on the development of extratropical disturbances. Although this hypothesis cannot be dismissed, and indeed, we have seen this effect to be both a plausible and potentially important one in generating potential vorticity, we are unable to estimate its effects for this case. However, our computations clearly show the cumulus-induced thermodynamic effect over the cyclone center to have been a substantial one.

As discussed earlier, operational numerical models are severely tested in such an initially shallow disturbance, where the quasi-geostrophic development is small compared with that observed (see Tables 3.1, 3.2, 3.3, and Fig. 3.24), and where convection is so prevalent. Thus, in a case such as this, in which cumulus-induced heating is clearly present, it is not sufficient for a model to predict correctly the vertical integral of this heating, but it is crucial dynamically that its vertical distribution be correctly simulated. This sensitivity discussed by Anthes and Keyser (1979) is applicable to numerical model tropical cyclone development (see Ooyama, 1969). The evidence indicates that an extraordinary cyclonic event such as this one is highly responsive to physical parameterizations absent or improperly treated in existing models. Bosart (1981) has examined the development of the massive snowstorm which affected the Washington D.C. area on President's

Day, 1979, and he found the NMC model forecasts to be gravely deficient in forecasts of precipitation and sea-level pressure. Cyclones such as these mainly affect maritime areas (see Sanders and Gyakum, 1980), but the startling suddenness with which they appear, and the large impact such intense storms may have on planetary wave development (see Gall et al., 1979) demand that observational efforts be expanded to corraborate the findings of this well-documented case.

Fig. 3.33. Geographical locator map, in which circled letters represent radiosonde stations. The set of stations includes those mentioned in the text, and radiosonde stations within the domain of Fig. 3.25. International identifier numbers follow, where applicable:
A-Atlantic City, New Jersey-72407, B-Fort Totten, N. Y.-74486,
C-Patuxent River, Md.-72404, D-Chatham, Mass.-74494,
E-Trenton, New Jersey, F-Wallops Island, Va.-72402,
G-Dulles International, Va.-72403, H-Portland, Me.-72606
I-Caribou, Me.-72712, J-Cape Hatteras, N.C.-72304,
K-Greensboro, N.C.-72317, L-Buffalo, N.Y.-72528,
M-Albany, N.Y.-72518, N-Sept-Iles, Quebec-72811,
O-Shelburne, Nova Scotia-74399, P-Sable Island, N.S.-72600,
Q-Stephenville, Newfoundland-72815,
R-St. John's, Newfoundland-72801.

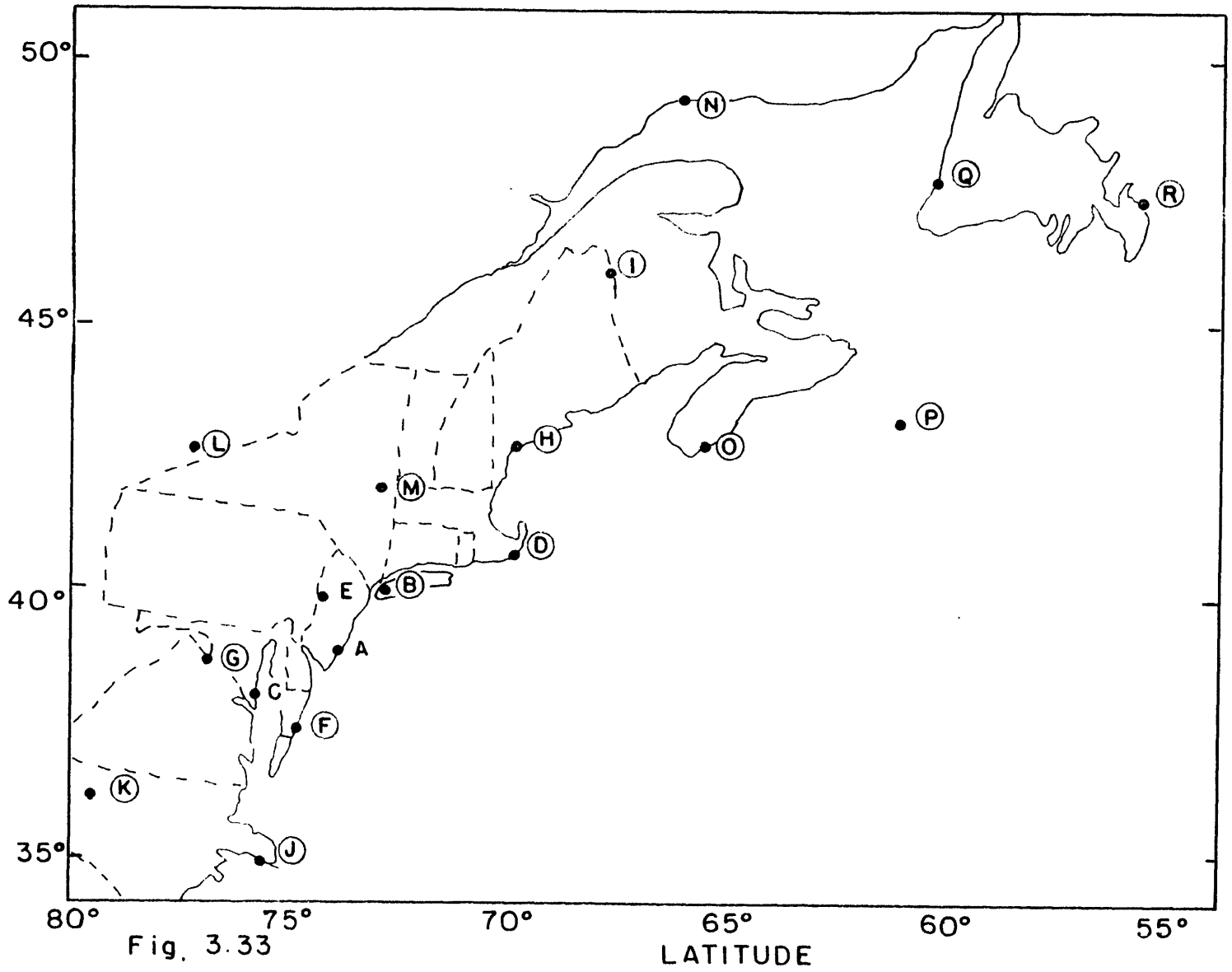


Fig. 3.33

CHAPTER 4

THE DYNAMICAL EFFECTS OF HEATING

4.1 Introduction

The preceding analysis of the QEII case has indicated a 25-35°C mean tropospheric warming over the surface low center during its 24-h explosive development subsequent to 12 GMT, 9 September. The primary cause of this warming appeared to be due to bulk heating effects of the cumulus convection observed during this period. The purpose of this chapter is to quantify the dynamical effects such heating might have on the development of the cyclone itself.

Much attention has been paid in the literature to the ensemble effects of cumulus convection on the dynamics of the tropical cyclone, as has been noted in Chapter 1. In particular, numerical modelers such as Yamasaki (1968) and Ooyama (1969) have indicated a strong sensitivity of a vortex to how these heating effects are distributed vertically. Koss (1976), in a linear stability analysis of CISK-induced disturbances, also found that properties of cyclone-scale disturbances are strongly dependent upon the vertical heating distribution.

The effect of varying this vertical heating distribution on extratropical cyclone development was, as noted in Chapter 3, also found by Anthes and Keyser (1979) to be important. Tracton (1973) estimated the size and magnitude of the bulk cumulus latent heating effects from his examination of some continental United States cyclones. He assumed all of the latent heat release was confined between 900 and 200 mb, and applied an assumed two-dimensional distribution of heating

to the ω-equation at each of two levels (325 and 775 mb). With ω at 550 mb assumed to be the arithmetic average of the aforementioned ω's, a parabolic fit to these three ω values was then performed to enable an estimate of the divergence at 1000 mb; and thus, an estimate of the 1000 mb geopotential tendency from the quasi-geostrophic vorticity equation was obtained. For a specified scale and amount of heating, computations of this 1000-mb geopotential tendency were made for various ratios of upper-to-lower tropospheric heating. The strong sensitivity of computed 1000-mb geopotential falls was demonstrated.

4.2 Model Description, Equations, and Solutions

The quantification of the dynamical effects of heating on the cyclone-scale will be in a more general form than Tracton's analysis allowed, for we will specify analytically a three-dimensional distribution of the heating, which will allow for analytic solutions to both the quasi-geostrophic omega and vorticity equations.

The quasi-geostrophic ω-equation forced by diabatic temperature changes may be expressed as

$$\left(\nabla^2 + \frac{f_0 \lambda_0}{6} \frac{\partial^2}{\partial p^2}\right) \omega = -\frac{R}{6 P C_p} \nabla^2 \dot{Q} \qquad (4.1)$$

where $\dot{Q}$ is the diabatic heating per unit mass, and the rest of the symbols are discussed in Appendix 3.A.

We shall specify this heating function to be zero at the 1000-mb surface, and at the top of the atmosphere, with a peak at some intermediate pressure surface, P_I. The horizontal distribution will be given by a two-dimensional harmonic variation, so that

in layer 1
$$\dot{Q} = \frac{(P_0 - P)}{(P_0 - P_I)} \frac{2Bg}{P_0} \cos\left(\frac{2\pi x}{L}\right) \cos\left(\frac{2\pi y}{M}\right) \quad \text{for } P_I \leq P \leq P_0 \tag{4.2a}$$

in layer 2
$$\dot{Q} = \frac{P(2Bg)}{P_I P_0} \cos\left(\frac{2\pi x}{L}\right) \cos\left(\frac{2\pi y}{M}\right) \quad \text{for } 0 \leq P \leq P_I \tag{4.2b}$$

where B represents the total heating in the column $\int_0^{P_0} \frac{\dot{Q}(PdP}{g}$, P_0 is the reference pressure (1000 mb), and L and M are the wavelengths of the heating perturbation in the x and y-directions, respectively.

A representation of the heating function's vertical variation is given in Fig. 4.1. The arbitrary specification of the peak in heating at a particular pressure level, P_I, is a simple means by which we may assess the dynamical importance, discussed earlier, of the vertical distribution of heating. Although our idealized heating profile extends unrealistically up to the top of the atmosphere, this problem above the tropopause will not seriously affect the tropospheric ω-profiles, and the resulting geopotential tendencies for a surface disturbance, expecially considering our uncertainty about the precise character of the heating taking place in the troposphere. The vertically-

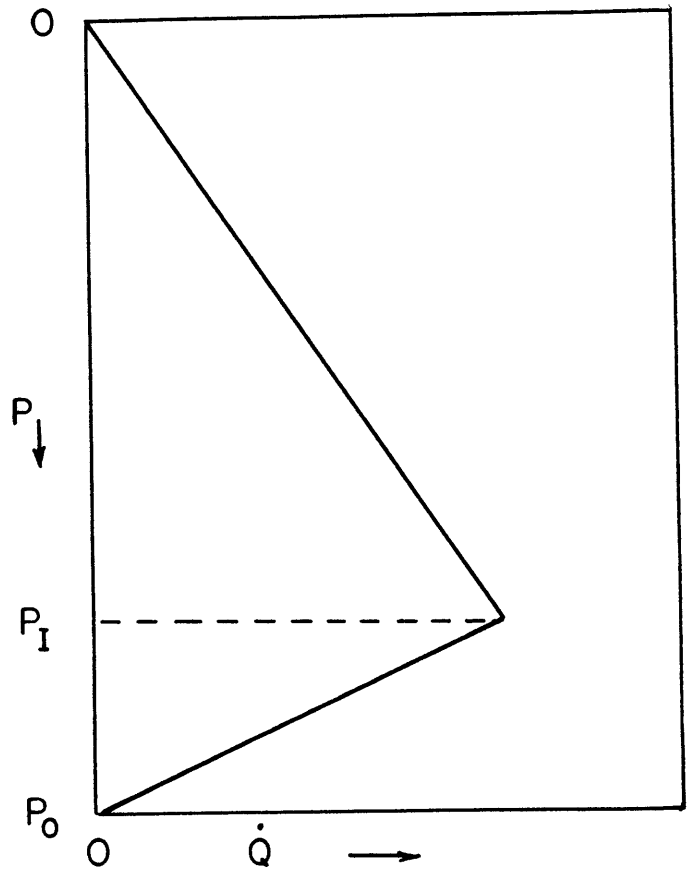


Fig. 4.1. Vertical profile of the heating function described in the text.

integrated heating range previously described for the QEII case (12-17°C/12 h) corresponds approximately to a 1000-250 mb thickness rise of from 500-700 m/12 h. If all of this heating were realized as consensation, rainfall rates of from .32 to .45 cm/h would be found. Although this implied heating is about five times that of Phillips' (1963) theoretical limit of .08 cm/h for the quasi-geostrophic approximation to be strictly valid, this small discrepancy should not alter the basic results of these calculations. Moreover, our values are still considerably less than the 3 cm/h value often observed raining out of individual convective cells. Our heating pattern is assumed to be organized on a scale comparable to the cyclone itself. The issue of this organization will be discussed in the next section.

The prescribed heating functions specify an ω-equation in each layer, so that in layer 1

$$\left(\nabla^2+\frac{f_0^2}{6}\frac{\partial^2}{\partial p^2}\right)\omega=\frac{b_1(p_0p-p^2)2Bq}{(p_0-p_I)\,p_0T_0\gamma c_p}\cos\left(\frac{2\pi x}{L}\right)\cos\left(\frac{2\pi y}{M}\right)$$

$$\text{for } p_I\le p\le p_0 \qquad (4.3a)$$

in layer 2

$$\left(\nabla^2+\frac{f_0^2}{6}\frac{\partial^2}{\partial p^2}\right)\omega=\frac{b_1p^2\,2Bq}{p_I\,p_0T_0\gamma c_p}\cos\left(\frac{2\pi x}{L}\right)\cos\left(\frac{2\pi y}{M}\right)$$

$$\text{for } 0\le p\le p_I \qquad (4.3b)$$

where $$b_1=\left(\frac{2\pi}{L}\right)^2+\left(\frac{2\pi}{M}\right)^2$$

We now have two second-order differential equations which specify the vertical motion field for the entire atmosphere. Solving the equations (4.3a) and (4.3b) involves specifying the boundary conditions; the first shall be $\omega = 0$ at the lower boundary of layer 1 (at $P=P_0$), and the second to be $\omega=0$ at $P=0$. The other two boundary conditions are at the interface between the two layers; that is, ω and $\frac{\partial \omega}{\partial P}$ match at $P=P_I$. This procedure is analogous to the one described in Appendix 3.A, in which we solved analytically for ω in three layers.

The solution for ω forced by our heating function $\dot{Q}$, is, for the first layer

$$\omega_H = C_H p^{q_1} + D_H p^{q_2} - \frac{k_{H_1} p}{b_1} - \frac{k_{H_2} p^2}{(2a_1 - b_1)} \quad \text{for } P_I \leq p \leq P_0 \qquad (4.4a)$$

and in the second layer,

$$\omega_H = A_H p^{q_1} + \frac{k_{H_3} p^2}{(2a_1 - b_1)} \quad \text{for } 0 \leq p \leq P_I \qquad (4.4b)$$

where

$$k_{H1} = \frac{(b_1 P_0)(2Bg)}{(P_0 - P_I)(P_0 T_0 \gamma c_p)} \cos\left(\frac{2\pi X}{L}\right) \cos\left(\frac{2\pi Y}{M}\right)$$

$$k_{H2} = \frac{k_1}{P_0}$$

$$k_{H3} = \frac{b_1 (2Bg)}{(P_I P_0 T_0 \gamma c_p)} \cos\left(\frac{2\pi X}{L}\right) \cos\left(\frac{2\pi Y}{M}\right)$$

$$A_H = \frac{k_H p_o^{(1-q_1)}}{b_1} + \frac{k_{H2} p_o^{(2-q_1)}}{(2a_1-b_1)} - \frac{(q_{12}-1)k_{H1} p_I^{q_{12}}}{b_1(q_{12}-q_1)} - \frac{(q_{12}-2)(k_{H2}+k_{H3}) p_I^{(q_{12}+1)}}{(2a_1-b_1)(q_{12}-q_1)}$$

$$+ \frac{p_o^{(q_{12}-q_1)}(q_1-1)k_{H1} p_I^{q_1}}{b_1(q_{12}-q_1)} + \frac{p_o^{(q_{12}-q_1)}(q_1-2)(k_{H2}+k_{H3}) p_I^{(q_1+1)}}{(2a_1-b_1)(q_{12}-q_1)}$$

$$C_H = \frac{k_{H1} p_o^{(1-q_1)}}{b_1} + \frac{k_{H2} p_o^{(2-q_1)}}{(2a_1-b_1)} + \frac{p_o^{(q_{12}-q_1)}(q_1-1)k_{H1} p_I^{q_1}}{b_1(q_{12}-q_1)}$$

$$+ \frac{p_o^{(q_{12}-q_1)}(q_1-2)(k_{H2}+k_{H3}) p_I^{(q_1+1)}}{(2a_1-b_1)(q_{12}-q_1)}$$

$$D_H = \frac{(1-q_1)k_{H1} p_I^{q_1}}{b_1(q_{12}-q_1)} + \frac{(2-q_1)(k_{H2}+k_{H3}) p_I^{(q_1+1)}}{(2a_1-b_1)(q_{12}-q_1)}$$

where $a_1 = \frac{f_o \lambda_o}{RT_o \gamma}$, $q_1 = .5 + .5\left(1 + 4(b_1/a_1)\right)$, $q_{12} = 1 - q_1$

Quantitative results for these solutions to the ω-equation will be shown in the next section.

4.3 Geopotential Tendency

In order to evaluate the geopotential height falls at 1000 mb associated with the heating-induced vertical motions found in the previous section, we may express the quasi-geostrophic vorticity equation as

$$\frac{\partial \zeta}{\partial t} = \lambda_0 \frac{\partial \omega}{\partial p} \tag{4.5}$$

By expressing the vorticity geostrophically as $\zeta = \nabla^2 \Phi / f_0$ (4.5) becomes

$$\nabla^2 \frac{\partial \bar{\Phi}}{\partial t} = f_0 \lambda_0 \frac{\partial \omega}{\partial p} \tag{4.6}$$

$\frac{\partial \omega}{\partial P}$ is obtained at 1000 mb by differentiating the solution (4.4a), and evaluating it at $P=P_0=1000$ mb. Assuming that $\frac{\partial \bar{\Phi}}{\partial t}$ has the same horizontal structure as the corresponding forcing function $f_0 \lambda_0 \frac{\partial \omega}{\partial p}$ (4.6) may be expressed as

$$\frac{\partial \bar{\Phi}}{\partial t} = -\frac{f_0 \lambda_0}{b_1} \frac{\partial \omega}{\partial p} \tag{4.7}$$

so that $$\chi_H = \hat{\chi}_H \cos\left(\frac{2\pi x}{L}\right)\cos\left(\frac{2\pi y}{M}\right) = \frac{\partial \hat{\Phi}(1000mb)}{\partial t}\cos\left(\frac{2\pi x}{L}\right)\cos\left(\frac{2\pi y}{M}\right)$$

and $$\hat{\chi}_H = \frac{-f_0\eta_0}{b_1}\left[\frac{\left[\left(\frac{p_I}{p_0}\right)^{q_1} - 1\right]k_{H_1}(1-q_1)}{b_1} + \frac{\left[(k_{H_2}+k_{H_3})p_I\left(\frac{p_I}{p_0}\right)^{q_1} - k_{H_2}p_0\right](2-q_1)}{(2a_1-b_1)}\right] \qquad (4.8)$$

Expression (4.8) indicates that $\hat{\chi}_H$ is dependent upon B (the vertical integral of the heating), P_I (the pressure level of the heating maximum), the vorticity-stability parameter $f_0\eta_0/T_0\gamma$, and the wavelengths L and M. $\hat{\chi}_H$ is linearly proportional to B. The calculations in this section will assume f_0=1. x 10^{-4} sec^{-1} (the Coriolis parameter at 45° latitude), T_0=250°K, and L=M.

Figure 4.2 shows $\hat{\chi}_H$ as a function of wavelength and P_I, for three values of vorticity-stability. For a typical static stability value of .06 (see Chapter 2), this would correspond to η_0 values of 1.5, 2.8, and 4.0 x 10^{-4} sec^{-1}. All of these calculations are for a B value of 21.9(m/sec) mb, corresponding to a 12-h heating-induced 1000-250 mb thickness increase of 500 m, or a mean column warming of 12.3°C/12 h, which is comparable to the lower-bound value of heating computed over the surface center for the 24-h period of explosive cyclogenesis discussed in Chapter 3. Greater height falls are noted as P_I increases, and also, as the wavelength increases. This dependence on P_I for lower tropospheric P_I's is

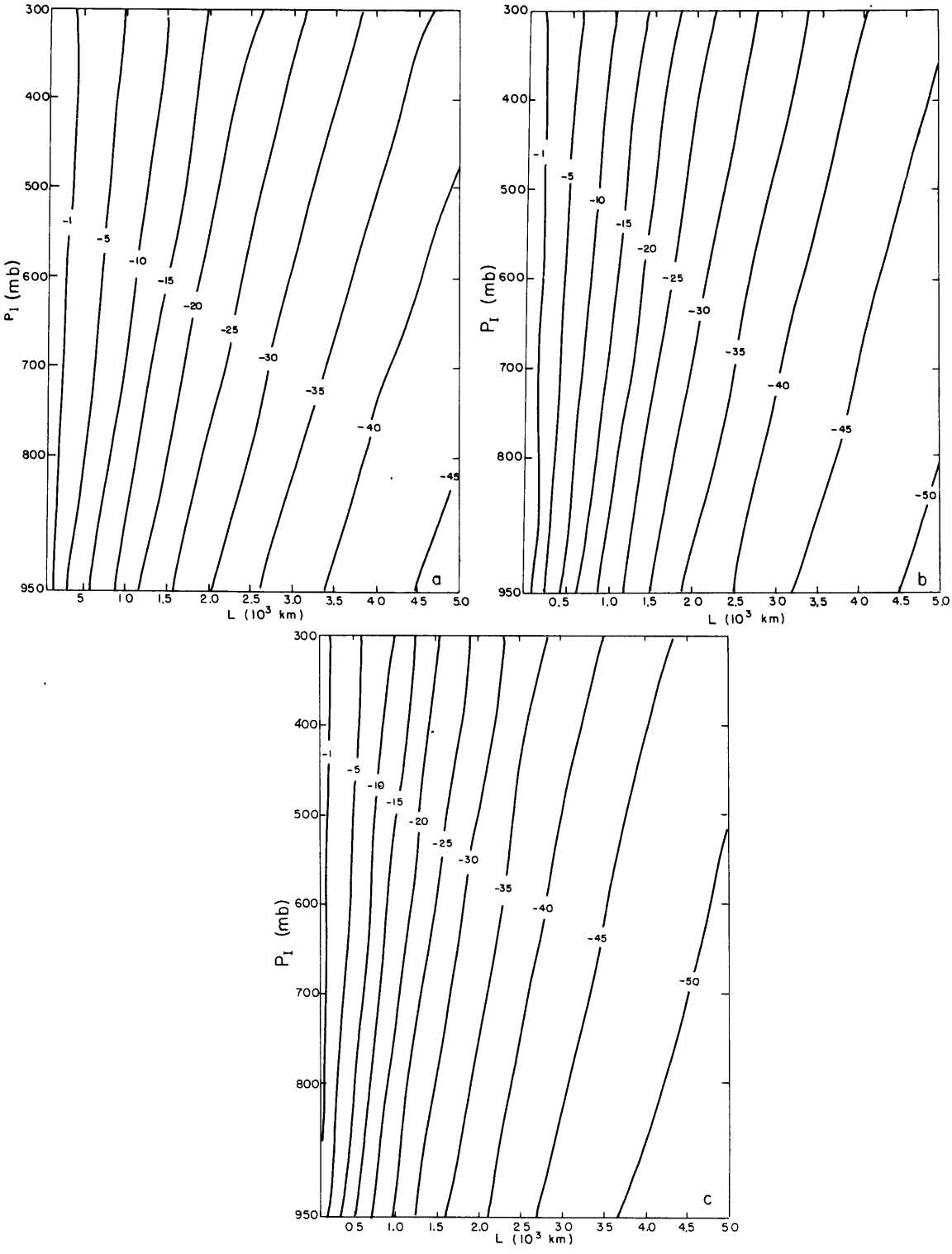


Fig. 4.2. Values of geopotential tendency $\hat{\chi}_H$ (units of 10^{-3} m^2 sec^{-3}) as a function of wavelength and peak level of heating, P_I. Values of vorticity-stability include (a) 1.0 x 10^{-9}, (b) 1.8 x 10^{-9}, and (c) 2.7 x 10^{-9} $sec^{-2} \cdot K^{-1}$.

particularly strong for the cyclone-scales (1000-2000 km). As the vorticity-stability parameter increases, the dependence of the largest disturbance growth rates on the vertical distribution of heating diminishes, while it remains strong for the cyclone-scale waves.

A fundamental question to ask, at this stage of the investigation is, what process(es) can organize these bulk heating effects? Clearly, the cyclone-scale is not seen as the preferred wavelength for deepening in Fig. 4.2. It appears plausible, from our previous analyses of the composite explosive cyclone and the QEII case, that baroclinic forcing, though quite weak itself, organizes the convective towers such that their bulk heating effects have a scale comparable to the cyclone itself. How can we write simultaneously of quasi-geostrophic baroclinic development and cumulus convection? After all, if the environment is gravitationally unstable on the cyclone-scale, the assumptions under which the quasi-geostrophic system of equations are derived become invalid. However, large-scale static instability does not appear to be a regular feature of the explosively developing extratropical cyclone, as is evidenced by Fig. 2.10, and by our calculations for the QEII case. Yet, we know that cumulus convection appears as a regular feature associated with these cyclones, and cumulus convection is generally associated with gravitational instability. Thus, we are arguing in favor of an environment that is statically stable for cyclone-scale motions, yet is gravitationally unstable for the micro- or cumulus-scale. Indeed, satellite images of the QEII case discussed in Chapter 3, and the large-scale conditionally unstable environment in

which it developed (see Fig. 3.29b), comparable images of the extraordinary cyclogenetic event on President's Day, 1979 (see Bosart, 1981), and Tracton's (1973) cases, all show a cyclone-scale environment that is unsaturated, yet associated with cumulus activity. This is precisely the basis for the CISK argument set forth by Charney and Eliassen (1964) in their study of the hurricane development problem. We now know from our Chapter 2 results that the bomb has comparably-strong deepening rates to some of the most explosively-developing tropical cyclones. We must now test this CISK-like hypothesis, as related to explosively-developing extratropical cyclogenesis.

Fig. 4.3 shows the geopotential tendency due to the divergence of $\omega_{11} + \omega_{12}$ for the quasi-geostrophic model described in Appendix 3.A. P_2 and P_3 are chosen to be 800 and 400 mb, respectively, to correspond to the computations performed for the QEII case at 12 GMT, 9 September. The vorticity-stability parameters correspond exactly to the three used in the corresponding computations for $\hat{\chi}_H$, found in Fig. 4.2. Note the maximum growth rates are found at wavelengths between 900 and 1200 km. This relatively short preferred wavelength is consistent with Staley and Gall's (1977) finding for disturbances forced by a shallow layer of baroclinicity. We find that, even though the observed scale of the perturbation corresponds approximately to the preferred scale of a baroclinic disturbance described in our model, the forcing vastly underestimates the instantaneous intensification of the surface cyclone, and that the vertical motions computed from this forcing similarly underestimate the "observed" ascent profile (compare Fig. 3.21a with Fig. 3.24b).

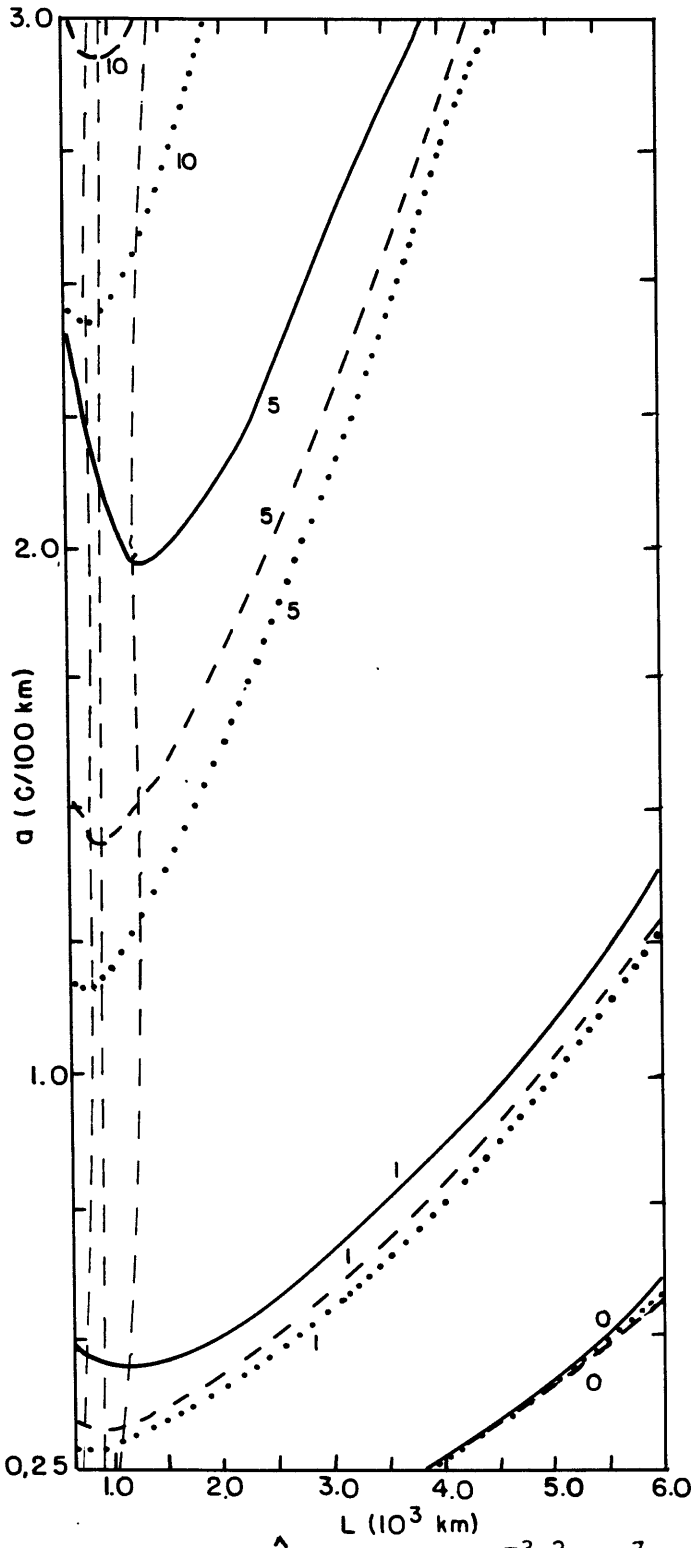


Fig. 4.3. Geopotential tendency $\hat{\chi}_1$ (units of $10^{-3} m^2 sec^{-3}$) as a function of wavelength and meridional temperature gradient, a, for $\hat{T}$=1° C. Vorticity-stability values are as in Fig. 4.2, and are indicated in their ascending magnitudes by solid, dashed, and dotted lines. The light dashed lines indicate the loci of the wavelength of maximum deepening rate.

We did, however, observe substantial diabatic warming in the column following the center during the 24-h period beginning 9 September 1978 at 12 GMT. As mentioned previously, the mean tropospheric temperature rise due to heating in the column probably ranged from 1000-1400 m/24 h during this 24-h period. We have computed vertical motions forced by our model heating distribution using the lower-bound value of integrated heating, and the parameters used in Chapter 3 for this time. Thus, the horizontal wavelength of the heating disturbance is assumed 1100 km in both the x and y directions, $\eta_0=1.3 \times 10^{-4}$ sec^{-1}, and $\gamma=.058$. Fig. 4.4 shows the vertical motion profiles according to expressions (4.4a) and (4.4b) for various values of P_I. We can see that, in spite of the same amount of heating in the column (corresponding to a rainfall rate of .32 cm/h, if all of this heating is the result of condensation), the manner in which this heating is distributed vertically has a profound effect on the vertical motion profiles it forces. Clearly, the lower the heating maximum, the lower the level of maximum ascent, and therefore, the stronger the convergence will be at 1000 mb. The resulting instantaneous central pressure falls, computed from expression (4.8), have been linearly extrapolated out to 12 h, and are also shown in Fig. 4.4b, as dashed lines. The dotted line indicates the observed central pressure of the cyclone at 12 GMT, 10 September. Consistent with the results of Fig. 4.2, and our ascent profiles, the choice of P_I has a profound effect on central pressure falls, with our numbers ranging from -18.8 mb/24 h for P_I=900 mb to -6.3 mb/24 h for P_I=300 mb.

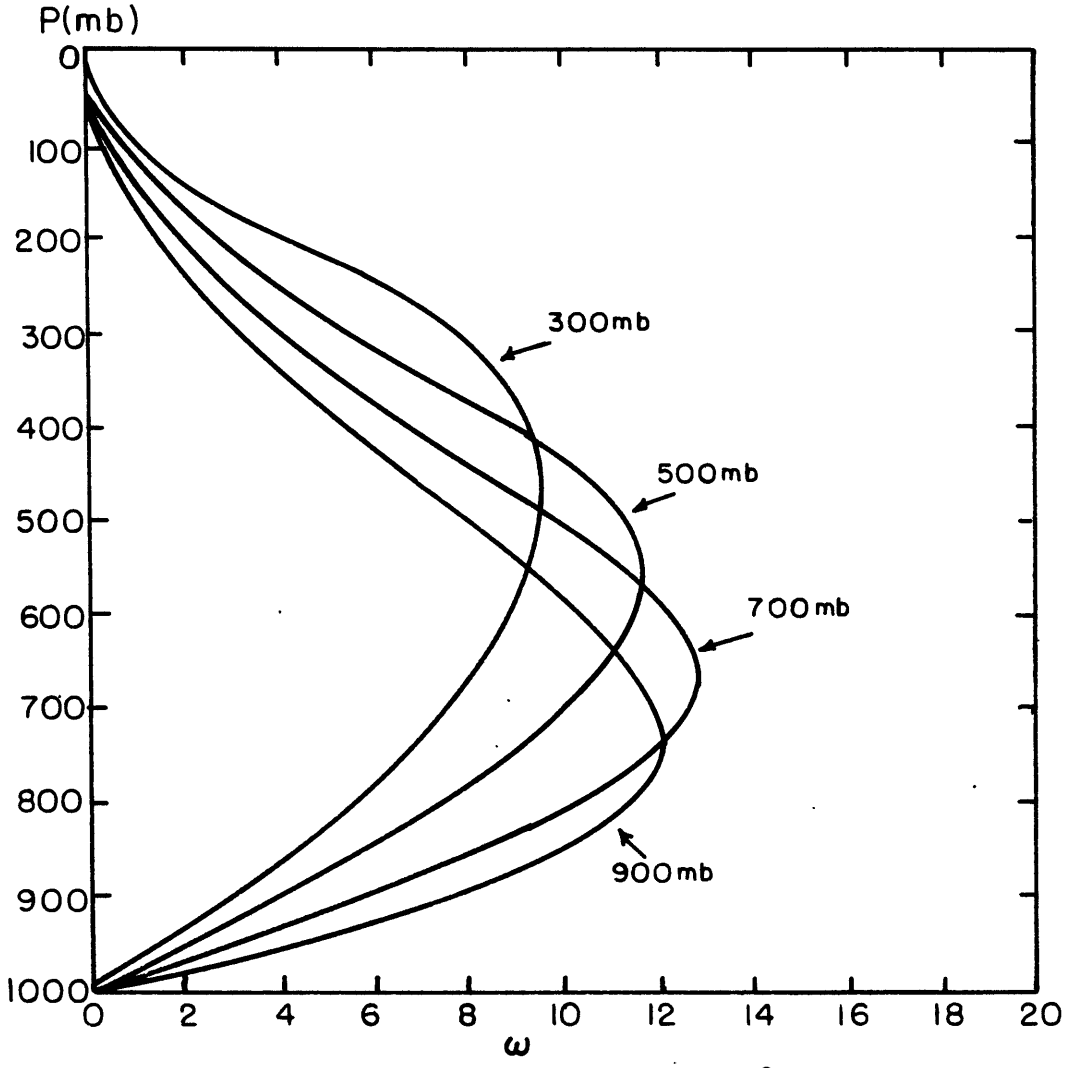


Fig. 4.4a. Heating-induced vertical motion (units of 10^{-3}mb/sec) profiles for the QE II case at 12 GMT, 9 September 1978, for the indicated values of P_I, and for B=21.9 (m/sec)mb.

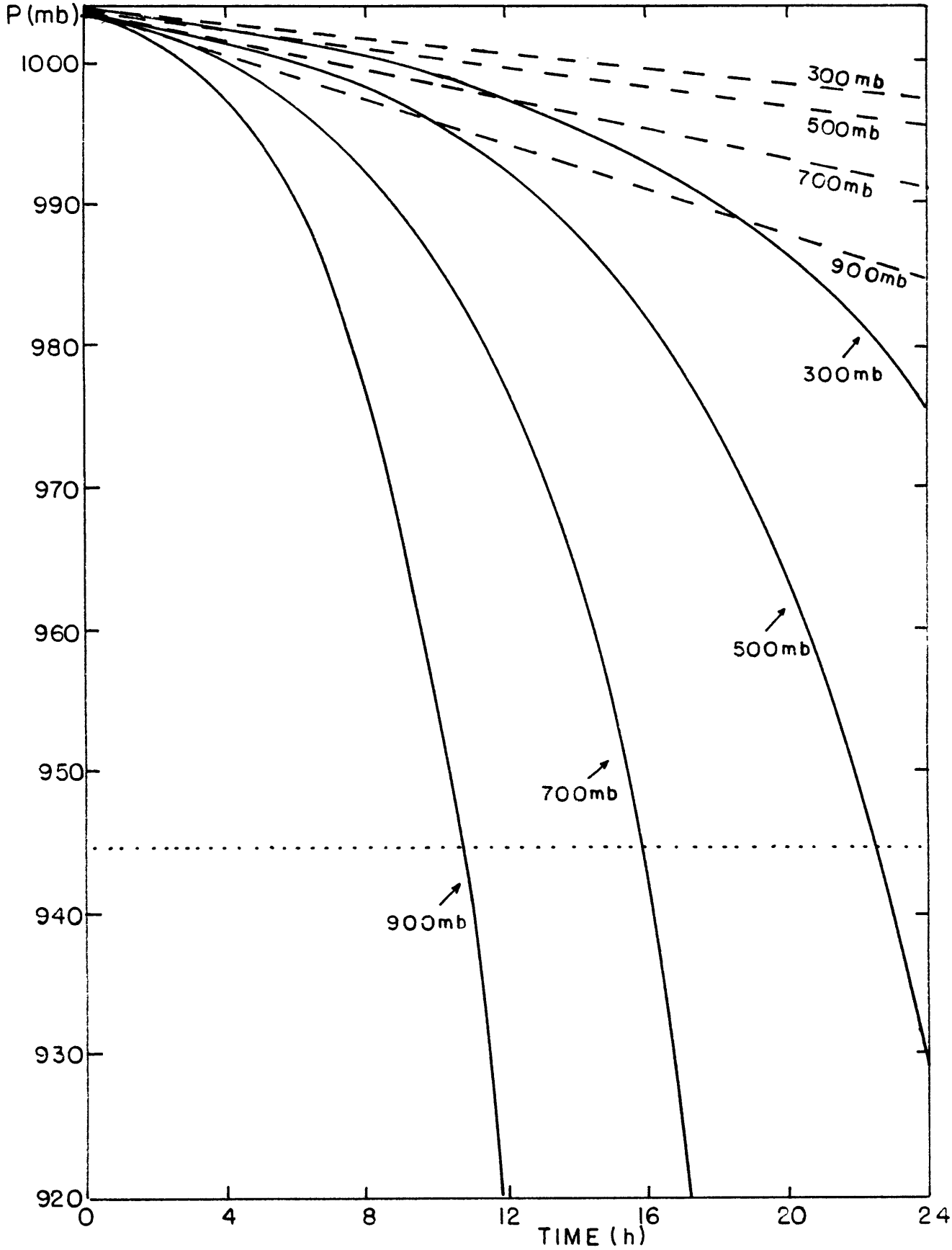


Fig. 4.4b. Theoretical linear and non-linear pressure traces as a function of time, and beginning at 12 GMT, 9 September for the same parameters as in (a), and for the indicated P_I values.

The extrapolation of the instantaneous value of $\eta_0 \frac{\partial \omega}{\partial p}$ (see Equation 4.5) out for such long time periods as 24 h is highly inaccurate, for the time rate of change of relative vorticity is itself a function of the relative vorticity. Thus, if we now express (4.5) as

$$\frac{\partial \ln \eta}{\partial t} = \frac{\partial \omega}{\partial p} \tag{4.9}$$

η will grow exponentially with time for a constant $\frac{\partial \omega}{\partial p}$. We can then compute the geopotential falls by expressing the vorticity geostrophically as we did earlier in this section. Thus,

$$\eta_{\text{geostrophic}}(t) = \eta_{\text{geostrophic initial}} \exp\left(\frac{\partial \omega}{\partial p} t\right) \tag{4.10}$$

Although this procedure is a vast improvement over our previous assumption of a constant value of $\eta_0 \frac{\partial \omega}{\partial p}$ with time, there are still two reasons why our method will still underestimate the actual central pressure fall due to this inviscid forcing. The first is $\frac{\partial \omega}{\partial p}$ itself a function of time, and generally increases with time in an intensifying cyclone. Next, the forcing expressed on the right side of (4.9) shows the logarithmic time rate of change of vorticity, with the winds more likely to be in gradient balance, rather than geostrophic balance. Thus, for a given amount of divergence, a greater height fall would be diagnosed under gradient balance conditions, than would be shown with the

assumption of geostrophic balance. With these caveats in mind, we shall proceed with our calculations.

Fig. 4.4b shows the central pressure changing with time (solid lines) according to (4.10). The sensitivity of the 24-h pressure fall to the choice of P_I is even more pronounced with this computation than it was with the assumption of a linear change of pressure with time. It appears the exponential heating-forced deepening rates easily account for the observed 24-h intensification, for choices of P_I below the 500-mb level. The heating profiles with peaks above the 500-mb level still fall a bit short of the observed deepening. The upper-bound estimate of heating forcing a 1400 m/24 h warming of the column has been used to construct Fig. 4.5. The other parameters used in this computation are precisely the same as those used for Fig. 4.4. The vertical motions are exactly 1.4 times those found in Fig. 4.4, for a given P_I and P, and thus, are not shown. The linear central pressure falls are also increased by a factor of 1.4, but the pressure traces using (4.10) are vastly changed for this 24 h of integration, with P_I's below the 300-mb level, more than accounting for the observed 24-h central pressure fall. Of course, these calculations do not take into account surface frictional dissipation, so we should expect an overestimate of the central pressure fall. If, indeed, the heating is distributed horizontally so as to reach a maximum at the surface low center, we see from our calculations a positive feedback from the cyclone scale to the convective scale, not unlike a CISK process. Here, the cyclone-scale perturbation in the baroclinic westerlies

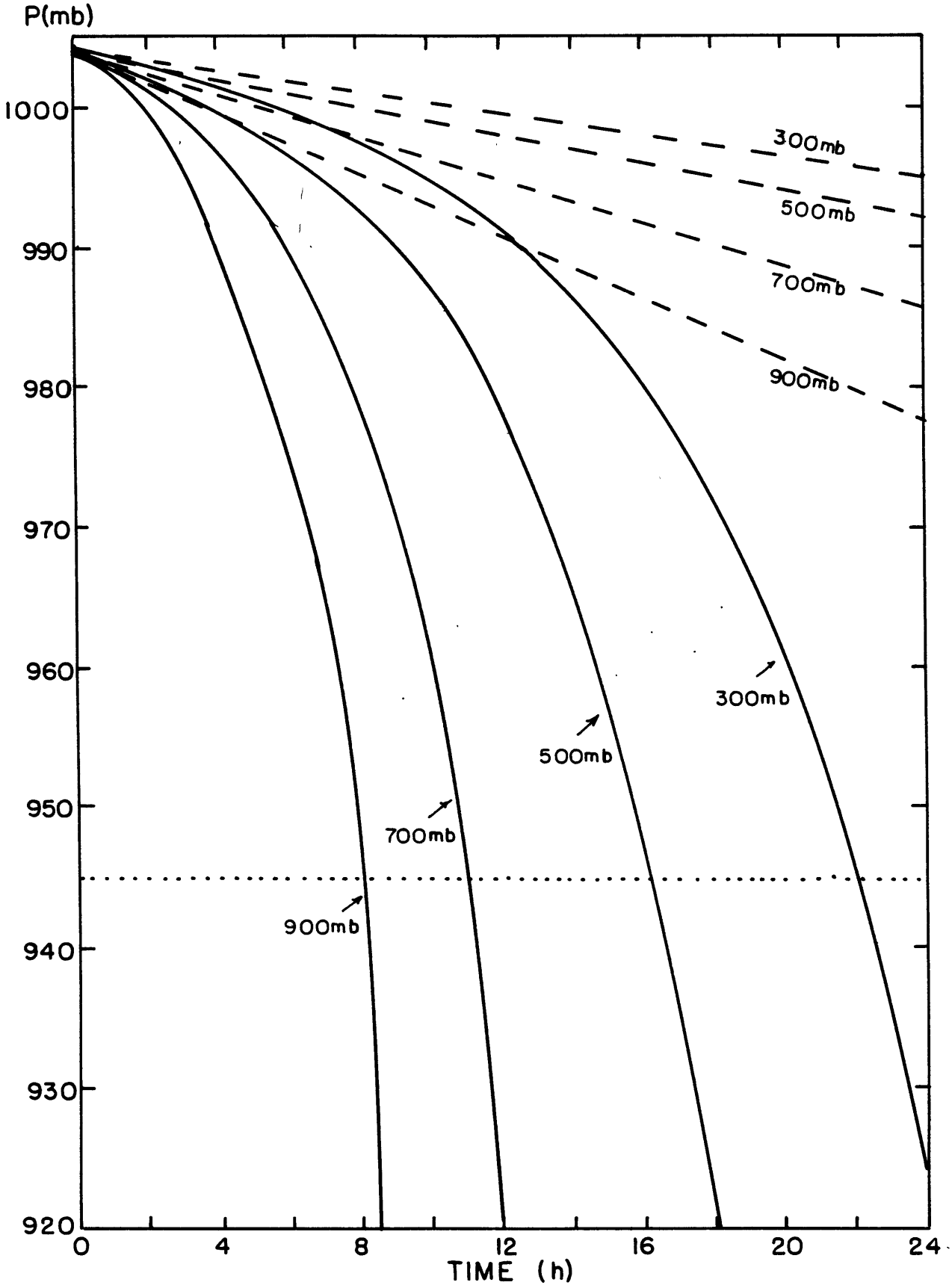


Fig. 4.5. As in Fig. 4.4b, except for B=30.7 (m/sec)mb.

apparently helps to organize the convection in such a way as to effect the bulk heating distribution, which in turn, provides a powerful dynamic intensification mechanism for the cyclone scale. This cyclone-scale intensification helps to converge more moisture into its center, thus helping the convection to maintain itself.

Of course, there is still the additional positive effect of baroclinic forcing pointed to earlier. This relatively weak forcing found at 12 GMT, 9 September (see Table 3.2) has been extrapolated linearly and exponentially forward 24 h, and is shown via such a format in Fig. 4.6. Although we have found this forcing to be relatively weak, when it is combined with various hypothesized three-dimensional heating distributions, our quasi-geostrophic calculations show explosive development for virtually all sets of reasonable heating profiles.

We also performed an independent check on consistency between our quasi-geostrophic surface convergences, with the implicit vertical motions used for the adiabatic cooling computations in column (4) of Table 3.5. The 24-h time mean surface convergence implied by the expression (3.17) for these thickness-change computations is about 7×10^{-5} sec^{-1}. Note this implicit vertical motion would include both the diabatically-forced and baroclinic components of omega, although there is no representation of the component of ascent due to surface frictional convergence. Thus, it would be satisfying to know that this implied "observed" convergence would be comparable to the sum of our theoretical baroclinic and diabatic surface convergences. Our 1000-mb convergence implied by the computations shown in Fig. 4.6 is 2.9×10^{-5} sec^{-1}, and the range of 1000-mb convergences implied by

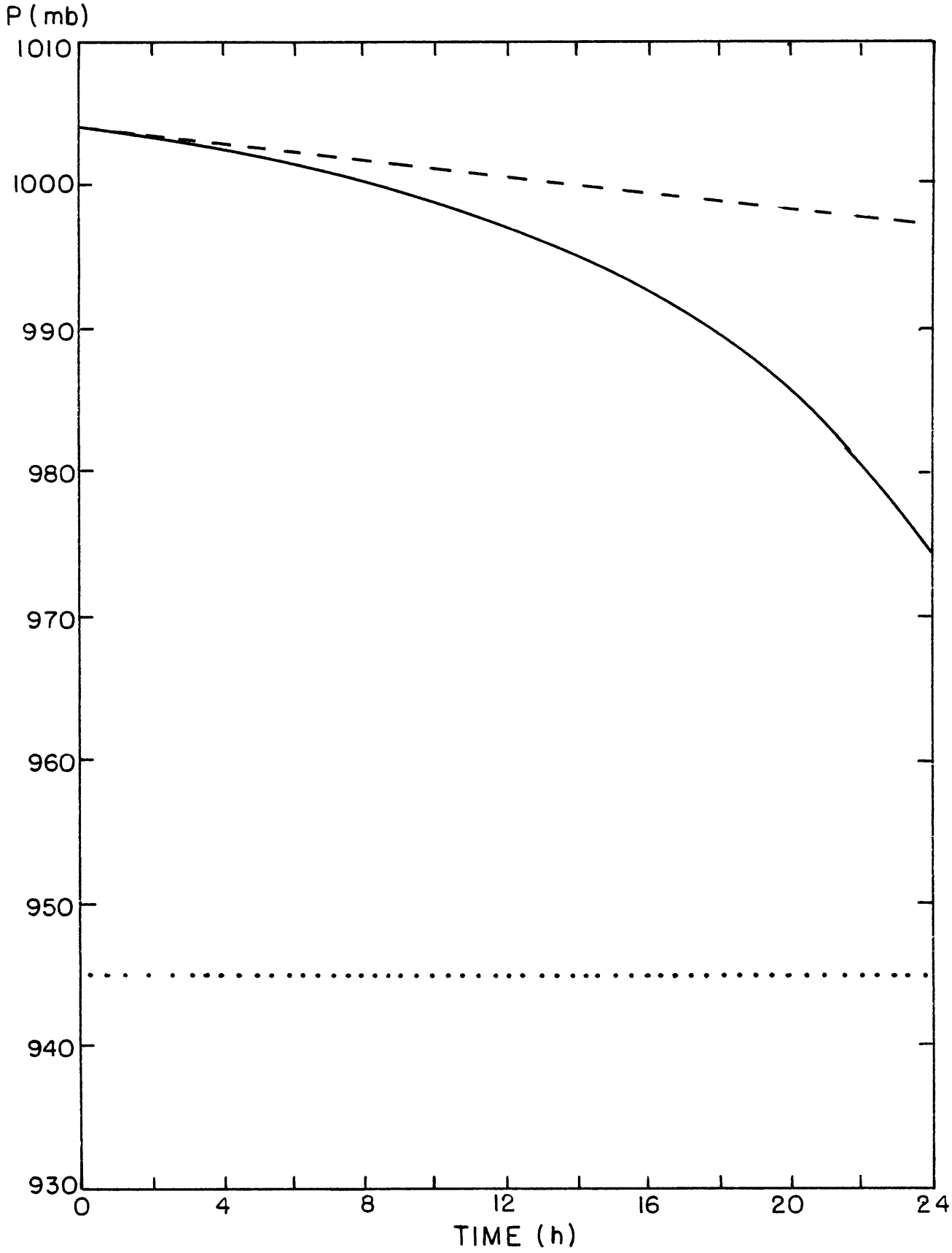


Fig. 4.6. Theoretical linear (dashed line) and non-linear (solid line) pressure traces as a function of time, and beginning at 12 GMT, 9 September, for the baroclinic forcing parameters indicated in Table 3.2.

the results of Figs. 4.4b and 4.5 includes 2.9×10^{-5} sec^{-1} for P_I=300 mb, and B=21.9 (m/sec)mb to 12×10^{-5} sec^{-1} for P_I=900 mb, and B=30.7 (m/sec)mb. Thus, while the component of vertical motion due to baroclinic forcing implied in Fig. 4.6 is insufficient to account for the observed divergence, the addition of the diabatically-forced surface convergence will allow the sum of these two convergences to account for the "observed" convergence implied by Table 3.5.

Thus, our observations of the explosive intensification of the QEII storm, concurrent with the development of its strong warm core, are all consistent with our quasi-geostrophic calculations, which incorporate both diabatic and baroclinic forcing. These calculations show similarly explosive development, using the observed vertically-integrated values of heating, throughout much of the spectrum of uncertainty of our measurements. Thus, while adiabatic, inviscid, quasi-geostrophic dynamics are unable to explain the observed explosive intensification, the total amount of heating observed for the column can be modeled quasi-geostrophically, and will simulate the observed rapid cyclogenesis found in the QEII case. Evidently, this kind of CISK mechanism is also operative in the tropical cyclone, another phenomenon which exhibits the extremely large growth rates found in explosive extratropical cyclogenesis.

CHAPTER 5

CONCLUSIONS AND SUGGESTIONS FOR FUTURE WORK

The explosively-developing extratropical cyclone, as defined in Chapter 2, is primarily a maritime, cold-season phenomenon. These cyclones are often associated with hurricane-force winds, and cloud patterns not unlike that of the tropical cyclone. The growth rates associated with this class of storm are comparable to the extraordinary intensifications frequently found in tropical cyclones (see Holliday and Thompson, 1979).

Operational numerical weather prediction models at NMC, and at FNOC almost invariably fall far short in attempting to predict this observed explosive cyclogenesis. We find the coarse mesh length is not the sole reason for the failure, as a halving of the horizontal computational mesh length produces only a small improvement in model performance concerning this phenomenon at NMC. Aside from the "bomb" posing a grave threat to shipping interests, because of the sudden and generally surprising ferocity with which this event strikes, it may be an important component in a realistic numerical model simulation of the general circulation. We found the vast majority of the Northern Hemisphere's deepest cyclones have reached their strong intensities through the explosive deepening process defined in this thesis. This suggests that the operational model deficiencies enumerated in this dissertation, and also present in other primitive-equation models used for general circulation simulations (see Druyan, 1974), may have serious implications for these climatological studies.

Furthermore, there is the potential problem of verifying these operational forecasts and climate simulations. We pointed out that operational real-time analyses almost always err on the side of conservatism in the central pressure estimates of these cyclones.

The effect of this error is to overestimate the quality of the operational model performance in simulating this explosive cyclogenesis. We have already established this inflated performance record to be a poor one. Another problem stemming from our ignorance of the precise location and intensity of many of these storms is in the verification of climate simulations, and in "observational" studies which utilize such sources as the NMC data files. In particular, our results suggest that the importance of transient eddy fluxes of heat and momentum in the explosive cyclogenetic regions may be substantially greater than is shown in the NMC coarse-mesh analyses. The problem is not one of having too few points in the grid, but rather one of having too few observations. Relatively fine-mesh grid analyses offer no benefit over coarse grids when the data are spaced too coarsely. Better use of existing ship reports is needed, for not all of these data are successfully incorporated into the NMC analysis cycle. Evidence for this statement comes from the fact that the *Euroliner* report, available in real time on the service "C" teletype at 12 GMT, 10 September 1978, was not incorporated into the NMC analysis. Further, work should be performed to utilize a system similar to that of the Seasat-A instrumentation package for the NMC data collection system. We found this Seasat data to have been crucial in helping to estimate

the location and intensity of the surface vorticity center for both times at 12 GMT on 9 and 10 September. This system will likely prove to be a major factor in improving upon the existing observational network in the maritime areas, the locations of which are important centers for the Northern Hemisphere's major cyclones.

Although the coverage of commercial aircraft winds, occasionally supplemented by satellite cloud-top winds, at approximately 250 mb over the maritime areas is quite extensive, as was shown in Chapter 3, documentation of the rest of the troposphere's thermodynamic and dynamic structure remains a problem. The trend in recent years has been to phase out the weather ships operating in the North Atlantic and in the North Pacific oceans. Progress with incorporating satellite temperature retrievals successfully into NMC's analysis and forecast system has been judged to be slow by some (see, for example, Traction et al., 1980). While Phillips (1979) has presented evidence of reliable microwave temperature retrievals from the TIROS-N polar orbiting satellite, he also has indicated these retrievals to be unacceptable in regions where at least moderate precipitation is occurring. More effort should be expended to develop a reliable system of retrieving temperature, humidity, and wind information throughout the troposphere in extratropical maritime areas. If the satellite information does not provide a solution now, the weather ships should be redeployed until a comparable alternative is produced.

Although we find the bomb generally occurs in a baroclinic atmosphere, the strength of this baroclinic forcing in our composite case was found to be far too weak to account for the observed explosive development. Furthermore, there appears to be no minimum SST over which the explosive cyclone forms, unlike the tropical cyclone. However, the bomb does occur in the vicinity of the strongest SST gradients. A notable exception to this rule is in the North Pacific ocean east of the dateline, where a pronounced maximum of bomb activity exists, and where the SST gradient magnitudes are relatively small.

A detailed examination of the explosive cyclone which damaged the liner *Queen Elizabeth II* has been accomplished with the aid of an unusually large and timely data base. The storm originated as a shallow baroclinic disturbance in the middle Atlantic states, propagated offshore, and subsequently intensified 60 mb in 24 h, during which time deep cumulus convection was observed in and around the storm center. Hurricane-force winds, a deep tropospheric warm core, and a clear eye in the storm center were all observed in this cyclone at 12 GMT on 10 September. The maximum growth rate associated with this cyclone was greater than those found in the majority of Pacific typhoons (see Holliday and Thompson, 1979).

In order to assess the amount of baroclinic forcing operational in this extremely well-documented case, we have solved analytically the non-linear quasi-geostrophic omega and vorticity equations for an idealized thermodynamic structure which can resolve baroclinic waves as shallow or as deep as we choose. We were able to observe

magnitudes are relatively small. The importance of strong SST gradients involves the implication of maritime areas with strong low-level baroclinicity, and with a susceptibility to a dramatic air-mass modification of the cold continental air flowing out over a relatively warm sea surface. We have shown this low-level baroclinic forcing to be important in the initial development and organization of the QEII case. Although the surface fluxes of sensible and latent heat do act to statically destabilize, and to add water vapor to the system, their direct dynamical effects on the evolution of the bomb appear to be small.

A detailed examination of the explosive cyclone which damaged the liner *Queen Elizabeth II* has been accomplished with the aid of an unusually large and timely data base. The storm originated as a shallow baroclinic disturbance in the middle Atlantic states, propagated offshore, and subsequently intensified 60 mb in 24 h, during which time deep cumulus convection was observed in and around the storm center. Hurricane-force winds, a deep tropospheric warm core, and a clear eye in the storm center were all observed in this cyclone at 12 GMT on 10 September. The maximum growth rate associated with this cyclone was greater than those found in the majority of Pacific typhoons (see Holliday and Thompson, 1979).

In order to assess the amount of baroclinic forcing operational in this extremely well-documented case, we have solved diagnostically the non-linear quasi-geostrophic omega and vorticity equations for an idealized thermodynamic structure which can resolve baroclinic waves as shallow or as deep as we choose. We were able to observe

relatively shallow cyclogenetic forcing (in the 1000-850 mb layer) for this case, which would not have been observed had we examined only the baroclinic forcing taking place as seen in the 1000-250 mb thickness analysis. Nevertheless, instantaneous vertical motions and deepening rates computed from this adiabatic and inviscid quasi-geostrophic model fall far short of those which were observed.

In order to assess the importance heating had on this cyclone's development, we have devised a method of evaluating the three-dimensional thermodynamic and dynamic structure of this cyclone, so as to evaluate potential vorticity changes in the vicinity of the storm. Our results indicate a 24-h lower tropospheric generation of from five to thirteen times the values observed at the initial time. Although we are unsure of the role "cumulus friction" played in this generation, if any, our calculations have demonstrated a large mean tropospheric temperature rise in the column following the storm center to be due to bulk heating effects of the cumulus convection observed within this storm system. This implicates these heating effects as being a significant factor in the extraordinary potential vorticity generation concurrent with this case's explosive development.

We have utilized these observed vertically-integrated values of heating as a motivation for finding analytic solutions to the non-linear quasi-geostrophic omega equation forced by an idealized heating function, with specified horizontal scale, level of maximum heating, P_I, and total heating. The resulting heating-forced solutions to the quasi-geostrophic vorticity equation have been found. The theoretical geopotential falls

calculated from the vorticity equation over a 24-h period for the observed integrated values of heating, observed values of vorticity-stability, and over a wide range of horizontal scales and levels of heating peaks easily account for and surpass the large observed geopotential falls. A particularly large sensitivity of growth rate to P_I was noted. This provides theoretical support for the numerical results of Yamasaki (1968), Ooyama (1969), and Anthes and Keyser (1979), all of whom found such a sensitivity in their simulations of both extratropical and tropical disturbances associated with cumulus convection.

We found the largest growth rates due to this heating function are found for the lowest levels of heating maximum. The reason for this is obvious, for the level of maximum forced ascent is lowered under these conditions, thereby producing a larger value of convergence at the surface. We find observational evidence that relatively low levels of heating <u>did</u>, in fact, occur in the QEII case. This includes the following: in spite of a strong tropospheric warm core observed in the disturbance (Fig. 3.11b), a comparably large temperature perturbation is not observed at 250 mb (Fig. 3.25c), and aircraft temperatures recorded at middle tropospheric levels indicate the soundings over the center with the lowest level warm temperature perturbations to be the most realistic (Fig. 3.27b). More cases need to be documented in a manner similar to that performed for the QEII case to verify that such conclusions hold more generally.

We may also infer from the analysis in Chapter 4 that, for a given divergence, as the cyclonic vortex of a bomb spins up in the

computed (and observed) explosive fashion, it likely reaches an equilibration with surface frictional dissipation on a time scale less than 24 h, and thus terminates its intensification long before the cold trough aloft has a chance to overtake the surface center. This latter process is commonly called occlusion, and is generally regarded in the Norwegian cyclone model (see, for example, p. 217 of Petterssen, 1956) as signaling the termination of cyclone intensification, which has occurred gradually over a period of several days. Our analysis of the QEII case indicates the cyclone has terminated its intensification by 12 GMT, 10 September -- long before the cold trough has a chance to overtake the surface center (see Fig. 3.11b). In fact, the thermal trough-ridge pattern, with the exception of the small-scale thermal ridge over the surface center, indicates much more cyclogenetic quasi-geostrophic forcing taking place over the surface center than was analyzed for any of the prior three times. It is quite probable this forcing (along with any positive diabatic forcing, which may be occurring) has been at least offset by the surface frictional dissipation at this time. The extremely rapid development of so many maritime cyclones indicates this equilibration process may be even more widespread. The surface shearing stress, commonly parameterized as proportional to the square of the wind speed, clearly explodes as the bomb does. It certainly seems unlikely that the upper-level cold trough could overtake the surface cyclone on so short a time scale. Further work is needed to determine the general validity of this hypothesis.

Thus, we have established both observationally and theoretically

the critical importance cumulus-induced heating effects may have in determining whether a cyclone explosively intensifies or not. Although the CISK mechanism is certainly a plausible means by which explosive cyclogenesis is accomplished in both hurricanes and in bombs, there remains the problem of successfully predicting or simulating the effects of cumulus convection on larger-scale circulation features, such as the cyclones we have studied. There are several cumulus schemes currently in use. The moist convective adjustment scheme (Manabe et al., 1965), is used in the Geophysical Fluid Dynamics Laboratory (GFDL) primitive-equation model, and in the National Center for Atmospheric Research (NCAR) model (Kasahara and Washington, 1971). A modification of the scheme devised by Kuo (1965) is currently in use at NMC. The Arakawa (1968) cumulus parameterization is used in the FNOC PE model (Kesel and Winninghoff, 1972), and in the GISS model (Somerville et al., 1974). A version of the Arakawa and Schubert (1974) cumulus scheme will be incorporated into the U.S. Navy's new global P.E. model. If, in fact, explosively-developing cyclones regularly occur as a primary result of the bulk thermodynamic effects of cumulus convection, as we have found in our analysis of the QEII case, and for which we have indirect evidence in our large sample of cases, the performance of the above schemes becomes much more critical for the extratropics than was previously realized. It is not sufficient to simply test precipitation forecasts generated by these convective schemes, as has been done by Krishnamurti et al. (1980). Work should be performed to assess the performance of the various cumulus schemes, particularly in the

extratropics, in predicting the vertical distributions of thermodynamic changes due to the cumulus. Unfortunately, Lord (1978) has found this prediction to be one of the major deficiencies of the Arakawa and Schubert (1974) parameterization, in spite of success being reported with predicting the vertically-averaged cumulus effects. Furthermore, the issue of whether the effects of cumulus on the larger-scale can in fact, be expressed in terms of the larger-scale variables should be re-examined. If this is not the case, then cumulus parameterization is not possible. Implicit in all cumulus schemes is the assumption of a separation of time scales between the large-scale processes, and those of the cloud scale. The preponderance of mesoscale convective complexes, similar to those described by Maddox (1980), in middle-latitude and tropical regions, and their oft-observed association with tropical cyclones (Weickmann et al., 1977) whose influence on the general circulation may be quite significant (see Frank, 1977b), flash floods and subsequent explosive cyclogenetic development (Bosart and Sanders, 1981), and indeed with the QEII storm, provide even more motivation to examine the possible mutual interaction between the cloud-scale, mesoscale, and synoptic-scale motions.

APPENDIX 3.A

The quasi-geostrophic ω-equation may be expressed as

$$\left(\nabla^2 + \frac{f_0 \eta_0}{6}\frac{\partial^2}{\partial p^2}\right)\omega = \frac{f_0}{6}\frac{\partial}{\partial p}\left(\underset{\sim}{V}\cdot\nabla\eta\right) - \frac{1}{6}\nabla^2\left(\underset{\sim}{V}\cdot\nabla\frac{\partial\Phi}{\partial p}\right) \tag{A.1}$$

where ∇^2 represents the horizontal Laplacian operator, 6 is $6(P) = \frac{\partial\Phi}{\partial p}\left(\frac{\partial \ln\theta}{\partial p}\right)$, and the rest of the variables are as defined in the text. We will assume the first layer (from $P=P_0$ to $P=P_2$) temperature structure to be of the form

$$T(x,y,p) = T_m(p) - \left(ay + \hat{T}\cos\left(\frac{2\pi}{L}x\right)\cos\left(\frac{2\pi}{L}y\right)\right), \quad P_2 \le P \le P_0 \tag{A.2}$$

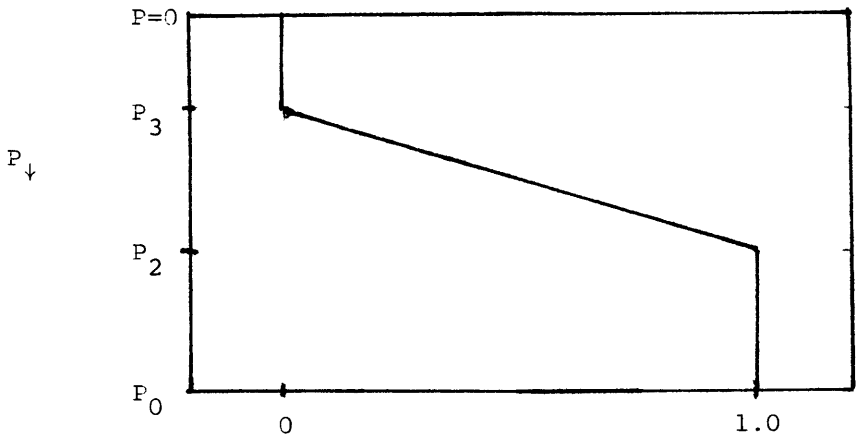
where the x and y axes are directed eastward and northward, respectively; a is the meridional temperature gradient, and $\hat{T}$ represents the amplitude of the two-dimensional harmonic temperature variation. There is no vertical variation of the horizontal temperature gradient in this layer. Now let us assume this horizontal gradient decreases linearly with pressure in the second layer, so that

$$T(x,y,p) = T_m(p) - \frac{(p-p_3)}{(p_2-p_3)}\left(ay + \hat{T}\cos\left(\frac{2\pi}{L}x\right)\cos\left(\frac{2\pi}{L}y\right)\right), \quad p_3 \le p \le p_2 \tag{A.3}$$

and for the pressure levels above and equal to $P=P_3$, the atmosphere is assumed barotropic:

$$T(x,y,p) = T_m(p), \qquad 0 \leq p \leq p_3 \tag{A.4}$$

where T_m is the mean temperature on a constant pressure surface. The lack of specification of the observed stratospheric horizontal temperature gradients (generally directed in the opposite direction to those found in the troposphere) is due to our concern with shallow baroclinic waves whose development probably has little to do with stratospheric dynamics. The vertical structure of the horizontal temperature gradients is shown in Fig. A.1:



The definitions of θ and σ, and the hydrostatic relation yield $\frac{\partial \ln \theta}{\partial p} = \left(\frac{\partial \ln T_m}{\partial p} - \frac{\kappa}{p}\right)$ and $\sigma = \left(\frac{\kappa}{p} - \frac{\partial \ln T_m}{\partial p}\right)\frac{RT_m}{p}$ with $\kappa = R/C_p$. Another static stability parameter $\gamma = \kappa - \frac{\partial \ln T_m}{\partial \ln p}$ is defined so that $\gamma = \kappa$ and $\gamma = 0$ correspond to isothermal and dry adiabatic lapse rates, respectively. This definition represents static stability referred to the dry adiabat, and may be generalized to take into account moist processes by defining γ as $\gamma = \left(\frac{d \ln T}{d \ln p}\right)_{\text{adiabatic}} - \left(\frac{\partial \ln T_m}{\partial \ln p}\right)$. With T_0 specified as a constant value of T_m, where it appears as a coefficient in the expression for σ, and γ assumed independent of pressure, the expression for σ becomes

$$\sigma(p) = RT_0\gamma/p^2 \tag{A.5}$$

We will assume the simple distribution of geopotential at $P=P_0=1000$ mb, which is given by

$$\Phi(x,y,p_0) = \hat{\Phi}_{10} \cos\frac{2\pi}{L}(x+\lambda)\cos\frac{2\pi}{L}y \tag{A.6}$$

where λ is the phase lag of the 1000 mb geopotential field relative to the temperature field. It is measured westward from the mean perturbation center to the 1000-mb low center. So, $\lambda = 0$ corresponds to a system of warm lows and cold highs, and $\lambda = L/2$ represents cold lows

and warm highs. The geopotential field may be found by hydrostatic integration, and for the first layer is

$$\Phi(x,y,p) = \Phi(x,y,p_0) + \int_{p_0}^{p} \frac{\partial \Phi}{\partial p}(x,y,p)\,dp$$

$$= \hat{\Phi}_{10}\cos\frac{2\pi}{L}(x+\lambda)\cos\frac{2\pi}{L}y + \Phi_m(p) - \left[R\ln\frac{p_0}{p}\left(ay + \hat{T}\cos\frac{2\pi}{L}x\cos\frac{2\pi}{L}y\right)\right] \tag{A.7}$$

where $\Phi_m(p) = \int_p^{p_0} RT_m(p)\,d\ln p$. If we represent the horizontal velocity, $\underset{\sim}{v}$, geostrophically as $\underset{\sim}{v} = \frac{1}{f_0}\left[-\frac{\partial \Phi}{\partial y}\underset{\sim}{i} + \frac{\partial \Phi}{\partial x}\underset{\sim}{j}\right]$, and the vertical component of the absolute vorticity by $\eta = \frac{\nabla^2\Phi}{f_0} + f$ then using the above relationships, and the definition of $\sigma(P)$ and $\Phi(x,y,P)$, the ω-equation (A.1) becomes for the first layer

$$\left(\nabla^2 + \frac{f_0^2}{RT_0\sigma}\frac{p^2\partial^2}{\partial p^2}\right)\omega = \left[\left(\frac{2\pi}{L}\right)^3\frac{Ra\hat{T}}{T_0\sigma}\left(\frac{4}{f_0}\right)p\ln\left(\frac{p_0}{p}\right) - \frac{2\pi\hat{T}}{L\,T_0\sigma}\left(\frac{\partial f}{\partial y}\right)_0 p\right]$$

$$\times \sin\frac{2\pi}{L}x\cos\frac{2\pi}{L}y - \left[\frac{4}{f_0}\left(\frac{2\pi}{L}\right)^3\frac{\hat{\Phi}_{10}}{\gamma T_0}\,dp\right]\sin\frac{2\pi}{L}(x+\lambda)\cos\frac{2\pi}{L}y$$

$$+\left[\frac{2}{f_0}\left(\frac{2\pi}{L}\right)^4\frac{\hat{\Phi}_{10}\hat{T}}{T_0\sigma}\sin\left(\frac{2\pi\lambda}{L}\right)p\right]\sin\frac{4\pi}{L}y \tag{A.8}$$

Similarly, the ω-equation for the second layer, $P_3 \leq P \leq P_2$, is

$$\left(\nabla^2 + \frac{f_0 \eta_0 p^2}{RT_0\gamma}\frac{\partial^2}{\partial p^2}\right)\omega = \left\{\frac{4Ra\hat{T}\ln\left(\frac{p_2}{p_3}\right)}{f_0(p_2-p_3)T_0\gamma}\left(\frac{2\pi}{L}\right)^3\left(p^2 - pp_3\right)\right.$$

$$+\frac{4Rp_3^2 a\hat{T}}{f_0(p_2-p_3)^2 T_0\gamma}\left(\frac{2\pi}{L}\right)^3 p\left(\ln\frac{p_2}{p}\right) + \frac{4Rp_3 a\hat{T}}{f_0(p_2-p_3)^2\gamma T_0}\left(\frac{2\pi}{L}\right)^3\left(-pp_2 - p^2\ln\frac{p_2}{p} + p^2\right)$$

$$\left.+\frac{4R}{f_0\gamma T_0}\frac{\left(p^2p_2 - p_3\right)}{(p_2-p_3)^2}a\hat{T}\left(\frac{2\pi}{L}\right)^3 - \frac{\hat{T}p(p-p_3)}{T_0\gamma(p_2-p_3)}\left(\frac{2\pi}{L}\right)\frac{\partial f}{\partial y}\right\}\sin\frac{2\pi}{L}x\cos\frac{2\pi}{L}y$$

$$-\left[\frac{4a\hat{\Phi}_{10}p(p-p_3)}{(p_2-p_3)f_0T_0\gamma}\left(\frac{2\pi}{L}\right)^3\right]\sin\frac{2\pi}{L}(x+\lambda)\cos\frac{2\pi}{L}y$$

$$+\left[2\left(\frac{2\pi}{L}\right)^4\frac{\hat{T}\hat{\Phi}_{10}p(p-p_3)}{f_0T_0\gamma(p_2-p_3)}\right]\sin\frac{2\pi}{L}\lambda\sin\frac{4\pi}{L}y \qquad \text{(A.9)}$$

The ω-equation for the third layer, $0 \leq P \leq P_3$, is

$$\nabla^2\omega + \frac{f_0\eta_0 p^2}{RT_0\gamma}\frac{\partial^2\omega}{\partial p^2} = 0 \qquad \text{(A.10)}$$

We now have three second-order differential equations which specify the vertical motion field for the entire atmosphere. The solutions are divided according to the various forcing functions on the right side of each of the above equations. ω_{11} is defined as that component of vertical motion associated with the vertical derivative of

the relative vorticity advection, and ω_{12} is defined as the vertical motion due to the advection of earth vorticity. Both of these forcing functions have a $\sin\frac{2\pi}{L}$ x $\cos\frac{2\pi}{L}$y dependence. Those terms with a $\sin\frac{2\pi}{L}(x+\lambda)\cos\frac{2\pi}{L}$y dependence are the forcing functions for ω_2. This component is forced by two identical contributions in each layer: one from the 1000 mb relative vorticity advection by the flow due to the mean north-south temperature gradient, and the other from the advection of this mean temperature gradient by the flow due to the 1000 mb geopotential field. The term in each equation with a $\sin\frac{2\pi}{L}\lambda$ $\sin\frac{4\pi}{L}$y dependence represents the advection of the perturbed temperature field by the 1000 mb flow, and provides the forcing for ω_3.

Solving the equations A.8 - A.10 entails the specification of six boundary conditions; we shall choose the first to be $\omega = 0$ at the lower boundary of layer 1 (at $P=P_0$), and the second to be $\omega = 0$ at the top of the atmosphere (P=0). The other boundary conditions are at the interfaces between layers; that is, ω matches at $P=P_2$, and at $P=P_3$, and $\frac{\partial\omega}{\partial P}$ from each layer is identical at $P=P_2$, and at $P=P_3$. That $\frac{\partial\omega}{\partial P}$ should match at the interior boundaries insures continuity of the horizontal divergence on a constant pressure surface in a hydrostatic atmosphere. Thus, these six boundary conditions specify uniquely the six constants in the general solution for ω.

The solutions for ω_{11} and ω_{12} which represent the adiabatic, inviscid quasi-geostrophic vertical motion, and provide the forcing for convergence (divergence) and intensification (filling) of the low center are given below.

For the first layer, $P_2 \leq P \leq P_0$:

$$w_{11} = \left\{ \frac{-q_1 A \left(\frac{P_0}{P_3}\right)^{q_2} \left(\frac{P}{P_0}\right)^{q_1}}{(q_2 - q_1)} + \frac{C q_1 \left(\frac{P_0}{P_2}\right)^{q_2} \left(\frac{P}{P_0}\right)^{q_1}}{(q_2 - q_1)} + E \left(\frac{P}{P_0}\right)^{q_1} \right.$$

$$\frac{-D P_2 \left(\frac{P_0}{P_2}\right)^{q_2} \left(\frac{P}{P_0}\right)^{q_1}}{(q_2 - q_1)} + \frac{B P_3 \left(\frac{P_0}{P_3}\right)^{q_2} \left(\frac{P}{P_0}\right)^{q_1}}{(q_2 - q_1)} + \frac{q_1 A \left(\frac{P}{P_3}\right)^{q_2}}{(q_2 - q_1)}$$

$$\left. \frac{-C q_1 \left(\frac{P}{P_2}\right)^{q_2}}{(q_2 - q_1)} + \frac{D P_2 \left(\frac{P}{P_2}\right)^{q_2}}{(q_2 - q_1)} - \frac{B P_3 \left(\frac{P}{P_3}\right)^{q_2}}{(q_2 - q_1)} + \left(\frac{a_1 P k_1}{b_1^2} + \frac{k_1 P}{b_1} \ln\left(\frac{P}{P_0}\right) \right) \right\}$$

$$\times \sin\left(\frac{2\pi}{L} x\right) \cos\left(\frac{2\pi}{L} y\right) \qquad \text{(A.11)}$$

$$w_{12} = \left\{ \frac{-q_1 A_4 \left(\frac{P_0}{P_3}\right)^{q_2} \left(\frac{P}{P_0}\right)^{q_1}}{(q_2 - q_1)} + \frac{q_1 C_4 \left(\frac{P_0}{P_2}\right)^{q_2} \left(\frac{P}{P_0}\right)^{q_1}}{(q_2 - q_1)} + E_4 \left(\frac{P}{P_0}\right)^{q_1} \right.$$

$$\frac{-D_4 P_2 \left(\frac{P_0}{P_2}\right)^{q_2} \left(\frac{P}{P_0}\right)^{q_1}}{(q_2 - q_1)} + \frac{B_4 P_3 \left(\frac{P_0}{P_3}\right)^{q_2} \left(\frac{P}{P_0}\right)^{q_1}}{(q_2 - q_1)} + \frac{q_1 A_4 \left(\frac{P}{P_3}\right)^{q_2}}{(q_2 - q_1)}$$

$$\left. \frac{-q_1 C_4 \left(\frac{P}{P_2}\right)^{q_2}}{(q_2 - q_1)} + \frac{D_4 P_2 \left(\frac{P}{P_2}\right)^{q_2}}{(q_2 - q_1)} - \frac{B_4 P_3 \left(\frac{P}{P_3}\right)^{q_2}}{(q_2 - q_1)} - \frac{k_4 P}{b_1} \right\} \sin\frac{2\pi}{L} x \cos\frac{2\pi}{L} y$$

(A.12)

For the second layer, $P_3 \leq P \leq P_2$,

$$w_{11} = \left\{ \frac{\left[B P_3 \left(\frac{P_0}{P_3}\right)^{q_2} - q_1 A \left(\frac{P_0}{P_3}\right)^{q_2} \right] \left(\frac{P}{P_0}\right)^{q_1}}{(q_2 - q_1)} + E \left(\frac{P}{P_0}\right)^{q_1} \right.$$

$$+ \frac{\left[P_2 \left(\frac{P}{P_2}\right)^{q_1} - P_2 \left(\frac{P_0}{P_2}\right)^{q_2} \left(\frac{P}{P_0}\right)^{q_1} \right] D}{(q_2 - q_1)} - \frac{C \left[q_2 \left(\frac{P}{P_2}\right)^{q_1} - q_1 \left(\frac{P_0}{P_2}\right)^{q_2} \left(\frac{P}{P_0}\right)^{q_1} \right]}{(q_2 - q_1)}$$

$$+ \frac{\left[q_1 A \left(\frac{P}{P_3}\right)^{q_2} - B P_3 \left(\frac{P}{P_3}\right)^{q_2} \right]}{(q_2 - q_1)} + \frac{-M_2 P^3}{(6a_1 - b_1)} - \frac{3 a_1 M_2 P_3 P^2}{(2a_1 - b_1)^2}$$

$$+ \frac{(M_1 + M_2 P_3 + M_2 P_2) P^2}{(2a_1 - b_1)} + \frac{(a_1 P_3^2 M_2 + b_1 M_1 P_3 + b_1 M_2 P_2 P_3) P}{b_1^2}$$

$$\left. + \frac{M_2 P_3 P^2}{(2a_1 - b_1)} \ln\left(\frac{P}{P_2}\right) + \frac{P_3^2 M_2 P \left(\ln\left(\frac{P}{P_2}\right)\right)}{b_1} \right\} \sin\frac{2\pi}{L} x \cos\frac{2\pi}{L} y \qquad \text{(A.13)}$$

$$w_{12} = \left\{ \frac{\left[B_4 P_3 - q_1 A_4 \right] \left(\frac{P_0}{P_3}\right)^{q_2} \left(\frac{P}{P_0}\right)^{q_1}}{(q_2 - q_1)} + E_4 \left(\frac{P}{P_0}\right)^{q_1} + \frac{\left[P_2 \left(\frac{P}{P_2}\right)^{q_1} - P_2 \left(\frac{P_0}{P_2}\right)^{q_2} \left(\frac{P}{P_0}\right)^{q_1} \right] D_4}{(q_2 - q_1)} \right.$$

$$- \frac{C_4 \left[q_2 \left(\frac{P}{P_2}\right)^{q_1} - q_1 \left(\frac{P_0}{P_2}\right)^{q_2} \left(\frac{P}{P_0}\right)^{q_1} \right]}{(q_2 - q_1)} + \frac{q_1 A_4 \left(\frac{P}{P_3}\right)^{q_2} - B_4 P_3 \left(\frac{P}{P_3}\right)^{q_2}}{(q_2 - q_1)}$$

$$\left. + \frac{M_4 P^2}{(2a_1 - b_1)} + \frac{M_4 P_3 P}{b_1} \right\} \sin\frac{2\pi}{L} x \cos\frac{2\pi}{L} y \qquad \text{(A.14)}$$

For the third layer, $0 \leq P \leq P_3$,

$$w_{11} = \left\{ E\left(\frac{p}{p_0}\right)^{q_{t1}} + \frac{\left[p_2\left(\frac{p}{p_2}\right)^{q_{t1}} - p_0\left(\frac{p_2}{p_0}\right)^{q_{t1}}\left(\frac{p}{p_0}\right)^{q_{t1}}\right]D}{(q_{t2}-q_{t1})} \right.$$

$$+ \frac{\left[q_{t1}\left(\frac{p_0}{p_2}\right)^{q_{t2}}\left(\frac{p}{p_0}\right)^{q_{t1}} - q_{t2}\left(\frac{p}{p_2}\right)^{q_{t1}}\right]C}{(q_{t2}-q_{t1})} + \frac{\left[p_3\left(\frac{p_0}{p_3}\right)^{q_{t2}}\left(\frac{p}{p_0}\right)^{q_{t1}} - p_3\left(\frac{p}{p_3}\right)^{q_{t1}}\right]B}{(q_{t2}-q_{t1})}$$

$$\left. + \frac{\left[q_{t2}\left(\frac{p}{p_3}\right)^{q_{t1}} - q_{t1}\left(\frac{p_0}{p_2}\right)^{q_{t2}}\left(\frac{p}{p_0}\right)^{q_{t1}}\right]A}{(q_{t2}-q_{t1})} \right\} \sin\frac{2\pi}{L}x \cos\frac{2\pi}{L}y \qquad \text{(A.15)}$$

$$w_{12} = \left\{ \left[E_4\left(\frac{p}{p_0}\right)^{q_{t1}}\right] + \frac{\left[p_2\left(\frac{p}{p_2}\right)^{q_{t1}} - p_0\left(\frac{p_2}{p_0}\right)^{q_{t1}}\left(\frac{p}{p_0}\right)^{q_{t1}}\right]D_4}{(q_{t2}-q_{t1})} \right.$$

$$+ \frac{\left[q_{t1}\left(\frac{p_0}{p_2}\right)^{q_{t2}}\left(\frac{p}{p_0}\right)^{q_{t1}} - q_{t2}\left(\frac{p}{p_2}\right)^{q_{t1}}\right]C_4}{(q_{t2}-q_{t1})} + \frac{\left[p_3\left(\frac{p_0}{p_3}\right)^{q_{t2}}\left(\frac{p}{p_0}\right)^{q_{t1}} - p_3\left(\frac{p}{p_3}\right)^{q_{t1}}\right]B_4}{(q_{t2}-q_{t1})}$$

$$\left. + \frac{\left[q_{t2}\left(\frac{p}{p_3}\right)^{q_{t1}} - q_{t1}\left(\frac{p_0}{p_3}\right)^{q_{t2}}\left(\frac{p}{p_0}\right)^{q_{t1}}\right]A_4}{(q_{t2}-q_{t1})} \right\} \sin\frac{2\pi}{L}x \cos\frac{2\pi}{L}y$$

(A.16)

where $k_1 = \left(\frac{2\pi}{L}\right)^3 \frac{R a \hat{T}\, 4}{T_0 \gamma\, f_0}$, $k_4 = \left(\frac{-2\pi}{L}\right)\frac{\hat{T}}{T_0\gamma}\frac{\partial f}{\partial y}$, $a_1 = \frac{f_0 \eta_0}{R T_0 \gamma}$, $b_1 = 2\left(\frac{2\pi}{L}\right)^2$

$$q_{t1} = .5 + .5\sqrt{1 + 4\left(b_1/a_1\right)}, \quad q_{t2} = 1 - q_{t1}, \quad M_1 = \frac{4 R a \hat{T}}{f_0 (p_2 - p_3) T_0 \gamma \left(\frac{2\pi}{L}\right)^3 \ln\left(\frac{p_0}{p_2}\right)}$$

$$M_2 = \frac{4\,R a \hat{T}}{f_0 (P_2 - P_3)^2 \gamma T_0} \left(\frac{2\pi}{L}\right)^3 , \quad M_4 = \frac{-\hat{T}}{\gamma T_0 (P_2 - P_3)} \left(\frac{2\pi}{L}\right) \frac{\partial f}{\partial \gamma}.$$

$$A = \left[\frac{-M_2 P_3^3}{(6a_1 - b_1)}\right] - \frac{3 a_1 M_2 P_3^3}{(2a_1 - b_1)^2} + \frac{2 a_1 P_3^2 \left(M_1 + M_2 P_2 + M_2 P_3 \ln\left(\frac{P_3}{P_2}\right)\right)}{b_1 (2a_1 - b_1)}$$

$$+ \frac{M_2 P_3^3}{(2a_1 - b_1)} + \frac{a_1 M_2 P_3^3}{b_1^2}$$

$$B = \frac{-3 M_2 P_3^2}{(6a_1 - b_1)} - \frac{6 a_1 M_2 P_3^2}{(2a_1 - b_1)^2} + \frac{(2a_1 + b_1) M_1 P_3 + (2(a_1 + b_1)) M_2 P_3^2 + (2a_1 + b_1) M_2 P_2 P_3}{(2a_1 - b_1) b_1}$$

$$+ \frac{a_1 P_3^2 M_2}{b_1^2} + \frac{(2a_1 + b_1) M_2 P_3^2 \ln\left(\frac{P_3}{P_2}\right)}{(2a_1 - b_1) b_1}$$

$$C = \frac{a_1 P_2 (P_3^2 M_2 - k_1)}{b_1^2} + \frac{P_2 \left(M_1 P_3 - k_1 \ln\left(\frac{P_2}{P_0}\right)\right)}{b_1} - \frac{M_2 P_2^3}{(6a_1 - b_1)} - \frac{3 a_1 M_2 P_3 P_2^2}{(2a_1 - b_1)^2}$$

$$+ \frac{P_2^2 (M_1 + P_2 M_2)}{(2a_1 - b_1)} + \frac{2 a_1 M_2 P_3 P_2^2}{b_1 (2a_1 - b_1)}$$

$$D = \frac{a_1 (P_3^2 M_2 - k_1)}{b_1^2} + \frac{P_3 (M_1 + P_3 M_2)}{b_1} - \frac{k_1}{b_1}\left[\ln\left(\frac{P_2}{P_0}\right) + 1\right] - \frac{3 M_2 P_2^2}{(6a_1 - b_1)}$$

$$- \frac{6 a_1 M_2 P_3 P_2}{(2a_1 - b_1)^2} + \frac{2 P_2 (M_1 + M_2 P_2)}{(2a_1 - b_1)} + \frac{2 (a_1 + b_1) M_2 P_2 P_3}{b_1 (2a_1 - b_1)}$$

$$E = \frac{-a_1 p_0 k_1}{b_1^2},$$

$$A_4 = \frac{2a_1 M_4 p_3^2}{b_1(2a_1 - b_1)}, \quad B_4 = \frac{(2a_1 + b_1) M_4 p_3}{b_1(2a_1 - b_1)}$$

$$C_4 = \frac{M_4 p_2^2}{(2a_1 - b_1)} + \frac{p_2(p_3 M_4 + k_4)}{b_1},$$

$$D_4 = \frac{2 M_4 p_2}{(2a_1 - b_1)} + \frac{(M_4 p_3 + k_4)}{b_1},$$

and

$$E_4 = \frac{k_4 p_0}{b_1}.$$

REFERENCES

American Association for the Advancement of Science, 1979: Seasat mission overview. Science, 204, 1405-1424.

Anthes, R.A., and D. Keyser, 1979: Tests of a fine-mesh model over Europe and the United States. Mon. Wea. Rev., 107, 963-984.

Arakawa, A., 1968: Parameterization of cumulus convection. Proc. WMO/IUGG Symp. Numerical Weather Prediction, Tokyo, 26 November-4 December, 1968, Japan Meteor. Agency, 8, 1-6.

_____, and W.H. Schubert, 1974: Interaction of a cumulus cloud ensemble with the large-scale environment. Part I. J. Atmos. Sci., 31, 674-701.

Austin, J.M., 1947: An empirical study of certain rules of forecasting the movement and intensity of cyclones. J. Met., 4, 16-20.

Berlin, Freien Universität. Institut für Meteorologie. Meteorologische Abhandlungen. Serie B Grundlagenmaterial, Bands 17 and 23.

Bjerknes, J., 1954: The diffluent upper trough. Arch. Meteor. Geophys. Bioklim., A7, 41-46.

Blackmon, M.L., J.M. Wallace, N.-C. Lau, and S.L. Mullen, 1977: An observational study of the Northern Hemisphere wintertime circulation. J. Atmos. Sci., 34, 1040-1053.

Bosart, L.F., 1981: The President's Day snowstorm of 18-19 February 1979: a subsynoptic scale event. to appear in July 1981 Mon. Wea. Rev.

_____, and F. Sanders, 1981: The Johnstown flood of July 1977: A long-lived convective storm. to appear in June 1981 Mon. Wea. Rev.

Böttger, H., M. Eckhardt, and U. Katergiannakis, 1975: Forecasting extratropical storms with hurricane intensity using satellite information. J. Appl. Meteor., 14, 1259-1265.

Bunker, A.F., 1976: Computations of surface energy flux and annual air-sea interaction cycles of the North Atlantic ocean. Mon. Wea. Rev., 104, 1122-1140.

Charney, J.G., 1947: The dynamics of long waves in a baroclinic westerly current. J. Meteor., 4, 135-162.

_____, and A. Eliassen, 1964: On the growth of the hurricane depression. J. Atmos. Sci., 21, 68-75.

Druyan, L.M., 1974: Short-range forecasts with the GISS model of the global atmosphere. Mon. Wea. Rev., 102, 269-279.

Eady, E.T., 1949: Long waves and cyclone waves. Tellus, 1, 33-52.

Ertel, H., 1942: Ein neuer hydrodynamischer wirbelsatz. Meteor. Z., 59, 277-281.

Fjørtoft, R., 1952: On a numerical method of integrating the barotropic vorticity equation. Tellus, 4, 179-194.

Frank, W.M., 1977a: The structure and energetics of the tropical cyclone I: storm structure. Mon. Wea. Rev., 105, 1119-1135.

_____, 1977b: The structure and energetics of the tropical cyclone II: dynamics and energetics. Mon. Wea. Rev., 105, 1136-1150.

Gall, R., R. Blakeslee, and R.C.J. Somerville, 1979: Cyclone-scale forcing of ultralong waves. J. Atmos. Sci., 36, 1692-1698.

Gidel, L.T., and M.A. Shapiro, 1979: The role of clear air turbulence in the production of potential vorticity in the vicinity of upper tropospheric jet streams-frontal systems. J. Atmos. Sci., 36, 2125-2138.

Gray, W.M., and D.J. Shea, 1973: The hurricane's inner core region, II. Thermal stability and dynamic characteristics. J. Atmos. Sci., 30, 1565-1576.

Grube, P., 1979: Convection-induced temperature change in GATE. Col. State Dept. of Atmospheric Science report #305. 128 pp.

Haurwitz, B., and J.M. Austin, 1944: Climatology (see p. 187 and Plate XVI). McGraw-Hill, 410 pp.

Holliday, C.R., and A.H. Thompson, 1979: Climatological characteristics of rapidly intensifying typhoons. Mon. Wea. Rev., 107, 1022-1034.

Holopainen, E.O., and A.H. Oort, 1981: On the role of large-scale transient eddies in the maintenance of the vorticity and enstrophy of the time-mean atmospheric flow. J. Atmos. Sci., 38, 270-280.

Harrold, T.W., and K.A. Browning, 1969: The polar low as a baroclinic disturbance. Quart. J. Rev. Meteor. Soc., 95, 710-723.

Holton, J.R., 1972: An Introduction to Dynamic Meteorology. Academic Press, 320 pp.

Jalu, M., 1973: Étude des perturbations cycloniques extratropicales par l'imagerie des satellites. Les Satellites Meteorologiques, Centre Nationale d'Études Spatiales, 409-422.

James, R.W., 1979: Anatomy of a storm. Mar. Wea. Log., 23, 71-75.

Kasahara, A., and W.M. Washington, 1971: General circulation experiments with a six-layer NCAR model, including orography, cloudiness, and surface temperature calculations. J. Atmos. Sci., 28, 657-701.

Kesel, P.G., and F.J. Winninghoff, 1972: The Fleet Numerical Weather Central operational primitive equation model. Mon. Wea. Rev., 100, 360-373.

Krishnamurti, T.M., Y. Ramanathan, H.-L. Pan, R.J. Pasch, and J. Molinari, 1980: Cumulus parameterization and rainfall rates I. Mon. Wea. Rev., 108, 465-472.

Koss, W.J., 1976: Linear stability of CISK-induced disturbances: Fourier component eigenvalue analysis. J. Atmos. Sci., 33, 1195-1222.

Kuo, H.L., 1965: On the formation and intensification of tropical cyclones through latent heat release by cumulus convection. J. Atmos. Sci., 22, 40-63.

Leary, C., 1971: Systematic errors in operational National Meteorological Center primitive-equation surface prognoses. Mon. Wea. Rev., 99, 409-413.

Lord, S.J., 1978: Development and observational verification of a cumulus cloud parameterization. Ph. D. thesis, UCLA, 359 pp.

Maddox, R.A., 1980: Mesoscale convective complexes. Bull. Amer. Meteor. Soc., 61, 1374-1387.

Manabe, S., 1956: On the contribution of heat released by condensation to the change in pressure pattern. J. Met. Soc. Japan, 34, 308-320.

_____, J. Smagorinsky, and R.F. Strickler, 1965: Simulated climatology of a general circulation model with a hydrological cycle. Mon. Wea. Rev., 93, 769-798.

Mansfield, D.A., 1974: Polar lows: the development of baroclinic disturbances in cold air outbreaks. Quart. J. Rev. Meteor. Soc., 100, 541-554.

Meteorological Office, 1977: The Marine Observer's Log. The Marine Observer, XLVII, 7-9.

Miller, B.I., 1958: On the maximum intensity of hurricanes. J. Meteor., 15, 184-185.

NOAA, 1976: The GOES/SMS User's Guide. 118 pp.

NOAA, 1979: Smooth log, North Atlantic weather, September and October 1978. Mar. Wea. Log, 23, p. 104.

NOAA, 1981: Rough log, North Atlantic weather, October and November 1980. Mar. Wea. Log, 25 p. 59.

Ooyama, K., 1969: Numerical simulation of the life cycle of tropical cyclones. J. Atmos. Sci., 26, 3-40.

Petterssen, S., 1956: Weather Analysis and Forecasting, Vol. 1, Motion and Motion Systems. McGraw-Hill, 428 pp.

_____, D.L. Bradbury, and K. Pedersen, 1962: The Norwegian cyclone models in relation to heat and cold sources. Geof. Publ., 24, 243-280.

Phillips, N.A., 1954: Energy transformations and meridional circulations associated with simple baroclinic waves in a two-level quasi-geostrophic model. Tellus, 6, 273-286.

_____, 1963: Geostrophic motion. Reviews of Geophysics., 1, 123-176.

_____, 1980: Two examples of satellite temperature retrievals in the North Pacific. Bull. Am. Meteor. Soc., 61, 712-717.

Pyke, C.B., 1965: On the role of air-sea interaction in the development of cyclones. Bull. Amer. Meteor. Soc., 46, 4-15.

Rasmussen, E., 1979: The polar low as an extratropical CISK disturbance. Quart. J. Roy. Meteor. Soc., 105, 531-549.

Reed, R.J., 1979: Cyclogenesis in polar air streams. Mon. Wea. Rev., 107, 38-52.

Rice, R.B., 1979: Tracking a killer storm. Sail, 10, 106-107.

Riehl, H., and J.S. Malkus, 1961: Some aspects of Hurricane Daisy, 1958. Tellus, 181-213.

Sanders, F., 1971: Analytic solutions of the non-linear omega and vorticity equation for a structurally simple model of disturbances in the baroclinic westerlies. Mon. Wea. Rev., 99, 393-407.

_____, 1976: The effect of incorrect initial analysis on the predicted deepening of oceanic cyclones. Paper delivered at the Sixth AMS Conference on Weather Forecasting and Analysis, May 1976, 278-284.

_____, and J.R. Gyakum, 1980: Synoptic-dynamic climatology of the "bomb". Mon. Wea. Rev., 108, 1589-1606.

Shuman, F.G., and J.B. Hovermale, 1968: An operational six-layer primitive equation model. J. Appl. Meteor., 7, 525-547.

Simpson, J., 1969: On some aspects of air-sea interaction in middle latitudes. Deep-Sea Res., Suppl., 16, 233-261.

_____, 1973: The global energy budget and the role of cumulus clouds. NOAA Tech. Mem. ERL WMPO-8. 175 pp.

Smith, R.K., 1980: Tropical cyclone eye dynamics. J. Atmos. Sci., 37, 1227-1232.

Somerville, R.C.J., P.H. Stone, M. Halson, J.G. Hansen, J.S. Hogan, L.M. Druyan, G. Russell, A.A. Cadis, W.J. Quirk, and J. Tenenbaum, 1974: The GISS model of the global atmosphere. J. Atmos. Sci., 31, 84-117.

Spiegler, D.B., 1971: The unnamed Atlantic tropical storms of 1970. Mon. Wea. Rev., 99, 966-976.

Staley, D.O., 1960: Evaluation of potential vorticity changes near the tropopause and the related vertical motions, vertical advection of vorticity, and transfer of radioactive debris from stratosphere to troposphere. J. Meteor., 17, 591-620.

_____, and R.L. Gall, 1977: On the wavelength of maximum baroclinic instability. J. Atmos. Sci., 34, 1679-1688.

Sverdrup, H.U., M.W. Johnson, and R.H. Fleming, 1942: The Oceans, Their Physics, Chemistry, and General Biology. Prentice-Hall, 1087 pp.

Taubensee, R.E., 1978: Weather and circulation of September 1978 - a warm month in the middle of the country. Mon. Wea. Rev., 106, 1750-1757.

Tracton, M.S., 1972: The role of cumulus convection in the development of extratropical cyclones. Ph.D. thesis, MIT, 157 pp.

_____, 1973: The role of cumulus convection in the development of extratropical cyclones. Mon. Wea. Rev., 101, 573-593.

_____, A. Desmarais, R. van Haaren, and R. McPherson, 1980: The impact of satellite soundings upon the National Meteorological Center's analysis and forecast system-data systems test results. Mon. Wea. Rev., 108, 543-586.

Weickmann, H.K., A.B. Long, and L.R. Hoxit, 1977: Some examples of rapidly growing oceanic cumulonimbus clouds. Mon. Wea. Rev., 105, 469-476.

Willoughby, H.E., 1979: Forced secondary circulations in hurricanes. J. Geophys. Res., 84, 3173-3183.

Winston, J.S., 1955: Physical aspects of rapid cyclogenesis in the Gulf of Alaska. Tellus, 7, 481-500.

Yamasaki, M., 1968: Numerical simulation of tropical cyclone development with the use of primitive equations. J. Meteor. Soc. Japan, 46, 178-201.

Yip, T.-C., and H. -R. Cho, 1980: Dynamics of quasi-geostrophic systems with cumulus convection. University of Toronto.

BIOGRAPHICAL NOTE

The author was born February 7, 1954 in Alexandria, Virginia. He grew up in the Washington, D.C. area, and attended public schools in Fairfax County, Virginia. During this period, he developed an interest in various pathological weather phenomena, such as thunderstorms, tornadoes, and blizzards. A particularly rewarding experience for him occurred during January, 1966, when the famous "blizzard of '66" struck the Washington, D.C. area. During the summer of 1972, he worked for the U.S. Geological Survey on a survey team investigating the extent of flooding caused by tropical storm Agnes. Following this experience, he decided that carrying a big stick around for someone else to read was not what it was cracked up to be. He enrolled at the Pennsylvania State University in September, 1972, and graduated with high honors in May, 1975, with a B.S. degree in meteorology. During the summers of 1974 and 1975, he worked in Dr. John Hovermale's hurricane research group at the National Meteorological Center. The author enrolled as a graduate student in meteorology at MIT in September 1975, after which time, he was introduced to the "bomb" by Professor Sanders.